Unveiling the mass assembly history of the Milky Way from its stellar halo

by

Daniel Horta Darrington

A thesis submitted in partial fulfillment for the
degree of Doctor of Philosophy

September 1, 2022

Declaration

The work presented in this thesis was carried out at the Astrophysics Research Institute, Liverpool John Moores University. Unless otherwise stated, it is the original work of the author.

While registered as a candidate for the degree of Doctor of Philosophy, for which submission is now made, the author has not been registered as a candidate for any other award. This thesis has not been submitted in whole, or in part, for any other degree.

Daniel Horta Darrington
Astrophysics Research Institute
Liverpool John Moores University
IC2, Liverpool Science Park
146 Brownlow Hill
Liverpool
L3 5RF
UK

September 1, 2022

Abstract

Stellar halos of galaxies retain crucial clues to their mass assembly history. It is in these galactic components that the remains of cannibalised galactic building blocks are deposited. For the case of the Milky Way, the opportunity to analyse the stellar halo's structure on a star-by-star basis in a multi-faceted approach provides a basis from which to infer its past and assembly history in unrivalled detail. Moreover, the insights that can be gained about the formation of the Galaxy not only help constrain the evolution of our Milky Way, but may also help place constraints on the formation of other disc galaxies in the Universe. This thesis aims to make progress toward answering the most fundamental question in the field of Galactic archaeology: *"How did the Milky Way form?"* Through the effort to answer this question, this thesis presents new insights into aspects of the history of assembly and evolution of our Galaxy and measurements of the structure of various of its Galactic components.

Providing further insight into the accretion history and mass assembly of the Milky Way, I present a detailed analysis of the properties of Milky Way halo stars in the heart of the Galaxy contained in both the APOGEE and *Gaia* data sets. I present evidence for the discovery of a new halo substructure (whose progenitor we attribute the name of "*Heracles*") that, given its chemical composition and dynamical properties, is likely to be the debris from a major building block of the Milky Way. I also compare its properties with expectations from the EAGLE numerical simulations to ascertain its nature, and make a quantitative prediction of the stellar mass of the disrupted satellite galaxy to comprise approximately one third of the estimated total stellar halo mass.

To ascertain the reality and nature of halo substructures, and to place further constraints on the mass assembly history of the Galaxy, I perform a detailed qualitative and quantitative analysis of the chemical compositions of halo substructures in the Milky Way

with APOGEE and *Gaia* data. The findings from this study revealed that many halo substructures identified in recent years, conjectured to be the debris from individual satellite accretions, likely belong to the *Gaia*-Enceladus/Sausage accretion event. They also showed that the Heracles halo substructure is statistically different from in situ populations given its chemical compositions, further confirming its accreted nature.

To understand how much mass dissolved and/or evaporated globular clusters (GC) contribute to the total stellar halo mass budget, I perform a density modelling analysis of stellar halo populations. By identifying GC escapees using a Gaussian mixture modelling and chemical tagging procedure, I model their density distribution accounting for the APOGEE selection function and assess their ratio to the halo field. The main finding of this work showed that in the inner $\sim$2-3 kpc from the Galactic centre, there is a much higher incidence of dissolved/evaporated GC stars that is on the order of five to six times larger than in the outer $\sim$10 kpc region.

In order to decipher the origin of the Galactic GC system, I undertook a study aimed at comparing the chemical composition of previously categorised GC subgroups classified based on their orbits. More specifically, by determining a homogeneous sample of GC star members in the APOGEE DR16 survey, and comparing the mean [α/Fe] and [Fe/H] abundances of GCs with field populations, I was able to place constraints on the origin of GCs in the Milky Way, that in turn help place constraints on the accretion history of the Galaxy.

The above results place constraints on our current understanding of the accretion and mass assembly history of the Milky Way. In discovering new halo substructures, assessing the reality of known ones, modelling the density of stars contributed from dissolved/evaporated GCs, and deciphering the origin of the Galactic GC system, I have tackled the question of *"How did the Milky Way form?"* from numerous different angles. All the findings contained in this thesis help pave the way for future work towards the goal of fully reconstructing the assembly history of our Galaxy and using that understanding to formulate robust and general models for the formation of disc galaxies.

Publications

During the course of the preparation of this thesis, the work within Chapters 2, 3, 4, and 5 has been presented in the following jointly authored publications:

1 *'Evidence from APOGEE for the presence of a major building block of the halo buried in the inner Galaxy'*
Horta, Danny., Schiavon, Ricardo P., Mackereth, J Ted., Pfeffer, Joel., Mason, Andrew C., Kisku, Shobhit., Fragkoudi, Francesca., Allende Prieto, Carlos., Cunha, Katia., Hasselquist, Sten., Holtzman, Jon., Majewski, Steven R., Nataf, David., O'Connell, Robert W., Schultheis, Mathias., Smith, Verne V., MNRAS, Volume 500, Issue 1.

2 *'The chemical characterisation of halo substructure in the Milky Way based on APOGEE'*
Horta, Danny., Schiavon, Ricardo P., Mackereth, J. Ted., Weinberg, David H., Hasselquist, Sten., Feuillet, Diane., O'Connell, Robert W.., Anguiano, Borja., Allende-Prieto, Carlos., Beaton, Rachael L. search by orcid., Bizyaev, Dmitry., Cunha, Katia., Geisler, Doug., García-Hernández, D. A.., Holtzman, Jon., Jönsson, Henrik., Lane, Richard R.., Majewski, Steve R.., Mészáros, Szabolcs., Minniti, Dante., Nitschelm, Christian., Shetrone, Matthew., Smith, Verne V.., Zasowski, Gail, arXiv, 2204.04233.

3 *'The contribution of N-rich stars to the Galactic stellar halo using APOGEE red giants'*
Horta, Danny., Mackereth, J. Ted., Schiavon, Ricardo P., Hasselquist, Sten., Bovy, Jo., Allende Prieto, Carlos., Beers, Timothy C.., Cunha, Katia., García-Hernández, D. A.., Kisku, Shobhit S.., Lane, Richard R.., Majewski, Steven R.., Mason, Andrew C.., Nataf, David M., Roman-Lopes, Alexandre., Schultheis, Mathias., MNRAS, Volume 500, Issue 4.

4 *'The chemical compositions of accreted and in situ galactic globular clusters according to SDSS/APOGEE'*

Horta, Danny., Schiavon, Ricardo P., Mackereth, J. Ted., Beers, Timothy C., Fernández-Trincado, José G., Frinchaboy, Peter M.., García-Hernández, D. A., Geisler, Doug., Hasselquist, Sten., Jönsson, Henrik., Lane, Richard R., Majewski, Steven R., Mészáros, Szabolcs., Bidin, Christian Moni., Nataf, David M., Roman-Lopes, Alexandre., Nitschelm, Christian., Vargas-González, J.., Zasowski, Gail., MNRAS, Volume 493, Issue 3.

Publication 1 forms the basis of Chapter 2, and is based on the discovery of a major building block of the Milky Way made by D. Horta using the APOGEE DR16 and *Gaia* DR2 data. All the analysis carried out was performed by D. Horta, with major scientific contributions from R.P. Schiavon. Accreted satellite galaxies were identified in the EAGLE simulations by J. Pfeffer, and significant scientific contributions were provided by J.T. Mackereth. The manuscript was prepared by D. Horta and R.P. Schiavon, with important contributions from the co-authors, colleagues, and an anonymous referee.

Publication 2 comprises Chapter 3. It provides a detailed chemical abundance analysis of all the Milky Way halo substructures using the *Gaia* DR3 and APOGEE DR17 data. All analysis was performed by D. Horta, with significant contributions from R.P. Schiavon. The manuscript was prepared by D. Horta, with important contributions from R.P. Schiavon, J.T. Mackereth, and moderate contributions from all the other co-authors.

Publication 3 forms the basis of Chapter 4. It provides a density modelling study of stellar halo populations to assess the contribution of disrupted/evaporated globular cluster stars to the total stellar halo mass budget of the Milky Way. This publication used APOGEE DR16 and *Gaia* DR2 data. All the analysis was carried out by D. Horta with pivotal scientific contributions from J.T. Mackereth. The manuscript was prepared by D. Horta, with important contributions from J.T. Mackereth and R.P. Schiavon, and moderate contributions from the other co-authors and anonymous referee.

Publication 4 is the basis of Chapter 5. In this work, a homogeneous globular cluster catalogue was determined using the APOGEE DR16 data in order to compare the

chemical abundances of Galactic globular clusters. The analysis was carried out by D. Horta, with important contributions from R.P. Schiavon. The manuscript was prepared by D. Horta, with pivotal contributions from R.P. Schiavon, and moderate contributions from all the co-authors and anonymous referee.

In addition to the publications that comprise the entirety of this thesis, there are two other articles that have been published during the course of this doctoral degree. For the details and results contained in these works, see Horta et al. (2021b) and Horta et al. (2022).

Acknowledgements

I would first like to express my gratitude towards my supervisor, Ricardo Schiavon. Ricardo, you took me in when I was in a tight spot, and for that I will be forever grateful. Since day one you have provided me with wise guidance and a warm embrace. I will cherish our days together at the ARI for the rest of my days. You have been an excellent PhD supervisor and mentor. From the bottom of my heart, obrigado.

To my second supervisor Nate Bastian, I thank you for all the help and chats over the years, and for always being there when I needed someone to talk to. To my elder PhD brother Ted, I thank you for all your help and assistance. To Marie, my labs guru, thank you for being so helpful and caring. Your passion for helping students does not go unnoticed. To Phil and Sue, thank you for great chats and for taking me to see an Everton match at Goodison Park. To Alis Deason and Ian McCarthy, thank you for taking the time to examine this thesis, and for an insightful and pleasant viva examination.

In addition to my ARI mentors, I would be neglectful not to mention my appreciation to other important academics that have made a meaningful impact during my time as a PhD student. To Melissa Ness, thank you for being so friendly and kind, and for "adopting" me as a student over the past two years. To Emily Cunningham, Robyn Sanderson, Kathryn Johnston, and other Flatiron CCA members who have helped me along the way, thank you for all your guidance during the second half of my PhD. To Yuan-Sen Ting, thank you for great scientific chats and for introducing me to the world of machine-learning. To Holger Baumgardt, Tamara Davis, Sara Sweet, Khaled Said, Cullan Howlett, and many others at UQ, thank you for your warm welcome and for looking after me whilst in Australia. To Sten Hasselquist, Katia Cunha, Rachael Beaton, Jon Holtzman, Chris Hayes, Steve Majewski, Gail Zasowski, David Nataf, David

Weinberg, Mathias Schultheis, Carlos Allende Prieto, and the rest of the APOGEE team, thank you for all your help.

Alongside my supervisors and mentors, I must acknowledge all the friends I have made at the ARI whilst undertaking my PhD. To Joaquin and Joe, my brothers from other mothers and my Liverpool família, I cannot thank you enough for everything you have done for me and for being who you are. My time at the ARI would not have been the same without you. Siempre tendréis una cama en mi casa, y un lugar en mi corazón. To Tom, Sarah, Alex, and Andrew, thank you for letting me stay at yours when I had nowhere to live, and for being great friends. To Shobhit, thank you for being an awesome colleague. All of you, thank you for making my time at the ARI a good one. Last but not least, thank you Anna Hodgkinson for being so caring and helpful to me and all astronomers at the ARI.

In addition to my academic mentors, I must acknowledge my basketball coach Marc Steutel. Marc, thank you ever so much for giving me a chance and taking in a young spanish guard as your player. Thank you for trusting in me to become a better athlete and human being. I would not be in this position if it wasn't for you letting me skip sport science class to let me make my A-level physics one, as well as all your help over the years.

The final and most important thank you goes to my family. Mum, words cannot express how much you mean to me, and how much I appreciate everything you have ever done for myself and for Alex. I will forever be in debt to you. Thank you for always being there when I needed someone, and for being the solid rock I needed during tough times. You are the best mother I could have ever wished for. To my brother Alex, thank you ever so much for being my right hand and my partner in crime. Your strength and success keeps me going, and makes me proud to say I am your older brother. To my beautiful Debra, my soulmate and other half. Thank you for being who you are. Your endless love boosts me, and you motivate me to be a better me. I don't know what I would do without you. To my nana and grandad, thank you for being there for me. Papa, mi ángel de la guardia, you may not be physically with us anymore but you walk alongside me daily and guide me in times of need. All of you, thank you for everything. This would not have possible without you. Os quiero mucho.

"Equipped with his five senses, man explores the Universe around him and calls the adventure science"

– Edwin Hubble

"If you do the work, you get rewarded. There are no shortcuts in life"

– Michael Jordan

"Con dos cojones"

– Susan Darrington & Xavier Horta Mora

Contents

List of Figures

List of Tables

To my family, friends, and ángel de la guardia ...

Chapter 1

Introduction

"In all things of nature there is something of the marvelous"

– Aristotle

In our current cosmological framework, the Universe is thought to be comprised of three types of substances: a mysterious dark energy (∼68%), believed to be the driving force of the accelerated expansion of the Universe; an elusive dark matter (∼27%), a particle that still remains undetected and whose gravitational influence strongly affects how matter is spatially distributed in the Universe; and baryonic (or more commonly referred to as "normal") matter (∼5%), visible thanks to its ability to emit, reflect, and/or absorb/scatter electromagnetic radiation. The latter is the most well understood type, and comprises all of the atoms in the Universe –which are the building blocks that make up molecules, planets, stars, and galaxies–, including those of which all living things are made of.

The baryonic matter that we observe in the Universe today, in addition to dark energy and dark matter, are the direct result of the complex interplay between the forces of nature (namely, gravity, the electromagnetic force, the strong nuclear force, and the weak nuclear force). Therefore, understanding how matter and energy are formed and how they are distributed in the Universe are profound questions that are deeply connected to the very nature of our existence. Answering these questions is the main goal of astrophysics and cosmology.

It is postulated that there are over two hundred billion galaxies in the Universe, all of which range in properties such as shape, size, and colour. Despite this vast number, there is only one galaxy for which I have the closest access to understand subtle aspects of its formation and evolution. It is also likely the most important galaxy (from a

philosophical point of view), as it is the one in which *we*, the human species, reside in. This galaxy is the Milky Way – i.e., "*the Galaxy*".

"*How did the Milky Way form?*" is the foundational question of the field of Galactic archaeology – the branch of astronomy dedicated to understanding how our Galaxy came into existence by unearthing fossilised records imprinted in its constituent stars–. The ability to examine the Galaxy on a star-by-star basis provides the opportunity to fully characterise the structure and history of the Milky Way. Furthermore, under the assumption that the Galaxy is typical for its characteristics (e.g., mass, size, shape), the ability to examine it and test models of its formation and evolution in unrivalled detail provides the means to generalise any insight of galaxy formation from the Milky Way to the extra-Galactic realm. This enables the Milky Way to also serve as a test-bed for current galaxy formation models, and to some degree even for our current cosmological paradigm: Λ-Cold Dark Matter (ΛCDM). Thus, questions such as "*How the Milky Way assembled its mass?*" and "*how did the Milky Way evolve into its present day structure?*" are a double-edged sword that can help solve important puzzles both in the Galactic and extra-Galactic realms. However, in order to use the Milky Way as a laboratory to test general galaxy formation models, one must first answer a fundamental question: *is the Milky Way a typical galaxy?*

The answer to this question provides the means of properly gauging any extrapolation for general galaxy formation models. If the Milky Way *is* typical, whose formation and evolution is representative of the majority of galaxies with similar characteristics, then it can be used as a robust test-bed on which to develop general galaxy formation models. If, however, the Milky Way is somehow *atypical*, for example in its assembly history, dark matter content, stellar population distribution, structure, or any other characteristic (or combination thereof), then the processes responsible for the current state of the MW cannot be assumed to have a general nature. Nevertheless, detailed insights into the MW history must shed *some* light into galaxy formation models. Moreover, they are obviously important to help understand our own place in the universe.

In order to answer all these vital questions, one must perform a detailed and robust examination of the complexities of the Milky Way. In this thesis, I intend to make progress towards such an understanding by:

- Developing a state-of-the-art picture of the present day spatial structure of the Milky Way, and modelling observable data to infer general properties of the Galaxy and its individual Galactic components.
- Making inferences on the mass assembly history and evolution of the Galaxy by unearthing fossilised records imprinted in its constituent stellar populations using

the latest Milky Way data, and comparing these to expectations from cosmological numerical simulations in order to frame the Galaxy in a cosmological setting.

The remainder of this chapter is divided into two sub-sections. The first part, Section 1.1 presents a broad introduction on our understanding of the formation and present day structure of the Milky Way. Section 1.2 provides an overview of the field of Galactic archaeology, and discusses how this branch of astrophysics has done remarkably well at shedding light into how our Galaxy has assembled its mass and is spatially distributed, and how we can utilise this information to map galaxy formation in a more general context. I then finalise the introduction chapter by presenting the outline for this thesis.

1.1 The Milky Way galaxy

First postulated by Immanuel Kant (1755) and later confirmed with "star-gages" measurements by William Herschel (1785, Timberlake, 2011), we reside in the disc component of the Milky Way (with the latest measurements positioning the Sun in the Orion spiral arm, approximately ~ 8.178 kpc from the Galactic centre (Gravity Collaboration, 2019) and ~ 0.02 kpc above the midplane (Bennett & Bovy, 2019)). The advent of better telescopes, the efforts of many astronomers, and the findings of Edwin Hubble in 1926 then showed that our Galaxy is just one of the billions of galaxies in the Universe (Hubble, 1926), and that (many of) the observed "nebulae", previously conjectured to be clouds of dust and gas belonging to the Milky Way, were in fact distant galaxies outside our Galactic home. We now know that the Milky Way can be loosely classified as a "*barred*-spiral" galaxy (or more precisely, an Sbc galaxy Gerhard, 2002), and that it sits in the so called "green valley" in the colour-magnitude diagram of galaxies (in between the old red galaxies and the young blue ones). It is a somewhat massive ($\sim 10^{12} M_{\odot}$ Fragione & Loeb, 2017; Posti & Helmi, 2019; Watkins et al., 2019) and sizeable galaxy ($\sim$25-30 kpc diameter for the Galaxy's disc Bland-Hawthorn & Gerhard, 2016, and $\sim$290 kpc for its dark matter halo Deason et al., 2020), that sits in the Local Group, part of the Virgo supercluster of galaxies. These findings are a clear demonstration of the great strides we have made as a community towards more properly characterising our observable Universe and the Galaxy, and have enabled us to compare the Milky Way with other galaxies we observe. However, much of this knowledge is currently being tested with the advent of the latest –and more powerful– data.

Morphology, mass, stellar population content, and chemical compositions of its various baryonic constituents are perhaps the most obvious characteristics one may focus on when attempting to characterise the Milky Way and compare it to extra-Galactic counterparts. However, equally as interesting is how the Milky Way resembles/differs from

other galaxies with regards to its mass assembly history. With respect to its structure, is well agreed upon that the Galaxy has an extended disc (comprised of several spiral arms), a central region referred to as "the bulge", a bar, a diffuse stellar halo, and an all-encompassing dark matter halo. The precise details of these features are difficult to establish for a number of reasons, namely: the inner spatial regions of the Galaxy are obscured by dust extinction, specific stellar populations (e.g., stellar halo) are overshadowed by the more prominent Galactic disc, and that we are unable to directly detect dark matter or understand its most fundamental properties. In terms of its assembly history, it was first postulated that the Galaxy assembled via a monolithic collapse of gas from a so-called "protogalaxy" (Eggen et al., 1962). This hypothesis was later challenged by Searle & Zinn (1978), who argued that the outer regions of the stellar halo continued to collapse for time after the collapse of its central regions had been completed. It is now conjectured that the Milky Way's stellar halo is bimodal in nature (i.e., the "dual halo" e.g., Carollo et al., 2007, 2010; Nissen & Schuster, 2010), where the inner ∼20-30 kpc regions of the Galaxy's stellar halo are predominantly formed by populations formed in situ, while the outer regions are comprised of the debris of disrupted satellites accreted by the Milky Way in its past (e.g., Font et al., 2011; McCarthy et al., 2012).

In the following, I provide an overview of our current understanding of the structure and morphology of the Milky Way and its components (Section 1.1.1), as well as the models proposed to explain the assembly history of the Galaxy (Section 1.1.2). I also discuss how the field of Galactic archaeology attempts to discern structure and formation history of the Galaxy (Section 1.2) by analysing the fossilised records imprinted in Milky Way stars, such as their elemental abundances (Section 1.2.1) and stellar dynamics (Section 1.2.2). Particular emphasis is placed on how the Galaxy's stellar halo can be exploited to gain in-depth insights into its mass assembly history, which is the subject of Section 1.2.3. In addition, in Section 1.2.4 I discuss how star clusters prove useful for further unravelling the assembly history of the Milky Way. The aim of this introduction is to provide context of our knowledge of the Milky Way to later bring this understanding to bear on models for the formation and mass assembly history of the Galaxy.

1.1.1 Present day structure: the Milky Way from the inside out

We view the Galaxy in a snapshot of time when globally averaged star formation rates are declining, the motions of its constituent stellar populations can be considered to be "static" due to long dynamical timescales, and nuclear activity is low. This yields a "frozen" picture of the Milky Way, enabling one to carefully examine its structure in an (almost) "unevolving" snapshot of time. The observed spatial structure can then subsequently be compared to sophisticated theoretical models, which provide the opportunity

to travel forwards and backwards in time, allowing one to place expectations on the past –and the future– of the evolution of the Galaxy.

The Milky Way is in key respects structurally typical of large galaxies today in low density environments (Bland-Hawthorn & Gerhard, 2016). Its estimated stellar mass is $M_\star \sim 5\times10^{10.8}\mathrm{M}_\odot$ (Bland-Hawthorn & Gerhard, 2016), implying a luminosity close to the characteristic value $L_\star$ of the galaxy luminosity function. It has a circular velocity around the Solar neighbourhood of ∼240 km/s (Gravity Collaboration, 2019), positioning it a little below (but still within 1σ) of the Tully-Fisher relation (Tully & Fisher, 1977), making it a slightly subluminous galaxy. The Milky Way is comprised by several visible components: a disc (subdivided into thin/thick components), a (possible) bulge, a bar, and a stellar halo (see Fig 1.1). Stars from each of these components are characterised by a specific spatial distribution, kinematic profile, and distributions in chemical composition and age spaces. This implies that these Galactic components are truly physically distinct, despite their inter-webbed origin.

In addition to all baryonic components of the Galaxy is the component referred to as the "dark matter halo". Unobservable in nature due to the elusive material of which it is comprised, it constitutes the majority of the mass of the Milky Way ($\sim0.4\times10^{12}\mathrm{M}_\odot$-$2\times10^{12}\mathrm{M}_\odot$. e.g., Wilkinson & Evans, 1999; Smith et al., 2007; Li & White, 2008; Xue et al., 2008; Watkins et al., 2010; McMillan, 2011; Deason et al., 2012; Kafle et al., 2012, 2014; Piffl et al., 2014; Posti & Helmi, 2019; Deason et al., 2021). Although the dark matter halo is a pivotal and interesting component of the Galaxy, for the purpose of this thesis we will not discuss it in detail, as the work that will be presented in the following chapters pertains primarily to the stellar components of the Milky Way. Extensive reviews of the Milky Way in the context of galaxy formation can be seen in Freeman & Bland-Hawthorn (2002) and Bland-Hawthorn & Gerhard (2016).

In the following subsections, I summarise our current knowledge of the characteristics of these different Galactic components, and attempt to frame the Milky Way in a cosmological context.

1.1.1.1 The Galactic bulge and bar

I begin this Section by discussing the Galactic bulge. I note that while historically this Galactic component has been defined to be an individual feature of the Galaxy, the latest data have revealed that it is instead comprised of the superposition of many different stellar populations: the thin/thick discs, the bar, and the stellar halo (e.g., Zasowski et al., 2016; Nataf, 2017; Schultheis et al., 2017; Schiavon et al., 2017a; Queiroz et al., 2021).

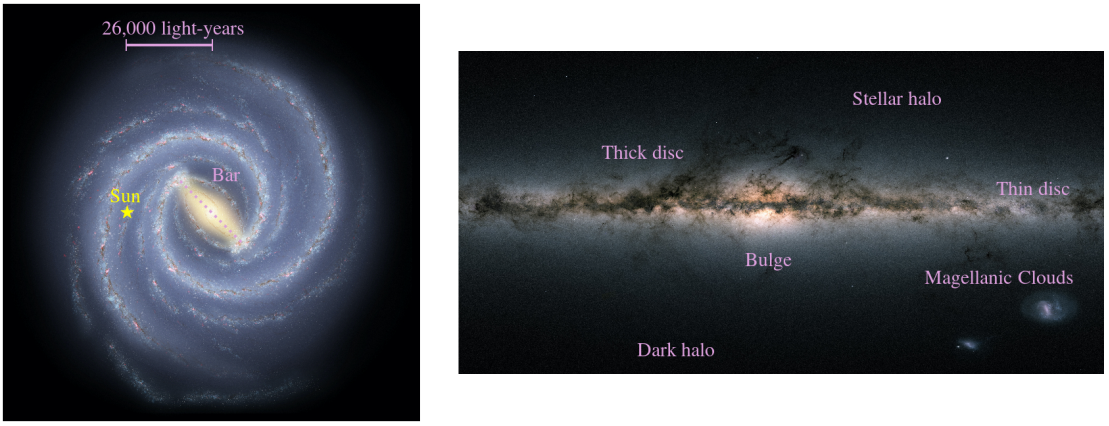

FIGURE 1.1: Artist illustration of the face-on projection (left) and edge-on projection (right) of the Milky Way. Illustrated on these diagrams are the different Galactic components that comprise the Milky Way galaxy, as well as the position of the Sun in the Orion arm. Image credit: *left*: NASA/JPL-Caltech/R. Hurt; *right*: ESA/Gaia/DPAC

The Galactic Bulge was first identified as a distinct component of our Galaxy by Baade (1946) (see also (Stebbins & Whitford, 1947)). Initially, it was conjectured as a structure resulting from the build up of mergers early in the formation of the Galaxy, now commonly referred to as a "*classical bulge*". This stemmed from the fact that stellar populations in this region were considered to be of type II (defined by Walter Baade himself), and were determined, largely thanks to inferences from color-magnitude diagrams, to be old (Nassau & Blanco, 1958; Ortolani et al., 1995; Clarkson et al., 2008). However, in later years Blitz & Spergel (1991) analysed the balloon observations by Matsumoto et al. (1982) to determine whether a significant nonaxisymmetric component of the emission existed within the data, and presented direct evidence for a bar at the Galactic Center. In addition, the near-infrared photometry with the COBE satellite in later years was the first to establish the "*boxy*" nature of the bulge (Weiland et al., 1994; Binney et al., 1997). This was later confirmed using the 2MASS star count map (Skrutskie et al., 2006). Following, more recent star count data unambiguously determined that the bulk of the Galactic bulge in fact forms part of a so-called "*box/peanut*" structure (b/p-bulge for short), which represents the inner part of the Galactic bar (Wegg & Gerhard, 2013), and is consistent with the observed cylindrical rotation (Kunder et al., 2012; Ness et al., 2013b). This b/p-bulge structure also reveals an X-shape when performing unsharp masking (McWilliam & Zoccali, 2010; Nataf et al., 2010; Portail et al., 2015; Ness et al., 2016), similar to what is observed in the sample of galaxies obtained by Bureau et al. (2006).

The culprit for the observed b/p-bulge distribution is conjectured to be the Galactic bar. This component has its semi-major axis in the first Galactic quadrant (i.e., $0° < l < 90°$). Measurements of the subjected angle between the bar's major axis and the Sun-Galactic centre line were first determined to be $\phi_{\rm bp}{\sim}27{\pm}2°$ (Wegg & Gerhard,

2013). This is consistent with earlier estimates from an array of studies, suggesting an angle between $\phi_{\rm bp}$∼20-35° (Dwek et al., 1995; Binney et al., 1997; Stanek et al., 1997; Rattenbury et al., 2007; Cao et al., 2013). The advent of the *Gaia* satellite (Gaia Collaboration, 2018) helped further constrain this value to the current estimate of $\phi_{\rm bp}$∼25° (Bovy et al., 2019). Moreover, the latest survey data show that the Milky Way's bar is approximately ∼ 10 kpc in length (Bovy et al., 2019), that it is rotating at approximately ∼41±km/s kpc^{-1} (Portail et al., 2017; Sanders et al., 2019; Bovy et al., 2019), and that it is comprised of stars which are older, and have less evolved chemical compositions, than stellar populations in the disc around the Solar neighbourhood (Bovy et al., 2019; Queiroz et al., 2021).

The observed properties of the bulge and bar of the Milky Way corroborate the initial hypothesis that the X-shaped bulge likely formed via the secular evolution and the process of bending instability of a prominent bar in these centremost regions of the Galaxy –albeit the existence of a classical bulge is still debated (Nataf, 2017; Barbuy et al., 2018)–. When compared to expectations from numerical cosmological simulations, the properties of the Milky Way's central regions suggest that the Galaxy has undergone no major accretions in the last ∼8 Gyr (Fragkoudi et al., 2020). As will be discussed in future chapters of this thesis, this hypothesis corroborates the most recent findings in the literature (Belokurov et al., 2018; Helmi et al., 2018; Mackereth et al., 2019a; Myeong et al., 2019; Naidu et al., 2020; Horta et al., 2021a). Finally, in addition to the Galactic bar, it is also worth mentioning that it is in these innermost regions that the peak in the density of the stellar halo is found (Iorio et al., 2018; Horta et al., 2021c), and where the oldest stars born in the Milky Way are most likely to be found (Beers & Christlieb, 2005; Yong et al., 2013; Nordlander et al., 2019; Arentsen et al., 2020c).

I finish this Section by providing direction for the reader to more extensive reviews of the Galactic bulge, which can be found in Rich (2013); Gonzalez & Gadotti (2016); Nataf (2017), and Barbuy et al. (2018).

1.1.1.2 The disc of the Galaxy and its spiral structure

The most massive baryonic component of the Milky Way is its disc, amounting to a M_d ∼ 5×10^{10} M$_\odot$ (McMillan, 2011). The Galactic disc has historically been understood as being the result of the overlapping of two structures, commonly referred to as a "thick" and "thin" disc (Yoshii, 1982; Gilmore & Reid, 1983; Jurić et al., 2008), making it similar to observations of local disc galaxies (Burstein, 1979; Tsikoudi, 1979). Historically, the "thick" disc has been characterised by older, kinematically hotter, and more α-enhanced

stellar populations, whereas the "thin" disc has been characterised by younger, kinematically cooler, and α-poor populations (Bensby et al., 2005; Nidever et al., 2014; Hayden et al., 2015). However, counter-arguing work has advanced that the disk populations, when analysed from the point of view of mono-abundance-populations, vary smoothly and span this range of chemo-dynamical and structural properties (Norris, 1987; Nemec & Nemec, 1991; Bovy et al., 2012, 2016; Mackereth et al., 2017).

I end this Section noting that the Milky Way disc appears structurally to be similar to observed discs of external galaxies of similar mass, but appears chemically to be peculiar at the $\sim$5-σ level (Mackereth et al., 2018). I provide the interested reader with more extensive reviews of the Galactic disc, found in Freeman & Bland-Hawthorn (2002), Rix & Bovy (2013) and Bland-Hawthorn & Gerhard (2016).

1.1.1.3 The stellar halo

Albeit it only amounts to less than $\sim$1% of the total stellar mass in the Milky Way (Bell et al., 2008), the stellar halo is a relic Galactic component that preserves the clues of the Galaxy's past and assembly history. It is in this region of the Galaxy that the debris of smaller satellite systems (such as dwarf galaxies and globular clusters) that have been accreted and disrupted via the process of hierarchical mass assembly are deposited (e.g., Ibata et al., 1997; Belokurov et al., 2006). Thus, it is an important region that retains vital clues for unravelling the past encounters that the Milky Way underwent, all of which can help decipher how the Galaxy assembled its mass. Moreover, it is also the Galactic component thought to contain the oldest stars in the Milky Way, which can serve as the Rosetta Stone for understanding the intricate physics of star formation in the early Universe.

Historically, early work focused on modelling the density of the Galactic stellar halo employed different stellar types as tracers, ranging from Main Sequence Turn Off (MSTO) stars (Morrison et al., 2000; Jurić et al., 2008) or Blue Horizontal branch (BHB) stars (Yanny et al., 2000), as the photometry is relatively easily calibrated to provide accurate distances. Initially, the stellar halo was fitted with a single power-law model, of the form:

$$\rho(r) = r^{-\alpha}, \tag{1.1}$$

where α is the exponent, classically attributed a value of $\alpha\sim3$. Using BHB stars from the SDSS survey, Deason et al. (2011) showed a better fitting profile, one that included a break radius at approximately $\sim$ 27 kpc, and whose inner exponential slope is shallow

($\alpha_{\rm in}$∼2.3) and outer slope is steep ($\alpha_{\rm out}$∼4.6) (see also Watkins et al., 2010; Sesar et al., 2011). Conversely, using the SDSS-SEGUE red giant stars, Xue et al. (2015) showed an alternative well fitting profile, a single power law of steep exponent (α∼4.2) and a flattening parameter q varying as a function of Galactocentric distance, which ranged in value between q∼0.5 and 0.8. The advent of the *Gaia* satellite mission then provided an unprecedented view of our Galactic stellar halo thanks to its delivery of exquisite astrometry for many hundreds of thousands of stars. These data enabled a more detailed characterisation of the stellar halo density profile covering a range between ∼3 kpc from the Galactic Centre to approximately ∼30 kpc. Using RR Lyrae stars from the second data release of the *Gaia* survey, Iorio et al. (2018) showed that a triaxial single power law, that included a flattening parameter and a parameter that modelled the tilt and/or offset of the halo with respect to the Galactic disc was the best fitting profile. Here, the authors found an exponent value of α∼2.96, with a flattening value between $0.57 < q < 0.75$, and a tilt on the order of ∼70° between the axis connecting the Sun and the Galactic Centre. These results are also in broad agreement with recent estimates using red giant branch star data from the APOGEE survey (Mackereth & Bovy, 2020), who also included a cut-off term to their profile, but find a steeper profile (on the order of α∼3.5).

In addition to its density profile, the structure of the Milky Way's stellar halo is diverse and rich in overdensities. Due to the difficulty in observing stars at very high distances, we have sadly only been able to map a small fraction of the distant stellar halo. Despite this, the efforts by many photometric, astrometric, and spectroscopic studies have helped reveal a wealth of structures in this region. In the past several decades, there has been a plethora of structures in the stellar halo discovered, ranging from stellar streams (Belokurov et al., 2006) to infalling satellite galaxies (Ibata et al., 1994). Towards the more inner ∼20 kpc regions, recent measurements suggest that the stellar halo is dominated by the debris of an accreted satellite galaxy referred to as *Gaia*-Enceladus (Helmi et al., 2018) or *Gaia*-Sausage (Belokurov et al., 2018) (but see also Haywood et al. (2018) and Mackereth et al. (2019a)), as well as smaller debris conjectured to arise from smaller accreted systems (e.g., Helmi et al., 1999; Myeong et al., 2019; Koppelman et al., 2020; Naidu et al., 2020). Due to the difficulty of observing the innermost ($R_{\rm GC} \lesssim 4$ kpc) regions of the stellar halo because of dust extinction and overcrowding by more metal-rich stellar populations, the innermost halo has remained obscured. As we will see in subsequent Chapters, one of the main objectives of this thesis has been to map the innermost halo of the Galaxy. Thus, I will reserve discussing this region of the stellar halo to the following Chapters.

For the interested reader who would like to learn more about the Milky Way stellar halo, I recommend the following reviews: Freeman & Bland-Hawthorn (2002) ,Helmi (2008),

Belokurov (2013), Bland-Hawthorn & Gerhard (2016), and Helmi (2020).

1.1.2 Mass assembly history

The current understanding of galaxy formation is based on a cold-dark-matter dominated Universe (ΛCDM). In this scenario, structure is a consequence of hierarchical merging and clustering of matter. Within this framework, baryonic matter (i.e., stars and galaxies) settle in large potential wells of dark matter haloes (White & Rees, 1978), and primarily grow via two overarching mechanisms: *i*) infall of gas from cosmic filaments; *ii*) hierarchical mass assembly of haloes. The ΛCDM theory has been successful in explaining the large-scale structure of the Universe (e.g., Frenk & White, 2012), but however struggles on the smaller (< 1 Mpc) scales (e.g., Navarro & Steinmetz, 2000; Abadi et al., 2003), and thus our understanding of galaxy formation and evolution is still incomplete (see the review by Bullock & Boylan-Kolchin 2017 on the topic).

For the case of the Milky Way, the first modern scenario proposed to describe the formation and assembly of the Galaxy was that by Eggen et al. (1962) (referred to as the ELS model). Based on the eccentric orbits and distinct chemical compositions observed for population type II stars when compared to the population type I stars, the ELS model proposed that the Milky Way formed via a collapse of an initial spherical cloud of gas (named a protogalaxy). This model postulated that initial gas was poor in metals, and due to gravity it collapsed and formed the first stars (population type II). Such stars kept the kinematic properties of the collapsing gas and obtained eccentric orbits around the centre of the galaxy. As more gas collapsed, the rotational velocities of the collapsing cloud would have increased to conserve angular momentum. These factors would lead the gas to collapse and start spinning along its rotational axis, shaping the galaxy into a flatter structure. As more stars formed and died through violent supernovae explosions, the galactic disc would have become more enriched in metals (released by the violent deaths of these stars) allowing for the formation of population type I stars; therefore explaining the different formation mechanisms for the different stellar populations known at the time.

Some time later, an alternative scenario was proposed by Searle & Zinn (1978). In this pioneering work, the authors applied a new method of abundance determination to a population of red giant stars in several GCs positioned at more than ∼8 kpc from the Galactic Centre. They chose to use these stars in faraway GCs as the distribution over abundance appeared to be independent of Galactocentric distance and is almost identical to that for halo subdwarfs in the solar neighbourhood. After performing their analysis, their results skewed them away from the idea of a collapsing protogalaxy as

proposed by the ELS model. Instead, their findings led them to postulate a new refined model in which they describe the formation of the Galaxy in a more chaotic manner. More specifically, they proposed that gas from which the clusters and stars of the outer halo formed continued to fall into the Galaxy for time after the collapse of its central regions had been completed. They suggested that the interactions of the infalling gas dissipated much of its kinetic energy and gave rise to transient high-density regions in which the halo stars and clusters formed. These regions then dispersed even while they underwent chemical evolution. The stars and clusters that had formed within these regions eventually fell into dynamical equilibrium with the Galaxy (constituting its present outer halo) and the gas lost from these protogalactic star-forming regions was eventually swept into the galactic disc[1].

Since these early works, more detailed models for the assembly history of galaxies like the Milky Way have been forwarded (e.g., Bullock & Johnston, 2005; Diemand et al., 2005; Font et al., 2006; De Lucia & Helmi, 2008; Johnston et al., 2008; Cooper et al., 2010). All of these have heavily relied on models which couple simple recipes for assigning stellar mass to infalling satellites in dissipationaless cosmological simulations (also referred as "hybrid" models). Overall, these models have been successful at reproducing the outer regions of the observed Milky Way stellar halo (e.g., Carollo et al., 2007; de Jong et al., 2010; Sesar et al., 2011), but run into problems when attempting to reproduce significant metallicity gradients in stellar spheroids (e.g., Font et al., 2006; Helmi, 2008; Cooper et al., 2010). Observational evidence suggests that the local stellar halo can be chemo-dynamically divided into two components (i.e., the "dual halo" e.g., Carollo et al., 2007, 2010; Nissen & Schuster, 2010) [2]. This duality feature has proven difficult to reconcile with purely dissipationless hybrid methods. However, this issue was largely mitigated in Font et al. (2011) using the GIMIC suite of simulations, who showed that when accounting for the change in the mass fraction of accreted and in situ populations at different Galactocentric radii, which have different characteristic metallicity distribution functions that overlap spatially, it is possible to reproduce the observed overall gradient out to radii of ∼30 kpc. Furthermore, McCarthy et al. (2012) also used these simulations to further assess the dual nature of the observed stellar halo in the Milky Way, and found that the in situ components of stellar halos contribute in copious amounts to the mass within ∼30 kpc, in line with the dual halo concept.

Theoretically, it is now widely agreed upon that the Galaxy (and its stellar halo) assembled via a combination of *in situ* star formation and the accretion of lower mass building

[1] It was due to the pioneering work by Searle & Zinn in the late 1970s that much of the following work started focusing on studying GCs to answer questions on the formation and mass assembly of the Milky Way.

[2] However, see counter-arguments by Schönrich et al. (2011) and Schönrich et al. (2014), who refute the dual halo hypothesis.

blocks (e.g., Deason et al., 2013; Tissera et al., 2013; Cooper et al., 2015; Rodriguez-Gomez et al., 2016; El-Badry et al., 2018; Monachesi et al., 2019; Fattahi et al., 2020; Font et al., 2020; Fragkoudi et al., 2020). Conversely, some of the latest observational findings argue in favour of either no in situ halo (e.g., Di Matteo et al., 2019; Naidu et al., 2020), for a large contribution to the inner stellar halo from accreted populations (e.g., Deason et al., 2019; Mackereth & Bovy, 2020), or for an in situ halo comprised of disc populations heated by merger events (e.g., Bonaca et al., 2017; Belokurov et al., 2020). Thus, a full picture is yet to be fully established.

1.2 Unveiling fossilised records of galaxy formation in the Milky Way

Similar to archaeologists who study human history by unearthing remnants from past civilisations, Galactic archaeologists trace the history and formation of the Milky Way by unveiling fossilised records embedded in the properties of its constituent stars, gas, and other structures observable from Earth. The opportunity to study the positions, motions, chemical compositions, and ages of stars in our Galaxy provide the means to unravel the structure and assembly history of the Milky Way. In the past few decades, the advent of large-scale stellar surveys have revolutionised Galactic archaeology, and mapped a significant region of the Galaxy, supplying a colossal archive of spectro-photo-astrometric properties for over $\gtrsim$1 million stars. In the following Sections, I present a short review of what these data tell us about the properties of Milky Way stellar populations in chemical (Section 1.2.1) and dynamical (Section 1.2.2) space. I also provide a more in-depth view of the Galactic stellar halo (Section 1.2.3) and the Galactic globular cluster system (Section 1.2.4), and discuss how these Galactic components retain the pivotal clues for unveiling the mass assembly history of the Milky Way. The content covered in this Section should provide the reader with an overview of this field of astronomy, and set the scene for the following chapters.

1.2.1 The Milky Way in chemical space

Chemical abundances of stars encode properties of the environment in which they formed and hold precious information on the formation of the Milky Way. The ability to "chemical tag" (Freeman & Bland-Hawthorn, 2002) stellar populations provides an avenue to unravel the history and evolution of the Galaxy. Beginning with the pioneering studies of the Sun and nearby stars (Payne, 1925; Russell, 1929), the pursuit of a complete understanding of the genesis of all elements remains as a fundamental question, relevant

to both astrophysics and nuclear physics (e.g., Fowler et al., 1955; Burbidge et al., 1957; Wallerstein et al., 1997). Significant progress has been made over the last half-century, and we can classify most elements into a small subset of primary groups, based on the their dominant nucleosynthetic channels. Broadly speaking, elements can be organised into the light, α, odd-Z, iron-peak, and neutron capture groups, and into further subgroups within each (see Johnson (2019) for further details). The analysis of these different elemental classifications in different chemical planes can subsequently be used to connect the relative conditions in which a stellar population is formed to the way the Galaxy has formed and evolved over time. Of particular interest is the fact that stellar populations formed in different environments should manifest different chemical abundances. This has been predicted based on expectations from numerical and cosmological simulations (Robertson et al., 2005; Font et al., 2006; Johnston et al., 2008), and confirmed with spectroscopic data collected for different regions of the Galaxy (Reddy et al., 2003; Bensby et al., 2005, 2014; Hayden et al., 2015; **?**) and dwarfs satellite galaxies around the Milky Way (Shetrone et al., 2001, 2003; Tolstoy et al., 2009; Nidever et al., 2020; Hasselquist et al., 2021).

Progress in our understanding of chemical element distributions in stars in the Milky Way in the last two decades has been driven by ground-based large-scale spectroscopic stellar surveys. These include APOGEE: Majewski et al. (2017), GALAH: Martell et al. 2017, LAMOST: Zhao et al. (2012), RAVE: Steinmetz et al. (2020), SEGUE: Yanny et al. (2009a), *Gaia*-ESO: Gilmore et al. (2012), amongst several others. The data supplied by these surveys has cemented the notion of an observed bimodality in the Milky Way disc manifested in the [α/Fe]-[Fe/H] plane (Fuhrmann, 1998; Prochaska et al., 2000; Reddy et al., 2006; Adibekyan et al., 2012; Haywood et al., 2013; Anders et al., 2014; Bensby et al., 2014; Nidever et al., 2014; Snaith et al., 2014; Hayden et al., 2015; Mackereth et al., 2017). Here, the so-called high-α track contains stars that are typically older, more [Fe/H]-poor, are positioned closer to the Galactic centre, and have higher vertical heights above the midplane; conversely, the low-α disc contains stars that are younger, span a wider range of metallicities (and are typically more [Fe/H]-rich), have radially more extended orbits, and a more confined to the midplane (see Fig 1.2). The high-α track displays a high-[α/Fe] ratio that is constant until [Fe/H] $\sim$–0.5, at which point there is a "*knee*" and the [α/Fe] ratio decreases at a constant rate with increasing [Fe/H], eventually merging with the low-α sequence at roughly solar-[α/Fe] at [Fe/H] $\sim$0.2 dex. Conversely, the low-α track spans across $-0.8 \lesssim$ [Fe/H] $\lesssim 0.5$ in metallicity, and shows no obvious *knee* feature. The observed knee in the high-α sequence is likely caused by the interplay between type II supernovae (or core-collapse supernovae: SNII) and type Ia supernovae (SNIa). Prior to formation of the knee, SNII caused by the explosion of stars with solar masses $M_\star \gtrsim 8 M_\odot$ are the primary source

of metals in the insterstellar medium (ISM), and primarily release α elements and Fe. Approximately $\sim 1 \times 10^8$ years leater, SNIa explosions begin to contribute metals to the ISM, primarily releasing iron-peak elements and Fe. The α-knee feature results from a declining star formation rate (as suggested by Tolstoy et al. (2009)), which leads to a decrease in the number of SNII detonations that contribute α elements and iron. It marks the metallicity after which SNIa dominate the chemical enrichment of a system as the smaller number of SNII explosions become less efficient at enriching the gas (see Mason et al., in prep for details). The origin of the α-bimodality is still uncertain, and can be to some degree explained under different mechanisms seen in cosmological simulations (e.g., Mackereth et al., 2018; Grand et al., 2018; Buck, 2019; Grand et al., 2020; Agertz et al., 2020; Khoperskov et al., 2021). Recent theoretical work suggests that it is perhaps an uncommon phenomenon (Mackereth et al., 2018), and suggests it is linked to the assembly history of the Milky Way. However, some observational results propose the contrary (Scott et al., 2021).

Furthermore, towards the more [Fe/H]-poor regime, the Milky Way is even more complex. It is in this region that the oldest and chemically least evolved stellar populations formed *in situ* inhabit this chemical plane (e.g., Carollo et al., 2007; Hayes et al., 2018; Di Matteo et al., 2019). Similarly, it is also in this low-metallicity regime that stellar populations formed in satellite galaxies accreted by the Milky Way appear (e.g., Nissen & Schuster, 2010; Hayes et al., 2018; Haywood et al., 2018; Helmi et al., 2018; Mackereth et al., 2019a). Albeit this region of the [α/Fe]-[Fe/H] plane is commonly attributed the umbrella name of the halo, observational results have also revealed the presence of a metal weak thick disc (MWTD, e.g., Norris et al., 1985; Morrison et al., 1990; Chiba & Beers, 2000; Beers et al., 2002; Carollo et al., 2010; Kordopatis et al., 2013; Di Matteo et al., 2019; Sestito et al., 2019; Fernández-Alvar et al., 2021), that reaches metallicities as low as [Fe/H]<-3. Similarly, there is also observational evidence for the presence of stars with disc-like chemical compositions on kinematically hot orbits (termed the "Splash" e.g., Bonaca et al., 2017; Belokurov et al., 2020), conjectured to be heated disc populations caused by the accretion of satellite galaxies.

All in all, the metal-poor Milky Way (i.e., [Fe/H]$\lesssim -0.7$) is more complex than previously thought, and the precise number of Galactic components overlapping in this chemical regime still needs to be fully established (although see the results by Nikakhtar et al. (2021)). The advent of large-scale stellar surveys is helping shed light on the properties of the metal-poor Milky Way. However, its complexity has not permitted us to fully characterise it, yet.

Aside from the [α/Fe] and [Fe/H] elemental ratios, other elements whose genesis does not involve SNII and SNIa provide us the opportunity to study how other nucleosynthetic

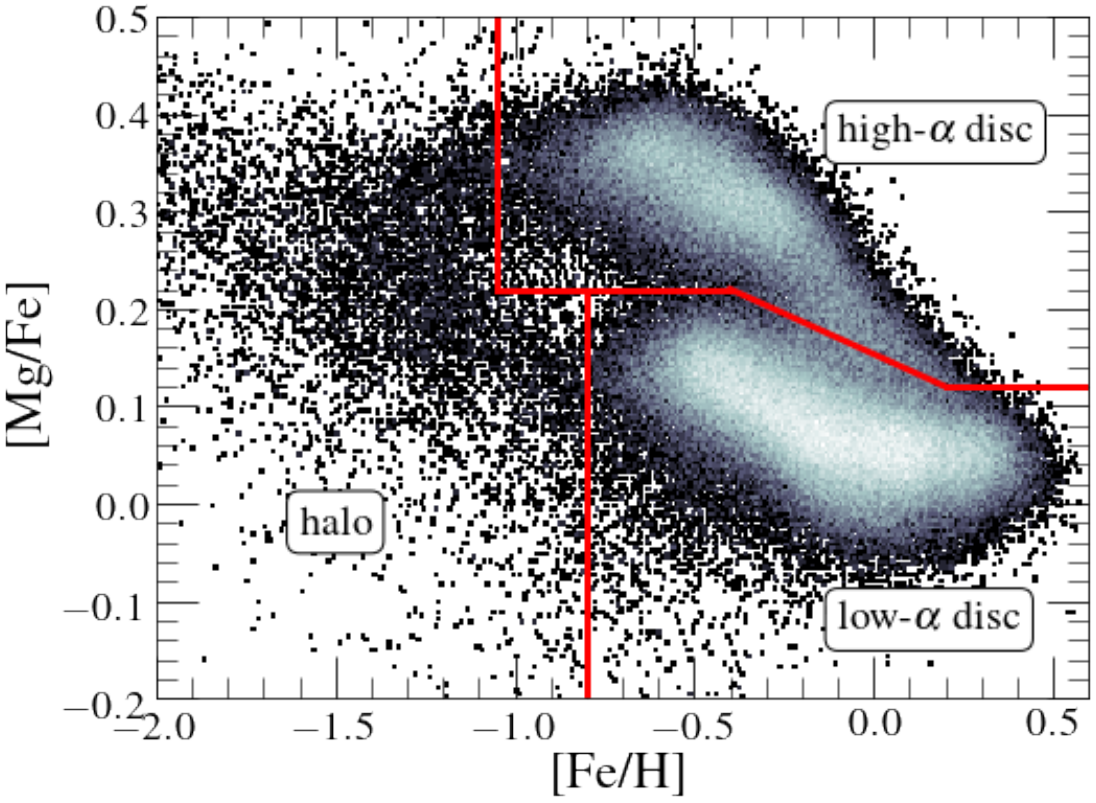

FIGURE 1.2: 2D density distribution of the Apache Point observatory Galactic Evolution Experiment data release 17 survey in the [α/Fe]-[Fe/H] (using Mg as our α tracer element). Red lines are illustrated in this plane to guide the eye to the division of the high-/low-α discs, as well as the "halo", components of the Milky Way.

channels contribute to the interstellar medium (ISM) of the Galaxy. As I discuss in the following chapters, the combination of elements formed in an array of nucleosynthetic channels enables the chemical characterisation of different stellar populations in the Galaxy, helping place constrains on the structure and mass assembly history of the Milky Way.

1.2.2 The Milky Way in dynamical space

The advent of the *Gaia* satellite mission has revolutionised the way we see the Milky Way, and has delivered an unprecedented view of the photo-spectro-astrometric properties of millions of stars in our Galaxy. More specifically, the first data releases of *Gaia* (Gaia Collaboration, 2018; Gaia Collaboration et al., 2020) provided a colossal archive of precise measurements of the magnitudes, positions, proper motions, and parallaxes of stars from all Galactic components. This information, when combined with the radial velocities supplied by the *Gaia*/RVS spectrograph and complementary spectroscopic surveys, supplies the 6-D phase space information necessary to fully characterise the

orbits and motions of stars in an assumed Galactic potential. This proves extremely useful for computing integrals of motion (IoM) (Binney, 2012), that are assumed to remain constant within a non-adiabatic axisymmetric potential, and thus are very useful for distinguishing stellar populations that appear different in orbital space.

Classically, the Milky Way can be dissected kinematically into a thin disc, thick disc, and halo components based on the velocities of stars in the so-called Toomre diagram (e.g., Toomre, 1964; Nissen, 2004; Kaempf et al., 2005; Schuster et al., 2012; Bensby et al., 2014; Jofré et al., 2015; Bonaca et al., 2017; Haywood et al., 2018; Helmi et al., 2018), as shown in Fig 1.3. In this space, the thin disc is characterised by a "cold" velocity profile, where stars are distributed over a small range of velocities, due to their nearly circular orbits near the Galactic plane. The thick disc spans a wider range in v_y and $\sqrt{v_x^2 + v_z^2}$, reaching approximately a value in both directions of $\sim$220 kms^{-1}. Conversely, the halo component is kinematically hot, and is comprised by stellar populations on more radial and eccentric orbits, occupying a position in Fig 1.3 spanning $v_y \sim 0$ km/s and $0 \lesssim \sqrt{v_x^2 + v_z^2} \lesssim 400$ km/s. The Toomre diagram has served as a purposeful plane to understand how different stellar populations orbit around the Milky Way.

However, velocities are variable quantities, so that diagnostic planes such as the Toomre diagram are only useful to study stellar populations in a snapshot of time. Conversely, IoM are conserved quantities (under the assumption of an axysimmetric and non-adiabatic potential) which makes them powerful tools to discriminate the evolutionary origin of stellar populations. One IoM plane that has been extensively studied is the orbital energy versus azimuthal angular momentum plane (also referred to as the Lindblad diagram, e.g., Lindblad, 1927; Bensby et al., 2014; Jean-Baptiste et al., 2017a; Helmi et al., 2018; Massari et al., 2019; Myeong et al., 2019; Koppelman et al., 2019c; Naidu et al., 2020), shown in Figure 1.4. This is because energy and angular momentum are parameters largely invariant to phase mixing and hence survive intact for many orbits (Helmi & de Zeeuw, 2000), and therefore substructures arising from the engulfment of satellite galaxies should appear as "clumps" in this orbital plane. This serves as a useful map to find the blueprints of the make up of the Milky Way's assembly history.

In summary, the motions and orbits of stars are important tracers of the formation and evolution of the Galaxy, from which any insights on Galactic dynamics can help place constraints on how other galaxies form in the Universe, and how dark matter interacts with baryonic matter due to its gravitational influence.

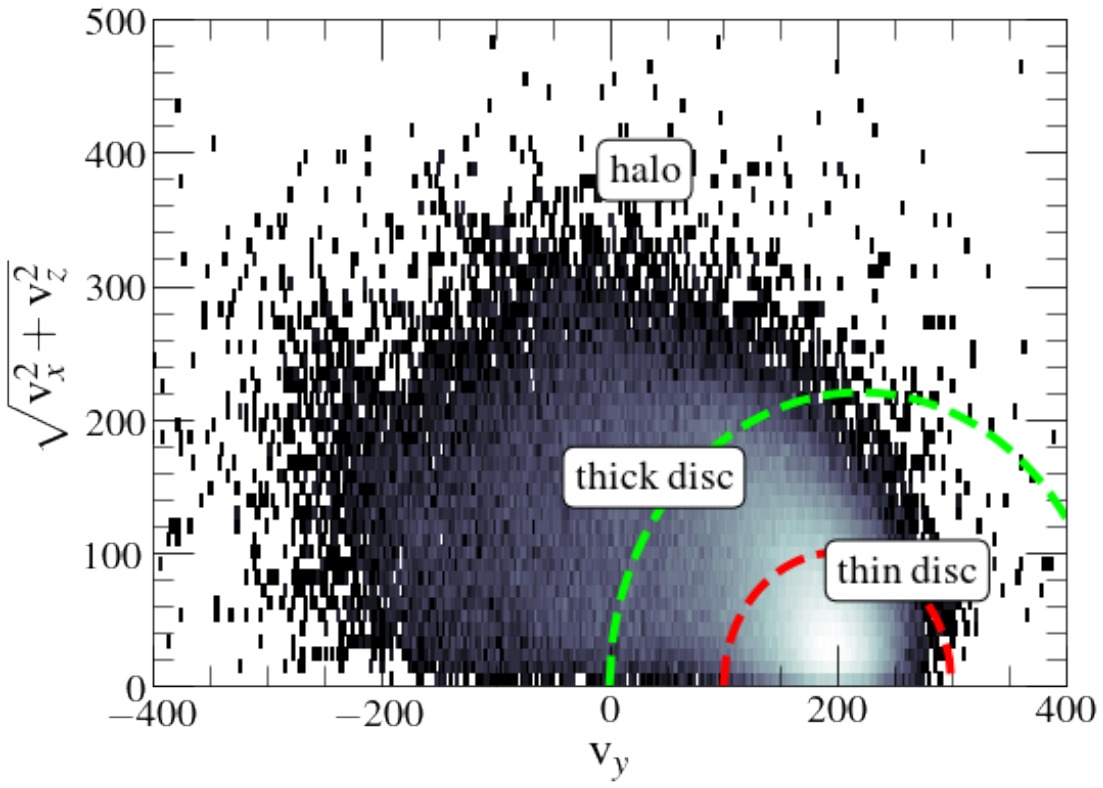

FIGURE 1.3: 2D density distribution of the Apache Point observatory Galactic Evolution Experiment data release 17 survey in the Toomre diagram. Red lines are illustrated in this plane to guide the eye to the division of the thin/thick discs, whereas green is illustrated to guide the division of the thick disc/halo components of the Milky Way. This kinematic plane gives an intuition of what fraction of the magnitude of a star's velocity vector is in the vertical, radial, and rotational velocity directions.

1.2.3 The stellar halo: a mosaic of stellar debris

In a ΛCDM Universe, galaxies (and the Milky Way) assemble their mass via the accretion of smaller galaxies (Bullock & Johnston, 2005; Abadi et al., 2006; Font et al., 2006; Johnston et al., 2008). As a natural consequence, cannibalised satellite galaxies deposited their debris in the stellar halo of the Milky Way, leaving behind the fossilised fingerprints of its accretion history and past encounters. As a result, the stellar halo component of the Milky Way appears as a "mosaic" of stellar debris, that can be characterised in order to deliver a better understanding of how our Galactic home assembled over time.

Early work based the identification of recent or ongoing accretion events on the location of substructure in real space, orbital phase, and/or phase space (Ibata et al., 1994; Helmi et al., 1999; Vivas et al., 2001; Majewski et al., 2003; Belokurov et al., 2006). The poster child example of this type of substructure is the Sagittarius dwarf spheroidal galaxy (Sgr dSph Ibata et al., 1994), identified due to the prominence of its core below the Milky

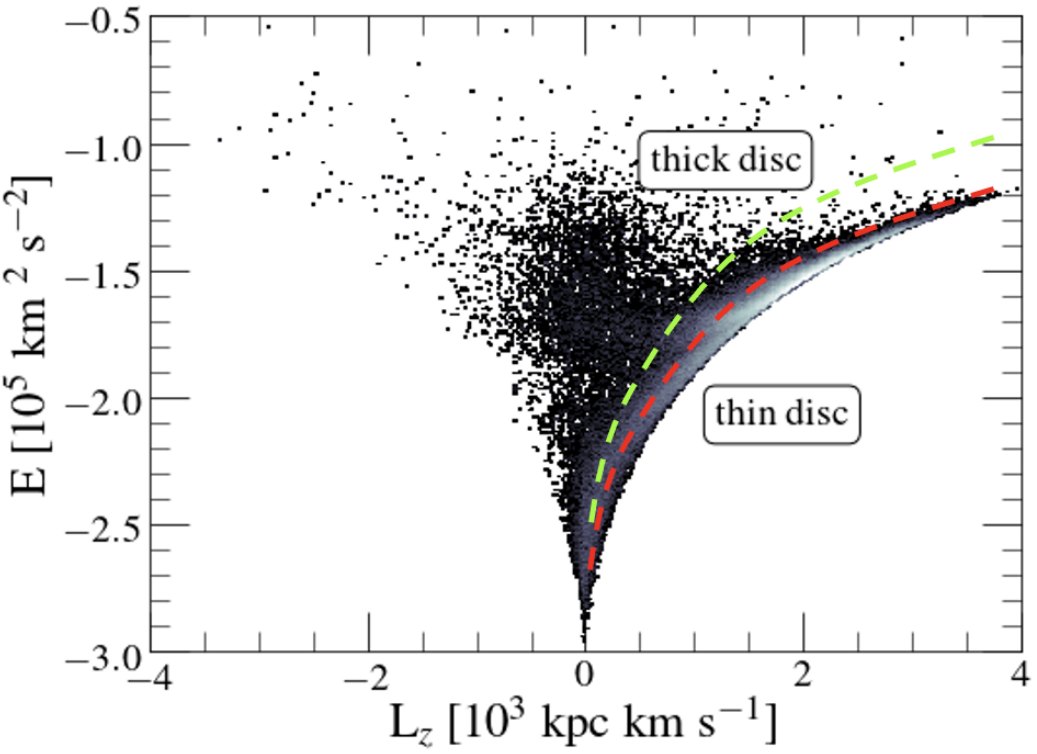

FIGURE 1.4: Same as Fig 1.3 but now in the Lindblad diagram: the orbital energy (E) versus azimuthal angular momentum plane (L_z). The red(green) line demarks, to first order, the region occupied by the thin(thick) disc. Here, positive(negative) L_z values correspond to orbits rotating in a prograde(retrograde) fashion, and more negative E values correspond to orbits more bound to the Milky Way pontential.

Way bulge and its long stellar streams wrapping around the Galaxy. However, phase mixing makes the identification of early accretion activity that occurred during the first few Gyr of the Milky Way's life more difficult, requiring additional information, usually in the form of detailed chemistry and/or ages (Nissen & Schuster, 2010; Hawkins et al., 2015; Hayes et al., 2018; Mackereth et al., 2019a; Das et al., 2020; Buder et al., 2022).

The combination of astrometric data from the *Gaia* satellite and spectroscopy from large-scale high-resolution spectroscopic surveys has enabled the identification of several distinct satellite accretions by various groups in the past few years, including the *Gaia*-Enceladus/Sausage system (GES Belokurov et al., 2018; Helmi et al., 2018; Haywood et al., 2018; Mackereth et al., 2019a), Sequoia (Barbá et al., 2019; Matsuno et al., 2019; Myeong et al., 2019), Thamnos (Koppelman et al., 2019c), Nyx (Necib et al., 2020), LMS-1 (Yuan et al., 2020), Arjuna/Aleph/I'itoi (Naidu et al., 2020), and Cetus (Newberg et al., 2009), and Pontus (Malhan et al., 2022).

It is evident that we have only scratched the surface in terms of characterising the stellar halo of the Galaxy. However, what is also clearly evident is that this Galactic

component is special as it retains vital clues required for an inference of the accretion and mass assembly history of the Milky Way, both of which are pivotal for an understanding of how the Galaxy, and maybe other disc galaxies in the Universe, form and evolve.

1.2.4 Globular clusters in the context of the Milky Way's assembly history

In addition to stellar debris, accreted satellite galaxies also deposit their surviving globular clusters (GC)[3] into the resulting larger mass host (Peñarrubia et al., 2009). Thus, GCs also serve as useful accretion tracers, and can be used to infer properties of the mass assembly history of the Galaxy (e.g., Searle & Zinn, 1978; Fall & Rees, 1985; Ashman & Zepf, 1992; Pritzl et al., 2005; Brodie & Strader, 2006; Forbes & Bridges, 2010; Myeong et al., 2018; Kruijssen et al., 2019b; Massari et al., 2019; Myeong et al., 2019; Forbes, 2020; Callingham et al., 2022), as well as properties of its dark matter halo and the Milky Way potential (Bahcall & Tremaine, 1981; Spitler & Forbes, 2009; Binney & Wong, 2017; Posti & Helmi, 2019).

Classically, the age-metallicity relation (AMR) of Galactic GCs has been used to make inferences about the Milky Way's mass assembly history (e.g., Forbes & Bridges, 2010; Kruijssen et al., 2019b). This is because the AMR of Galactic GCs has been shown to bifurcate (Marín-Franch et al., 2009; Forbes & Bridges, 2010; Leaman et al., 2013), where one branch is believed to trace the GCs formed *in situ* and is comprised of GCs that are more [Fe/H]-rich -at fixed age- than those positioned in the other branch, constituted by GCs thought to having been accreted via the process of hierarchical mass assembly. However, the advent of *Gaia* (and its precise astrometric measurements) and spectroscopic surveys (and their chemical abundance measurements) have also enabled the characterisation of the Galactic GC system in orbital (e.g., Myeong et al., 2018; Massari et al., 2019; Myeong et al., 2019) and chemical (Pritzl et al., 2005) space. While the origin of the Galactic GC system is still a debated topic, all these data have helped place constraints on the mass assembly history of the Galaxy.

In addition to the role of chemo-dynamic tracers, GCs also play an important role in terms of mass contribution to the total stellar halo mass budget. Theoretical and observational evidence suggest that GCs contribute relevantly to the stellar mass budget of galaxies. The leading GC formation scenarios propose a framework in which GCs formed in the turbulent discs of their host galaxies at $z \sim$2-3, where, due to tidal shocks (Gnedin, 2001) and the so called "cruel cradle effect" (Kruijssen et al., 2012b), GCs

[3] Albeit star clusters can be divided into multiple subgroups based on their age, size, mass and shape (namely, young-massive clusters, intermediate-age clusters, and globular clusters), for this thesis I will refer to all bound spherical systems of stars orbiting the Milky Way as globular clusters.

formed in situ were largely destroyed (Elmegreen, 2010; Kruijssen et al., 2011; Kruijssen, 2014). As galaxies evolved, mergers redistributed GC systems of accreted satellites onto the host galaxies, typically depositing them in the outer regions of the stellar halo, where mass loss via evaporation takes place over a longer timescale. The search for dissolved/evaporated GCs in the stellar halo of the Milky Way, and an assessment of their mass contribution to the total stellar halo mass budget, has now been possible thanks to ""weak chemical tagging". That is the adaptation of the concept of chemical tagging proposed originally by Freeman & Bland-Hawthorn (2002) to the purpose of identifying field stars associated with destroyed/evaporated globular clusters (Martell & Grebel, 2010; Lind et al., 2015; Schiavon et al., 2017a; Koch et al., 2019; Fernández-Trincado et al., 2019; Tang et al., 2020). This is because GCs have been shown to host multiple populations (MP) (see Bastian & Lardo (2018) for a review). Here, the so-called *first population* stars present chemical abundance properties that resemble the halo field; however, the *second population* type manifest light-element abundance patterns that distinguish them from both the field and the first population stars. Efforts attempting to chemically tag these second population stars in the stellar halo have found that there is a much higher contribution of disrupted/evaporated GC stars in the inner regions of the Galaxy (Schiavon et al., 2017a) than in the outermost regions (Martell et al., 2016; Koch et al., 2019). This difference is postulated to be due to the assembly history of the Milky Way (Hughes et al., 2020; Kisku et al., 2021), however further evidence is required to fully attest this hypothesis.

In a closing remark, I note that GCs hold vital clues in their observable properties that can help decipher the mass assembly history of the Galaxy and the build up of its stellar halo.

1.3 Summary and thesis outline

This thesis has so far consisted of an overview of the field of Galactic archaeology, relating the main properties of the Milky Way (Section 1.1) and the avenues Galactic archaeology attempts to use to place constraints on the formation and mass assembly history (Section 1.2). More specifically, I have provided an overview of the Milky Way's structure (Section 1.1), the leading models proposed to explain its mass assembly history (Section 1.1.2), how it appears in chemical and kinematic space (Section 1.2.1 and Section 1.2.2, respectively), and how we can use the Galactic stellar halo (Section 1.2.3) and its globular cluster system (Section 1.2.4) to gain insights on the accretion and mass assembly history of the Galaxy.

In the following chapters, I describe my efforts towards advancing our understanding of the history of the Milky Way on the basis of a combination of cutting edge observational data and state-of-the-art cosmological numerical simulations. In detail:

- In Chapter 2, I present novel results on the discovery of a halo substructure positioned in the heart of the Galaxy who's chemo-dynamical properties are consistent with an accreted origin.
- Chapter 3 presents an in-depth analysis of the chemical properties of all phase-mixed halo substructures identified so far in the Milky Way using the latest Milky Way survey data.
- In Chapter 4, I present the findings of a study focused on deciphering the total contribution to the stellar halo mass budget from dissolved and/or evaporated globular clusters via an assessment of the stellar density profile of second population globular cluster escapees, identified via a chemical tagging technique.
- Chapter 5 includes a study focused on discerning the origin of the Galactic globular cluster system based on a chemical analysis of globular clusters in the [α/Fe]-[Fe/H] plane.

I present the general conclusions of the thesis in Chapter 6, and outline future developments of my thesis work towards better constraining the formation and evolution, the mass assembly history, and typicality of the Galaxy.

Chapter 2

Unearthing building blocks of the Milky Way

2.1 Introduction

As already discussed in Chapter 1, the mass assembly of galaxies is largely determined by the accretion of low mass structures. It follows naturally that the accretion history of a galaxy plays a key role in defining how its various components are organized today. Our own Galaxy is no exception. Much of the accretion activity of the Milky Way has happened in the early stages of its formation, and the footprints are frozen in the chemo-dynamical record of its halo stellar populations. Since the seminal papers by Eggen et al. (1962) and Searle & Zinn (1978), many groups sought to characterise halo stellar populations, associating them with *in situ* formation or an accretion origin. Detection of substructure in phase space has worked very well for the identification of ongoing and/or recent accretion events (e.g., Ibata et al., 1994; Helmi et al., 1999; Majewski et al., 2003; Belokurov et al., 2006). However, phase mixing makes the identification of early accretion activity that occurred during the first few Gyr of the Milky Way's life more difficult, requiring additional information, usually in the form of detailed chemistry (e.g., Nissen & Schuster, 2010; Hayes et al., 2018; Mackereth et al., 2019a).

The combination of data from the *Gaia* satellite (Gaia Collaboration, 2018) and chemistry from massive high resolution spectroscopic surveys (e.g., Gilmore et al., 2012; Majewski et al., 2017; Martell et al., 2017) is transforming this field. In the past few years, several distinct satellite accretions have been suggested by various groups, including the Gaia-Enceladus/Sausage system (Haywood et al., 2018; Helmi et al., 2018; Belokurov et al., 2018; Mackereth et al., 2019a), Sequoia (Myeong et al., 2019), the *Kraken* (Kruijssen et al., 2019a), and Thamnos 1 and 2 (Koppelman et al., 2019b). More recently,

a number of additional structures were identified by Naidu et al. (2020) on the basis of data collected as part of the H3 survey (Conroy et al., 2019). While the reality of some of those events still needs to be fully established (e.g., Jean-Baptiste et al., 2017b; Koppelman et al., 2020), it certainly is clear that we are just scratching the surface and the field is ripe for exciting new findings in the near future.

The central few kpc of the Galactic halo are obviously extremely important when it comes to retelling the early accretion history of the Milky Way and discerning the contribution of *in situ* formation to the stellar halo mass. Assuming a single power law density profile with exponent $\alpha = -2.96$ (e.g., Iorio et al., 2018; Horta et al., 2021c) with spherical symmetry, roughly 50% of the halo stellar mass (out to R_{GC} ∼30 kpc) is located within ∼3 kpc of the Galactic centre. Moreover the inner few kpc of the Galaxy is the region one would expect to host most of the early *in situ* halo star formation, including the oldest stars in the Galaxy (e.g., Tumlinson, 2010; Savino et al., 2020), as well as the remnants of early accretion events driven there by dynamical friction (e.g., Tremaine et al., 1975; Pfeffer et al., 2020). Observational access to inner halo populations is however quite difficult. They inhabit a region of the Milky Way that by convention is referred to as the Galactic bulge, whose stellar population content consists of a superposition of structures that are far more densely populated than the halo itself, including the thick and thin disks, and the bar (e.g., Ness et al., 2013a; Rich, 2013; Nataf, 2017; Barbuy et al., 2018). Moreover, observations of the Galactic bulge are further hampered by severe extinction towards the inner several degrees from the Galactic centre.

Since the groundbreaking work by Rich (1988), a truly herculean effort has been invested by several groups towards mapping the stellar population content of the Galactic bulge, mostly based on optical spectroscopy (e.g., McWilliam & Rich, 1994; Ibata et al., 1994; Zoccali et al., 2006; Fulbright et al., 2007; Howard et al., 2008; Gonzalez et al., 2011; Rich et al., 2012; García Pérez et al., 2013; Rojas-Arriagada et al., 2014; Ryde et al., 2016; Rojas-Arriagada et al., 2017 [1]). However, until very recently, the detailed chemistry of the *metal-poor* population inhabiting the inner few kpc of the Galactic centre has been poorly characterized, with most studies being based on small samples with metallicities below [Fe/H] ~ -1. With the advent of the Apache Point Observatory Galactic Evolution Experiment (Majewski et al., 2017), detailed chemistry (combined with precision radial velocities) has recently been obtained for a statistically significant sample of metal-poor stars within a few kpc of the Galactic centre. A number of studies resulted from that database. Nidever et al. (2012) identified cold velocity peaks in the radial velocity distribution of stars within $\sim 20°$ of the Galactic centre, which may

[1] This is of course an incomplete list. For a more comprehensive account of previous observational work see reviews by Rich (2013), Nataf (2017) and Barbuy et al. (2018).

be associated with resonant bar orbits (Molloy et al., 2015). García Pérez et al. (2013) identified some of the most metal-poor stars known in the Galactic bulge; Zasowski et al. (2016) showed that the kinematics of metal-poor bulge stellar populations is dynamically hotter than that of their metal-rich counterparts; Schultheis et al. (2017) found evidence for the presence of a young component among the bulge stellar populations, in agreement with previous work; Schiavon et al. (2017b) discovered a large number of field stars likely resulting from the destruction of an early population of globular clusters; García Pérez et al. (2018) studied the metallicity distribution function (MDF) of bulge populations, and its spatial variation; Zasowski et al. (2019) scrutinised the detailed chemistry of bulge populations, showing that they seem to be consistent with a single evolutionary track, across a wide metallicity range; Rojas-Arriagada et al. (2019) suggests the presence of a bimodal distribution of bulge stellar populations in the Mg-Fe plane, and Rojas-Arriagada et al. (2020) argues for a bulge MDF that is characterised by only three metallicity peaks; Hasselquist et al. (2020) presented the age distribution of several thousand bulge stars, showing the presence of a sizeable population with moderately young ages; last, but not least, Queiroz et al. (2020a) made a detailed characterization of bulge stellar populations on the basis of their kinematics and chemistry.

In this chapter I report evidence based on APOGEE spectroscopy, distances based on *Gaia* DR2, and EAGLE numerical simulations, for the presence of a metal-poor stellar population within ∼4 kpc of the Galactic centre, that is both chemically and dynamically distinct from its co-spatial, more metal-rich counterparts. We argue that this population is likely the remnant of a massive accretion event that probably occurred in the early stages of the Milky Way formation. Due to its location at the heart of the Galaxy, I name this system the Inner Galaxy Structure (IGS). In Section 2.2 I briefly describe the data upon which this work is based, and the sample selection criteria. In Section 2.3 I discuss the chemical criteria to distinguish accreted from *in situ* populations. In Section 2.4 I discuss the identification of substructure in integrals of motion (IoM) space, arguing that the newly identified structure is dynamically detached from other components of the inner Galaxy. Section 2.5 presents a discussion of the chemical properties of the new structure, where I provide evidence that it is chemically detached from the other populations inhabiting the inner Galaxy. In Section 2.6 I discuss the origins of the metal-poor stellar populations providing an assessment of the contribution of accreted and *in situ* populations to the stellar mass budget of the inner halo. I also estimate physical properties of the putative satellite progenitor of the IGS, such as mass and star formation history. The conclusions are summarised in Section 2.7.

2.2 Data and sample

The results contained in this chapter are based on a combination of data from the SDSS/APOGEE survey (Blanton et al., 2017; Majewski et al., 2017), data release 16 (DR16, Ahumada et al., 2019b), with 6D phase information and orbital parameters inferred from *Gaia* DR2 distances and proper motions (Gaia Collaboration, 2018) and APOGEE radial velocities (Nidever et al., 2015). I make use of the distances from Leung & Bovy (2019a) for the APOGEE DR16 data, generated using the `astroNN` python package (for a full description see Leung & Bovy, 2019b). These distances are determined using a previously trained `astroNN` neural-network, which predicts stellar luminosity from spectra using a training set comprising of stars with APOGEE spectra and *Gaia* DR2 parallax measurements (Gaia Collaboration, 2018). The model is able to simultaneously predict distances and account for the parallax offset present in *Gaia*-DR2, producing high precision, accurate distance estimates for APOGEE stars, which match well with external catalogues and standard candles. Orbital parameters were calculated using the publicly available code `galpy` [2] (Bovy, 2015; Mackereth & Bovy, 2018), and employing a McMillan (2017) potential. I checked the quality of the Gaia astrometry for the whole sample finding that, save for a very small number of outliers, the renormalized unit weight error (RUWE) for the bulge sample is within the safe recommended region (RUWE<1.44)[3], which speaks for the reliability of the orbital parameters.

APOGEE data are based on observations collected with twin high resolution multi-fiber spectrographs (Wilson et al., 2019) attached to the 2.5 m Sloan telescope at Apache Point Observatory (Gunn et al., 2006) and the du Pont 2.5 m telescope at Las Campanas Observatory (Bowen & Vaughan, 1973). Elemental abundances are derived from automatic analysis of stellar spectra using the ASPCAP abundance pipeline (García Pérez et al., 2016). The spectra themselves were reduced by adoption of a customized pipeline (Nidever et al., 2015). For a detailed description of the APOGEE data, see Jönsson et al. (2020) for DR16 and Holtzman et al. (2015, 2018) and Jönsson et al. (2018) for previous data releases. For details on targeting procedures, see Zasowski et al. (2017).

The parent sample upon which the work is based is defined as follows. Stars were selected from the DR16 catalog that match the following criteria: $4000 < T_{\rm eff} < 6000$ K, $1 < \log g < 3$, [Fe/H]> -1.7, S/N>70, $d_{\rm err}/d < 0.2$ (where d and $d_{\rm err}$ are distance and its uncertainty). The S/N and stellar parameter criteria are designed to maximise the quality of the elemental abundances, minimise systematic effects at low and high $T_{\rm eff}$, minimise/eliminate contamination of the sample by AGB and nearby dwarf stars

[2] https://github.com/jobovy/galpy
[3] See discussion in `https://www.cosmos.esa.int/web/gaia/dr2-known-issues`

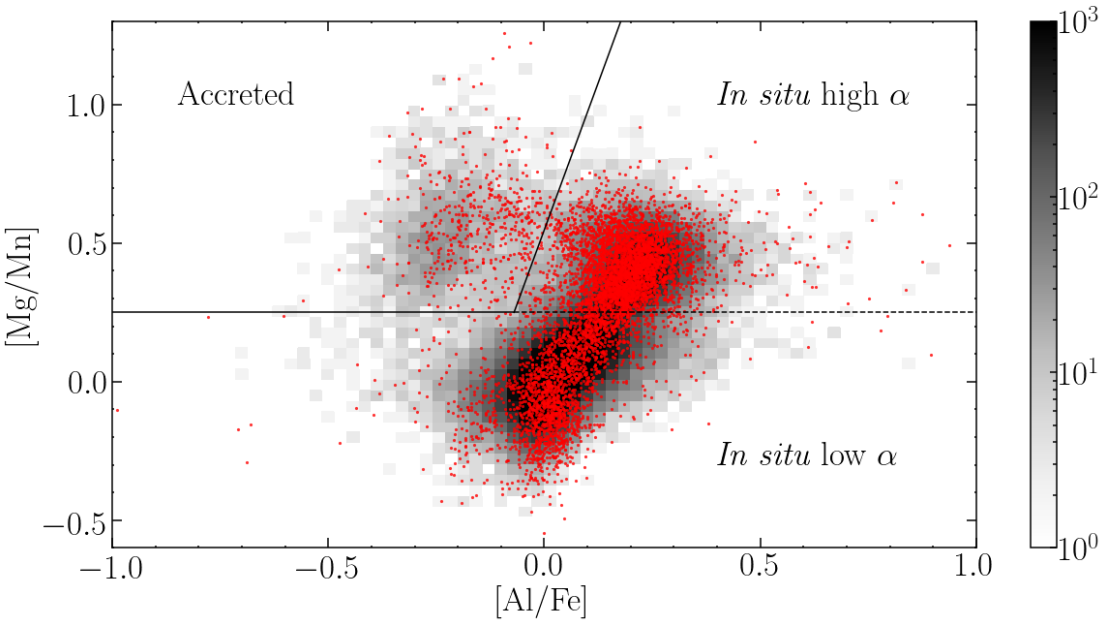

FIGURE 2.1: Parent and bulge sample displayed in the [Mg/Mn] vs. [Al/Fe] plane. The 2D histogram shows the entire parent sample, and the red dots highlight stars located at $R_{GC} < 4$ kpc. The black solid line defines the criterion to distinguish *in situ* from *accreted* populations. The dotted line further splits the latter group between low- and high-α stars. See details in Section 2.2.

at low and high $\log g$, respectively, and remove stars with very low metallicity, for which abundances of elements such as Mn and N are uncertain. I also remove stars for which ASPCAP did not provide reliable abundances for Fe, Mg, Al, and Mn, and any stars with `STAR_BAD` flags set. Finally, 6,022 globular cluster stars, identified following the procedure described by Horta et al. (2020), were also removed from consideration. The resulting parent sample contains 144,490 stars with high quality elemental abundances and phase space information, 6,350 of which are located within $R_{GC} = 4$ kpc of the Galactic centre.

2.3 Chemical distinction between accreted and *in situ* populations

The first step in this chapter is to distinguish stars within the parent sample that were formed *in situ* from those that were likely accreted. For that purpose I display the parent sample on the [Mg/Mn] vs. [Al/Fe] plane in Figure 2.1. Das et al. (2020) showed that stars in the APOGEE DR14 sample occupied three major distinct loci on this plane (see also Hawkins et al., 2015). Most of the stars occupy two large concentrations which, in the DR16 data, are centered at ([Al/Fe],[Mg/Mn]) $\sim$ (0,0) and (0.3,0.4), corresponding to the low- and high-α disk populations, respectively (e.g., Bovy et al., 2012; Bensby

et al., 2014; Nidever et al., 2014; Hayden et al., 2015; Mackereth et al., 2017; Queiroz et al., 2020b). A third group of stars populates a more diffuse "blob" apparent in Figure 2.1, which is centered roughly at ([Al/Fe],[Mg/Mn]) = (–0.2,0.5), which Das et al. (2020) associate with an accreted origin. That association was originally proposed by Hawkins et al. (2015), who identified accreted halo stars as those with low [α/Fe], and whose radial velocities deviate strongly from those of the bulk of disk stars at the same Galactic longitude. The solid line in Figure 2.1 defines the locus occupied by accreted stars in that chemical plane (top left corner). According to Das et al. (2020), stars to the right and below that line are thus deemed to have formed *in situ*. The latter population is further divided into two sub-classes characterized by low and high α-element abundances, as indicated by the dotted line in Figure 2.1. In total the *in situ* and *accreted* samples contain 141,514 and 2,976 stars, respectively.

The red points on top of the 2D histogram in Figure 2.1 include only stars within 4 kpc of the Galactic centre. A sizable sub-sample of these so-called bulge stars are located in the accreted locus of chemical space, suggesting that the bulge may host an accreted population. The sample contains 463 supposedly accreted stars within 4 kpc of the Galactic centre, modulo a contamination by stars formed *in situ*, which I estimate by different means in Sections 2.3.1 and 2.4.2.

2.3.1 Predictions from chemical evolution models

Before proceeding with the analysis, it is interesting to examine the association of abundance patterns and stellar origin on the basis of standard Galactic chemical evolution modelling. In this way I hope to ground the empirical definition of accreted vs. *in situ* chemistry on a theoretical basis.

Figure 2.2 displays the bulge population on the same chemical plane as Figure 2.1, but now overlaid by two chemical evolution models starting from the same initial chemical composition, calculated using the flexCE package by Andrews et al. (2017). The red line shows the "fiducial" model calculated by those authors, with parameters chosen to match the properties of the stellar populations in the solar neighbourhood. I adopt it as a proxy for the behaviour of an *in situ* population. The blue line represents a model calculated by Hasselquist et al. (2021) to match the properties of the Gaia-Enceladus/Sausage system, which I therefore choose to mimic the expected behaviour of accreted populations. The parameters adopted for each model are listed in Table 2.1. While the fiducial model adopts a standard exponentially decaying inflow law, for the accreted population gas inflow follows a dependence of the te^{-t} type. Both models adopt a Kroupa (2001) IMF with stellar mass ranging from 0.1 to 100 $M_{\odot}$. In both models the distribution of time

TABLE 2.1: Parameters adopted for chemical evolution models in Figure 2.2

Parameter	*In Situ*	Accreted
Initial gass mass	$2 \times 10^{10} M_{\odot}$	$3 \times 10^{9} M_{\odot}$
Inflow mass scale	$3.5 \times 10^{11} M_{\odot}$	$6 \times 10^{10} M_{\odot}$
Outflow mass loading factor	2.5	6
Star formation efficiency	1.5×10^{-9}yr^{-1}	1.0×10^{-10}yr^{-1}
Exponential inflow timescale	6.0 Gyr	2.5 Gyr

delays before the occurrence of SN Ia is an exponential with timescale 1.5 Gyr and a minimum delay time of 150 Myr. Tests were performed to verify that the overall mass scaling is not important for chemical evolution. The deciding factors in fact are the ratio between initial and inflow masses, the outflow mass loading factor, and the star formation efficiency.

The filled circles along the model lines indicate the positions at evolutionary time t = 300 Myr, 1 Gyr, and 5 Gyr. The black cross on both curves indicates the point at which the models reach [Fe/H]=–0.8. The models are far from a perfect match to the data, but provide a reasonable qualitative description of the main trends, which suffices for these purposes.

The first point to be taken from this model comparison is that the "Accreted" region of chemical space in Figure 2.1 is inhabited by old metal-poor stars from both models, suggesting that both *in situ* and accreted stars share that area of chemical space. In fact, the accreted stars in halo samples are located in that particular locus of Figure 2.1 not due to an intrinsic evolutionary property of dwarf galaxies, but rather because their star formation was quenched at the moment when they were disrupted while merging into the Milky Way. As a result, all the stars ever formed by such accreted systems inhabit the *unevolved* region of Figure 2.1. The natural implication of this conclusion is that the "Accreted" region of the chemical plane in Figure 2.1 is likely to also contain stars that were in fact formed *in situ*.

Secondly, one can try to exploit the different timescales and star formation rates of the two models to attempt a zero-th order estimate of the expected contribution of *in situ* and accreted populations to the sample within the "Accreted" region of chemical space. It is clear that chemical enrichment proceeds at a much faster pace in the *in situ* model, whose gas leaves the "Accreted" region of the chemical plane at $t \sim 250$ Myr. Conversely, the gas in the low mass galaxy remains within the "Accreted" locus for about ∼3 Gyr. On the other hand, the star formation rate at the early stages of the evolution of the high mass galaxy, according to the models, is of the order of $\sim 20\ M_{\odot}\ \mathrm{yr}^{-1}$, whereas in the case of the dwarf galaxy it is $\sim 0.3\ M_{\odot}\ \mathrm{yr}^{-1}$. Therefore, considering the characteristic star formation rates and timescales for the two types of systems, one would expect that

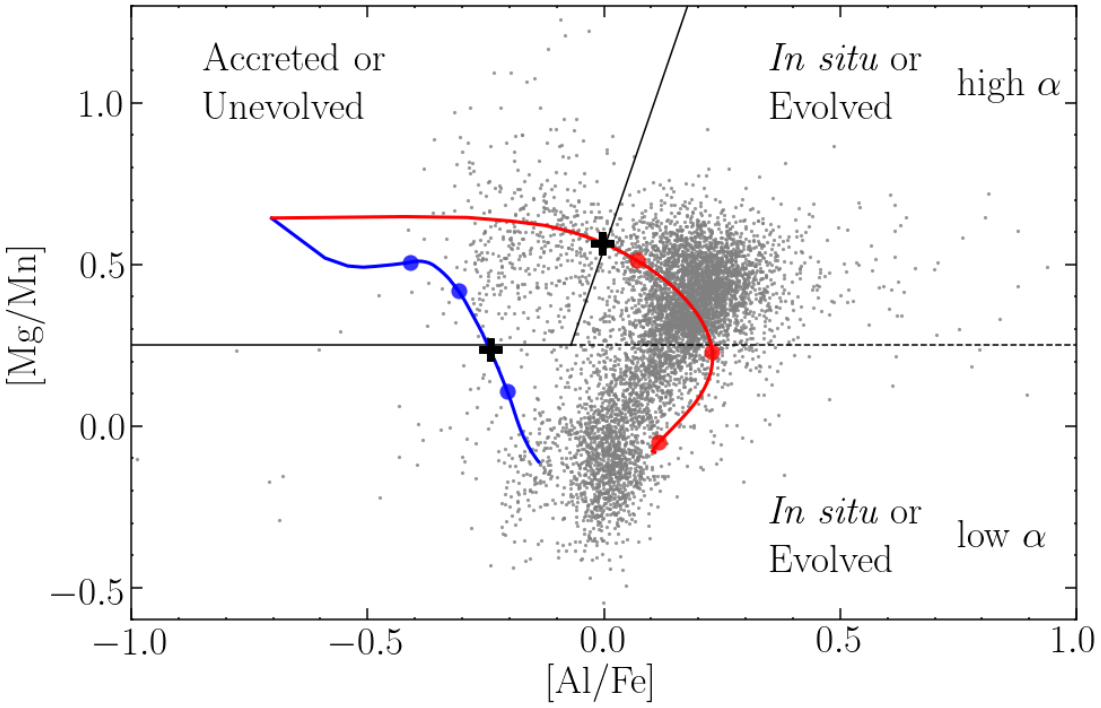

FIGURE 2.2: APOGEE sample for stars with $R_{GC} < 4$ kpc compared with chemical evolution models. The red line shows a model for a Milky Way like galaxy and the blue line the model for a dwarf satellite. Both models start from the same chemical composition, and initially occupy the region of parameter space usually ascribed to "Accreted" stellar populations, but which also hosts *in situ* populations that are chemically unevolved. The filled circles indicate the positions along the evolution after $t = 0.3$, 1, and 5 Gyr after the beginning of chemical evolution. The black cross in both curves indicates the point at which [Fe/H]=–0.8. Evolution of the massive galaxy is a lot faster, but the star formation rate is much higher, so the two systems are expected to produce similar total stellar mass within the "Accreted" area of the diagram.

the total stellar mass associated with *in situ* and accreted populations in the "Accreted" region of Figure 2.1 to be of the same order of magnitude. In Section 2.6.1.1 I provide a more accurate estimate of the contribution of *in situ* and accreted populations to the stellar mass budget of the metal-poor bulge, based on their distributions in the $E - L_z$ plane.

I conclude that, on the basis of position on the [Mg/Mn] vs. [Al/Fe] plane, it is in principle impossible to completely separate *in situ* from accreted stars. However, I argue that the clumpy nature of the distribution of stellar populations in Figure 2.1 speaks in favour of a different origin for at least part of the stellar populations in the "Accreted" region of that plane, and those in the *in situ* region. In Section 2.4.2 I show that by imposing selection criteria based on orbital parameters it is possible to keep the contamination of the accreted sample by stars formed *in situ* to an acceptable level.

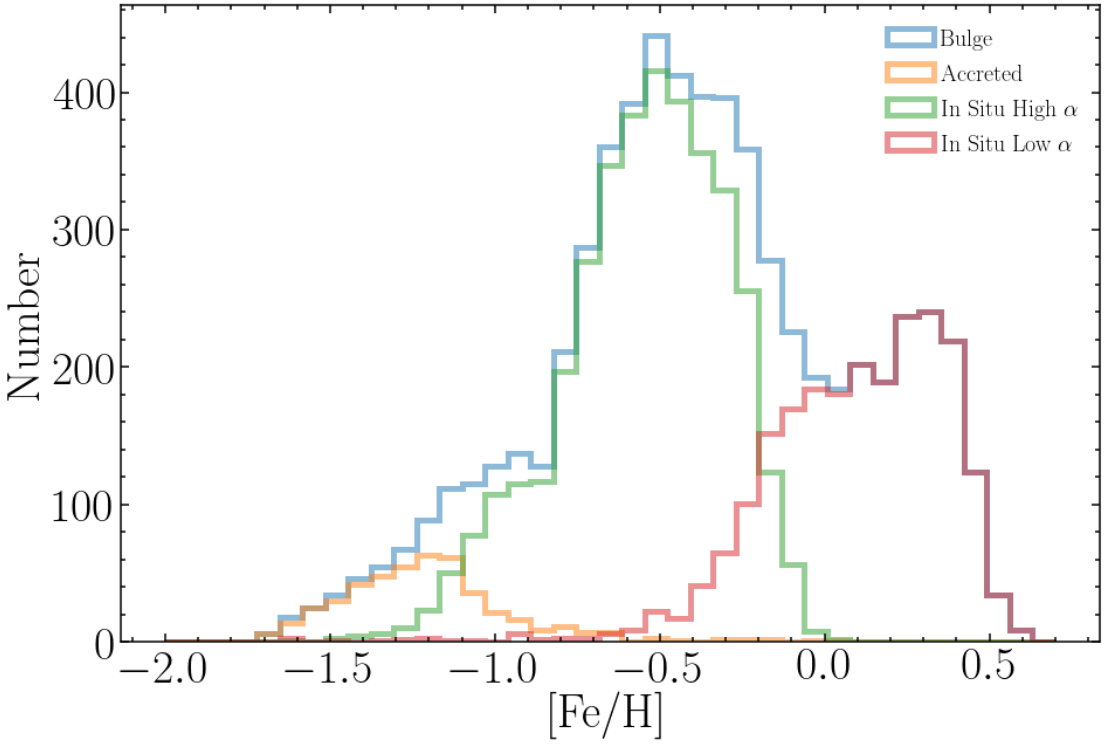

FIGURE 2.3: Raw metallicity distribution functions of accreted and *in situ* populations within $R_{GC} < 4$ kpc, selected as described in the text. The accreted population straddles the metal-poor end of the bulge MDF, with [Fe/H]< -0.8. It overlaps strongly with *in situ* populations, particularly in the high metallicity end.

2.4 Detection of Substructure in IoM Space

2.4.1 Raw MDFs and the definition of the metal-poor sample

In this section I examine the orbital properties of accreted and *in situ* stellar populations, as defined in the previous section. I begin this exercise by focusing on the orbital properties of *metal-poor* populations, with an eye towards establishing whether the chemically defined accreted and *in situ* groups also differ in their orbital properties. For that purpose, I must first define where I draw the line between metal-poor and metal-rich populations.

I begin by examining the metallicity distribution of the sub-populations defined in Figure 2.1 in order to determine the [Fe/H] threshold defining "metal-poor" stars for the purposes of this exercise. The *raw* metallicity distribution functions of the accreted, high- and low-α populations are displayed in Figure 2.3, together with that for the entire $R_{GC} < 4$ kpc population. I stress that this *raw* MDF is not corrected for selection effects, so it is presented here just as a rough guide to the relative metallicities covered by the populations defined in Figure 2.1. The MDFs of the high- and low-α populations cover the thin disk, bar, and thick disk structures identified in previous works (e.g., Ness

et al., 2013a; Rojas-Arriagada et al., 2017; García Pérez et al., 2018; Rojas-Arriagada et al., 2020). The MDF of the accreted population peaks at [Fe/H]∼–1.2, and overlaps substantially with that of the high-α population, extending all the way to [Fe/H]∼–0.8 with a tail towards higher metallicity. As a compromise between obtaining a good representation of the accreted and high-α populations, without pushing too far into the metal-rich regime, I adopt an [Fe/H]=–0.8 cutoff. Henceforth, when referring to the "metal-poor" bulge, unless otherwise noticed, I mean stars with [Fe/H]<–0.8. In Section 2.5.2 I go beyond a simple MDF approach in order to better explore the chemical complexity of bulge stellar populations. Since the goal in this Section is simply to contrast orbital properties of accreted and *in situ* stars within the same metallicity regime, a straight [Fe/H] cutoff should suffice.

2.4.2 Orbital properties of metal-poor stars

In Figure 2.4 metal-poor stars ([Fe/H]<–0.8) are displayed on the energy vs angular momentum plane. In the top panel stars in the *in situ* locus of Figures 2.1 and 2.2 are displayed, whereas accreted stars are shown in the bottom panel. The [Fe/H]<–0.8 cutoff leaves us with a sub-sample of 2,688 accreted stars and 2,488 *in situ* stars. Of the latter, only 179 belong to the low-α group, as expected given the MDF of the low-α disk (e.g., Hayden et al., 2015). Arrows of different colours are placed on the positions of the main *in situ* and accreted structures identifiable in the $E - L_z$ plane, which stand out in the top and bottom panels, respectively. The positioning of the arrows in both panels are exactly the same, to guide the eye.

One can readily spot significant differences between the two panels, which at face value validate the chemical distinction between accreted and *in situ* populations. Features associated with well known *in situ* populations show much more prominently in the top panel, and nearly vanish in the bottom panel. The main *in situ* structures identifiable are the *low-α/thin disk*, indicated by the *orange* arrow, *high-α/thick disk* stars are indicated by the *black* arrow. An extended prograde "branch" at about $E/10^5 \sim -1.75$ km^{2}s^{-2}, which seems to be associated with the "Splash" population identified by Belokurov et al. (2019), is indicated by the *green* arrow. Because of the focus on the metal-poor end of the parent sample, these structures are relatively weak, but in the Appendix the loci of these populations on the IoM plane are shown in better detail.

The clumpy distribution of accreted populations in IoM space is clear even under a casual visual inspection of the bottom panel of Figure 2.4. By far the most prominent substructure is the large "blob" centered around $L_z \sim 0$ km s^{-1}kpc and $E/10^5 \sim -1.5$km^2 s^{-2} (*blue arrow*) which is associated with the Gaia-Enceladus/Sausage (GE/S)

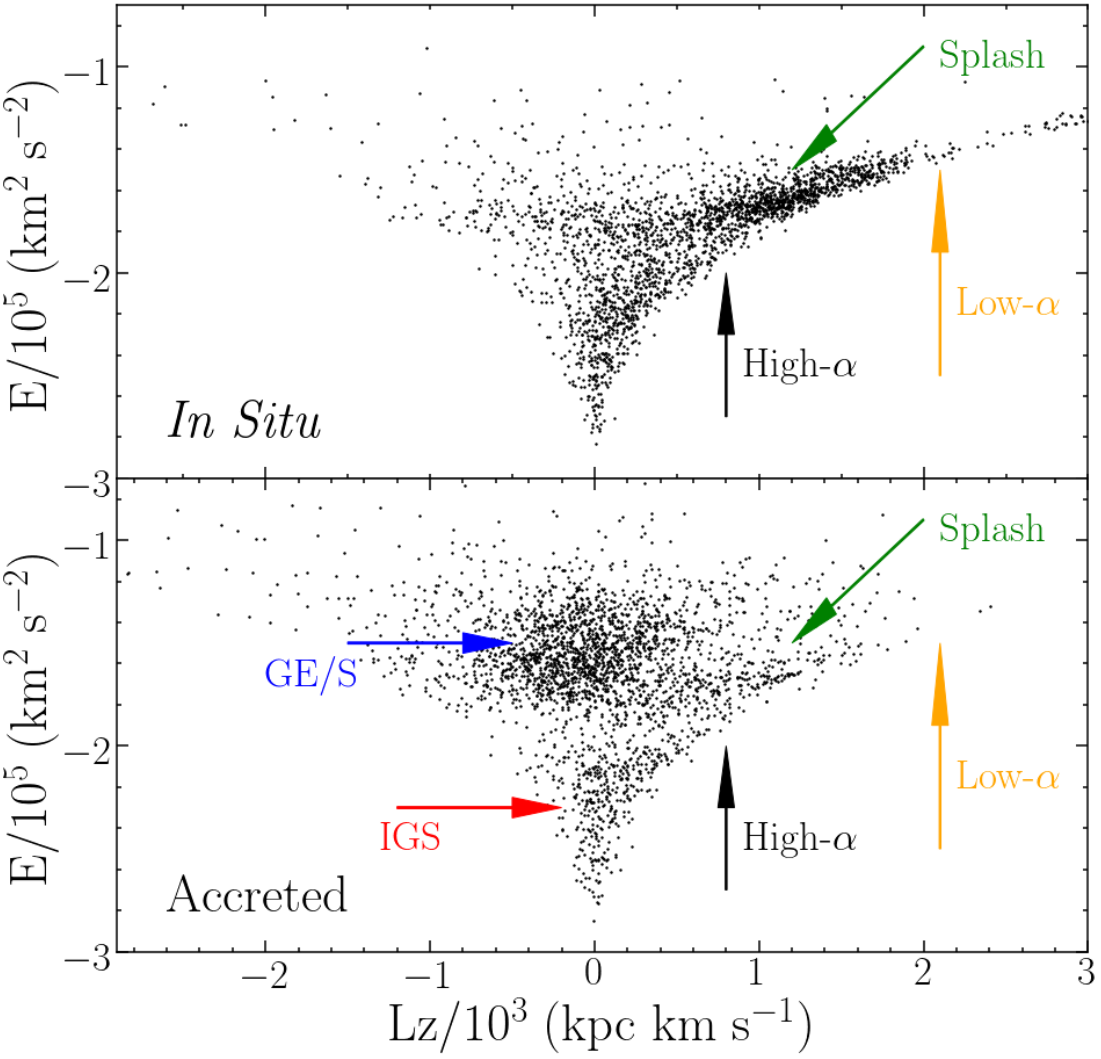

FIGURE 2.4: Distribution of metal-poor ([Fe/H]<–0.8) bulge stars in the energy-angular momentum plane. The *top panel* shows *in situ* stars and their accreted counterparts are displayed in the *bottom panel*. Arrows indicate the positions of the main structures visible on this plane: thin disk (orange arrow), thick disk (black arrow), *Splash* (green arrow), Gaia-Enceladus/Sausage (GE/S, blue arrow), and the inner Galaxy Structure (IGS, red arrow). The low- and high-α disks and the *Splash* show prominently in the *in situ* population (top) panel, whereas the GE/S and IGS can be clearly distinguished in the accreted population (bottom panel).

system (Haywood et al., 2018; Belokurov et al., 2018; Helmi et al., 2018; Mackereth et al., 2019a), and is largely absent in the top panel where *in situ* populations are displayed. Additional substructures can be discerned in the bottom panel, which are absent in the top panel of Figure 2.4. The focus of this paper is a low energy clump centred at $L_z/10^3$ ~0.1 km s^{-1}kpc (*red arrow*) with energies in the interval –2.6 E/10^5 –2.0km^{2}s^{-2}, whose position coincides with that of the low energy (L-E) family of globular clusters identified by Massari et al. (2019). The bulk of the stars associated with this group are located within ~4 kpc of the Galactic centre, so I refer to it as the Inner Galaxy Structure (IGS).

An energy gap is clearly visible in the bottom panel at about $E/10^5 \sim -1.9$ km^{2}s^{-2}, which separates stars belonging to the GE/S and the *Splash* from stars belonging to the IGS. In the top panel, that gap is filled by stars belonging to the thick disk and the *Splash*, which present a predominantly smooth distribution, much as expected from numerical simulations of Milky Way-like disks undergoing satellite accretion (e.g., Jean-Baptiste et al., 2017b). This energy gap is not entirely empty in the accreted sample, which is partly due to measurement errors and partly due to the fact that *in situ* structures, in particular the high-α disk and the *Splash* make a small, but noticeable, contribution to the data in the bottom panel. This is to be expected on the basis of the discussion in Section 2.3, where I showed that standard chemical evolution models predict *in situ* contamination in the accreted sample. Under this interpretation of the data, the distribution of the chemically-defined accreted sample in $E - L_z$ space consists of two overlapping populations: one of them consists of various clumps associated with accreted structures, most prominently the GE/S and the IGS, and the other is comprised of a predominantly smooth, metal-poor, residual contamination associated with high-α disk stars, which include both the unperturbed disk and the *Splash*.

These results suggest that the IGS is dynamically detached from other metal-poor populations in the halo and disk. This is an important result, so it is vital that the reality of this energy gap is firmed up quantitatively. To do that I measure the ratio between the number of stars with energies within the gap and those below it in both the accreted and *in situ* samples. I consider stars within the gap to have energies given by $-2.00 < E/10^5 < -1.85$ km^2 s^{-2} and those below it have $E/10^5 < -2.00$ km^2 s^{-2}. The ratio in the *in situ* sample is 0.40±0.04 and in the accreted sample 0.27±0.04, configuring a difference that is significant at the 2σ level. I thus conclude that the gap is real, and an indication of the presence of real substructure in the distribution of accreted stars in the low energy locus of IoM space.

Finally, it is worth mentioning that a relatively small number of stars can be seen scattered at high energy levels ($E/10^5 - 1.6$ km^2 s^{-2}) among the *in situ* population (top panel), on a wide range of angular momenta. These are predominantly low-α metal-poor stars and are likely accreted contaminants in the *in situ* sample (c.f. Figure 2.2).

2.4.3 IGS definition and contamination by *in situ* stars

As pointed out in the previous section, the IGS corresponds to a low energy substructure visually discernible in IoM space. In order to define the IGS sample in an easily reproducible manner, I initially ran an algorithm to identify data clustering in multi-parameter

space. The algorithm of choice was HDBSCAN (Campello et al., 2013) and the parameters adopted were energy, vertical and radial action (J_r and J_z), angular momentum (L_z), and eccentricity. I ran HDBSCAN on several combinations of these parameters, varying the input parameters *minimum cluster size* and *minimum samples* in such a way that the structures visible in action space could be detected. However, the specific subsamples associated by HDBSCAN to the various substructures are very sensitive to the input parameters adopted. Therefore, I do not feel confident that HDBSCAN-selected samples represent the distribution of the properties of the accreted systems in action space in a statistically robust fashion.

I thus adopt simple, easily reproducible criteria to establish IGS membership. Stars belonging to the IGS are those belonging to the "Accreted" region of chemical space in Figure 2.1, which meet the following simple orbital energy and eccentricity criteria:

- $-2.60 < E_{\rm IGS}/10^5 < -2.00$ km^2 s^{-2}
- $e_{\rm IGS} > 0.6$

The energy criterion restricts the sample to the clump that is visually identified in Figure 2.4. The eccentricity criterion is aimed at minimising contamination by stars belonging to the inner high-α disk (see Figure A.2).

As discussed in the previous section, examination of Figure 2.4 reveals a discernible signature of *in situ* structures in the distribution of accreted stars in the bottom panel of Figure 2.4, which overlap the IGS. Those are metal-poor *in situ* stars that inhabit the "Accreted" locus of the chemical plane in Figure 2.1, as discussed in Section 2.3.1. I can use those *in situ* features that are present in the distribution of accreted stars in IoM as a means to estimate the contamination of *in situ* stars in the IGS sample.

To assess that contamination, I use sub-samples of the chemically defined "Accreted" and *in situ* samples, displayed in Figure 2.5, overlaid on the same data originally displayed in Figure 2.4. I assume that the energy distribution of stars in the high-α disk is smooth (as predicted by simulations, see, e.g., Jean-Baptiste et al., 2017b) and can be estimated from the distribution of *in situ* stars in the $E - L_z$ plane (upper panel of Figure 2.5). I further assume that that energy distribution is the same as that of the contaminants in the accreted sample (bottom panel of Figure 2.5). If those assumptions are correct, one can calculate the ratio in the *in situ* sample between the numbers of low energy stars in the IGS region, $n(\text{low E})_{InS}$ (*red symbols in the top panel* of Figure 2.5), and those in a reference high energy locus that is free from accreted stars, $n(\text{high E})_{InS}$ (*blue symbols in the top panel* of Figure 2.5). That ratio can then be used to convert the number of

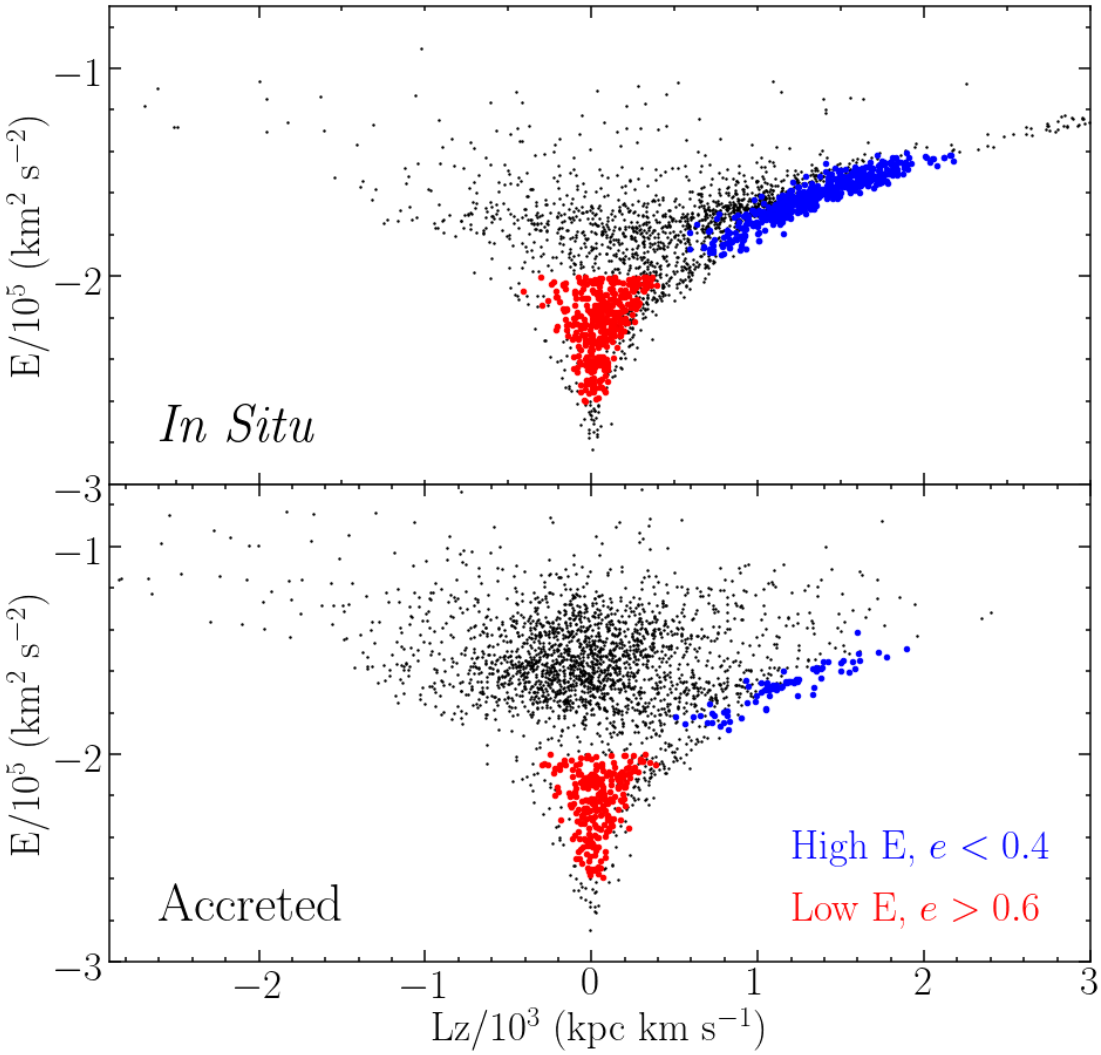

FIGURE 2.5: Subsamples used to estimate the contamination of the IGS sample by *in situ* stars. In both panels, red symbols mark stars located within the locus in orbital space defined by the IGS stars. Blue symbols indicate stars in a reference region of orbital space occupied by high-α stars alone. The ratio between numbers of red and blue stars in the *in situ* population (*top panel*) is used to infer the number of *in situ* contaminants among the IGS stars (red symbols in the *bottom panel*). We estimate that somewhere between 22 and 40% of stars in the IGS sample are actually high-α disk contaminants.

high energy disk stars in the accreted sample, $n(\text{high E})_{Acc}$ (*blue symbols in the bottom panel* of Figure 2.5), into the number of contaminating disk stars in the IGS sample, N_{cont}, as follows:

$$N_{\text{cont}} = \left[\frac{n(\text{low E})}{n(\text{high E})}\right]_{InS} \times \; n(\text{high E})_{\text{Acc}} \tag{2.1}$$

That number can then be compared to the actual number of stars meeting the above defined criteria for the IGS in the accreted region (*red symbols in the bottom panel* of

TABLE 2.2: Numbers for the assessment of the contamination of the IGS sample by *in situ* stars.

$[Fe/H]_{cut}$	$n(\text{low E})_{InS}$	$n(\text{high E})_{InS}$	$n(\text{low E})_{Acc}$	$n(\text{high E})_{Acc}$	$\%_{cont}$
–0.8	370	516	244	74	22%
–1.0	153	116	226	68	40%

Figure 2.5) to estimate the contamination fraction.

For that purpose I must select a region of the $E-L_z$ space that provides a pure sample of *in situ* stars belonging predominantly to the high-α disk. I choose such a locus by picking stars with eccentricity < 0.4 and in the energy range $-1.9 < E/10^5 < -1.4$ km^2 s^{-2}. Stars in this reference region and in the IGS locus defined above are displayed as blue and red dots in Figure 2.5.

By proceeding in this fashion, I obtain the numbers listed in Table 2.2, which mean that approximately 22% of the IGS sample actually consist of high-α disk stars. A fundamental systematic uncertainty in this procedure concerns the metallicity cut adopted for the accreted and *in situ* samples. The calculation above was based on the [Fe/H]=–0.8 definition of metal-poor stars adopted throughout this paper. However, if a slightly more conservative cut is adopted at, say, [Fe/H]=–1.0, the inferred contamination goes up to 40%. This is due to how the numbers in the *in situ* population, particularly the reference disk stars, depend on metallicity. The angular momentum distribution of disk stars in the sample is strongly dependent on metallicity. At lower metallicity, the L_z distribution is shifted towards lower values, leading to a higher $[n(\text{lowE})/n(\text{high})]_{In\ situ}$, and thus a higher number of estimated contaminants (N_{cont}).

I therefore conclude that the contamination of the IGS sample by high-α disk stars ranges between roughly 22 and 40%.

2.4.4 Orbital properties of bulge stars

The bulk of the stars belonging to the substructure identified in Section 2.4.2 are contained within 4 kpc of the Galactic centre. Therefore, it is useful to inspect the orbital behaviour of *in situ* and accreted stars within that central volume of the Galaxy, with an eye towards determining whether the properties of the accreted population mimic those of their *in situ* counterparts, or whether they are distinct and cannot be derived from the latter. Figure 2.6 displays high- and low-α *in situ* stars of all metallicities with $R_{GC} < 4$ kpc, as well as their accreted counterparts on various IoM spaces. Plotted as a function of angular momentum (L_z) are the vertical action (J_z, top panels), radial action (J_r, middle panels), and total energy (E, bottom panels).

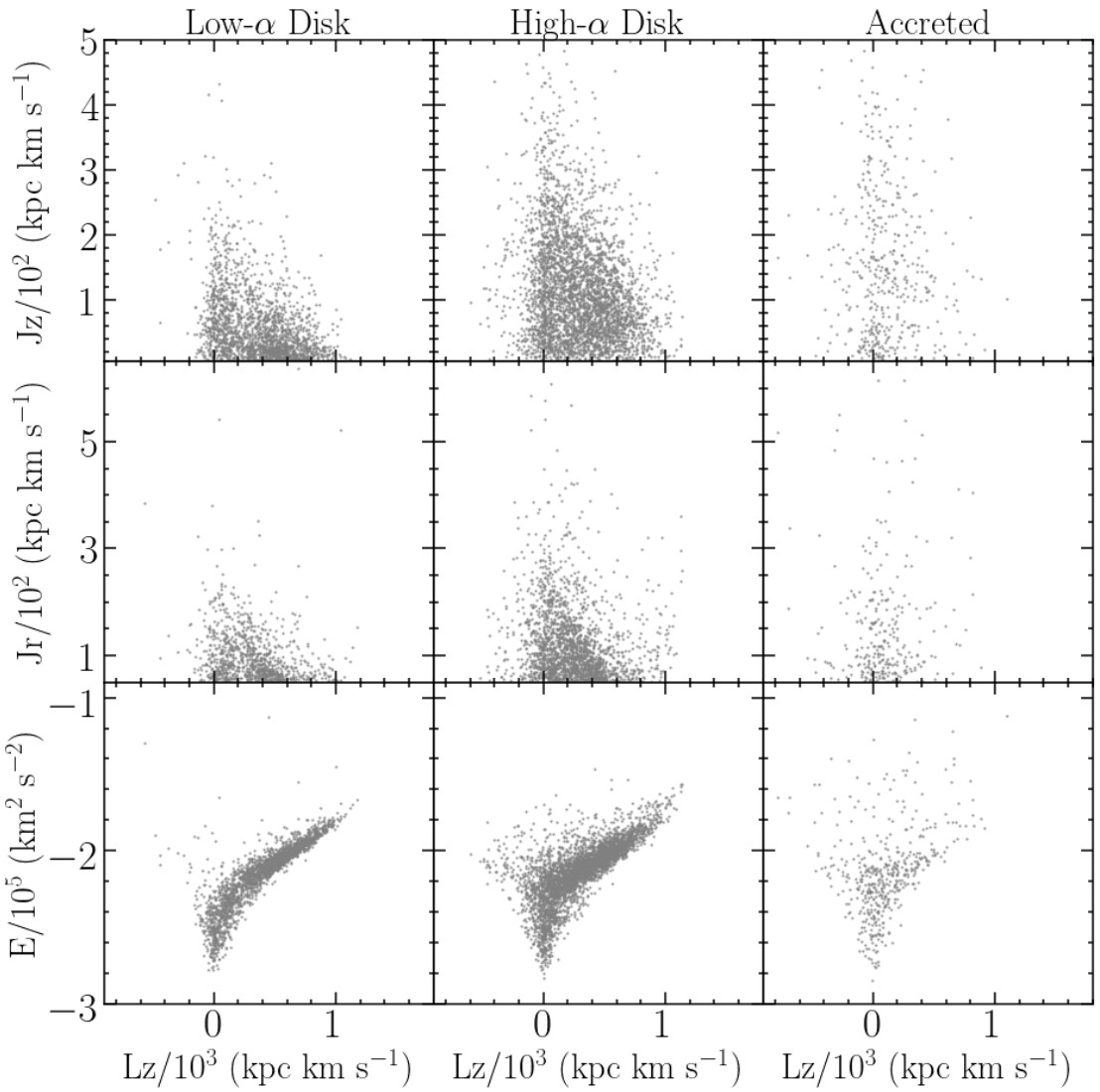

FIGURE 2.6: Distribution of low-α (left panels), high-α (middle panels), and accreted stars (right panels) in action space. Only stars within $R_{\rm GC} < 4$ kpc are shown. Chemically defined accreted populations in the bulge have on average lower angular momentum, and higher radial and vertical actions.

The shift to a focus on the inner 4 kpc causes obvious changes in the distribution of stellar populations. The clearest one is the near complete absence of stars with $L_{\rm z}/10^3$1 kpc km s^{-1} in the inner Galaxy, which is understandable on purely geometric grounds. Interestingly, *Splash* populations are nearly absent at $R_{\rm GC} < 4$ kpc. Of the three main *in situ* structures apparent in Figure 2.4, one can only find a mix of the low $L_{\rm z}$ high-α populations and the extension of the low-α towards lower $L_{\rm z}$. The former also manifests itself by the presence of stars with large $J_{\rm z}$ in the top middle panel. From the disk through the disk to the accreted population, there is a consistent trend towards a larger fraction of the stars having larger vertical and radial actions, as well as lower angular momentum. Accreted populations are dominated by hot, low kinematics.

The distribution of stars in the accreted population on all planes differs markedly from that of their *in situ* counterparts. To gain further confidence on the reality of this critical result, we display in Figure 2.7 histograms comparing the distributions of action variables of the accreted and *in situ* inner Galaxy populations. I limit the comparison to the population only, since the differences between accreted and stars can be easily recognised by eye on Figure 2.6.

Substantial differences can be seen in the distributions of all integrals of motion. This is particulary obvious when comparing the 1D distributions of each integral of motion separately, as shown in Figure 2.7. I perform Kolmogorov-Smirnoff (KS) tests comparing the distributions of accreted and *in situ* populations in those variables, finding that the two samples are not extracted from the same parent population in (p-value=1×10^{-34}), (6×10^{-15}) (7×10^{-7}), and E (5×10^{-6}). This result persists, with decreased statistical significance, when only metal-poor stars are considered, with p-value<0.01 in all cases. To isolate stars that are only associated with the IGS, I repeat the KS tests for L_z, J_z, and J_r, by restricting the comparison only to stars with $E < -2 \times 10^5$ km^2 s^{-2}. The results are unchanged except for the case of J_r, for which the KS test cannot rule out the null hypothesis.

I conclude that the distribution of accreted stars in the inner Galaxy differs from those of major *in situ* components in action space. This result agrees with the findings by Ness et al. (2013b) and Arentsen et al. (2020b), who show that metal-poor populations are characterised by hot kinematics (see also Minniti, 1996), even though without detailed chemical compositions they were unable to distinguish *in situ* from accreted populations. In the most detailed investigation of the kinematics of bulge stellar populations to date, Ness et al. (2013b) found that the metal-poor component of the bulge ([Fe/H] $-$ 1) does not partake in its cylindrical rotation, being characterised by slightly lower rotation and higher velocity dispersion (see also Zasowski et al., 2016).

I point out that the differences between accreted and *in situ* populations are reduced when only metal-poor ([Fe/H]<–0.8), low-energy stars ($E/10^5 < -2$ km^{2}s^{-2}) are considered. In that case, the only variable for which a residual statistically significant difference is found is L_z (p-value=0.004). This is an interesting result. Such similarity in action space is partly due to the fact that the contamination of the accreted sample by *in situ* stars is not negligible. Recall that in Section 2.4.3 I showed that the IGS sample is contaminated at the 22-40% level. The *in situ* contamination for the accreted sample displayed in Figure 2.7 is higher, since unlike the IGS sample, it includes stars of all eccentricities. Nevertheless, taken at face value, this result suggests that, if indeed the IGS is the remnant of an accretion event, it has had the time to mix well with its

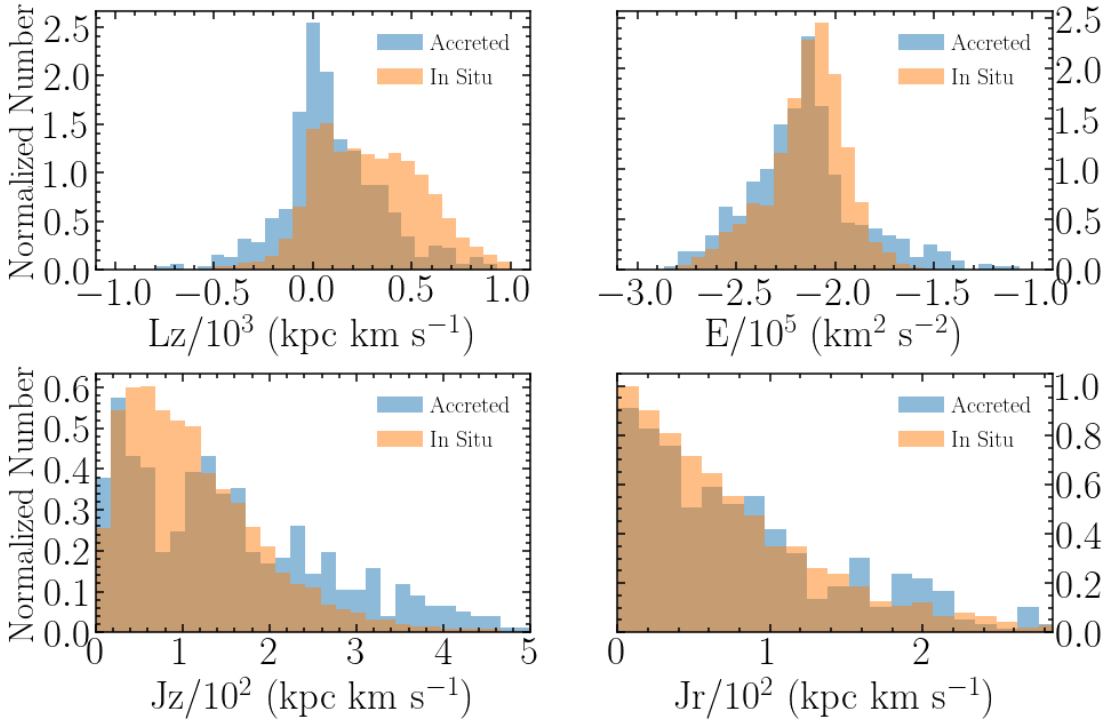

FIGURE 2.7: Comparison between the distributions of high-α *in situ* and accreted inner Galaxy populations in action variables. Statistically significant differences can be seen in L_z and J_z, whereby accreted stars are dynamically hotter, being distributed towards smaller angular momentum (L_z) and larger vertical action (J_z). The energy distributions differ substantially due to the presence of GE/S stars with E$> -2 \times 10^5 \mathrm{km}^2\mathrm{s}^{-2}$. Removal of that contamination does not change the results.

co-spatial *in situ* population, which suggests a very early accretion event. We discuss this and other possible interpretations of the data in Section 2.6.1 .

In summary, I conclude that the chemically defined accreted populations in the bulge are not dynamically associated with their *in situ* counterparts. They are dynamically hotter than the *in situ* population typically possessing low angular momentum and being distributed towards large values of vertical and radial action. I take these results as suggestive of an accretion origin. In the next section I discuss the chemical properties of the IGS.

2.5 Chemical Properties

In the previous section I investigated the orbital properties of the IGS, concluding that they are distinct from those of co-spatial *in situ* populations, which supports an accretion origin. In this section I examine the chemical compositions of the stars from the IGS alongside those of their inner Galaxy counterparts. Our main objective is to check whether detailed chemistry is consistent or not with an accretion scenario. In Figure 2.9

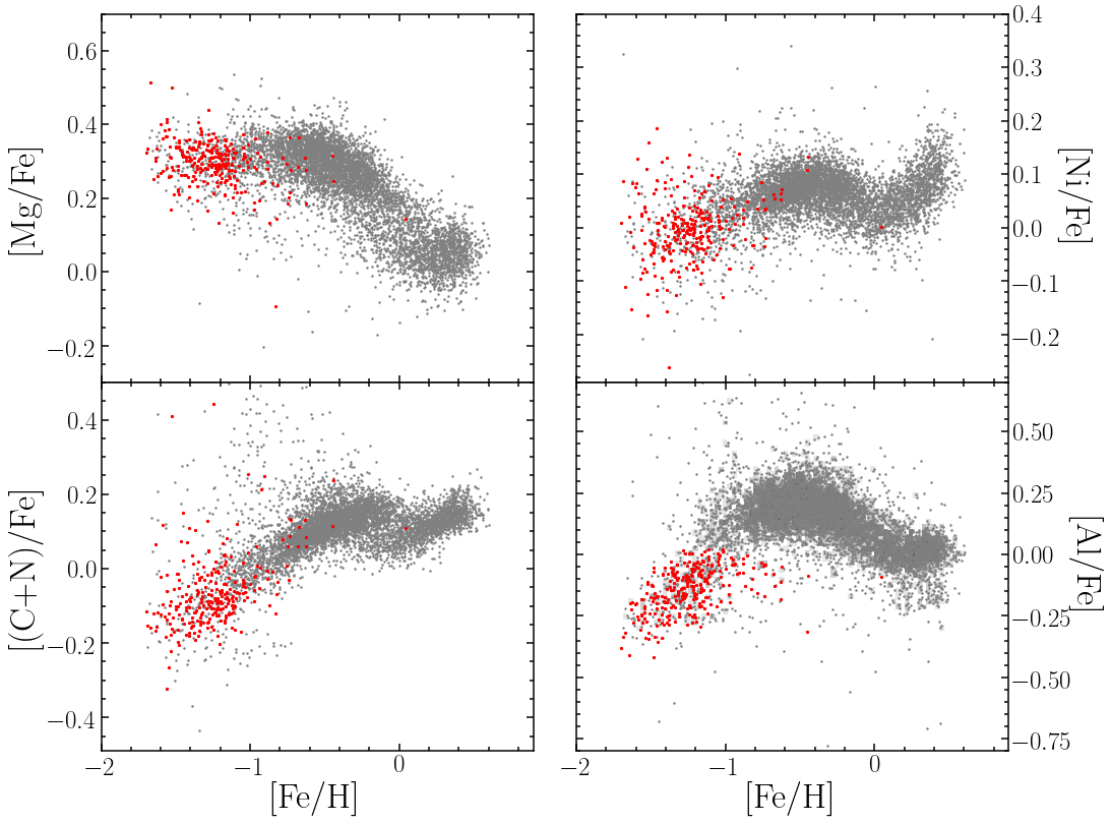

FIGURE 2.8: Comparison between stars from the IGS (red dots) with their bulge counterparts (gray dots). The IGS has an abundance pattern that is characteristic of those of dwarf satellites of the Milky Way, yet they seem to form a single sequence with the remainder of the bulge populations, even though they all are associated with different Galactic components.

we display again the accreted stars shown in the bottom panel of Figure 2.4, this time marking stars deemed to be members of the IGS and GE/S systems as red and blue dots, respectively. The IGS sample is defined in Section 2.4.3. We consider members of the GE/S system to be those stars with $-0.4 < L_z/10^3 < 0.3$ kpc km s^{-1} and $-1.75 < E/10^5 < -1.3$ km^2 s^{-2}. According to these criteria, the samples contain 259 candidate members of the IGS and 1,026 associated with the GE/S system. These definitions are henceforth adopted in the discussion of the chemical properties of the IGS.

In Figure 2.8 I contrast the stars from the IGS with their *in situ* $R_{GC} < 4$ kpc counterparts in chemical space. I limit the comparison to a few elements that sample a range of nucleosynthetic pathways, with Mg being mostly contributed by SN II, C and N by massive and AGB stars, and Ni by SN Ia (e.g., Chiappini et al., 2003; Nomoto et al., 2013). The latter element is additionally interesting due to it being typically depressed in dwarf satellites of the Milky Way (e.g., Shetrone et al., 2003). For more comprehensive studies of the detailed abundance patterns of bulge stars, I refer the reader to the

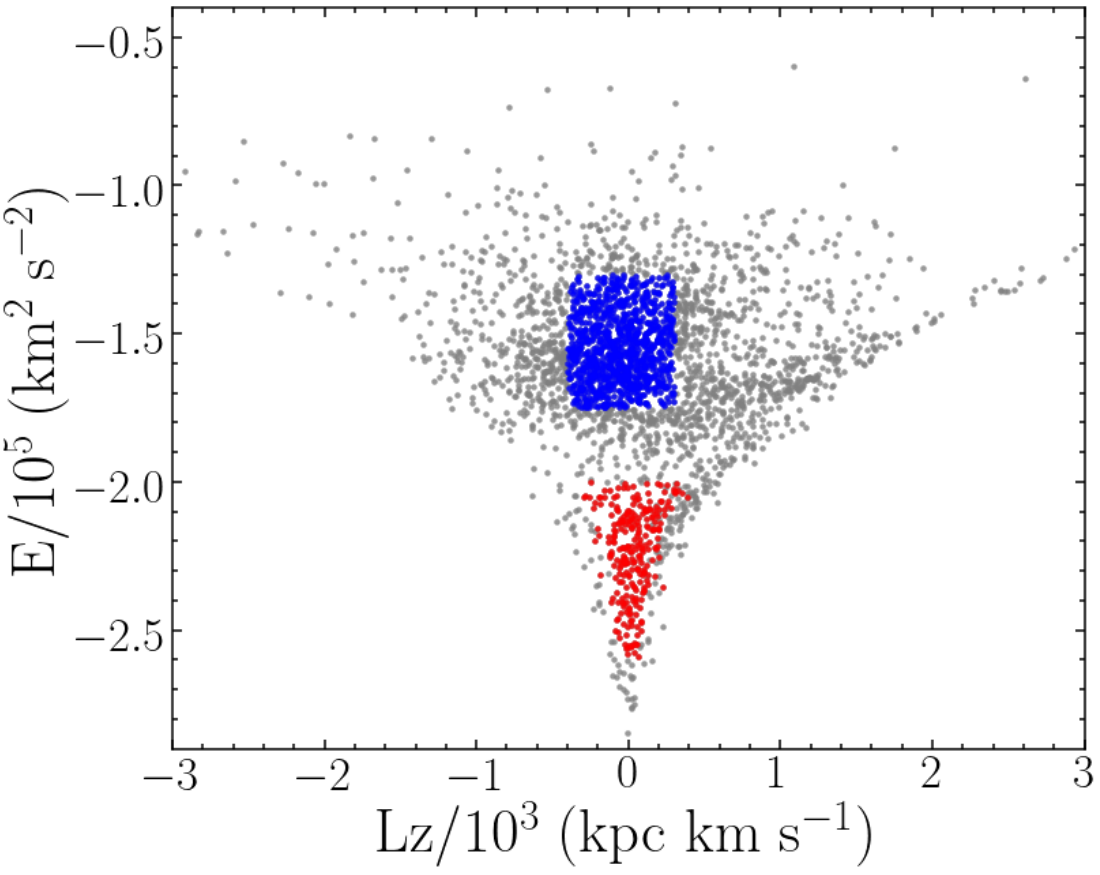

FIGURE 2.9: Same as bottom panel of Figure 2.4, identifying stars deemed to be members of the GE/S system (blue dots) and the IGS (red dots).

excellent studies by Schultheis et al. (2017) and Zasowski et al. (2019) and the review by Barbuy et al. (2018).

Two main results emerge from this comparison: *(i)* the stars belonging to the IGS have an abundance pattern that is typical of dwarf galaxies, characterised by low abundances of elements such as Al (by construction), C, N, and Ni (e.g., Hayes et al., 2018; Mackereth et al., 2019a; Helmi, 2020; Das et al., 2020)); *(ii)* the abundance pattern of the IGS apparently behaves as a natural extension of the bulge field population towards [Fe/H] < -1, a result that has also been noted by Schultheis et al. (2017) and Zasowski et al. (2019). To be clear, this extension of the trends towards metal-poor populations concerns only the *locus* occupied by stars in the various chemical planes, not the relative counts. The latter are examined in Section 2.5.2. Similar behaviour is seen in the data presented by Queiroz et al. (2020a)[4], who examine the spatial variation of the stellar distribution on the α-Fe plane across the Galactic disk and bulge. Naively, one would consider this seeming continuity between the IGS and its *in situ* counterparts surprising, given the

[4]Note that Queiroz et al. (2020b) report the presence of an α-bimodality in the distribution of bulge stars *on the high metallicity end* of the α-Fe plane, at variance with the results. I suspect this discrepancy may result from the adoption of different distances by the two studies.

alleged accreted nature of the IGS. In Section 2.5.1 I show that continuity between the chemical compositions of the IGS and its more metal-rich bulge counterparts is actually *expected* on the basis of numerical simulations.

Despite this apparent continuity, it is worth noting that slight deviations of this pattern are apparent in elements such as Mg, Ni, and Si (not shown), for which the mean of the abundances of IGS stars is lower than those of their *in situ* metal-poor counterparts. In all cases this result does not have a high statistical significance, as the differences in mean abundance ratios are slighlty smaller than the standard deviation of the distributions. Considering the three elements in aggregate, I get $\langle[(\mathrm{Mg}+\mathrm{Si}+\mathrm{Ni})/\mathrm{Fe}]\rangle_{\mathrm{IGS}} = 0.54 \pm 0.11$ and $\langle[(\mathrm{Mg}+\mathrm{Si}+\mathrm{Ni})/\mathrm{Fe}]\rangle_{in\ situ} = 0.68 \pm 0.17$ when only stars with $-1.1 < [\mathrm{Fe/H}] < -0.9$ and $R_{GC} < 4$ kpc are considered. That a larger difference is not found may not at all be surprising, given that the IGS sample is contaminated by *in situ* stars at the 22–40% level (c.f. Section 2.4.3).

It is also worth pointing out that IGS stars with [Fe/H]>–1.0 show a variety of different behaviours. Some of them follow the same trend as the disk in Mg, Ni, and C+N, whereas others display a behaviour more similar to those of dwarf satellites, with low [Mg/Fe], [Ni/Fe], and [(C+N)/Fe]. By construction, all of them display low [Al/Fe]. I hypothesise that these metal-rich IGS stars are a mixture of thick disk contaminants (whose low [Al/Fe] ratios would be difficult to understand), thin disk contaminants, and genuine IGS members.

In summary, the results presented in this Section and Sections 2.4.2 and 2.4.4 show that a metal-poor stellar population located in the inner Galaxy shares chemical and IoM properties with well known halo accreted systems. Figure 2.8 suggests on the other hand that the abundance pattern of this same structure is consistent with sharing a common chemical evolution path with its bulge counterparts potentially associated with other co-spatial Galactic components. Yet the analysis in Sections 2.4.2 and 2.4.4 suggests that the IGS is dynamically detached from the rest of the bulge (Figures 2.6 and 2.7). This is a puzzling result. In the next subsections I look into the theoretical expectations for the chemical evolution of Milky Way-like galaxies that underwent comparable accretion events (Section 2.5.1) and inspect the data for the presence of a chemical connection between the accreted and *in situ* populations in the inner Galaxy.

2.5.1 Predictions from Numerical Simulations

The discussion above naturally prompts us to enquire into the theoretical predictions for the chemical evolution of Milky Way-like Galaxies with accretion histories similar to that seemingly implied by the results. For that purpose I resort to the predictions from the

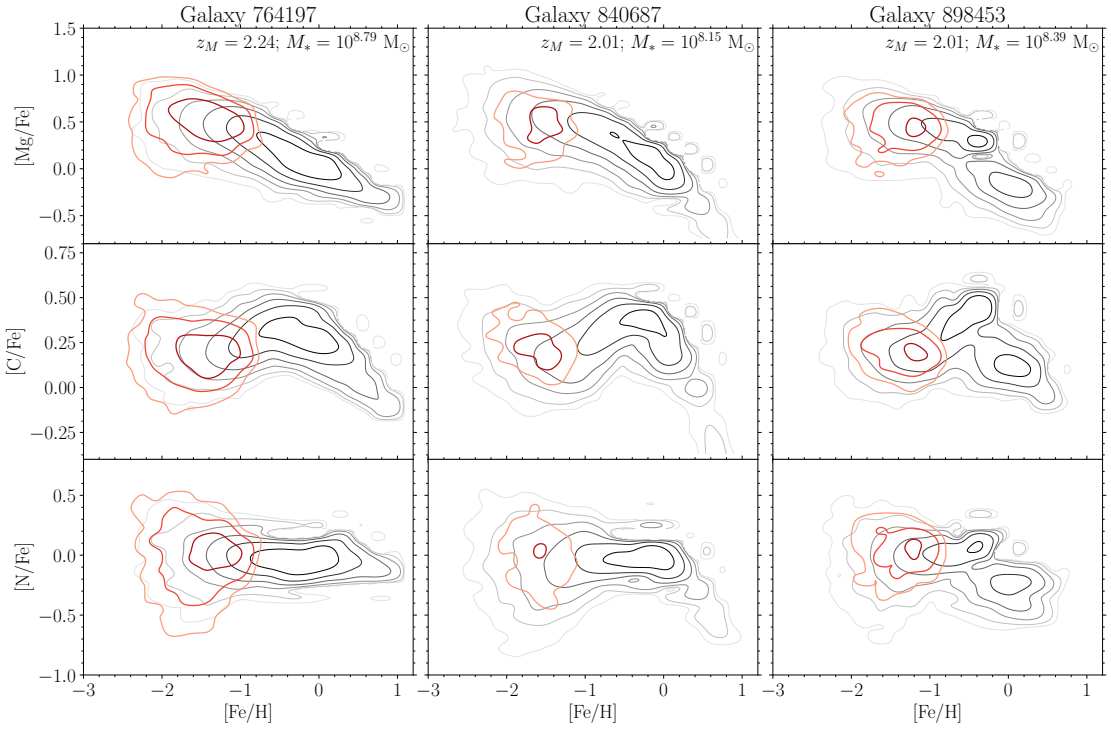

FIGURE 2.10: Chemical compositions of stellar particles in Milky Way-like galaxies in the EAGLE simulations. Shown are three examples of a sample of simulated galaxies selected with masses similar to that of the Milky Way, which underwent a massive accretion event at $z \geq 2$. Red countours indicate the distribution of stars belonging to the accreted system, and black contours indicate the distribution of stars formed *in situ*. Contouring starts at 10 stars per bin, increasing logarithmically in 0.5 dex steps. In all systems, for all abundances tracked by EAGLE, the accreted stars possess chemical compositions that are in good agreement with those of the *in situ* populations of same metallicity.

suite of cosmological numerical simulations by the Evolution and Assembly of GaLaxies and their Environments (EAGLE) project (Schaye et al., 2015; Crain et al., 2015). The question guiding this analysis is the following: what are the chemical properties of Milky Way like galaxies undergoing an important early accretion event? More specifically, do I expect the chemical properties of the stars belonging to the accreted system to differ substantially from those of the *in situ* population?

The EAGLE simulations provide excellent material for this enquiry. The large volumes included in the various sets of simulations make possible robust statistical analyses of the evolutionary outcomes for a broad gamut of final galaxy properties, and at a wide enough range of resolutions to address the needs of different types of investigations. To maximise resolution I choose to study the 25^3 Mpc^3 L025N752-Recal simulation, whose volume is large enough to yield a substantial number of galaxies with Milky Way-like masses and accretion histories similar to that suggested by our results. The chemical evolution prescriptions of the simulations track only elements relevant to the thermal balance of the interstellar medium, yet this is sufficient for the purposes, as predictions

for crucial elements Fe, C, N, and Mg are included. For more details on the simulations I refer the reader to (Schaye et al., 2015) and (Crain et al., 2015).

The analysis was conducted as follows. I selected galaxies with Milky Way-like masses within the interval $7 \times 10^{11} < M_{200}/M_{\odot} < 3 \times 10^{12}$ and looked for those that underwent an accretion of a satellite with stellar mass $M_{\star}/M_{\odot} \geq 10^{8}$ at $z \geq 2$ (see Section 2.6.2 for an estimate of the mass of the IGS progenitor). I found a total of 15 accreted galaxies with such a profile (34% of the host galaxy sample within that halo mass range). The particles for the accreted galaxies were selected when they were at their peak stellar mass. For three of those galaxies I display chemical composition data in Figure 2.10. The data are displayed in the form of contour maps indicating the distribution of stars on abundance planes, with *in situ* and accreted populations shown in gray and red, respectively. *In situ* populations in this context are defined as stellar particles that were bound to a halo in the main galaxy branch at the snapshot prior to star formation. The abundance planes shown are Mg-Fe, C-Fe, and N-Fe, which track the contribution of SN II, SN Ia, and AGB stars, sampling a range of chemical enrichment timescales.

The answer to the question posed above immediately strikes the eye upon inspection of Figure 2.10. For all three galaxies, and all three elemental abundances, the abundance ratios of the accreted populations are in good agreement with those of the *in situ* populations at same metallicity. This is the case for *all* the 15 galaxies meeting the selection criteria. It is also the case for all the other elemental abundances tracked by EAGLE. This result is also fully consistent with the analytical model presented in Figure 2.2, which shows that the early chemical evolution of a Milky Way-like galaxy and its satellite are similar. I conclude therefore that the approximate continuity between the abundances of the accreted and *in situ* populations in Figure 2.8 is in fact not surprising, but actually an expectation from theory, at least for the elements whose chemical evolutions are modelled by EAGLE.

This is a very important result, the implications of which configure the proverbial double-edged sword. On one hand the theoretical predictions for the *locus* of accreted populations in chemical space cannot rule out the accreted nature of the IGS. On the other, it cannot ascertain it either, as the apparent continuity between the chemistry of the IGS and its *in situ* populations could alternatively be a by-product of pure *in situ* chemical evolution.

To find the way out of this conundrum I invoke relative number counts in chemical space. In trying to understand the apparent chemical continuity between the accreted and *in situ* populations in Figure 2.8 I ask the following question: is the distribution of stellar data on abundance planes consistent with the accreted population being an additional structure, or do the number counts suggest that it is just the tail end of the distribution

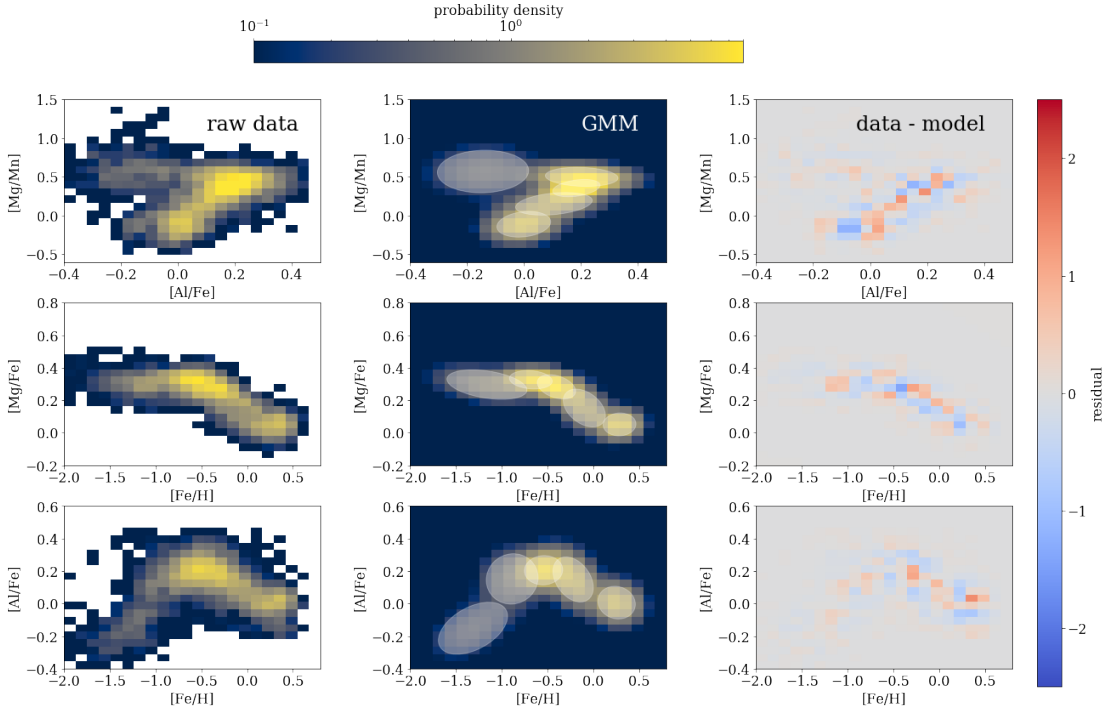

FIGURE 2.11: *Left Panels:* Distribution of stars with $R_{GC} < 4$ kpc in various chemical planes; *middle panels:* Gaussian Mixture Modelling (GMM) of substructure of the data distribution on the same chemical planes; *right panels:* residuals from GMM fit. A satisfactory match to the density distribution of data points is obtained by adopting five *detached yet overlapping* substructures. Each of those correspond to peaks in the metallicity distribution function of bulge populations (Ness et al., 2013a), after accounting for zero point differences in [Fe/H].

of the *in situ* populations? In the next section I address this question in a quantitative fashion.

2.5.2 Substructure in Chemical Space

2.5.2.1 Matching the distribution with multiple components

In this Section I tackle the problem of understanding the apparent chemical continuity between the IGS and its more metal-rich inner Galaxy counterparts (Figure 2.8) from a purely observational perspective. I center the approach around the following question: can the stellar density distribution in chemical space be described by a discrete number of *detached* substructures? Ness et al. (2013a) showed that the bulge MDF can be well modelled by a combination of five components, which they ascribe, in order of increasing metallicity, to the inner halo, the metal-poor thick disk, the bulk of the thick disk itself, the bar, and the thin disk. Some of these peaks can be identified in the raw MDF in Figure 2.3, although a one-to-one mapping with the Ness et al. (2013a) MDF is quite difficult due to differences in the two metallicity scales and in the relative strengths of

the various peaks (recall that the MDF is not corrected for selection effects), and the uncertainties associated with multiple gaussian fitting in 1D space. These difficulties are particularly important towards low metallicity, where the statistics is not as robust and the results of abundance analysis may be afflicted by important systematics.

The exceptional quality of the detailed chemical compositions comes in handy in this juncture. By considering the distribution of our sample in higher dimensional space I hope to gain additional leverage in distinguishing the different components making up the stellar population mix of the inner Galaxy. The stellar distribution on some chemical planes, such as [Mg/Mn]-[Al/Fe] and [Al/Fe]-[Fe/H], show a clumpy distribution which suggests that the data may be amenable to such an approach. In other words, one should be able to model the stellar density distribution in chemical space as a combination of overlapping structures, which are not necessarily connected to one another by a coherent chemical evolution path. To test this hypothesis I check whether the stellar density distribution in a few chemical planes can be reproduced by a Gaussian Mixture Modelling (GMM) approach. Obviously a Gaussian distribution is only a zero-th order approximation to the stellar density distributions in chemical space. A massive stellar system such as, for instance, the Galactic disk, underwent star formation long enough that the run of the number of stars with metallicity and abundance ratios is strongly determined by the star formation history. Conversely, in a less massive system whose star formation was quenched during an early accretion to a massive halo, the distribution of stellar metallicities should be narrower and thus the GMM approach may work better.

I am particulary concerned with modelling the metal-poor end of the metallicity distribution to check whether the IGS is detached from its more metal-rich peers in the inner Galaxy. The key measure of chemical detachment of the IGS from its more metal-rich counterparts in the inner Galaxy is provided by the ability of a GMM approach to account for the density distribution of the IGS, so that no important residual connection between that and the other populations is left after model subtraction (although *some* residual should be expected given the contamination by *in situ* populations discussed in Section 2.3).

The sample for analysis is displayed in the left panels of Figure 2.11. It consists of all stars within $R_{\rm GC} < 4$ kpc, but removing outliers with [Al/Fe]>+0.5, as their abundances are affected by the N-rich-star phenomenon (Schiavon et al., 2017b). I also removed relatively metal-poor stars with low [Mg/Fe] ([Fe/H]<–0.5 and [Mg/Fe]<+0.15), which have high orbital energy and are not associated with the IGS, but rather with the GE/S system (see Section 2.6.1.1 and Figure 2.12). The stars thus selected are shown in three chemical planes, where the 2D histograms are cast in terms of probability

density. On the top row, stars are displayed in the [Mg/Mn] vs [Al/Fe] plane, and on the middle and bottom rows their distribution can be seen on the Mg-Fe and Al-Fe planes, respectively. According to the definition (Figure 2.1), accreted stars occupy the upper left quadrant of the [Mg/Mn]-[Al/Fe] plane (top left panel of Figure 2.11). On the other planes, accreted stars are located in the low metallicity end of the distribution ([Fe/H]<–1). I fit a separate GMM to the distribution of these stars on each of the three chemical planes. The ideal number of components was decided by calculating the Bayesian Information Criterion (BIC) for each fit. I found that the best match is found when either 4 or 5 components are adopted. I allow the mean and covariances of each component to be entirely free with no informative or uninformative priors. The GMMs for the 5 component case are overlaid on the data in the middle panels of Figure 2.11. The standard deviation of the residuals around the fits are 0.23, 0.19, and 0.17 for the top, middle, and bottom panels, respectively.

The residuals after subtraction of the best fit models and the data are displayed in the right panels. The residuals are relatively small, and slightly larger towards higher metallicity, which reflects the much larger stellar density in that regime. When normalized by the Poisson fluctuations per bin, the residuals are homogeneously distributed across the planes, and are everywhere smaller than $\sim 2\sigma$ of the Poisson uncertainty in each bin. These numbers suggest that the distribution of the stellar density in the locus of accreted stars is well accounted for by the GMM approach, showing that they can be matched by a simple combination of detached, yet overlapping structures. Interestingly, the GMM fit to the stellar distribution in the Mg-Fe plane highlights the fact that the lowest metallicity component has a slightly lower [Mg/Fe] than the next one in order of increasing metallicity. This result supports the notion that the most metal-poor component is dominated by an accreted stellar population, as one would expect [Mg/Fe] to be constant in an *in situ* population within the metallicity interval involved. Also quite importantly, even though the GMM match was performed independently to the data on the three chemistry planes, the associations of stars to a given group were largely consistent across the three models, which attests for the reality of these groups.

2.5.2.2 Breaking the MDF degeneracy with additional chemistry

The five-component match identifies peaks located at [Fe/H] $\sim$ –1.3, –0.8, –0.5, and –0.2 and +0.3, which are very roughly consistent with the five MDF peaks identified by Ness et al. (2013a), after allowing for a $\sim$0.2-0.4 dex difference between the zero points of the metallicity scales of the APOGEE and ARGOS surveys (see, for instance, the positions of the peaks in the APOGEE bulge MDF determined by García Pérez et al., 2018; Rojas-Arriagada et al., 2020). The bulge MDF has been analysed exhaustively in recent

work based, e.g., on the ARGOS (Ness et al., 2013a), Gaia-ESO (Rojas-Arriagada et al., 2017), and APOGEE (Schultheis et al., 2017; García Pérez et al., 2018; Rojas-Arriagada et al., 2020) surveys. The number of peaks in the bulge MDF, which in turn constrains the number of physically distinct components cohabiting the bulge, have been subject to debate in the recent literature (see discussion by Fragkoudi et al., 2018).

I do not aim at a detailed analysis of the topic in this paper. However, I wish to highlight the fact that the consideration of additional abundances helps untangling the two most metal-poor populations in the sample. The task of disentangling these populations in the MDF of Figure 2.3 is far from straightforward, as the distributions of these components overlap strongly in one-dimensional metallicity space. However, consideration of additional elemental abundances lifts the degeneracy between these components, bringing them to sharp relief on elemental abundance planes such as those in the middle and bottom rows in Figure 2.11.

The analysis presented in Section 2.5.2 leads to a few important conclusions: *(i)* the distribution of the numbers of stars over various chemical planes can be modelled by the combination of overlapping yet detached sub-structures. This is particularly true in the low metallicity end, where residuals are the lowest, adding further support to the notion that the IGS has an accreted origin; *(ii)* the fit in the Mg-Fe suggests that the [Mg/Fe] distribution of the lowest metallicity component is consistent with an accretion origin; and *(iii)* the GMM method consistently picks out the same substructures in various chemical planes, involving the abundances of Fe, Mg, Al, and Mn. The metallicities of these substructures are a reasonably good match to those of well known peaks in the MDF of the Galactic bulge (Ness et al., 2013a). This latter result validates the application of the GMM method to describe the distribution of stellar data in chemical space.

2.6 Discussion

I start this section by briefly summarising the results before proceeding with a discussion of their implications. In Sections 2.4 and 2.5 I discussed evidence for the presence of a remnant of an accretion event in the inner Galaxy, on the basis of the existence of substructure in orbital and chemical space. While the whole body of evidence for accretion is strong, when considered in isolation, the interpretation of either dynamical or chemical evidence may reasonably be called into question.

The evidence from the orbital side hinges on two main results: *(i)* the statistically significant differences in orbital properties between the accreted stars and their more metal-rich

in situ counterparts in the inner Galaxy (Figures 2.6 and 2.7); *(ii)* the existence of an energy gap separating the IGS from other metal-poor halo substructure. The presence of this energy gap seems to be immune to selection effects, since it is absent in chemically defined metal-poor *in situ* populations (Figure 2.4), whose spatial distribution, uncorrected for selection effects, is the same as that of their accreted counterparts.

It is important to note, however, that when $R_{\rm GC} < 4$ kpc stellar populations are considered in isolation, there is a smooth dependence of orbital properties on metallicity, which could be accommodated by a fully *in situ* scenario. On the other hand such smooth behaviour would also be expected in the accreted case, given that the orbital and chemical properties of substructures overlap strongly due to a combination of observational error and cosmic variance.

On the chemistry side, evidence for accretion relies on *(i)* the similarity between the chemical composition of the IGS and those of satellites of the Milky Way and other accreted systems (Figure 2.13), and *(ii)* the presence of clumpiness of the stellar distribution in various chemical spaces (Figures 2.1 and 2.11). Regarding *(i)*, I showed that the chemistry of unevolved *in situ* populations are also similar to that of their accreted counterparts (Figure 2.2). Moreover, there is an apparent continuity between the chemical compositions of the IGS and its bulge counterparts (Figure 2.8). However I also showed that similarity between the chemical compositions of accreted and *in situ* populations is an actual expectation from cosmological numerical simulations (Figure 2.10). Regarding *(ii)* I showed that the data in chemical space can be well matched by the combination of detached substructures (Figure 2.11). However, one cannot rule out that such clumpiness is the result of a bursty history of star formation and chemical enrichment.

Despite the above caveats, when considered in aggregate, chemical and orbital information suggest the presence of a previously unidentified structure located in inner Galaxy, the IGS. We hypothesise that this structure is the remnant of a galaxy accreted to the Milky Way in its very early life. In the next Subsections we discuss the properties of the hypothetical progenitor of the IGS. In Section 2.6.1 I discuss the origin of the metal-poor populations in the Galactic bulge, in Section 2.6.2 I discuss the properties of the putative progenitor of the IGS; and in Section 2.6.3 I present a speculative scenario for the early evolution of the Milky Way halo.

2.6.1 The origin of metal-poor bulge stars

In this Section I estimate the contribution of accreted and *in situ* stars to the metal-poor star content of the Galactic bulge, and contrast that estimate with predictions from fully

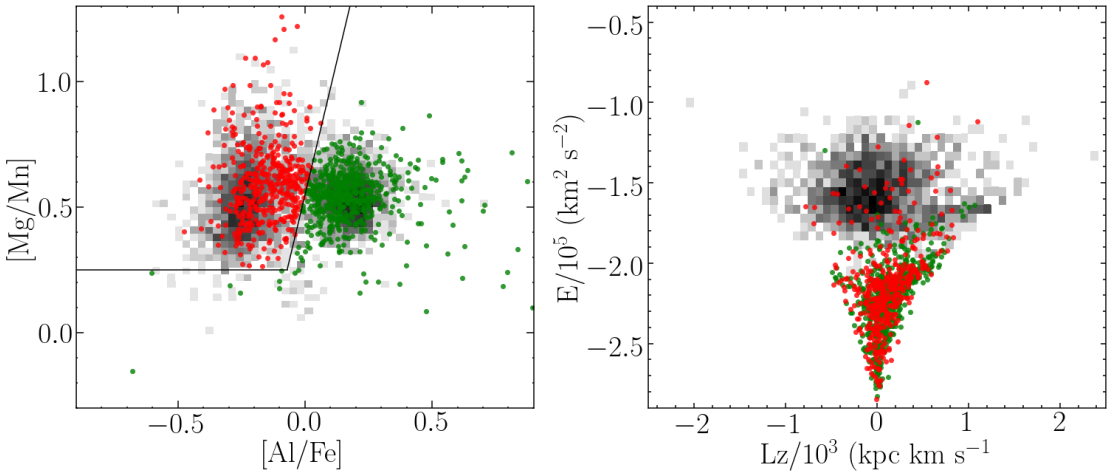

FIGURE 2.12: *Left panel:* Data for metal-poor stars ([Fe/H] < -0.8) are displayed on the chemistry plane used to distinguish accreted from *in situ* populations. The dividing line is the same as shown in Figure 2.1. The 2D histogram shows metal-poor stars at $R_{GC} > 4$ kpc, and the red (green) dots represent accreted (*in situ*) stars in the inner Galaxy. A clear bimodal distribution in [Al/Fe] is visible in the data for both the inner and outer Galaxy. *Right panel:* Same stars displayed on the energy-angular momentum plane. The data for the outer Galaxy are dominated by the GE/S and *Splash* systems. In the inner Galaxy, the accreted sample is dominated by the IGS, but about 1/10 of the sample is consistent with an association with the GE/S system ($E > -1.85 \times 10^5$ km^2 s^{-2}). The *in situ* sample is dominated by thick disk stars, although a small fraction seems to belong to the *Splash*. Note that the distributions of accreted and *in situ* stars in IoM space are different at a statistically significant level (see Section 2.4.2).

in situ chemical evolution models.

2.6.1.1 Contribution by accreted and *in situ* formation to the stellar mass budget

I begin by assessing the relative contribution of accreted and *in situ* stars to the metal-poor stellar mass budget of the inner Galaxy. The data shown in Figure 2.12 may help shed light on this question. I display metal-poor stars ([Fe/H] < -0.8) on the [Mg/Mn] vs. [Al/Fe] plane, which I used in Section 2.2 to distinguish accreted from *in situ* populations (Figure 2.1). The underlying 2D histogram shows the metal-poor populations located at $R_{GC} > 4$ kpc. The dividing line defining the border between accreted (upper left quadrant) and *in situ* populations is also shown. Inner Galaxy stars in the accreted (*in situ*) region of the diagram are shown in red (green). A clear bimodal distribution of [Al/Fe] data for the stars in the inner Galaxy can be seen. In total, there are 430 stars in the accreted area of this chemical plane, and 602 stars in the *in situ* region. Recall, moreover, that in Section 2.4.2 I estimated that the chemically-defined sample of metal-poor accreted stars within the IGS region of $E - L_Z$ space was contaminated by thick disk stars at the 22–40% level. Accounting for that additional

factor, *I estimate that approximately 25–33% of the stars with [Fe/H]<–0.8 in our inner Galaxy sample have an accreted origin.*

The right panel of Figure 2.12 shows the distribution of accreted and *in situ* stars on the $E - L_z$ plane. The accreted star sample is dominated by low energy stars, mostly associated to the IGS. About 10% of the accreted stars are located at high energies and are likely stars associated to the GE/S system (large gray blob) which are currently crossing the inner Galaxy. Notably, very few *in situ* stars (green points) have such high energies. They predominantly occupy the low energy region of the plane, with a number of stars positioned along the *Splash* (to the right of GE/S, see green arrow in Figure 2.4).

Other studies have spotted duplexity in the properties of metal-poor bulge samples, which may be attributed to the presence of a mix of accreted and *in situ* populations. Pietrukowicz et al. (2015) identified two major sequences in the period-amplitude plane for a large sample of fundamental-mode RR Lyr variable stars. The two populations differ slightly in metallicity, with the more metal-poor population outnumbering their metal-rich counterparts by approximately a factor of 4. Those authors suggest that this duality is indicative of merging activity in the early history of the Milky Way bulge. Kunder et al. (2020) obtained radial velocities for a few thousand RR Lyrae stars from the Pietrukowicz et al. (2015) sample and determined the presence of two kinematically distinct populations. One population follows bar-like orbits and the other one is more centrally concentrated, being characterised by hotter kinematics. They suggest that the latter may result from an accretion event that preceded the formation of the bar.

On the theory side, cosmological numerical simulations predict relatively intense accretion activity in the first few Gyr of the lives of massive galaxies. They have reached a degree of sophistication that enables a quantitative confrontation with the data. Early numerical simulations by Kobayashi & Nakasato (2011) propose that the bulge was fully formed by the merger of galaxies with $M \sim 5 \times 10^9$ $M_\odot$ at z >3. On the other hand, the more recent EAGLE simulations provide more detailed information that can be compared with the data. For instance, in the simulated galaxies whose abundances are displayed in Figure 2.10, the fraction of accreted stars within 4 kpc of the centre for [Fe/H] < -1 varies from 0.10 to 0.55. Along the same lines, the analysis of FIRE simulations by El-Badry et al. (2018) finds that same fraction within 1 kpc of simulated Milky Way-like galaxy centres to be around 0.5. More recently, Fragkoudi et al. (2020) analysed high resolution data for Milky Way-like galaxies from the Auriga suite of cosmological numerical simulations. They found that the fraction of the stellar mass with [Fe/H] < -1 within 4 kpc of the centre that has an accretion origin to vary between 0.13 and 0.8. Moreover, for the two simulated galaxies matching the properties of the Milky Way best, that fraction was smaller than 0.4.

Considering all the uncertainties on the observational and theoretical fronts, and taking into account the relative arbitrariness of the spatial and [Fe/H] limits adopted in such comparisons, the results broadly confirm the predictions by numerical simulations from various groups. Obviously, better statistics on both the observational and numerical simulation fronts will be required for such data to provide stringent constraints on models.

2.6.1.2 A Fully *in situ* bulge?

It is encouraging that the main tentative result presented in this paper does not fall into a theoretical void, that it is in consonance with expectations from cosmological numerical simulations. Recourse to theoretical predictions to validate an observational result is nonetheless methodologically, and indeed philosophically, unsound. Thus, before discussing the properties of the putative progenitor of the IGS, it behooves us to mention theoretical predictions by various groups which match data for bulge stellar populations without resort to satellite accretion.

The history of modelling the chemo-kinematic properties of bulge stellar populations is decades long, so that paying tribute to all the excellent work done in the past is beyond the scope of this paper. For that I refer the reader to Section 4 of the review by Barbuy et al. (2018). I restrict the discussion to recent work by Matteucci et al. (2019, 2020), because to my knowledge it is the only instance of a detailed comparison betwen model predictions and multiple chemical compositions for a large sample based on APOGEE data. Their analytical model for the history of star formation and chemical enrichment of the bulge stellar populations provides a good match to the MDF (Matteucci et al., 2019) and the abundances of O, Mg, Si, Ca, Al, K, Mn, Cr, and Ni. While such models resort to *ad hoc* assumptions about gas infall for different Galactic components, and some non-negligible amount of yield adjustment, they match the observed data very well. The implication is that the fraction of the stellar mass within the bulge that is due to accretion is *zero* at all metallicities. In that scenario, the entirety of the bulge stellar populations, including those deemed *accreted* by the criteria described in Figure 2.1, were actually formed *in situ*.

In light of the discussion in Section 2.3, where I showed that *in situ* and accreted populations share a similar path in chemical space (Figure 2.2), the results by Matteucci et al. (2019, 2020) are not surprising. As pointed out in Section 2.6, orbital information such as that discussed in Section 2.4 is indeed required for that distinction to be made. Moreover, recall that according to the criteria there are 463 accreted stars out of a total sample of 6,350 stars within 4 kpc of the Galactic centre. Assuming a contamination at

the 22–40% level of the accreted sample by *in situ* thick disk stars, the total accreted stellar mass amounts to only ∼4–5% of the sample[5]. Therefore, as far as the chemical evolution of the bulge is concerned, Matteucci's work offers, at face value and without consideration of the Milky Way's insertion into the cosmological context, a viable *in situ* formation scenario that can possibly explain the chemical compositions of the vast majority of the stellar populations therein. Notwithstanding this remarkable success, accounting for the considerable morphological and kinematic differences between the overlapping components within a few kpc of the Galactic centre under a single unified chemodynamical evolutionary picture remains a challenge.

While the IGS contributes a very small fraction of the stellar mass of the Galactic bulge, it is a major contributor to the stellar mass budget of the stellar *halo*. Therefore, it is important to give further consideration to the reality of its discrimination as a separate system, which is the topic of the next sub-section.

2.6.1.3 Core of Gaia-Enceladus/Sausage?

Recent studies based on N-body simulations (e.g., Jean-Baptiste et al., 2017b; Koppelman et al., 2020) have shown that substructure in kinematic and orbital planes cannot be ascribed to individual accretion events in a straightforward manner. In particular, Jean-Baptiste et al. (2017b) simulated the evolution of orbital properties of accreted and *in situ* populations in the event of accretion by single and multiple satellites with varying merger mass ratio. The main conclusions from that work have consequences for the interpretation of the results.

Firstly, Jean-Baptiste et al. (2017b) show that distributions on the $E - L_z$ plane that resemble qualitatively those presented in Figures 2.4 and 2.9 can result from the accretion of one single satellite with a 1:10 mass ratio. It can be seen from their Figure 2 that several Gyr after the occurrence of the accretion event, satellite remnants are distributed across a large range of energies and angular momenta, spanning the loci occupied by both the IGS and GE/S in Figure 2.9. Most of the substructure in orbital space in their simulations is associated to the accreted populations, including low energy clumps resembling that characterising the IGS in Figure 2.4. By the same token, the distribution of the *in situ* population is a lot smoother and strikingly similar to the distribution in the upper panel of Figure 2.4 (minus the Splash), and in the bottom panel of Figure A.2 in the Appendix. Their simulations also show that accretion moves stars formed *in situ* into high energy and low angular momentum orbits, where accreted stars are usually found. In fact, *in situ* stars contribute to some of the substructure on the $E - L_z$

[5]Note however that our data are not corrected for selection effects, so this is an order of magnitude estimate

plane, although not at the same level as the accreted populations, which dominate the substrucutre, particularly at low energy. Along the same lines, Koppelman et al. (2020) analysed a set of N-body simulations that match the observed properties of the GE/S debris today. According to those simulations, the core of the accreted satellite spirals in and is dissolved, with some of the stars acquiring slightly prograde orbits.

On the basis of such simulations one might reasonably argue in favour of a scenario in which the GE/S and the IGS are both part of the same progenitor. In that situation, one could conceive that the core of GE/S, being more massive and denser than the outskirts, could have sunk into the inner Galaxy under the effect of dynamical friction, leaving its less bound stellar tenants behind to be observed in higher energy orbits today, where GE/S stars are found (c.f. Figure 2.4).

It is not easy to reconcile such a scenario with the relative distribution of IGS and GE/S data in chemical space in Figure 2.13. Stars belonging to the IGS on average present higher mean [Mg/Fe] and lower mean [Fe/H] than their GE/S counterparts. As pointed out in Section 2.6.2, the IGS lacks a substantial "knee-shin" component to its distribution in the Mg-Fe plane, unlike the GE/S. Note that these differences exist despite the fact that the chemical criteria defining both samples are identical. The IGS is clearly less chemically evolved than the GE/S. Therefore, if the IGS was indeed the core of the GE/S, that hypothetical progenitor system would be characterised by a positive metallicity gradient in the early universe. Galaxies in the nearby and intermediate redshift universe are predominantly characterised by negative metallicity gradients (e.g., Stott et al., 2014; Goddard et al., 2017). That is also the behaviour of satellites of the Milky Way such as the Magellanic Clouds (e.g., Cioni, 2009) and the Sagittarius Dwarf (e.g., Hayes et al., 2020). This is understood as being due to the fact that star formation in galaxies takes place in an inside-out manner, since their central regions evolve more quickly than their outskirts, due to availability of larger amounts of gas for star formation. On the other hand, higher redshift galaxies with positive metallicity gradient have been identified, an occurrence that may be caused by strong winds associated with intense star formation in the centres of dwarf galaxies at $z \sim 2$ (e.g., Wang et al., 2019). It is not clear however how prevalent that phenomenon is.

Secondly, it is worth highlighting additional results presented by Jean-Baptiste et al. (2017b) where simulated Milky Way-like galaxies undergo 1:10 mergers with more than one satellite. Those lead to very thorough mixing of the stars from different satellites in orbital space, particularly in the low energy region of the $E-L_z$ plane, where the IGS was identified. This suggests that our accreted sample should include stars from more than one satellite in the low energy regime. Under that light the result above is surprising. Even if the IGS and the GE/S were indeed separate systems, I would expect that *some* of

the low energy accreted stars show an abundance pattern consistent with an association with the GE/S. On the contrary, it is only the high energy stars ($E/10^5 - 2$ km^{2}s^{-2}) in the bulge accreted sample (c.f. Figure 2.12) that possess abundances that are consistent with an association with the GE/S.

I conclude that it is unlikely, though not impossible, that the IGS is the core of the Gaia Enceladus/Sausage system. That would require that the progenitor of the Gaia Enceladus/Sausage system have a slightly positive metallicity gradient and have a core that is less chemically evolved than its outskirts, which is uncommon.

2.6.2 The Properties of the IGS Progenitor

In the previous Sections I showed that the inner ∼4 kpc of the Milky Way hosts a stellar population with the following properties: *(i)* it presents a chemical composition that resembles those of accreted systems (e.g., Hayes et al., 2018; Mackereth et al., 2019a; Helmi, 2020); *(ii)* it is detected as substructure in IoM space; *(iii)* on average it presents slower rotation, higher vertical action, and slightly higher radial action than metal-rich bulge populations; *(iv)* it is chemically detached from its metal-rich counterparts. In aggregate these properties suggest the presence of an accreted stellar population within 4 kpc of the Galactic centre. In this Section I use the observed properties of the remnant population to estimate the mass and history of the putative progenitor system. This is achieved through comparison with data for a better known accreted system (GE/S) and the predictions of the EAGLE simulations.

In Figure 2.13 I compare the chemical properties of the IGS with those of the GE/S system (Haywood et al., 2018; Belokurov et al., 2018; Helmi et al., 2018; Mackereth et al., 2019a), a massive satellite ($M_\star \sim 10^{8.5}$M$_\odot$ Mackereth & Bovy, 2020), that was accreted to the Milky Way about 8-10 Gyr ago. For details on the selection of GE/S stars, see Figure 2.9 and related discussion. I ignore, for the sake of simplicity, any selection effects that may bias the relative distribution of chemical properties of the observed stellar populations associated with the two galaxies. In other words, I assume that the samples displayed in Figure 2.9 represent the bulk of the populations of the two systems. Consequently the conclusions drawn from comparison of the IGS and GE/S should be considered qualitative, and subject to revision should that assumption be demonstrated to be incorrect. With that caveat in mind, Figure 2.13 displays stars from the two systems on various abundance planes. The IGS is represented by red symbols, the GE/S as blue symbols, and the parent sample, which is dominated by stars from the high- and disks, is plotted as gray-scale 2D histograms. The data show that stars belonging to the IGS have slightly higher average Mg, Ni, C, and N abundances

than those of GE/S at [Fe/H] ~ -1. This result suggests that the progenitor galaxy of the IGS was likely more massive than GE/S. I recall that Mackereth et al. (2019a) used predictions from the EAGLE numerical simulations to estimate the stellar mass of GE/S. In particular, they showed that the mean [Fe/H] and [Mg/Fe] of the stellar particles associated with dwarf simulated galaxies were good indicators of stellar mass (see Figure 11 of Mackereth et al., 2019a).

I resort to that predicted relation between mass and chemistry in order to estimate the mass of the progenitor of the IGS. I used the scipy `curve_fit` optimisation routine to fit the data for satellites of Milky Way-like galaxies in the L0025N075-RECAL simulation (see Mackereth et al., 2019a, for details) with a bivariate $M_\star$([Fe/H],[Mg/Fe]) relation. Only galaxies with at least 20 star particles were included in the fit, excluding all galaxies with $M_\star < 10^{7.5}\mathrm{M}_\odot$ or $\langle[\mathrm{Fe/H}]\rangle < -2.0$.

The equation that describes the trend is the following:

$$\log M_\star = 10.28 + 2.18\,\langle[\mathrm{Fe/H}]\rangle + 3.60\,\langle[\mathrm{Mg/Fe}]\rangle - 0.30\,\langle[\mathrm{Fe/H}]\rangle \times \langle[\mathrm{Mg/Fe}]\rangle \quad (2.2)$$

Where the zero-th order term has been adjusted to match the mass inferred by Mackereth & Bovy (2020) for GE/S, $3 \times 10^8 M_\odot$, and adopting the following mean values: $\langle[\mathrm{Fe/H}]\rangle_{\mathrm{GE/S}} = -1.20$, $\langle[\mathrm{Mg/Fe}]\rangle_{GE/S} = +0.20$. In this way, the theoretical relation is used in a strictly relative way, to minimise uncertainties. From the IGS, I have mean $\langle[\mathrm{Fe/H}]\rangle_{\mathrm{IGS}} = -1.26$, $\langle[\mathrm{Mg/Fe}]\rangle_{\mathrm{IGS}} = +0.30$, resulting in $M_\star \sim 5 \times 10^8 M_\odot$ for the progenitor of the IGS, or about twice the mass of GE/S[6]. Consequently the progenitor of the IGS is likely to have been an important contributor to the stellar mass budget of the Milky Way halo.

The distribution of the data for the IGS in the Mg-Fe plane may be used to constrain the history of star formation of the progenitor, and thus the time of accretion. One cannot help but notice the fact that the data for the IGS and GE/S differ in one fundamental aspect: the IGS sample has almost no stars with [Fe/H] > 1, and some of them are likely thick disk contaminants (see Section 2.5). That is the regime where the GE/S displays a strong decline in [Mg/Fe] for increasing [Fe/H], associated with the onset of enrichment by SN Ia, which takes place on a timescale of $\sim 10^{8-9}$ year (e.g., Maoz et al., 2012; Nomoto et al., 2013). Assuming I am not being deceived by an unforeseen selection effect, the absence of this more metal-rich population in the data for the IGS may indicate an early quenching of star formation, likely associated with the accretion to the Milky Way at a very early time.

[6]For these estimates I lifted the original constraint on [Fe/H] > -1.7 (c.f. Section 2.2) to avoid biasing the mean abundance values.

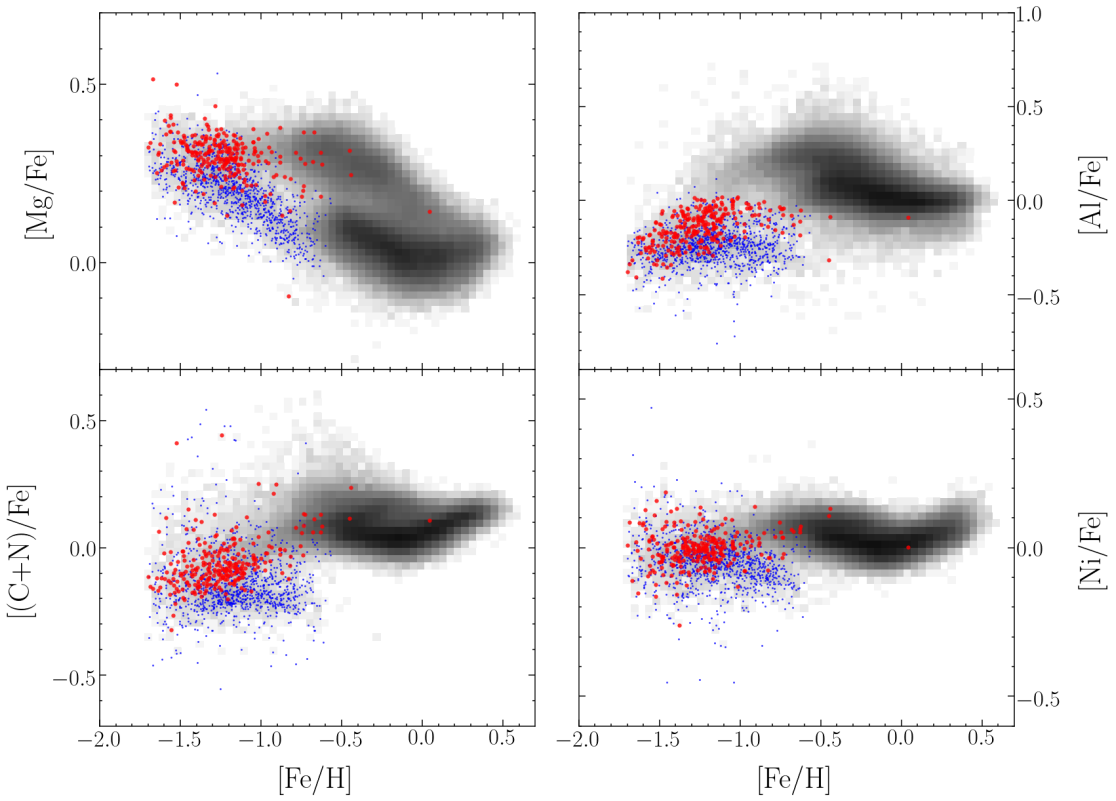

FIGURE 2.13: Comparison between the IGS (red symbols) and Gaia-Enceladus/Sausage (GE/S, blue symbols) in chemical space. The data for the parent sample are also plotted (gray), to mark the positions of the low and high-α disks in these diagrams. The IGS is characterized by higher average [Mg/Fe], [(C+N)/Fe], and [Ni/Fe] than GE/S while having approximately the same mean [Fe/H]. This suggests that the progenitor of the IGS was slightly more massive than GE/S. It is also noteworthy from the top left panel that the locus occupied by the IGS lacks the declining [Mg/Fe] sequence that is visible in the case of GE/S at [Fe/H]∼-1.2 (the "shin" of the α-Fe relation). This may indicate an early truncation of star formation.

This result confirms theoretical expectations from the E-MOSAICS simulations by Pfeffer et al. (2020) and the EAGLE predictions for the chemical compositions of early accreted satellites (Figure 2.10). Pfeffer et al. (2020) analysed the expected orbits of globular clusters connected with accreted satellites in the E-MOSAICS simulations, concluding that the orbits of surviving accreted clusters tend to have lower energies if their host satellites were more massive and/or were accreted at higher redshifts. Furthermore, this observed truncation at [Fe/H] ~ -1 is in agreement with results from a previous study by the group (Horta et al., 2020), where the chemical compositions of Galactic GCs in APOGEE were studied. In that paper I showed that the more metal-poor half of the GCs associated with the L-E subgroup, whose position in IoM space coincides with that of the IGS, have chemical compositions that are consistent with an accreted origin. It is possible that the more metal-rich GCs in that group have an *in situ* origin, associated with the thick disk (see Figure 3 from Horta et al., 2020).

As pointed out in Section 2.4, the locus of the IGS in IoM space matches closely that of the L-E family of globular clusters identified by Massari et al. (2019). Those authors showed that the L-E clusters followed a tight age-metallicity relation, suggesting that they might be associated with a massive satellite. Indeed, both the orbital properties and time of accretion of the progenitor of the IGS agree with the predictions by Kruijssen et al. (2019a, 2020) for the *Kraken* accretion event. According to those authors, the *Kraken* was a satellite of the Milky Way that was accreted within the first few Gyr of the Galaxy's existence (see also Forbes, 2020). The prediction is based on a detailed comparison of the ages, metallicities, and orbital properties of the Milky Way globular cluster system with predictions of the E-MOSAICS suite of cosmological numerical simulations (Pfeffer et al., 2018; Kruijssen et al., 2019b). Although the specific identities of the globular clusters associated to the *Kraken* or the L-E group are not unique, their median metallicities are roughly similar to that of the IGS ([Fe/H]~ -1.5 and -1.24, respectively). The orbital properties of those globular clusters, with apocentric distances between 3 and 5 kpc, are also consistent with an association with the IGS.

Finally, Kruijssen et al. (2020) estimate the stellar mass of the *Kraken* to be $\sim 2\times10^8 M_\odot$, or approximately 70% of the mass of GE/S. the estimate from equation (1) is that the progenitor of the IGS is more massive than the *Kraken*, with approximately twice the mass of GE/S. Considering the uncertainties associated with the various methods, I do not deem the absolute differences worrying. Further details on the physical properties of the progenitor of the IGS, as well as a definitive association with the *Kraken* will have to await a more careful examination of both upcoming new data and predictions from improved numerical simulations.

2.6.3 A speculative scenario

With the above caveats in mind, I conclude by summarising the *speculative* views on the most likely story implied by the data presented in this paper. While the vast majority of the stars in the Milky Way were likely formed *in situ* (e.g., Bland-Hawthorn & Gerhard, 2016), it is generally agreed that, under a Λ-CDM framework, galaxies such as the Milky Way experienced intense accretion activity in their early lives (e.g., Naab & Ostriker, 2017).

In Section 2.6.1.1 I found that somewhere between 1/4 and 1/3 of the *metal-poor* stars[7] in the inner Galaxy were accreted, and the rest were formed *in situ*. the inability to perfectly distinguish one group from the other leaves a key question in the air: is there

[7]Which themselves amount to only ∼5% of the stellar mass budget of the Galactic bulge (see Ness et al., 2013b)

an evolutionary connection between the two or were they formed and evolved in entire isolation before co-habiting the inner few kpc of the Galaxy?

A possible sequence of events, is one whereby the most metal-poor stars in the inner Galaxy were formed *in situ*, followed by the early accretion of the progenitor of the IGS which, under the effect of dynamical friction, took a quick dive towards the heart of the young Milky Way. Assuming the IGS brought with it fresh gas[8], it is likely that dissipation brought it to the Galactic centre, triggering a burst of star formation which would influence the later course of the chemical evolution in the inner Galaxy, explaining the chemical continuity apparent in Figure 2.8[9].

It will be interesting to see whether such speculative scenarios will survive scrutiny by more detailed observations and sophisticated modeling and, if so, how it will jibe with the understanding of the formation, evolution, and interaction between other structures co-habiting the inner Galaxy.

2.7 Conclusions

I report evidence to the existence of an accreted structure located in the inner Galaxy (the IGS). To reveal its existence I resorted to a search for clustering in multi-dimensional parameter space, based on the best available data from APOGEE and *Gaia*, and astroNN distances. This structure consists of a metal-poor population with detailed chemistry resembling that of low mass satellites of the Milky Way with low abundances of Al, C, N, and Ni. It is chemically and dynamically detached from the more metal-rich populations with which it shares its location in the heart of the Galaxy, and from other accreted populations across the Milky Way halo. I suggest that this population is the remnant of a satellite that was accreted early in the history of the Milky Way. The chemistry of this population is characterised by a plateau of relatively high [Mg/Fe] and the absence of a "knee" towards higher [Fe/H] indicating an early quenching of star formation activity, which is consistent with a very early accretion event. Comparison with mean chemical composition predictions from numerical simulations, I infer a stellar mass of $M_\star \sim 5 \times 10^8 M_\odot$, or approximately twice that of the Gaia-Enceladus/Sausage system. If indeed its existence is confirmed by further investigation, one would be led to conclude that its progenitor was a major building block of the Galactic halo, which has until now remained elusive due to its location behind a curtain of extinction and

[8]This assumes ram pressure stripping was not important, which may be reasonable. Ram pressure stripping is proportional to v^2 and since the IGS is located at the Galactic centre, the putative merger must have occurred at a low velocity.

[9]Along similar lines, Whitten et al. (2019) proposed that the steep age gradient of stellar populations in the inner halo ($R_{\rm GC} < 14$ kpc), inferred from BHB star mean color gradients, can be possibly associated with occurrence of a few dissipative mergers in the early Milky Way history.

foreground crowding. The orbital and chemical properties of the IGS, the implied time of accretion, and the mass of its progenitor are in good qualitative agreement with those predicted by Pfeffer et al. (2020) and Kruijssen et al. (2020). I summarise below the main implications and questions raised by this finding:

- According to the favoured interpretation of the data, the IGS is a remnant of a satellite galaxy accreted to the Milky Way a long time ago. That such an accretion event happened in the Milky Way's very early history is an expectation from cosmological numerical simulations that predict an intense accretion activity in massive galaxies at $z \sim 2-3$ (e.g., El-Badry et al., 2018; Pfeffer et al., 2020; Fragkoudi et al., 2020). The Milky Way itself may have been the subject of unusually strong accretion activity at those early times, which may explain observed properties of its disk and halo populations (e.g., Mackereth et al., 2018; Schiavon et al., 2020);

- I present evidence for an accretion event that took place *before* the main structures inhabiting the region we understand today as the Galactic bulge were formed. Thus, the IGS should be viewed as a major building block of the Galactic halo, rather than a very minor component of the Milky Way bulge, to whose stellar mass budget it contributes no more than a few percent. The vast majority of the stars in the bulge today were most likely formed *in situ* (e.g., Kunder et al., 2012; Di Matteo, 2016; Debattista et al., 2017; Fragkoudi et al., 2018).

- The abundance ratios of stars associated with the IGS are well aligned with the sequence occupied by more metal-rich populations located within the inner ∼4 kpc of the Galactic centre. Naively, that would be a surprising result, as one may expect that accreted and *in situ* populations might have undergone distinct early histories of star formation and chemical enrichment. I show that numerical simulations actually predict such seeming continuity between the loci occuppied by accreted and *in situ* populations in all abundances tracked by the EAGLE simulations.

- As a logical path for further enquiry, one would like to explore at least three possible avenues: *(i)* verify whether models can match the distribution of stellar density in chemical space, which may be a key discriminator between accretion and *in situ* formation scenarios; *(ii)* contrast accreted and *in situ* populations in other abundance planes including elements that sample additional nucleosynthetic pathways, such as those resulting from s- and r-process production. *(iii)* contrast the age distributions of stars in the chemo-dynamically defined accreted and *in situ* populations. All these lines of investigation will benefit from additional data made available in forthcoming observational efforts.

- The combined mass of the progenitor of the IGS and the GE/S adds up to $8 \times 10^8 M_\odot$. Considering mass estimates for other accreted systems (e.g., Koppelman et al., 2019b; Forbes, 2020; Kruijssen et al., 2020) and dissolved globular clusters (Horta et al., 2021c; Schiavon et al., 2017b), the total mass in accreted satellites may be well in excess of $\sim 1.6 \times 10^9 M_\odot$. Although all these mass estimates are subject to considerable zero point uncertainties, this result is, at face value, in mild tension with independent estimates of the total stellar mass of the Galactic halo (e.g., Deason et al., 2019; Mackereth & Bovy, 2020).

- There seems to be an interesting connection between the finding reported in this paper and the presence of a population of N-rich stars in the inner Galaxy (Schiavon et al., 2017b), which is generally interpreted as resulting from the destruction of an early population of globular clusters (e.g., Martell & Grebel, 2010; Martell et al., 2016; Koch et al., 2019; Savino & Posti, 2019; Hanke et al., 2020; Fernández-Trincado et al., 2020). The frequency of this population has been shown to be larger by an order of magnitude within the inner few kpc of the halo than in its outer regions (Horta et al., 2021c). Moreover, Kisku et al. (2021) show that roughly 1/4 of the N-rich population within $\sim$ 4 kpc of the Galactic centre has elemental abundances consistent with an accretion origin, and orbital properties that are similar to those of the IGS. In future work I intend to examine how these finding jibe together vis à vis the current understanding of the accretion history of the Milky Way and models for globular cluster formation and destruction in a cosmological context.

This chapter presents an exploration of the chemical complexity of the metal-poor bulge on the basis of a statistically significant sample. The window into the bulge metal-poor bulge populations will be further widened by observational projects taking place in the near future. The Pristine Inner Galaxy Survey (PIGS) is performing AAOmega+2dF spectroscopy with the 3.9 m Anglo-Australian Telescope of ∼8,000 targets selected on the basis of CaHK photometry collected with MegaCam on the Canada-France-Hawaii Telescope, (Arentsen et al., 2020a) amassed the largest sample to date of very metal-poor stars (∼1,300 stars with [Fe/H]< -2) in the inner Galaxy. Detailed abundance analysis of such a sample will certainly shed light onto the nature of the early populations of the bulge. Further into the near future, the MOONS[10] surveys of the Milky Way (Gonzalez et al., 2020) will likely increase the sample of bulge metal-poor stars with detailed chemical compositions by an order of magnitude.

[10]MOONS is the European Southern Observatory Multi Object Optical and Near-infrared Spectrograph for the VLT (Cirasuolo & MOONS Consortium, 2016).

For the remainder of this thesis, the progenitor of the IGS is given the name Heracles, after the great hero of Greek mythology. Heracles was born of an illicit affair between the god Zeus and the mortal woman, Alcmene, queen of Tyrinth. According to some accounts of the myth, Zeus took the infant to nurse at the breast of his sleeping wife, Hera, knowing that the goddess's milk would give the infant immortality. Naturally, however, she woke — and when she pushed the baby away, it is said that her milk spilled across the sky, creating the Milky Way. Reminiscent of Heracles, a surprising outsider who was gifted with immortality, the progenitor of the IGS also has an external origin, and its presence likely precedes the formation of the Milky Way disc.

Chapter 3

The nature of halo substructures in the Milky Way

3.1 Introduction

"How did the Milky Way form?" is likely the most fundamental question facing the field of Galactic archaeology. As already discussed in Chapter 1 and Chapter 2, when posed in a cosmological context, the Λ-CDM model predicts that the Galaxy formed in great measure via the process of hierarchical mass assembly. In this scenario, nearby satellite galaxies are consumed by the Milky Way due to them being attracted to its deeper gravitational potential, and as a result merge with the Galaxy. In such cases, these merger events shape the formation and evolution of the Milky Way. Therefore, an understanding of the assembly history of the Milky Way in the context of Λ-CDM depends critically on the determination of the properties of the systems accreted during the Galaxy's history, including their masses and chemical compositions. Moreover, the merger history of the Galaxy has a direct impact on its resulting stellar populations at present time, and plays a vital role in shaping its components.

Since the seminal work by Searle & Zinn (1978), many studies have aimed at characterising the stellar populations of the Milky Way, linking them to either an "*in situ*" or accreted origin. Although detection of substructure in phase space has worked extremely well for the identification of on-going and/or recent accretion events (e.g. Sagittarius dSph, Ibata et al., 1994; Helmi stream, Helmi et al., 1999), the identification of accretion events early in the life of the Milky Way has proven difficult due to phase-mixing. A possible solution to this conundrum resides in the use of additional information, typically in the form of detailed chemistry and/or ages (e.g., Nissen & Schuster, 2010; Hawkins et al., 2015; Hayes et al., 2018; Haywood et al., 2018; Mackereth et al., 2019b; Das et al.,

2020; Montalbán et al., 2020; Horta et al., 2021a; Hasselquist et al., 2021; Buder et al., 2022; Carrillo et al., 2022).

The advent of large spectroscopic surveys such as APOGEE (Majewski et al., 2017), GALAH (De Silva et al., 2015), SEGUE (Yanny et al., 2009a), RAVE (Steinmetz et al., 2020), LAMOST (Zhao et al., 2012), H3 (Conroy et al., 2019), amongst others, in combination with the outstanding astrometric data supplied by the *Gaia* satellite (Gaia Collaboration, 2018; Gaia Collaboration et al., 2020), revolutionised the field of Galactic archaeology, shedding new light into the mass assembly history of the Galaxy.

The core of the Sagittarius dSph system and its still forming tidal stream (Ibata et al., 1994) have long served as an archetype for dwarf galaxy mergers in the Milky Way. Moreover, in the past few years, several phase-space substructures have been identified in the field of the Galactic stellar halo that are believed to be the debris of satellite accretion events, including the *Gaia*-Enceladus/Sausage (GE/S, Helmi et al., 2018; Belokurov et al., 2018; Haywood et al., 2018; Mackereth et al., 2019b), Heracles (Horta et al., 2021a), Sequoia (Barbá et al., 2019; Matsuno et al., 2019; Myeong et al., 2019), Thamnos 1 and 2 (Koppelman et al., 2019a), Nyx (Necib et al., 2020), the substructures identified using the H3 survey: namely Aleph, Arjuna, I'itoi (Naidu et al., 2020), LMS-1 (Yuan et al., 2020)[1], Icarus (Re Fiorentin et al., 2021), Cetus (Newberg et al., 2009), and Pontus (Malhan et al., 2022). While the identification of these substructures is helping constrain the understanding of the mass assembly history of the Milky Way, their association with any particular accretion event still needs to be clarified. Along those lines, predictions from numerical simulations suggest that a single accretion event can lead to multiple substructures in phase space (e.g., Jean-Baptiste et al., 2017a; Koppelman et al., 2020). Therefore, in order to ascertain the reality and/or distinction of these accretion events, one must combine phase-space information with detailed chemical compositions for large samples.

Recent work modelling the stellar halo suggests that accreted populations constitute over two thirds of all of the halo stellar mass within ∼25 kpc from the Galactic centre (e.g., Mackereth & Bovy, 2020), of which approximately 30%-50% (∼3×10^8M$\odot$), is associated with GE/S. This result is in agreement with recent work by Naidu et al. (2020), which find that $>$ 65% of stellar halo populations in the inner ∼20 kpc have an accreted origin, with the majority being from the GE/S progenitor. Other studies have estimated an even higher stellar mass to this accretion event (namely, ∼0.5-2 $\times$ 10^9M$\odot$), suggesting that most (if not all) of the mass of the inner ∼20 kpc of the Galactic stellar halo is comprised of a single accretion event (e.g., Helmi et al., 2018; Vincenzo et al., 2019; Das et al., 2020). Another important source of halo stellar mass not accounted for in previous

[1]This structure also goes by the name of Wukong (Naidu et al., 2020).

studies is Heracles, whose progenitor mass was estimated by Horta et al. (2021a) to be of the order of $\sim 5 \times 10^8 M\odot$.

The combined estimated mass from accreted populations within ∼20kpc, when added to the estimated mass from dissolved and/or evaporated globular clusters (GCs, namely, $\sim$1-2$\times 10^8 M\odot$ Schiavon et al., 2017a; Horta et al., 2021c), outweighs earlier estimates of the mass of the Galactic stellar halo, namely $\sim$4-7$\times 10^8 M\odot$ (see Bland-Hawthorn & Gerhard, 2016, and references therein). When compared to more recent estimates, the sum of the mass arising from accreted populations and dissolved and/or evaporated globular clusters yields a total mass that is approximately equivalent to the total estimated mass of the stellar halo, namely $\sim$1-1.3$\times 10^9 M\odot$ (e.g., Deason et al., 2019; Mackereth & Bovy, 2020), therefore suggesting a very small contribution from *in situ* halo populations at low [Fe/H].

Aside from assessing the mass contributed from accreted halo populations, understanding the chemo-dynamical properties of each substructure enables the characterisation of each accretion event. By comparing the chemo-dynamical properties of each substructure with *in situ* populations, it is possible to infer properties of the debris' progenitor, helping shed light into the Galaxy's past life and environment. The properties of these disrupted satellite galaxies also provide a window for near-field cosmology, and the study of lower-mass galaxies in unrivalled detail.

In this work I set out to combine the latest data releases from the APOGEE and *Gaia* surveys in order to dynamically determine and chemically characterise previously identified halo substructures in the Milky Way. I attempt, where possible, to define the halo substructures using kinematic information only, so that the distributions of stellar populations in various chemical planes can be studied in an unbiased fashion. This allows us to understand in more detail the reality and nature of these identified halo substructures, as chemical abundances encode more pristine fossilised records of the formation environment of stellar populations in the Galaxy.

The Chapter is organised as follows: Section 5.2 presents the selection of the parent sample used in this work. Section 5.3 includes a detailed description of how I identified the halo substructures. In Section 5.2, I discuss the resulting orbital distributions of the identified structures in the orbital energy and angular momentum plane. Section 3.4 presents an in-depth chemical analysis of the identified halo substructures in different chemical abundance planes, where I show the α elements in Section 3.4.1, the iron-peak elements in Section 3.4.2, the odd-Z elements in Section 3.4.3, the carbon and nitrogen abundances in Section 3.4.4, a neutron capture element (namely, Ce) in Section 3.4.5, and other interesting chemical composition planes in Section 3.4.6. The chemical abundances for each halo substructure are then quantitatively compared in Section 3.5. I then

discuss the results in the context of previous work in Section 4.5, and finalise this work by presenting the conclusions in Section 5.5.

3.2 Data and sample

In this chapter, I combine the latest data release (DR17, Abdurro'uf et al., 2021) of the SDSS-III/IV (Eisenstein et al., 2011; Blanton et al., 2017) and APOGEE survey (Majewski et al., 2017) with distances and astrometry determined from the early third data release from the *Gaia* survey (EDR3, Gaia Collaboration et al., 2020). The celestial coordinates and radial velocities supplied by APOGEE (Nidever et al., 2015, Holtzman et al, in prep), when combined with the proper motions and inferred distances (Leung & Bovy, 2019a) based on *Gaia* data, provide complete 6-D phase space information for approximately ∼730,000 stars in the Milky Way, for most of which exquisite abundances for up to ∼20 different elements have been determined.

All data supplied by APOGEE are based on observations collected by (almost) twin high-resolution multi-fibre spectrographs (Wilson et al., 2019) attached to the 2.5m Sloan telescope at Apache Point Observatory (Gunn et al., 2006) and the du Pont 2.5 m telescope at Las Campanas Observatory (Bowen & Vaughan, 1973). Elemental abundances are derived from automatic analysis of stellar spectra using the ASPCAP pipeline (García Pérez et al., 2016) based on the FERRE[2] code (Allende Prieto et al., 2006). The spectra themselves were reduced by a customized pipeline (Nidever et al., 2015). For details on target selection criteria, see Zasowski et al. (2013) for APOGEE and Zasowski et al. (2017) for APOGEE-2, and Beaton et al. (2021) for APOGEE north, and Santana et al. (2021) for APOGEE south.

I make use of the distances for the APOGEE DR17 catalogue generated by Leung & Bovy (2019a), using the `astroNN` python package (for a full description, see Leung & Bovy, 2019b). These distances are determined using a re-trained `astroNN` neural-network software, which predicts stellar luminosity from spectra using a training set comprised of stars with both APOGEE DR17 spectra and *Gaia* EDR3 parallax measurements (Gaia Collaboration et al., 2020). The model is able to simultaneously predict distances and account for the parallax offset present in *Gaia*-EDR3, producing high precision, accurate distance estimates for APOGEE stars, which match well with external catalogues (Hogg et al., 2019) and standard candles like red clump stars (Bovy et al., 2014). I note that the systematic bias in distance measurements at large distances for APOGEE DR16 as described in Bovy et al. (2019) have been reduced drastically in APOGEE DR17. Therefore, I are confident that this bias will not lead to unforeseen issues during the

[2] github.com/callendeprieto/ferre

calculation of the orbital parameters. the samples are contained within a distance range of ∼20 kpc and have a mean $d_{\rm err}/d$ ∼0.13 (except for the Sagittarius dSph, which extends up to ∼30 kpc and has a mean $d_{\rm err}/d$ ∼0.16).

I use the 6-D phase space information[3] and convert between astrometric parameters and Galactocentric cylindrical coordinates, assuming a solar velocity combining the proper motion from Sgr A* (Reid & Brunthaler, 2020) with the determination of the local standard of rest of Schönrich et al. (2010). This adjustment leads to a 3D velocity of the Sun equal to $[U_\odot, V_\odot, W_\odot] = [-11.1, 248.0, 8.5]$ km s^{-1}. I assume the distance between the Sun and the Galactic Centre to be $R_0 = 8.178$ kpc (Gravity Collaboration, 2019), and the vertical height of the Sun above the midplane $z_0 = 0.02$ kpc (Bennett & Bovy, 2019). Orbital parameters were then determined using the publicly available code `galpy`[4] (Bovy, 2015; Mackereth & Bovy, 2018), adopting a McMillan (2017) potential and using the Stäckel approximation of Binney (2012).

The parent sample employed in this work is comprised of stars that satisfy the following selection criteria:

- APOGEE-determined atmospheric parameters: $3500 < T_{\rm eff} < 5500$ K and $\log g < 3.6$,
- APOGEE spectral S/N > 70,
- APOGEE `STARFLAG` = 0,
- astroNN distance accuracy of $d_{\odot,\rm err}/d_\odot < 0.2$,

where $d_\odot$ and $d_{\odot \rm err}$ are heliocentric distance and its uncertainty, respectively. The S/N criterion was implemented to maximise the quality of the elemental abundances. The $T_{\rm eff}$ and $\log g$ criteria aimed to minimise systematic effects at high/low temperatures, and to minimise contamination by dwarf stars. I also removed stars with `STARFLAG` flags set, in order to not include any stars with issues in their stellar parameters. A further 7,750 globular cluster stars were also removed from consideration using the APOGEE Value Added Catalogue of globular cluster candidate members from Schiavon et al. (2022, in prep.), (building on the method from Horta et al., 2020, using primarily radial velocity and proper motion information). Finally, stars belonging to the Large and Small Magellanic clouds were also excluded using the sample from Hasselquist et al. (2021) (removing 3,748 and 1,002 stars, respectively). The resulting parent sample contains 199,077 stars.

[3]The positions, proper motions, and distances are taken/derived from *Gaia* EDR3 data, whilst the radial velocities are taken from APOGEE DR17.

[4]https:/docs.galpy.org/en/v1.6.0/.

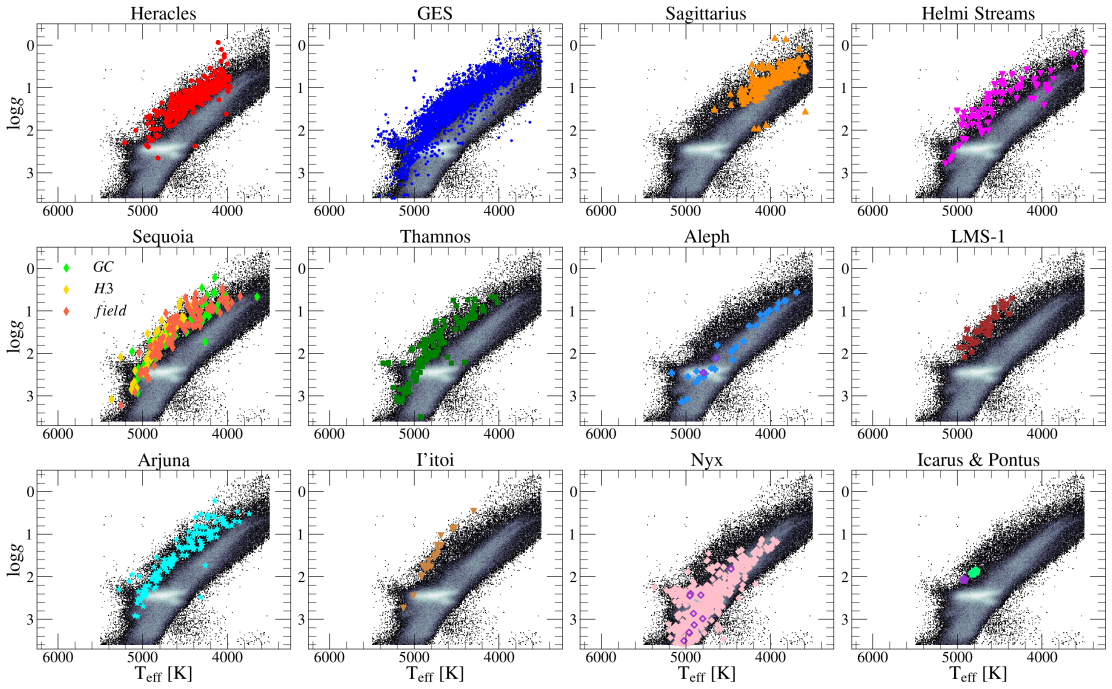

FIGURE 3.1: Distribution of the identifed substructures in the spectroscopist Hertzprung-Russell diagram. The parent sample is plotted as a 2D histogram, where white/black signifies high/low density regions. The coloured markers illustrate the different halo substructures studied in this work. For the bottom right panel, green points correspond to Pontus stars, whereas the purple point is associated with Icarus. Additionally, in the Aleph and Nyx panels, I also highlight with purple edges those stars that overlap between the APOGEE DR17 sample and the samples determined in Naidu et al. (2020) and Necib et al. (2020), respectively, for these halo substructures.

In the following subsection I describe the motivation behind the selection criteria employed to select each substructure in the stellar halo of the Milky Way. The criteria are largely built on selections employed in previous works and are summarised in Table 3.1 and in Figure 3.1.

3.2.1 Identification of substructures in the stellar halo

I now describe the method employed for identifying known substructures in the stellar halo of the Milky Way. I set out to select star members belonging to the various halo substructures. I strive to identify substructures in the stellar halo by employing solely orbital parameter and phase-space information where possible, with the aim of obtaining star candidates for each substructure population that are unbiased by any chemical composition selection. I take a handcrafted approach and select substructures based on simple and reproducible selection criteria that are physically motivated by the data and/or are used in previous works, instead of resorting to clustering software algorithms, which I find cluster the n-dimensional space into too many fragments. In the

following subsections I describe the selection procedure for identifying each substructure independently.

I note that the samples for the various substructures are defined by a strict application to the APOGEE survey data of the criteria defined by other groups, often on the basis of different data sets. The latter were per force collected as part of a different observational effort, based on specific target selection criteria. It is not immediately clear whether or how differences between the APOGEE selection function and those of other catalogues may imprint dissimilarities between the samples and those of the original studies. I nevertheless do not expect such effects to influence the conclusions in an important way.

3.2.1.1 Sagittarius

Since its discovery (Ibata et al., 1994), many studies have sought to characterise the nature of the Sagittarius dwarf spheroidal (hereafter Sgr dSph; e.g., Ibata et al., 2001; Majewski et al., 2003; Johnston et al., 2005; Belokurov et al., 2006; Yanny et al., 2009b; Koposov et al., 2012; Carlin et al., 2018; Vasiliev & Belokurov, 2020), as well as interpret its effect on the Galaxy using numerical simulations (e.g., Johnston et al., 1995; Ibata et al., 1997; Law et al., 2005; Law & Majewski, 2010; Purcell et al., 2011; Gómez et al., 2013). More recently, the Sgr dSph has been the subject of comprehensive studies on the basis of APOGEE data. This has enabled a detailed examination of its chemical compositions, both in the satellite's core and in its tidal tails (e.g., Hasselquist et al., 2017, 2019; Hayes et al., 2020). Moreover, in a more recent study, Hasselquist et al. (2021) adopted chemical evolution models to infer the history of star formation and chemical evolution of the Sgr dSph. Therefore, in this paper the Sgr dSph is considered simply as a template massive satellite whose chemical properties can be contrasted to those of the halo substructures that are the focus of the study.

While it is possible to select high confidence Sgr dSph star candidates using Galactocentric positions and velocities (Majewski et al., 2003), Hayes et al. (2020) showed it is possible to make an even more careful selection by considering the motion of stars in a well-defined Sgr orbital plane. I identify Sgr star members by following the method from Hayes et al. (2020). Although the method is fully described in their work, I summarise the key steps for clarity and completeness. I take the Galactocentric positions and velocities of stars in the parent sample and rotate them into the Sgr orbital plane according to the transformations described in Majewski et al. (2003). This yields a set of position and velocity coordinates relative to the Sgr orbital plane, but still centered on the Galactic Centre. As pointed out in Hayes et al. (2020), Sgr star members should stand out with respect to other halo populations in different Sgr orbital planes. Using

this orbital plane transformation, I select from the parent sample Sgr star members if they satisfy the following selection criteria:

- $|\beta_{\rm GC}| < 30$ (°),
- $1.8 < {\rm L}_{z,{\rm Sgr}} < 14$ ($\times 10^3$ kpc kms^{-1}),
- $-150 < {\rm V}_{z,{\rm Sgr}} < 80$ (kms^{-1}),
- ${\rm X}_{\rm Sgr} > 0$ (kpc),
- ${\rm Y}_{\rm Sgr} > -5$ (kpc) or ${\rm Y}_{\rm Sgr} < -20$ (kpc),
- ${\rm Z}_{\rm Sgr} > -10$ (kpc),
- ${\rm pm}_{\alpha} > -4$ (mas),
- $d_{\odot} > 10$ (kpc),

where $\beta_{\rm GC}$ is the angle subtended between the Galactic Centre and the Sgr dSph, ${\rm L}_{\rm z,Sgr}$ is the azimuthal component of the angular momentum in the Sgr plane, ${\rm V}_{\rm z,Sgr}$ is the vertical component of the velocity in the Sgr plane, (${\rm X}_{\rm Sgr}$, ${\rm Y}_{\rm Sgr}$, ${\rm Z}_{\rm Sgr}$) are the cartesian coordinates centred on the Sgr dSph plane, ${\rm pm}_{\alpha}$ is the right-ascension proper motion, and $d_{\odot}$ is the heliocentric distance, which for Sgr has been shown to be ~ 23 kpc (Vasiliev & Belokurov, 2020). the selection yields a sample of 266 Sgr star members, illustrated in the ${\rm L}_{\rm z,Sgr}$ vs ${\rm V}_{\rm z,Sgr}$ plane in Fig 3.2.

3.2.1.2 Heracles

Heracles is a recently discovered metal-poor substructure located in the heart of the Galaxy (Horta et al., 2021a). It is characterised by stars on eccentric and low energy orbits. Due to its position in the inner few kpc of the Galaxy, it is highly obscured by dust extinction and vastly outnumbered by its more abundant metal-rich (*in situ*) co-spatial counterpart populations. Only with the aid of chemical compositions has it been possible to unveil this metal-poor substructure, which is discernible in the [Mg/Mn]-[Al/Fe] plane. It is important at this stage that I mention a couple of recent studies which, based chiefly on the properties of the Galactic globular cluster system, proposed the occurrence of an early accretion event whose remnants should have similar properties to those of Heracles (named Kraken and Koala, by Kruijssen et al., 2020; Forbes, 2020, respectively). In the absence of a detailed comparison of the dynamical properties and detailed chemical compositions of Heracles with these putative systems, a definitive association is impossible at the current time.

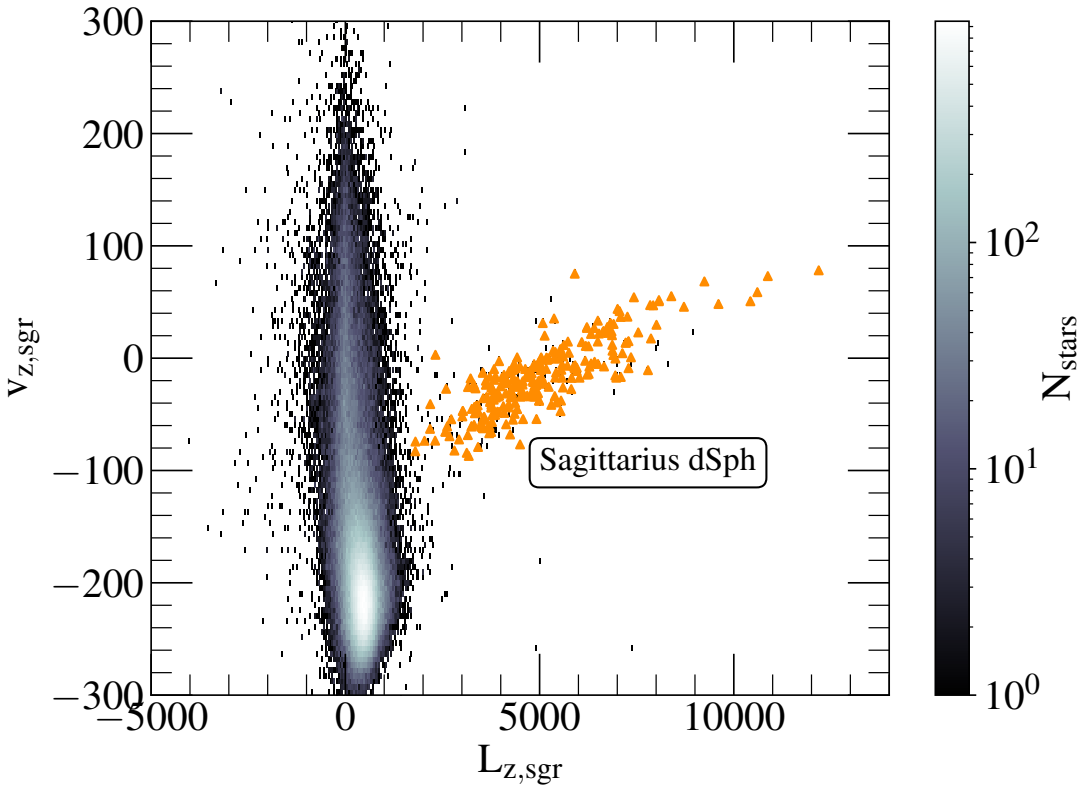

FIGURE 3.2: Parent sample used in this work in the $L_{z,Sgr}$ vs $V_{z,Sgr}$ plane (see Section 3.2.1.1 for details). Here, Sgr stars clearly depart from the parent sample, and are easily distinguishable by applying the selection criteria from Hayes et al. (2020), demarked in this illustration by the orange markers.

In this work I define Heracles candidate star members following the work by Horta et al. (2021a), and select stars from the parent sample that satisfy the following selection criteria:

- $e > 0.6$,
- $-2.6 < E < -2$ ($\times 10^5$ km^{2}s^{-2}),
- [Al/Fe] < -0.07 & [Mg/Mn] $\geqslant 0.25$,
- [Al/Fe] $\geqslant -0.07$ & [Mg/Mn] $\geqslant 4.25 \times$[Al/Fe] $+ 0.5475$.

Moreover, I impose a [Fe/H] > -1.7 cut to select Heracles candidate star members in order to select stars from the parent sample that have reliable Mn abundances in APOGEE DR17. the selection yields a resulting sample of 281 Heracles star members.

3.2.1.3 Gaia-Enceladus/Sausage

Recent studies have shown that there is an abundant population of stars in the nearby stellar halo (namely, $R_{GC} \lesssim$ 20-25 kpc) belonging to the remnant of an accretion event dubbed the *Gaia*-Enceladus/Sausage (GES, e.g., Belokurov et al., 2018; Haywood et al., 2018; Helmi et al., 2018; Mackereth et al., 2019b). This population is characterised by stars on highly radial/eccentric orbits, which also appear to follow a lower distribution in the α-Fe plane, presenting lower [α/Fe] values for fixed metallicity than *in situ* populations.

For this paper, I select GES candidate star members by employing a set of orbital information cuts. Specifically, GES members were selected adopting the following criteria:

- $|L_z| < 0.5$ ($\times 10^3$ kpc km^{-1}),
- $-1.6 < E < -1.1$ ($\times 10^5$ km^{2}s^{-2}).

This selection is employed in order to select the clump that becomes apparent in the E-L_z plane at higher orbital energies and roughly $L_z \sim 0$ (see Fig 3.4), and to minimise the contamination from high-α disc stars on eccentric orbits (namely, the "Splash" Bonaca et al., 2017; Belokurov et al., 2020), which sit approximately at E$\sim -1.8\times 10^5$ km^{2}s^{-2} (see Kisku et al, in prep). The angular momentum restriction ensures I are not including stars on more prograde/retrograde orbits. I find that by selecting the GES substructure in this manner, I obtain a sample of stars with highly radial ($J_R \sim$1x10^3 kpc kms^{-1}) and therefore highly eccentric ($e\sim$0.9) orbits, in agreement with selections employed in previous studies to identify this halo substructure (e.g., Mackereth & Bovy, 2020; Naidu et al., 2020; Feuillet et al., 2021; Buder et al., 2022). The final GES sample is comprised of 2,353 stars.

I note that in a recent paper, Hasselquist et al. (2021) undertook a thorough investigation into the chemical properties of this halo substructure and compared it to other massive satellites of the Milky Way (namely, the Magellanic Clouds, Sagittarius dSph, and Fornax). Although their selection criteria differs slightly from the one employed in this study, I find that their sample is largely similar to the one employed here, as both studies employed APOGEE DR17 data.

3.2.1.4 Retrograde halo: Sequoia, Thamnos, Arjuna, and I'Itoi

A number of substructures have been identified in the retrograde halo. The first to be discovered was Sequoia (Barbá et al., 2019; Matsuno et al., 2019; Myeong et al.,

2019), which was suggested to be the remnant of an accreted dwarf galaxy. The Sequoia was identified given the retrograde nature of the orbits of its stars, which appear to form an arch in the retrograde wing of the Toomre diagram. Separately, an interesting study by Koppelman et al. (2019a) showed that the retrograde halo can be further divided into two components, separated by their orbital energy values in the E-L_z plane. They suggest that the high energy component corresponds to Sequoia, whilst the lower energy population would be linked to a separate accretion event, dubbed Thamnos. In addition, Naidu et al. (2020) proposed the existence of additional retrograde substructure overlapping with Sequoia, characterised by different metallicities, which they named Arjuna and I'Itoi.

As the aim of this paper is to perform a comprehensive study of the chemical abundances of substructures identified in the halo, I utilise all the selection methods used in prior work and select the same postulated substructures in multiple ways, in order to compare their abundances later. Specifically, I build on previous works (e.g., Myeong et al., 2019; Koppelman et al., 2019a; Naidu et al., 2020) that have aimed to characterise the retrograde halo and select the substructures following a similar selection criteria.

For reference, throughout this work I will refer to the different selection criteria of substructures in the retrograde halo as the "*GC*", "*field*", and "*H3*" selections, in reference to the method/survey employed to determine the Sequoia substructure in Myeong et al. (2019), Koppelman et al. (2019c), and Naidu et al. (2020), respectively. I will now go through the details of each selection method independently.

The *GC* method (used in Myeong et al. 2019) selects Sequoia star candidates by identifying stars that satisfy the following conditions:

- $E > -1.5$ ($\times 10^5$ km^{2}s^{-2}),
- $J_\phi/J_{tot} < -0.5$,
- $J_{(J_z - J_R)}/J_{tot} < 0.1$.

Here, J_ϕ, J_R, and J_z are the azimuthal, radial, and vertical actions, and J_{tot} is the quadrature sum of those components. This selection yields a total of 116 Sequoia star candidates.

The *field* method (used in Koppelman et al. 2019c) identifies Sequoia star members based on the following selection criteria:

- $0.4 < \eta < 0.65$,

- $-1.35 < \mathrm{E} < -1$ ($\times 10^5$ km^{2}s^{-2}),
- $\mathrm{L}_z < 0$ (kpc kms^{-1}),

where η is the circularity and is defined as $\eta = \sqrt{1 - e^2}$ (Wetzel, 2011). These selection criteria yield a total of 95 Sequoia stars.

Lastly, I select the Sequoia based on the *H3* selection criteria (used in Naidu et al. 2020) as follows:

- $\eta > 0.15$,
- $\mathrm{E} > -1.6$ ($\times 10^5$ km^{2}s^{-2}),
- $\mathrm{L}_z < -0.7$ (10^3 kpc kms^{-1}).

This selection produces a preliminary sample comprised of 236 Sequoia stars. However, I note that Naidu et al. (2020) use this selection to define not only Sequoia, but all the substructures in the high-energy retrograde halo (including the Arjuna and I'itoi substructures). In order to distinguish Sequoia, I'itoi, and Arjuna, Naidu et al. (2020) suggest performing a metallicity cut, motivated by the observed peaks in the metallicity distribution function (MDF) of their retrograde sample. Thus, I follow this procedure and further refine the Sequoia, Arjuna and I'itoi samples by requiring [Fe/H] > -1.6 cut for Arjuna, $-2 <$ [Fe/H] < -1.6 for Sequoia, and [Fe/H] < -2 for I'itoi, based on the distribution of the initial sample in the MDF (see Fig 3.3). This further division yields an *H3* Sequoia sample comprised of 65 stars, an Arjuna sample constituted by 143 stars, and an I'itoi sample comprised of 22 stars.

Following the selection of substructures in the high-energy retrograde halo, I set out to identify stars belonging to the intermediate-energy and retrograde Thamnos 1 and 2 substructures. Koppelman et al. (2019c) state that Thamnos 1 and 2 are separate debris from the same progenitor galaxies. For this work I consider Thamnos as one overall structure, given the similarity noted by Koppelman et al. (2019c) between the two smaller individual populations in chemistry and kinematic planes. Stars from the parent sample were considered as Thamnos candidate members if they satisfied the following selection criteria:

- $-1.8 < \mathrm{E} < -1.6$ ($\times 10^5$ km^{2}s^{-2}),
- $\mathrm{L}_z < 0$ (kpc kms^{-1}),
- $e < 0.7$,

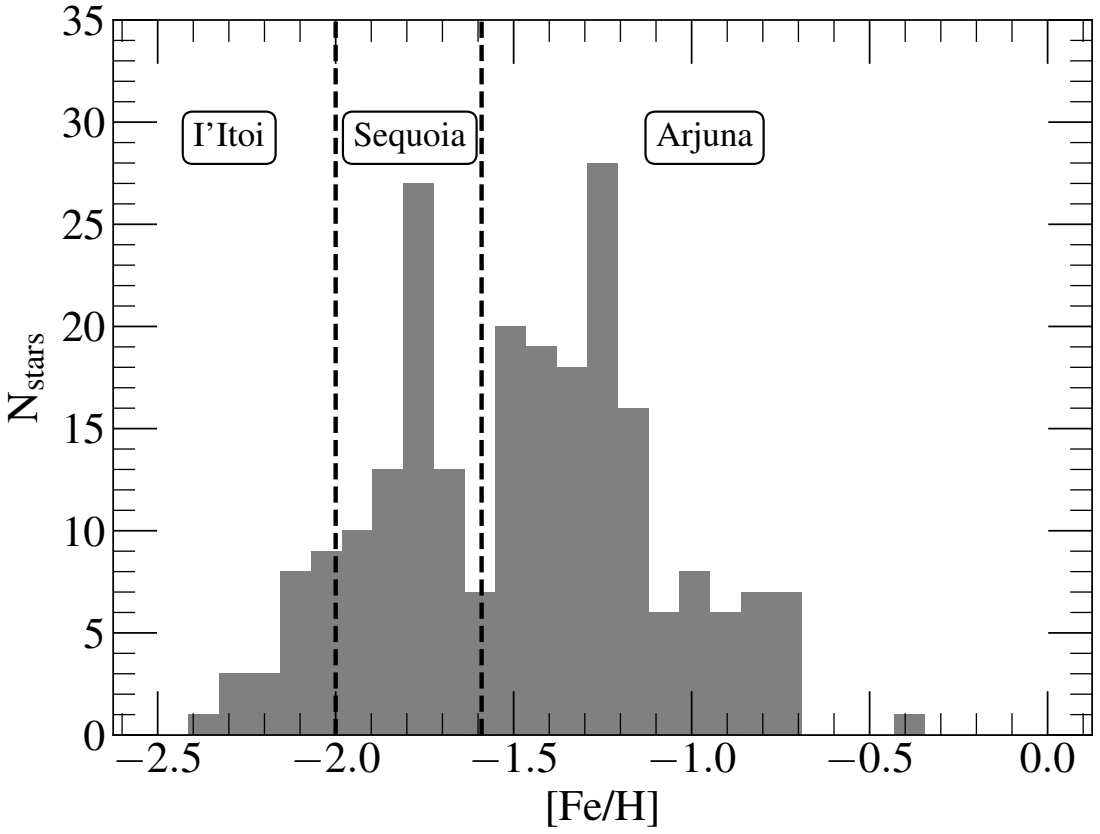

FIGURE 3.3: Metallicity distribution function of the high-energy retrograde sample determined using the selection criteria from Naidu et al. (2020). The dashed black vertical lines define the division of this sample used by Naidu et al. (2020) to divide the three high-energy retrograde substructures: Arjuna, Sequoia, and I'itoi. This MDF dissection is based both on the values used in Naidu et al. (2020), and the distinguishable peaks in this plane (I do not use a replica value of the [Fe/H] used in Naidu et al. (2020) in order to account for any possible metallicity offsets between the APOGEE and H3 surveys).

These selection cuts are performed in order to select stars in the parent sample with intermediate orbital energies and retrograde orbits (see Fig 3.4 for the position of Thamnos in the E-L_z), motivated by the distribution of the Thamnos substructure in the E-L_z plane illustrated by Koppelman et al. (2019c). This selection yields a Thamnos sample comprised of 121 stars.

3.2.1.5 Helmi stream

The Helmi stream was initially identified as a substructure in orbital space due to its high V_z velocities (Helmi et al., 1999). More recent work by Koppelman et al. (2019b) characterised the Helmi stream in *Gaia* DR2, and found that this stellar population is best defined by adopting a combination of cuts in different angular momentum planes.

Specifically, by picking stellar halo stars based on the azimuthal component of the angular momentum (L_z), and its respective perpendicular value ($L_\perp = \sqrt{L_x^2 + L_y^2}$), the authors were able to select a better defined sample of Helmi stream star candidates. I build on the selection criteria from Koppelman et al. (2019b) and define the Helmi stream sample by including stars from the parent population that satisfy the following selection criteria:

- $0.75 < L_z < 1.7$ ($\times 10^3$ kpc kms^{-1}),
- $1.6 < L_\perp < 3.2$ ($\times 10^3$ kpc kms^{-1}),

Our final sample is comprised of 85 Helmi stream stars members.

3.2.1.6 Aleph

Aleph is a newly discovered substructure presented in a detailed study of the Galactic stellar halo by Naidu et al. (2020) on the basis of the H3 survey (Conroy et al., 2019). It was initially identified as a sequence below the high α-disc in the [α/Fe]-[Fe/H] plane. It is comprised by stars on very circular prograde orbits. For this paper, I follow the method described in Naidu et al. (2020) and define Aleph star candidates as any star in the parent sample which satisfies the following selection criteria:

- $175 < V_\phi < 300$ (kms^{-1}),
- $|V_R| < 75$ (kms^{-1}),
- [Fe/H] > -0.8,
- [Mg/Fe] < 0.27,

where V_ϕ and V_R are the azimuthal and radial components of the velocity vector (in Galactocentric cylindrical coordinates), and I use Mg as the α tracer element. The selection criteria yield a sample comprised of 128,578 stars. I find that the initial selection criteria determine a preliminary Aleph sample that is dominated by *in situ* disc stars, likely obtained due to the prograde nature of the velocity cuts employed as well as the chemical cuts. Thus, in order to remove disc contamination and select *true* Aleph star members, I employ two further cuts in vertical height above the plane (namely, $|z| > 3$ kpc) and in vertical action (i.e., $170 < J_z < 210$ kpc kms^{-1}), which are motivated by the distribution of Aleph in these coordinates (see Section 3.2.2 from Naidu et al. 2020). I also note that the vertical height cut was employed in order to mimic the H3 survey selection function. After including these two further cuts, I obtain a final sample of Aleph stars comprised of 28 star members.

3.2.1.7 LMS-1

LMS-1 is a newly identified substructure discovered by Yuan et al. (2020). It is characterised by metal poor stars that form an overdensity at the foot of the omnipresent GES in the E-L_z plane. This substructure was later also studied by Naidu et al. (2020), who referred to it as Wukong. I identify stars belonging to this substructure adopting a similar selection as Naidu et al. (2020), however adopting different orbital energy criteria to adjust for the fact that I adopt the McMillan (2017) Galactic potential (see Fig 23 from Appendix B in that study). Stars from the parent sample were deemed LMS-1 members if they satisfied the following selection criteria:

- $0.2 < L_z < 1$ ($\times 10^3$ kpc kms^{-1}),
- $-1.7 <$ E < -1.2 ($\times 10^5$ km^{-2}s^{-2}),
- [Fe/H] < -1.45,
- $0.4 < e < 0.7$,
- $|z| > 3$ (kpc).

I note that the e and z cuts were added to the selection criteria listed by Naidu et al. (2020). This is because I conjectured that instead of eliminating GES star members from the selection (as Naidu et al. (2020) do), it is more natural in principle to find additional criteria that distinguishes these two overlapping substructures. Thus, I select stars on less eccentric orbits than those belonging to GES, but still more eccentric than most of the Galactic disc (i.e., $0.4 < e < 0.7$). Furthermore, in order to ensure I are observing stars at the same distances above the Galactic plane as in Naidu et al. (2020) (defined by the selection function of the H3 survey), I add a vertical height cut of $|z| > 3$ (kpc). the selection identifies 31 stars belonging to the LMS-1 substructure.

3.2.1.8 Nyx

Nyx has recently been put forward by Necib et al. (2020), who identified a stellar stream in the solar neighbourhood, that they suggest to be the remnant of an accreted dwarf galaxy (Necib et al., 2020). Similar to Aleph, it is characterised by stars on very prograde orbits, at relatively small mid-plane distances (|Z| < 2 kpc) and close to the solar neighbourhood (i.e., |Y| < 2 kpc and |X| < 3 kpc). The Nyx structure is also particularly metal-rich (i.e., [Fe/H] ~ -0.5). Based on the selection criteria used in Necib et al. (2020), I select Nyx star candidates employing the following selection criteria:

- $110 < \mathrm{V}_R < 205$ (kms^{-1}),
- $90 < \mathrm{V}_\phi < 195$ (kms^{-1}),
- $|\mathrm{X}| < 3$ (kpc), $|\mathrm{Y}| < 2$ (kpc), $|\mathrm{Z}| < 2$ (kpc).

The above selection criteria yield a sample comprising of 589 Nyx stars.

3.2.1.9 Icarus

Icarus is a substructure identified in the solar vicinity, comprised by stars that are significantly metal-poor ([Fe/H] $\sim$ –1.45) with circular (disc-like) orbits (Re Fiorentin et al., 2021). In this work, I select Icarus star members using the mean values reported by those authors and adopting a two sigma uncertainty cut around the mean. The selection used is listed as follows:

- [Fe/H] $<$ –1.45,
- [Mg/Fe] < 0.2,
- $1.54 < \mathrm{L}_z < 2.21$ ($\times 10^3$ kpc kms^{-1}),
- $\mathrm{L}_\perp < 450$ (kpc kms^{-1}),
- $e < 0.2$,
- $z_{\mathrm{max}} < 1.5$ (kpc).

These selection criteria yield an Icarus sample comprised of 1 star. As I have only been able to identify 1 star associated with this substructure, I remove it from the main body of this work and focus on discerning why the selection method only identifies 1 star in Appendix B.1. Furthermore, I combine the 1 Icarus star found in APOGEE DR17 with 41 stars found by Re Fiorentin et al. (2021) in APOGEE DR16, in order to study the nature of this substructure in further detail. the results are discussed in Appendix B.1.

3.2.1.10 Pontus

Pontus is a halo substructure recently proposed by Malhan et al. (2022), on the basis of an analysis of *Gaia* EDR3 data for a large sample of Galactic globular clusters and stellar streams. These authors identified a large number of groupings in action space, associated with known substructures. Malhan et al. (2022) propose the existence of a previously unknown susbtructure they call *Pontus*, characterised by retrograde orbits

and intermediate orbital energy. Pontus is located just below *Gaia*-Enceladus/Sausage in the E-Lz plane, but displays less radial orbits (Pontus has an average radial action of $J_R \sim 500$ kpc kms^{-1}, whereas *Gaia*-Enceladus/Sausage displays a mean value of $J_R \sim 1{,}250$ kpc kms^{-1}). In this work, I utilise the values listed in Section 4.6 from Malhan et al. (2022) to identify Pontus candidate members in the sample. I note that because both that study and ours use the McMillan (2017) potential to compute the IoM, the orbital energy values will be on the same scale. the selection criteria for Pontus are the following:

- $-1.72 < E < -1.56$ ($\times 10^5$ km^{-2}s^{-2}),
- $-470 < L_z < 5$ ($\times 10^3$ kpc kms^{-1}),
- $245 < J_R < 725$ (kpc kms^{-1}),
- $115 < J_z < 545$ (kpc kms^{-1}),
- $390 < L_\perp < 865$ (kpc kms^{-1}),
- $0.5 < e < 0.8$,
- $1 < R_{\rm peri} < 3$ (kpc),
- $8 < R_{\rm apo} < 13$ (kpc),
- [Fe/H] < -1.3,

where $R_{\rm peri}$ and $R_{\rm apo}$ are the perigalacticon and apogalacticon radii, respectively. Using these selection criteria, I identify two Pontus candidate members in the parent sample. As two stars comprise a sample too small to perform any statistical comparison, I refrain from comparing the Pontus stars in the main body of this work. Instead, I display and discuss the chemistry of these two Pontus stars in Appendix B.2, for completeness.

3.2.1.11 Cetus

As a closing remark, I note that I attempted to identify candidate members belonging to the Cetus (Newberg et al., 2009) stream. Using the selection criteria defined in Table 3 from Malhan et al. (2022), I found no stars associated with this halo substructure that satisfied the selection criteria of the parent sample. This is likely due to a combination of two factors: *(i)* Cetus is a diffuse stream orbiting at large heliocentric distances ($d_\odot \gtrsim 30$ kpc, Newberg et al., 2009), which APOGEE does not cover well; *(ii)* it occupies a region of the sky around the southern polar cap, where APOGEE does not have many field pointings, at approximately $l \sim 143°$ and $b \sim -70°$ (Newberg et al., 2009).

Name	Selection criteria	N_{stars}
Heracles	$e > 0.6$; –2.6 < E < –2 ($\times 10^5$ km^{2}s^{-2}); [Al/Fe] < –0.07 & [Mg/Mn] $\geqslant$ 0.25; [Al/Fe] $\geqslant$ –0.07; [Mg/Mn] $\geqslant$ 4.25$\times$[Al/Fe] + 0.5475; [Fe/H] > –1.7	281
Gaia-Enceladus/Sausage	$\lvert L_z \rvert$ < 0.5 ($\times 10^3$ kpc km s^{-1}) ; –1.6 < E < –1.1 ($\times 10^5$ km^{2}s^{-2})	2353
Sagittarius	$\lvert \beta_{GC} \rvert$ < 30 (°); 1.8 < $L_{z,Sgr}$ < 14 ($\times 10^3$ kpc kms^{-1}); –150 < $V_{z,Sgr}$ < 80 (kms^{-1}); X_{Sgr} > 0 (kpc); Y_{Sgr} > –5 (kpc) or Y_{Sgr} < –20 (kpc); Z_{Sgr} > –10 (kpc); pm_α > –4 (mas); $d_\odot$ > 10 (kpc)	266
Helmi stream	0.75 < L_z < 1.7 ($\times 10^3$ kpc kms^{-1}); 1.6 < $L_\perp$ < 3.2 ($\times 10^3$ kpc kms^{-1})	85
(*GC*) Sequoia	E > –1.5 ($\times 10^5$ km^{2}s^{-2}); J_ϕ/J_{tot}<–0.5; $J_{(J_z-J_R)}/J_{tot}$<0.1	116
(*field*) Sequoia	0.4<η<0.65; –1.35<E<–1 ($\times 10^5$ km^{2}s^{-2}); L_z<0 (kpc kms^{-1})	95
(*H3*) Sequoia	η>0.15; E>–1.6 ($\times 10^5$ km^{2}s^{-2}); L_z<–0.7 ($\times 10^3$ kpc kms^{-1}); –2 < [Fe/H] < –1.6	65
Thamnos	–1.8 < E < –1.6 ($\times 10^5$ km^{2}s^{-2}); L_z < 0 (kpc kms^{-1}); e < 0.7	121
Aleph	175 < V_ϕ < 300 (kms^{-1}); $\lvert V_R \rvert$ < 75 (kms^{-1}); Fe/H > –0.8; Mg/Fe < 0.27; $\lvert z \rvert$ > 3 (kpc); 170 < J_z < 210 (kpc kms^{-1})	28
LMS-1	0.2 < L_z < 1 ($\times 10^3$ kpc kms^{-1}); –1.7 < E < –1.2 ($\times 10^5$ km^{-2}s^{-2}); [Fe/H] < –1.45; 0.4 < e < 0.7; $\lvert z \rvert$ > 3 (kpc)	31
Arjuna	η > 0.15; E > –1.6 ($\times 10^5$ km^{2}s^{-2}); L_z < –0.7 ($\times 10^3$ kpc kms^{-1}); [Fe/H] > –1.6	143
I'itoi	η > 0.15; E > –1.6 ($\times 10^5$ km^{2}s^{-2}); L_z < –0.7 ($\times 10^3$ kpc kms^{-1}); [Fe/H] < –2	22
Nyx	110 < V_R < 205 (kms^{-1}); 90 V_ϕ < 195 (kms^{-1}); |X| < 3 (kpc), |Y| < 2 (kpc), |Z| < 2 (kpc)	589
Icarus	[Fe/H] < –1.45; [Mg/Fe] < 0.2; 1.54 < L_z < 2.21 ($\times 10^3$ kpc kms^{-1}); $L_\perp$ < 450 (kpc kms^{-1}); e < 0.2; z_{max} < 1.5	1
Pontus	–1.72 < E < –1.56 ($\times 10^5$ km^{-2}s^{-2}); –470 < L_z < 5 ($\times 10^3$ kpc kms^{-1}); 245 < J_R < 725 (kpc kms^{-1}); 115 < J_z < 545 (kpc kms^{-1}); 390 < $L_\perp$ < 865 (kpc kms^{-1}); 0.5 < e < 0.8; 1 < R_{peri} < 3 (kpc); 8 < R_{apo} < 13 (kpc); [Fe/H] < –1.3	2

TABLE 3.1: Summary of the selection criteria employed to identify the halo substructures, and the number of stars obtained for each sample. For a more thorough description of the selection criteria used in this work, see Section 5.3. I note that all the orbital energy values used are obtained adopting a McMillan (2017) potential.

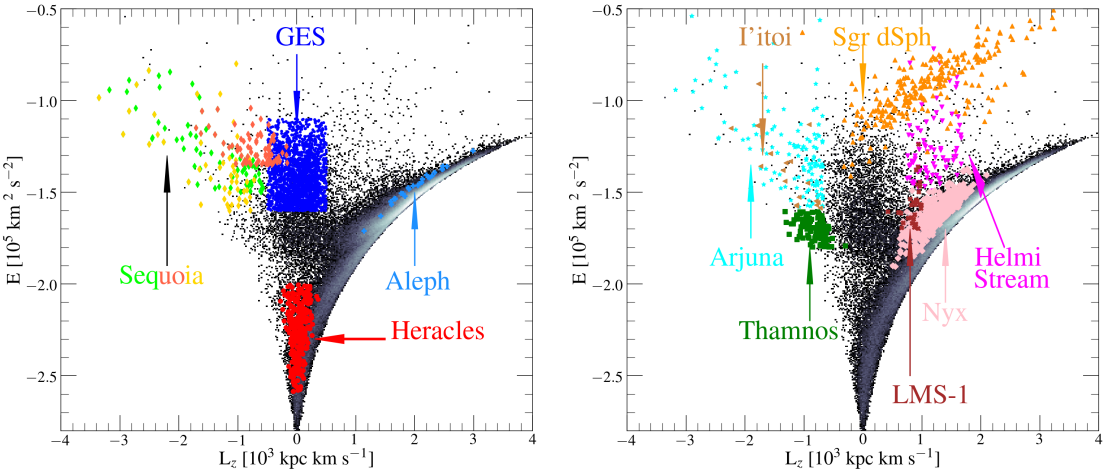

FIGURE 3.4: Distribution of the identified halo substructures in the orbital energy (E) versus angular momentum w.r.t. the Galactic disc (L_z) plane. The parent sample is plotted as a 2D histogram, where white/black signifies high/low density regions. The coloured markers illustrate the different structures studied in this work, as denoted by the arrows (I do not display Pontus(Icarus) as I only identify 2(1) stars, respectively. The figure is split into two panels for clarity.

3.3 Kinematic properties

In this Section, I present the resulting distributions of the identified halo substructures in the orbital energy (E) versus the azimuthal component of the angular momentum (L_z) plane in Fig 3.4. The parent sample is illustrated as a density distribution and the halo substructures are shown using the same colour markers as in Fig 3.1. By construction, each substructure occupies a different locus in this plane. However, I do notice some small overlap between some of the substructures (for example, between GES and Sequoia, or GES and LMS-1), given their similar selection criteria. More specifically, I find that Heracles dominates the low energy region (E < –2×10^5 $km^{-2}s^{-2}$), whereas all the other substructures are characterised by higher energies. As shown before (e.g., Koppelman et al., 2019c; Horta et al., 2021a), I find that GES occupies a locus at low L_z and relatively high E, which corresponds to very radial/eccentric orbits. I find the retrograde region (i.e., L_z < 0 ×10^3 kpc kms^{-1}) to be dominated by Thamnos at intermediate energies (E ∼ –1.7×10^5 $km^{-2}s^{-2}$), and by Sequoia, Arjuna and I'itoi at higher energies (E > –1.4×10^5 $km^{-2}s^{-2}$); on the other hand, in the prograde region (L_z > 0 ×10^3 kpc kms^{-1}), I find the LMS-1 and Helmi stream structures, which occupy a locus at approximately E ∼ –1.5×10^5 $km^{-2}s^{-2}$ and L_z ∼ 500 kpc kms^{-1}, and E ∼ –1.4×10^5 $km^{-2}s^{-2}$ and L_z ∼ 1,000 kpc kms^{-1}, respectively. Furthemore, the loci occupied by the Aleph and Nyx substructures closely mimic the region defined by disc orbits. Lastly, sitting above all other structures I find the Sagittarius dSph, which occupies a position at high energies and spans a range of angular momentum between 0 < L_z < 2,000 kpc kms^{-1}.

3.4 Chemical Compositions

In this Section I turn the attention to the main focus of this work: a chemical abundance study of substructures in the stellar halo of the Milky Way. In this Section, I seek to first characterise these substructures qualitatively in multiple chemical abundance planes that probe different nucleosynthetic pathways. In Section 3.5 I then compare mean chemical compositions across various substructures in a quantitative fashion. the aim is to utilise the chemistry to further unravel the nature and properties of these halo substructures, and in turn place constraints on their star formation and chemical enrichment histories. I also aim to compare their chemical properties with those from *in situ* populations (see Fig 3.5 for how I determine *in situ* populations). By studying the halo substructures using different elemental species I aim to develop an understanding of their chemical evolution contributed by different nucleostynthetic pathways, contributed either by core-collapse supernovae (SNII), supernovae type Ia (SNIa), and/or Asymptotic Giant Stars (AGBs). Furthermore, as the method for identifying these substructures relies mainly on phase space and orbital information, the analysis is not affected by chemical composition biases (except for the case of particular elements in the Heracles, Aleph, LMS-1, Arjuna, I'itoi, and (H3) Sequoia sample).

Our results are presented as follows. In Section 3.4.1 I present the distribution of the halo substructures in the [α/Fe]-[Fe/H] plane, using Mg as the α element tracer. In Section 3.4.2, I show the distribution of these substructures in the [Ni/Fe]-[Fe/H] abundance plane, which provides insight into the chemical evolution of the iron-peak elements. Section 3.4.3 displays the distribution of the halo substructures in an odd-Z-Fe plane, where I use Al as the tracer element. Furthermore, I also show the C and N abundance distributions in Section 3.4.4, the Ce abundances (namely, an *s*-process neutron capture element) in Section 3.4.5, and the distribution of the halo substructures in the [Mg/Mn]-[Al/Fe] plane in Section 3.4.6 [5]. This last chemical composition plane is interesting to study as it has recently been shown to help distinguish stellar populations from "*in situ*" and accreted origins (e.g., Hawkins et al., 2015; Das et al., 2020; Horta et al., 2021a). Upon studying the distribution of the substructures in different chemical composition planes, I finalise the chemical composition study in Section 3.5 by performing a quantitative comparison between the substructures studied in this work for all the (reliable) elemental abundances available in APOGEE.

[5]For each chemical plane, I impose a further set of cuts of `X_FE_FLAG=0` and $[X/Fe]_{error}<0.15$ to ensure there are no unforeseen issues when determining the abundances for these halo substructures in `ASPCAP`.

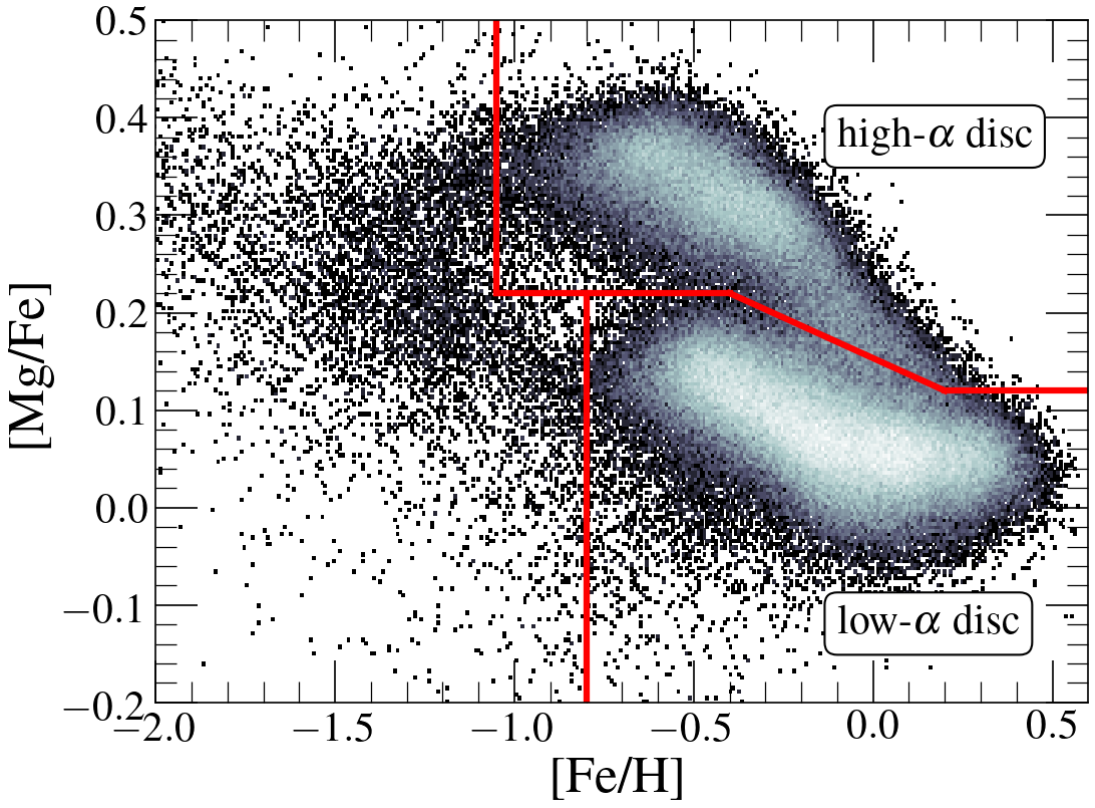

FIGURE 3.5: Parent sample in the [Mg/Fe]-[Fe/H] plane. The solid red lines indicate cut employed to select the high- and low-α disc samples that I use in the χ^2 analysis, where the diagonal dividing line is defined as [Mg/Fe] > –0.167[Fe/H] + 0.15.

As mentioned in Section 5.2, I exclude the Pontus and Icarus substructures from the quantitative chemical comparisons as the number of candidate members of these substructures in the APOGEE catalogue is too small. The properties of Icarus and Pontus are briefly discussed in Appendices B.1 and B.2, respectively.

3.4.1 α-elements

I first turn the attention to the distribution of the substructures in the α-Fe plane. This is possibly the most interesting chemical composition plane to study, as it can provide great insight into the star formation history and chemical enrichment processes of each subtructure (e.g., Matteucci & Greggio, 1986; Wheeler et al., 1989; McWilliam, 1997; Tolstoy et al., 2009; Nissen & Schuster, 2010; Bensby et al., 2014). Specifically, I seek to identify the presence of the α-Fe knee. For this work, I resort to magnesium as the primary α element, as this has been shown to be the most reliable α element in previous APOGEE data releases (e.g., DR16; Jönsson et al., 2020). For the distributions of the remaining α elements determined by ASPCAP (namely, O, Si, Ca, S, and Ti), I refer the reader to Fig B.4-Fig. B.8 in Appendix B.4.

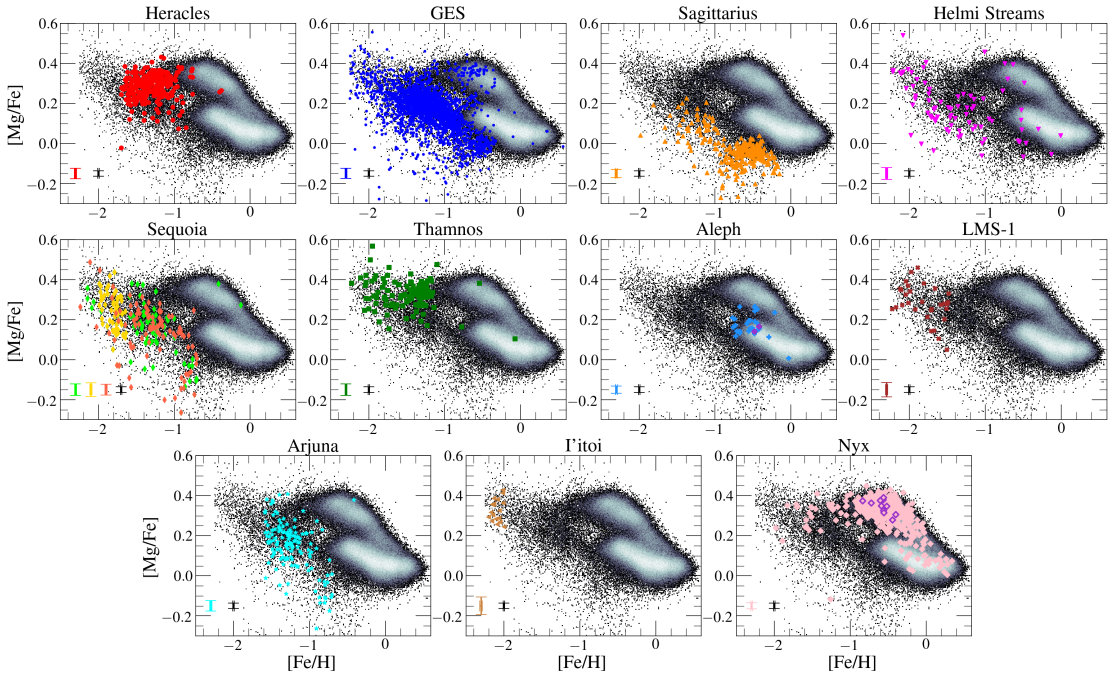

FIGURE 3.6: The resulting parent sample and identified structures from Fig 3.4 in the [Mg/Fe]-[Fe/H] plane. The mean uncertainties in the abundance measurements for halo substructures (colour) and the parent sample (black) are shown in the bottom left corner. Colour coding and marker styles are the same as Fig 3.4. For the Aleph and Nyx substructures, I also highlight with purple edges stars from the APOGEE DR17 data that are also contained in the Aleph and Nyx samples from the Naidu et al. (2020) and Necib et al. (2020) samples, respectively.

Figure 3.6 shows the distribution of each substructure in the Mg-Fe plane (coloured markers) compared to the parent sample (2D density histogram). I find that all the substructures –except for Aleph and Nyx– occupy a locus in this plane which is typical of low mass satellite galaxies and accreted populations of the Milky Way (e.g., Tolstoy et al., 2009; Hayes et al., 2018; Mackereth et al., 2019b), characterised by low metallicity and lower [Mg/Fe] at fixed [Fe/H] than *in situ* populations. Moreover, I find that different substructures display distinct [Mg/Fe] values, implying certain differences despite their overlap in [Fe/H]. However, I also note that at the lowest metallicities ([Fe/H] < -1.8), the overlap between different halo substructures increases.

Next I discuss the distribution on the Mg-Fe plane of stars in the sample belonging to each halo substructure.

- *Sagittarius*: As shown in Hasselquist et al. (2017), Hasselquist et al. (2019) and Hayes et al. (2020), the stellar populations of the Sgr dSph galaxy are characterised by substantially lower [Mg/Fe] than even the low-α disc at the same [Fe/H] and traces a tail towards higher [Mg/Fe] with decreasing [Fe/H]. Conversely, at the higher [Fe/H] end, I find that Sgr stops decreasing in [Mg/Fe] and shows an upside-down "*knee*", likely caused by a burst in SF at late times that may be due to its

interaction with the Milky Way (e.g., Hasselquist et al., 2017, 2021). Such a burst of star formation intensifies the incidence of SNe II, with a consequent boost in the ISM enrichment in its nucleosynthetic by-products, such as Mg, over a short timescale ($\sim 10^7$ yr). Because Fe is produced predominantly by SN Ia over a considerably longer timescale ($\sim 10^8 - 10^9$ yr), Fe enrichment lags behind, causing a sudden increase in [Mg/Fe].

- *Heracles*: The [Mg/Fe] abundances of the Heracles structure occupy a higher locus than that of other halo substructures of similar metallicity, with the exception of Thamnos. As discussed in Horta et al. (2021a), the distribution of Heracles in the α-Fe plane is peculiar, differing from that of GES and other systems by the absence of the above-mentioned α-knee. As conjectured in Horta et al. (2021a), I suggest that this distribution results from an early quenching of star formation, taking place before SN Ia could contribute substantially to the enrichment of the interstellar medium (ISM).

- *Gaia-Enceladus/Sausage*: Taking into account the small yet clear contamination from the high-α disc at higher [Fe/H] (see Fig 3.7 for details), the distribution of GES dominates the metal-poor and α-poor populations of the Mg-Fe plane (as pointed out in previous studies e.g., Helmi et al., 2018; Hayes et al., 2018; Mackereth et al., 2019b), making it easily distinguishable from the high-/low-α discs. I find that GES reaches almost solar metallicities, displaying the standard distribution in the Mg-Fe plane with a change of slope –the so-called "α-knee"– occurring at approximately [Fe/H]$\sim$–1.2 (Mackereth et al., 2019b). The metallicity of the "knee" has long been thought to be an indicator of the mass of the system (e.g., Tolstoy et al., 2009), and indeed it occurs at [Fe/H]$>$–1 for both the high- and low-α discs. As a result, GES stars in the *shin* part of the α-*knee* are characterised by lower [Mg/Fe] at constant metallicity than disc stars. Interestingly, even at the plateau ([Fe/H]$<$–1.2), GES seems to present lower [Mg/Fe] than the high-α disc, although this needs to be better quantified. Furthermore, I note the presence of a minor population of [Mg/Fe] < 0 stars at $-1.8 <$ [Fe/H] < -1.2, which could be contamination from a separate halo substructure, possibly even a satellite of the GES progenitor (see Fig 3.7 for details).

  Based purely on the distribution of its stellar populations on the Mg-Fe plane, one would expect the progenitor of GES to be a relatively massive system (see Mackereth et al., 2019b, for details). The fact that the distribution of its stellar populations in the Mg-Fe plane covers a wide range in metallicity, bracketing the knee and extending from [Fe/H]$<$–2 all the way to [Fe/H]$\sim$–0.5 suggests a substantially prolonged history of star formation.

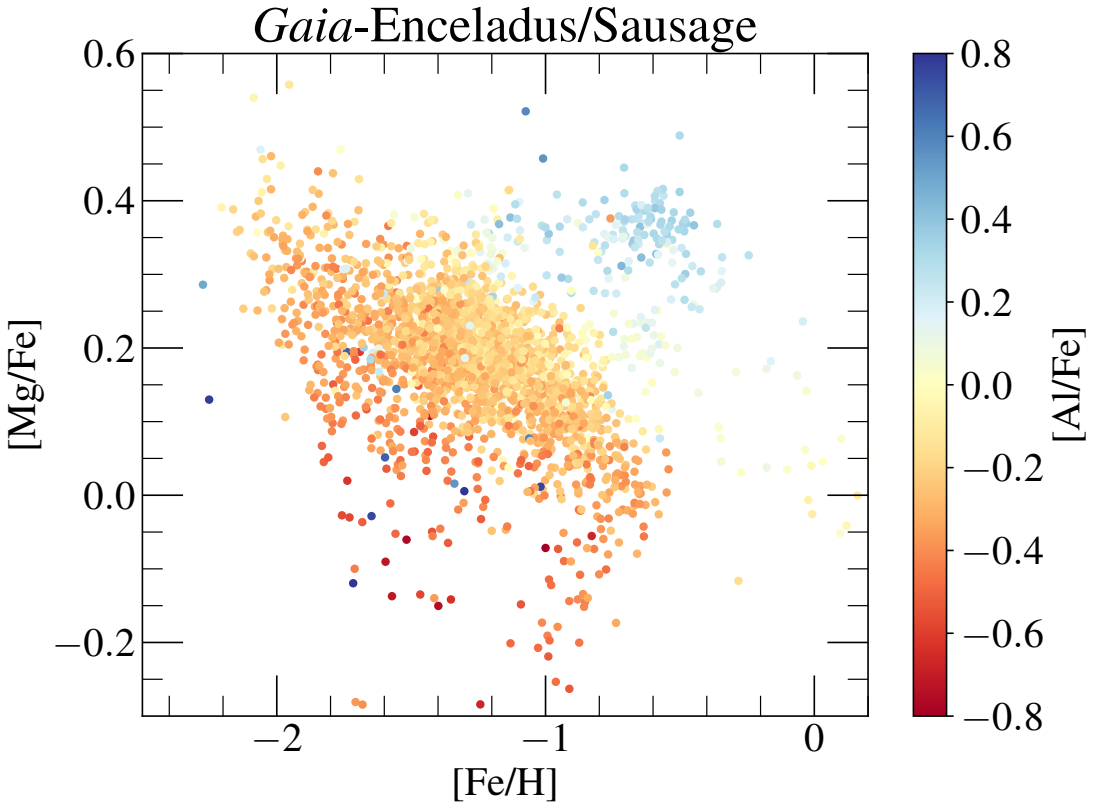

FIGURE 3.7: *Gaia*-Enceladus/Sausage (GES) sample in the [Mg/Fe]-[Fe/H] plane, colour coded by the [Al/Fe] abundance values. The low [Al/Fe] stars are true GES star candidates, which display the expected low [Al/Fe] abundances observed in accreted populations (see Section 3.4.3 for details). Conversely, the high [Al/Fe] stars are clear contamination from the high-α disc, likely associated with disc stars on very eccentric and high energy orbits (Bonaca et al., 2017; Belokurov et al., 2020). A striking feature becomes apparent in this plane: at –1.8 < [Fe/H] < –0.8, there is a population of very [Mg/Fe]-poor stars (i.e., [Mg/Fe] below ∼0), that could possibly be contamination from a separate halo substructure (although these could also be due to unforeseen problems in their abundance determination).

.

- *Sequoia*: The distribution of the *GC*, *field*, and *H3* selected samples (selected on the criteria described in Myeong et al. (2019), Koppelman et al. (2019c), and Naidu et al. (2020), respectively) occupy similar [Mg/Fe] values ([Mg/Fe]∼0.1) at lower metallicities ([Fe/H] $\lesssim$–1). More specifically, I find that all three Sequoia samples occupy a similar position in the [Mg/Fe]-[Fe/H] plane, one that overlaps with that of GES and other substructures at similar [Fe/H] values. Along those lines, I find that the *field* and *GC* Sequoia samples seem to connect with the *H3* Sequoia sample, where the *H3* sample comprises the lower metallicity component of the *field*/*GC* samples. I examine in more detail the distribution of the Sequoia stars in the α-Fe plane in Section 3.6.1.3.

- *Helmi stream*: Despite the low number of members associated to this substructure, its chemical composition in the [Mg/Fe]-[Fe/H] plane appears to follow a

single sequence, and is confined to low metallicities ([Fe/H]<-1.2) and intermediate magnesium values ([Mg/Fe]$\sim$0.2). However, I do note that the stars identified for this substructure appear to be scattered across a wide range of [Fe/H] values. Specifically, the Helmi stream occupies a locus that overlaps with the GES for fixed [Fe/H]. In Fig 3.19 I show that the best-fitting piece-wise linear model prefers a knee that is "inverted" similar to, although less extreme than, the case of Sgr dSph. I discuss this in more detail in Section 3.6.1.4.

- *Thamnos*: The magnesium abundances of Thamnos suggest that this structure is clearly different from other substructures in the retrograde halo (namely, Sequoia, Arjuna, and I'itoi). It presents a much higher mean [Mg/Fe] for fixed metallicity than the other retrograde substructures, and appears to follow the Mg-Fe relation of the high-α disc. I find that Thamnos presents no α-knee feature, and occupies a similar locus in the [Mg/Fe]-[Fe/H] plane to that of Heracles. The distribution of this substructure in this plane with the absence of an α-Fe "knee" suggests that this substructure likely quenched star formation before the onset of SN Ia.

- *Aleph*: By construction, Aleph occupies a locus in the [Mg/Fe]-[Fe/H] plane that overlaps with the metal-poor component of the low-α disc. Given the distribution of this substructure in this chemical composition plane, and its very disc-like orbits, I suggest it is possible that Aleph is constituted by warped/flared disc populations. Because the data upon which the work and that by Naidu et al. (2020) are based come from different surveys, it is important however to ascertain that selection function differences between APOGEE and H3 are not responsible for the samples to have very different properties, even though they are selected adopting the same kinematic criteria. In an attempt to rule out that hypothesis I cross-matched the Naidu et al. (2020) catalogue with that of APOGEE DR17 to look for Aleph stars in common to the two surveys. I find only two such stars[6], which I highlight in Fig 3.6 with purple edges. While this is a very small number, the two stars seem to be representative of the chemical composition of the APOGEE sample of Aleph stars, which is encouraging.

- $LMS-1$: the results from Fig 3.6 show that the LMS-1 occupies a locus in the [Mg/Fe]-[Fe/H] plane which appears to form a single sequence with the GES at the lower metallicity end. Based on its Mg and Fe abundances, and the overlap in kinematic planes of LMS-1 and GES, I suggest it is possible that these two substructures could be linked, where LMS-1 constitutes the more metal-poor component of the GES. I investigate this possible association further in Section 3.5.

[6] I find that these two stars have a `STARFLAG` set with `PERSIST_LOW` and `BRIGHT_NEIGHBOUR`, and thus do not survive the initial parent selection criteria. However, these warnings are not critical, and should not have an effect on their abundance determinations.

- *Arjuna*: This substructure occupies a distribution in the [Mg/Fe]-[Fe/H] plane that follows that of the GES. Despite the sample being lower in numbers than that for GES, I still find that across –1.5 < [Fe/H] < –0.8 this halo substructure overlaps in the [Mg/Fe]-[Fe/H] plane with that of the GES substructure. Given the strong overlap between these two systems, as well as their proximity in the E-L_z plane (see Fig 3.4), I suggest it is possible that Arjuna could be part of the GES substructure, and further investigate this possible association in Section 3.5.

- *I'itoi*: Despite the small sample size, I find I'itoi presents high [Mg/Fe] and low [Fe/H] values (the latter by construction), and occupies a locus in the [Mg/Fe]-[Fe/H] plane that appears to follow a single sequence with the Sequoia (all three samples) and the GES sample.

- *Nyx*: The position of this substructure in the [Mg/Fe]-[Fe/H] strongly overlaps with that of the high-α disc. Given this result, and the disc-like orbits of stars comprising this substructure, I conjecture that Nyx is constituted by high-α disc populations, and further investigate this association in Section 3.5. Furthermore, in a similar fashion as done for the Aleph substructure, I highlight in Fig 3.6 with purple edges those stars in APOGEE DR17 that are also contained in the Nyx sample from Necib et al. (2020), in order to ensure that the results are not biased by the APOGEE selection function. I find that the overlapping stars occupy a locus in this plane that overlaps with the Nyx sample determined in this study, and the high-α disc.

3.4.2 Iron-peak elements

Following the analysis of the various substructures in the [Mg/Fe]-[Fe/H] plane, I now focus on studying their distributions in chemical abundance planes that probe nucleosynthetic pathways contributed importantly by Type Ia supernovae. I focus on nickel (Ni), which is the Fe-peak element that is determined the most reliably by ASPCAP, besides Fe itself. For the distribution of the structures in other iron-peak element planes traced by ASPCAP (e.g., Mn, Co, and Cr), I refer the reader to Fig. B.10– Fig. B.12 in Appendix B.6.

The distributions of the halo substructures in the [Ni/Fe]-[Fe/H] plane are shown in Fig. 3.8. I find that the distributions of GES, Sgr dSph, the Helmi stream, Arjuna, LMS-1, and the three Sequoia samples occupy a locus in this plane that is characteristic of low mass satellite galaxies and/or accreted populations of the Milky Way, displaying lower [Ni/Fe] abundances than the low- and high-α disc populations (e.g., Shetrone et al., 2003; Mackereth et al., 2019b; Horta et al., 2021a, Shetrone et al. 2022, in prep.). In

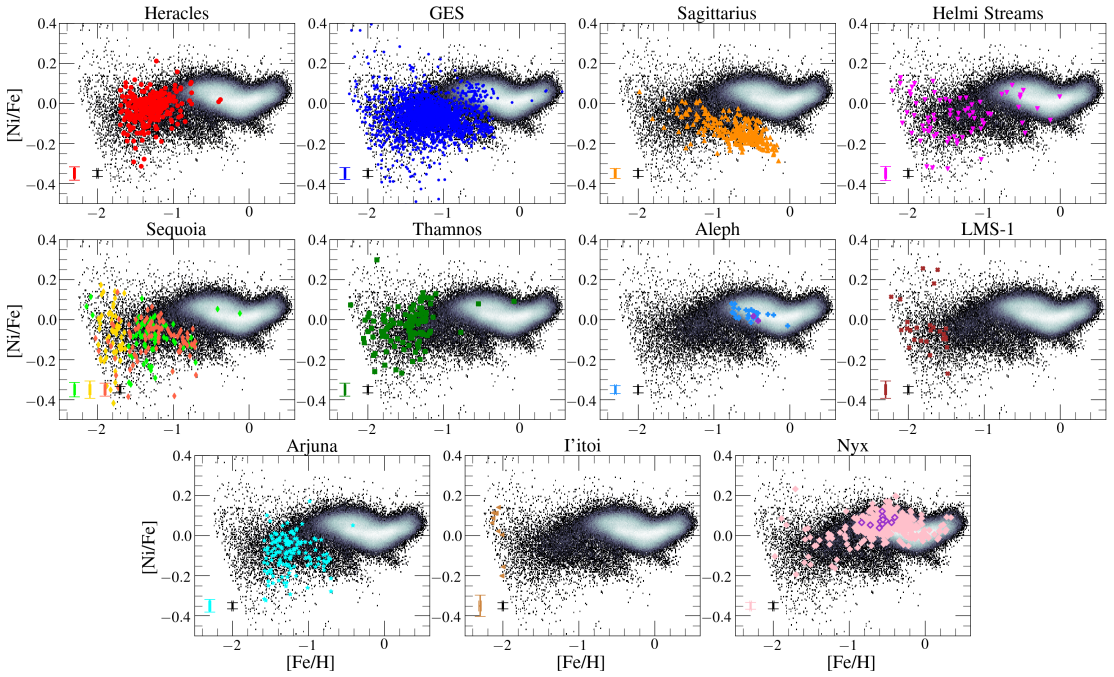

FIGURE 3.8: The same illustration as in Fig 3.6 in the [Ni/Fe]-[Fe/H] space. I note that the grid limit of appears clearly in this plane at the lowest [Fe/H] values.

contrast, the data for Heracles and Thamnos display a slight correlation between [Ni/Fe] and [Fe/H], connecting with the high-α disc at [Fe/H] ~ -1 (despite the differences of these substructures in the other chemical composition planes with *in situ* populations). Conversely, I find that the Aleph and Nyx structures clearly overlap with *in situ* disc populations at higher [Fe/H] values, agreeing with the result for these substructures on the [Mg/Fe]-[Fe/H] plane. The distribution of I'itoi shows a spread in [Ni/Fe] for a small range in [Fe/H], that is likely due to observational error at such low metallicities.

Interpretation of these results depends crucially on an understanding of the sources of nickel enrichment. Like other Fe-peak elements, nickel is contributed by a combination of SNIa and SNe II (e.g., Weinberg et al., 2019; Kobayashi et al., 2020). The disc populations display a bimodal distribution in Figure 3.8, which is far less pronounced than in the case of Mg. This result suggests that the contribution by SNe II to nickel enrichment may be more important than previously thought (but see below). It is thus possible that the relatively low [Ni/Fe] observed in MW satellites and halo substructures has the same physical reason as their low [α/Fe] ratio, namely, a low star formation rate (e.g., Hasselquist et al., 2021). This hypothesis can be checked by examining the locus occupied by halo substructures in a chemical plane involving an Fe-peak element with a smaller contribution by SNe II, such as manganese (e.g., Kobayashi et al., 2020). If indeed the [Ni/Fe] depression is caused by a decreased contribution by SNe II, one would expect [Mn/Fe] to display a different behaviour. Figure B.10 confirms that expectation, with substructures falling on the same locus as disc populations on the Mn-Fe plane.

Another possible interpretation of the reduced [Ni/Fe] towards the low metallicity characteristic of halo substructures is a metallicity dependence of nickel yields (Weinberg et al., 2021). I may need to entertain this hypothesis since, in contrast to the results presented in Figure 3.8, no [Ni/Fe] bimodality is present in the solar neighbourhood disc sample studied by Bensby et al. (2014), which may call into question the conclusion that SNe II contribute relevantly to nickel enrichment. It is not clear whether the apparent discrepancy between the data for nickel in Bensby et al. (2014) and this work is due to lower precision in the former, sample differences, or systematics in the APOGEE data.

Given the distribution of the substructures in the Ni-Fe plane, the results suggest that: *i)* Sgr dSph, GES, Sequoia (all three samples), and the Helmi stream substructures show a slightly lower mean [Ni/Fe] than *in situ* populations at fixed [Fe/H], as expected for accreted populations in the Milky Way on the basis of previous work (e.g., Nissen & Schuster, 1997; Shetrone et al., 2003); *ii)* Heracles and Thamnos fall on the same locus on the Ni-Fe plane, presenting a slight correlation between [Ni/Fe] and [Fe/H]; *iii)* as in the case of the Mg-Fe plane, Arjuna and LMS-1 occupy a similar locus in the Ni-Fe plane to that of GE/S, further supporting the suggestion that these substructures may be associated; *iv)* Aleph/Nyx mimic the behaviour of in situ low-/high-α disc populations, respectively.

3.4.3 Odd-Z elements

Aside from α and iron-peak elements, other chemical abundances provided by ASPCAP/APOGEE that are interesting to study are the odd-Z elements. These elements have been shown in recent work to be depleted in satellite galaxies of the MW and accreted systems relative to populations formed *in situ* (e.g., Hawkins et al., 2015; Das et al., 2020; Horta et al., 2021a; Hasselquist et al., 2021). For this paper, I primarily focus on the most reliable odd-Z element delivered by ASPCAP: aluminium. For the distribution of the structures in other odd-Z chemical abundance planes yielded by APOGEE (namely, Na, and K), I refer the reader to Fig. B.13 and Fig. B.14 in Appendix B.7.

Fig. 3.9 displays the distribution of the substructures and parent sample in the [Al/Fe]-[Fe/H] plane, using the same symbol convention as adopted in Fig. 3.6. I note that the parent sample shows a high density region at higher metallicities, displaying a bimodality at approximately [Fe/H] $\sim$ –0.5, where the high-/low-[Al/Fe] sequences correspond to the high-/low-α discs, respectively. In addition, there is a sizeable population of aluminium-poor stars with -0.5[Al/Fe]0 ranging from the most metal-poor stars in the sample all the way to [Fe/H] ~ -0.5[7]. This is the locus occupied by MW satellites and most

[7]The clump located at [Al/Fe] ~ -0.1 and [Fe/H] > 0 is not real, but rather an artifact due to systematics in the abundance analysis which does not affect the bulk of the data.

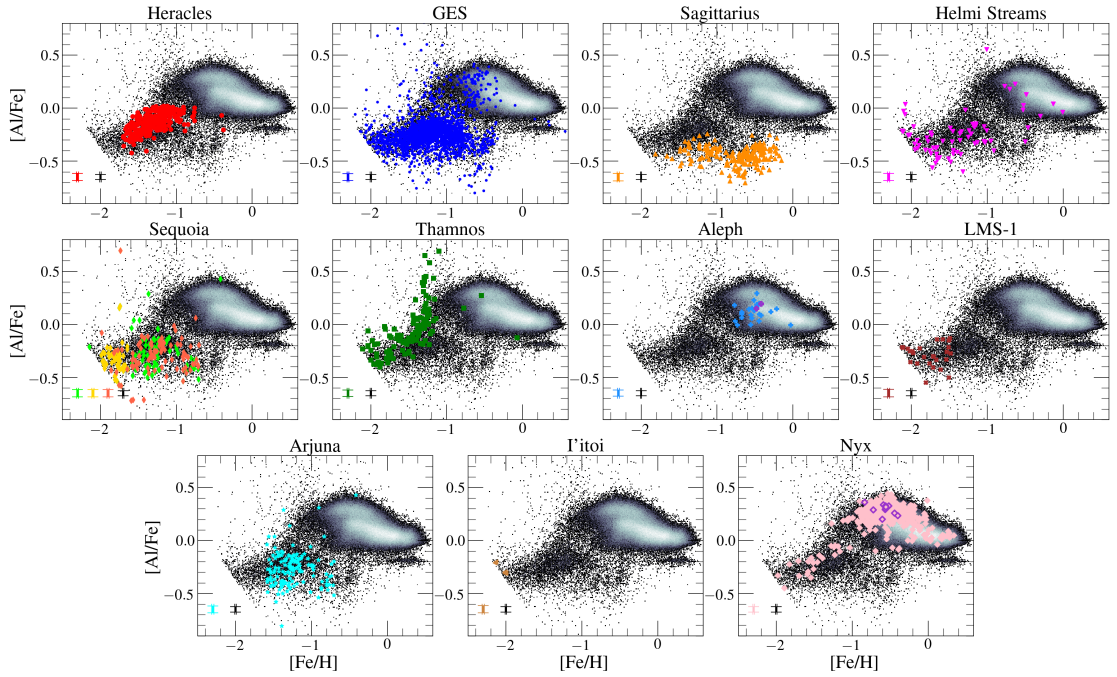

FIGURE 3.9: The same illustration as in Fig 3.6 in [Al/Fe]-[Fe/H] space. I note that the grid limit appears clearly in this plane at the lowest [Fe/H] values.

accreted substructures, with the exception of Aleph and Nyx. Note also that the upper limit of the distribution of the Heracles population on this plane is determined by the definition of the sample (see Horta et al., 2021a, for details).

The majority of the substructures studied occupy a similar locus in this plane, which agrees qualitatively with the region where the populations from MW satellites are usually found (e.g., Hasselquist et al., 2021). There is strong overlap between stars associated with the GES, the Helmi stream, Arjuna, Sequoia (all three samples), and LMS-1 substructures. More specifically, I find that GES dominates the parent population sample at [Fe/H] $<$ –1, being located at approximately [Al/Fe] $\sim$ –0.3. At a slightly higher value of [Al/Fe] $\sim$ –0.15 and similar metallicities, I find Heracles and Thamnos. In contrast, Sgr dSph is characterised by an overall lower [Al/Fe] $\sim$ –0.5 value, which extends below the parent disc population towards higher [Fe/H], reaching almost solar metallicity. Within the -2[Fe/H] $-$ 1 interval, Heracles, GES, Helmi streams, Thamnos, Nyx, and, to a lesser extent, Sequoia, show some degree of correlation between [Al/Fe] and [Fe/H]. Towards the metal-poor end, I find the LMS-1 located at [Al/Fe]$\sim$–0.3, which is consistent with the value found for I'itoi, although the sample of aluminium abundances for this latter structure is very small and close to the detection limit. As in the case of magnesium and nickel, all three Sequoia samples occupy the same locus in the Al-Fe plane as Arjuna, which strongly overlap with GES. Again in the case of the Al-Fe plane, I find that the case for Nyx and Aleph follow closely the trend established by *in situ* disc populations.

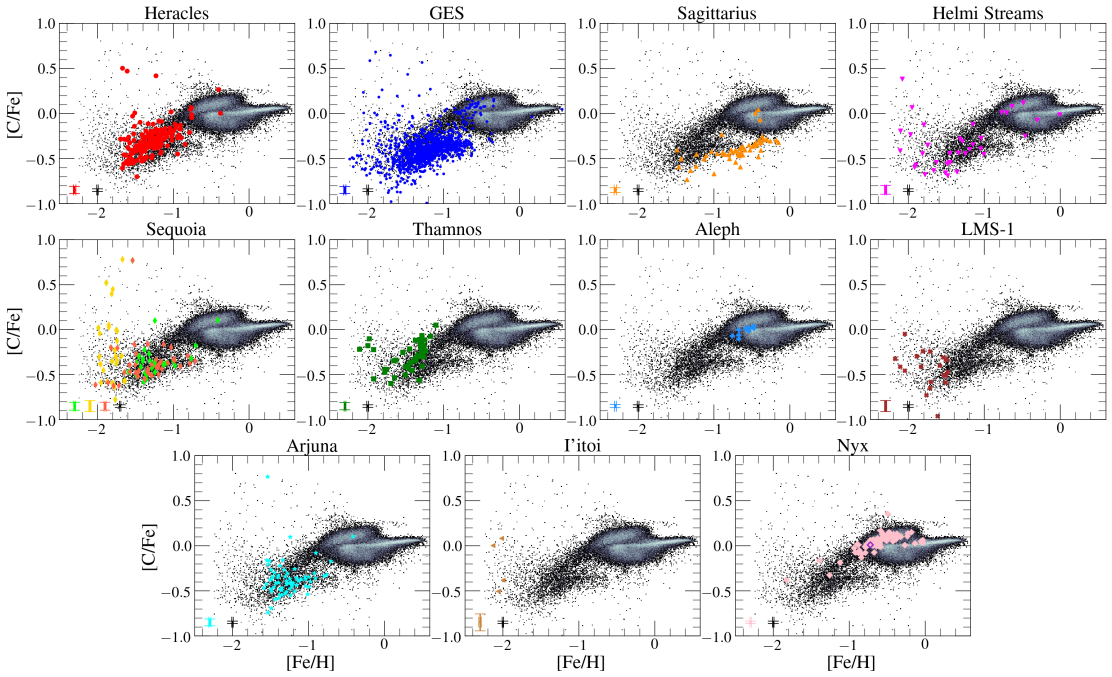

FIGURE 3.10: The same illustration as Fig. 3.6 in the [C/Fe]-[Fe/H] plane. For this chemical plane I restrict the sample to a surface gravity range of $1 < \log g < 2$ in order to minimise the effect of internal mixing

in red giant stars.

3.4.4 Carbon and Nitrogen

In this subsection, I examine the distribution of stars belonging to various substructures in the C-Fe and N-Fe abundance planes, shown in Figures 3.10 and 3.11, respectively. I note that in these chemical planes, I impose an additional surface gravity constraint of $1 < \log g < 2$ in order to minimise the effect of internal mixing along the giant branch.

In the C-Fe plane, most substructures are characterised by sub-solar [C/Fe], displaying a clear correlation between that abundance ratio and metallicity. The exceptions, as in all previous cases, are Aleph and Nyx, which again follow the same trends as *in situ* populations. Interestingly, the Sgr dSph presents the lowest values of [C/Fe] at fixed [Fe/H], tracing a tight sequence at approximately [C/Fe]$\sim$–0.5, spanning from –1.4 < [Fe/H] < –0.2, approximately $\sim$0.5 dex below that of the Galactic disc. In the case of I'itoi, due to the low numbers of stars in this sample I am unable to draw any conclusions.

The distribution of substructures in the N-Fe plane follows a different behaviour than seen in all other chemical planes. Again, except for Aleph and Nyx, all systems display a trend of increasing [N/Fe] towards lower metallicities, starting at [Fe/H] $-$ 1. This trend cannot be ascribed to systematics in the ASPCAP abundances or evolutionary effects, as the abundances are corrected for variations with $\log g$. Nitrogen abundances are notoriously uncertain, particularly in the low metallicity regime. The compilation

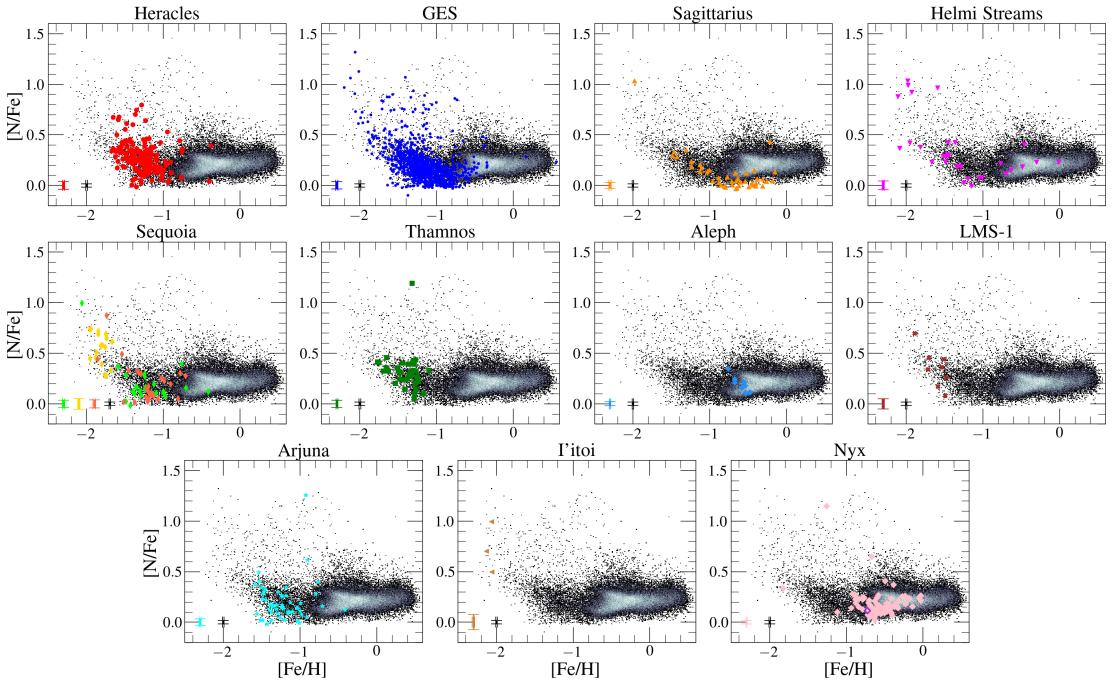

FIGURE 3.11: The same illustration as Fig. 3.6 in the [N/Fe]-[Fe/H] plane. As done in Fig 3.10, for this chemical plane I restrict the sample to a surface gravity range of $1 < \log g < 2$ in order to minimise the effect of internal mixing in red giant stars. I note that the grid limit appears clearly in this plane at the lowest [Fe/H] values.

by Kobayashi et al. (2020) shows that the [N/Fe] trend at low metallicity is strongly dependent on the analysis methods. Discerning the source of systematics in the ASPCAP abundances at [Fe/H] -1 is beyond the scope of this paper, which focuses on a strictly differential analysis of the data, within a metallicity regime where ASPCAP elemental abundances attain exceedingly high precision (Section 3.5).

For completeness, data covering the whole range of $\log g$ for all substructures are displayed in the [(C+N)/Fe]-[Fe/H] plane in Fig B.9 in Appendix B.5. By combining carbon and nitrogen abundances, I minimise the effect of CNO mixing along the giant branch. In this plane, MW satellites and accreted populations typically display a lower [(C+N)/Fe] chemical composition than their *in situ* counterparts (e.g., Horta et al., 2021a; Hasselquist et al., 2021). This is in fact what I observe for all the structures identified, again with the exception of Aleph and Nyx, whose locus overlaps with that of *in situ* disc populations.

3.4.5 Cerium

Cerium is a neutron capture element of the s-process family, with a large enrichment contribution from AGB stars (Sneden et al., 2008; Jönsson et al., 2020; Kobayashi et al., 2020). In Fig. 3.12, the disc sample at [Fe/H]>−1 has a roughly horizontal locus at

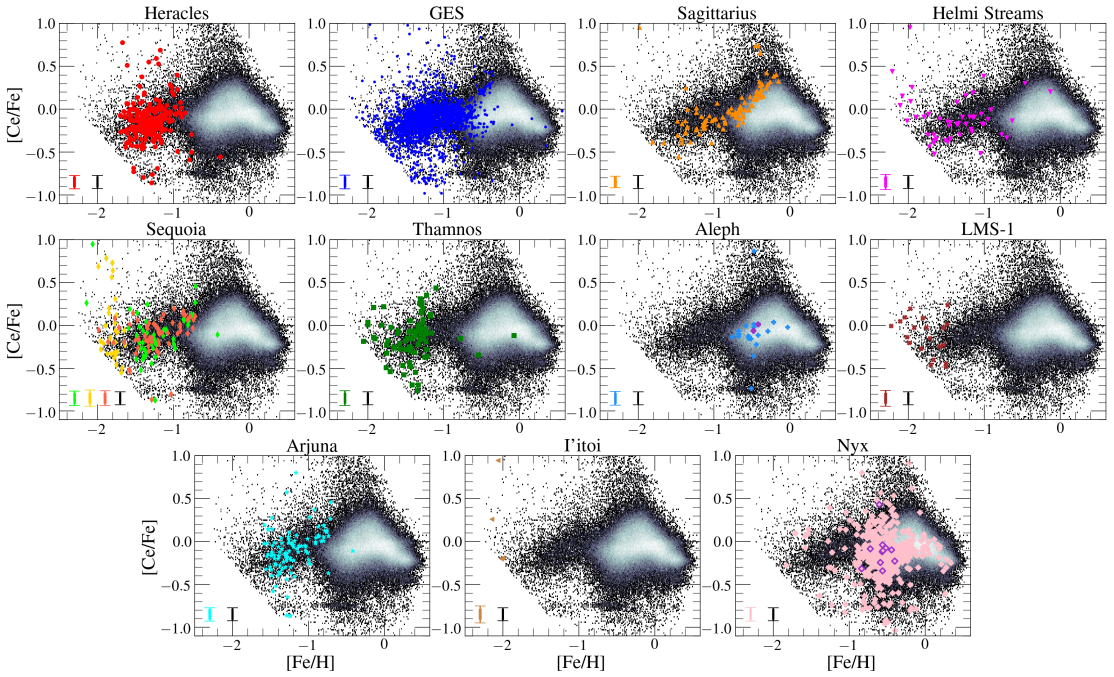

FIGURE 3.12: The same illustration as Fig. 3.6 in the [Ce/Fe]-[Fe/H] plane. I note that the grid limit appears clearly in this plane at the lowest [Fe/H] values.

≈ -0.1 dominated by stars in the *high-*α population and an upward-pointing triangular locus dominated by stars in the *low-*α sequence, reaching [C/Fe]$\approx +0.4$ at [Fe/H]≈ -0.2. The scatter within each of these components is large and may be partly observational. The presence of substantial Ce in high-α stars suggests that massive stars with short lifetimes make a significant, prompt contribution. The rising-then-falling trend in the low-α population is expected from the metallicity-dependent yield of intermediate mass AGB nucleosynthesis: at low [Fe/H] the number of seeds available for neutron capture increases with increasing metallicity, but at high [Fe/H] the number of neutrons per seed becomes to low to produce the heavier s-process elements (Gallino et al., 1998). See Weinberg et al. (2021) for plots of [Ce/Mg] vs. [Mg/H] and further discussion of the disc trends.

In this chemical composition plane, I find that all the identified substructures, with the exception of Aleph and Nyx, present [Ce/Fe] abundances that follow the mean trend with [Fe/H] of the parent population until [Fe/H] ~ -1. Aleph and Nyx have higher [Fe/H] stars that generally lie within the broad disc locus. Interestingly, the Sgr stars with [Fe/H] >-1 show a rising [Ce/Fe] trend that tracks the behaviour of the low-α disc population. This trend is not obvious in the other substructures, though with the exception of Aleph and Nyx they have few stars at [Fe/H] >-1. I interpret this upturn in both Sgr and the low-α disc as the signature of an AGB contribution with a metallicity dependent yield.

At [Fe/H] <–1, the parent halo population and most substructure stars exhibit mildly sub-solar [Ce/Fe] with substantial scatter, which may have a significant observational component. The [Ce/Fe] is similar to that of typical high-α disc stars at [Fe/H] >–1. However, these stars have lower [α/Fe] than the high-α disc, the signature of Fe enrichment from Type Ia SNe, so if the Ce in these populations is a prompt contribution from massive stars one might have naively expected them to have depressed [Ce/Fe]. It is difficult to disentangle the effects of metallicity-dependent Ce yields, differences in the relative contributions of high-mass and intermediate-mass stars, and the impact of Type Ia SN enrichment on the Fe abundance; further observational investigation and theoretical modeling will be needed to do so. The [Ce/Fe] locus of substructure stars at –2 < [Fe/H] < –1 is similar to that in the dwarf satellites studied by Hasselquist et al. (2021).

3.4.6 The [Al/Fe] vs [Mg/Mn] plane

Having studied the distribution of the identified structures in chemical abundance planes that aimed to give us an insight into the different nucleosynthetic pathways, contributed either by core-collapse, type Ia supernovae, and AGB stars, I now focus the attention on analysing the distribution of substructures in the stellar halo in an abundance plane that lends insights into the accreted or *in situ* nature of Galactic stellar populations: namely, the [Mg/Mn]-[Al/Fe] plane.

Fig. 3.13 shows the resulting distribution of the various structures in the [Mg/Mn]-[Al/Fe] plane. This chemical plane has been proposed by Das et al. (2020) as a means to distinguishing accreted populations from those formed *in situ*. Horta et al. (2021a) showed that *in situ* stellar populations with a small degree of chemical evolution occupy the same locus in that plane as accreted populations. By construction, the Heracles substructure falls in the accreted locus of the diagram (see Fig 1 in Horta et al. (2021a) for reference). However, the results show that all the other structures, except for Aleph and Nyx, also occupy the accreted locus of this plane. Interestingly, I find that although the GES, Sgr dSph, the Helmi stream, Sequoia (all three samples), Thamnos, LMS-1, Arjuna, and I'itoi substructures occupy the same locus, they appear to show some small differences. Specifically, I find that Sgr dSph occupies a locus in this plane positioned at lower mean [Mg/Mn] than the other structures. This is likely due to Sgr being more recently accreted by the Milky Way, and thus had more time to develop stellar populations with enriched Mn abundances that have been contributed on a longer timescale by type Ia supernovae. This feature is also seen to a lesser extent for I'itoi. Conversely, at higher [Mg/Mn] values (but still low [Al/Fe]) I find GES, Heracles (by construction),

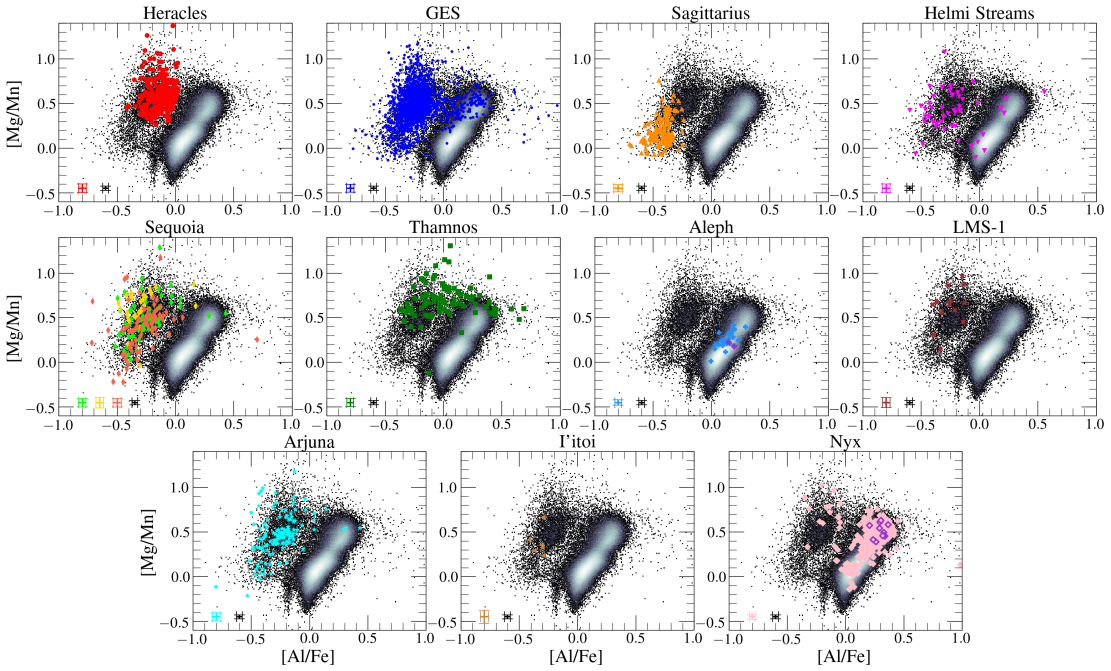

FIGURE 3.13: The same illustration as Fig. 3.6 in the [Mg/Mn]-[Al/Fe] plane.

Thamnos, LMS-1, the Helmi stream, Sequoia (all three samples), and Arjuna. The distribution of these substructures in this chemical plane reinforces the hypothesis of these halo substructures arising from an accreted origin.

In a similar fashion to the other chemical composition planes, I find that Aleph and Nyx overlap with *in situ* (disc) populations at higher [Al/Fe], suggestive that Aleph and Nyx are likely substructures comprised of *in situ* disc populations.

3.5 A quantitative comparison between halo substructure abundances

After qualitatively examining the chemical compositions of the previously identified halo substructures in a range of chemical abundance planes, I now focus on comparing the abundances in a quantitative fashion using a χ^2 method. To do so, I compare the mean value of thirteen different elemental abundances, manufactured in different nucleosynthetic channels, for each substructure at a fixed metallicity that is well covered by the data. The set of elemental abundances chosen to run this quantitative test was determined based on the distribution of the parent sample in the respective chemical composition plane, where I only chose those elements that did not display a large scatter towards low metallicity due to increased abundance uncertainties (on the order of σ $\sim$0.15 dex). Out of the initial 20 elemental abundances available in ASPCAP (excluding

Fe), I utilise the following thirteen elements: C, N, O, Mg, Al, Si, S, K, Ca, Ti, Mn, Ni, and Ce. I note that Na, P, V, Cr, and Co were removed due to the large scatter at low metallicity, whereas Cu and Nd were not considered due to `ASPCAP` not being able to determine abundances for these elements in APOGEE DR17.

For the quantitative comparison, I proceeded as follows:

i) I select a high- and low-α disc population based on Fig 3.5 for reference, and utilise these samples as representative disc samples for any comparison between *in situ* populations and halo substructures. In order to account for any distance selection function effects, I restrict the high-/low-α samples to stars within $d < 2$ kpc, and also determine an "inner high-α disc" sample (restricted to $R_{GC} < 4$ kpc which I will use to compare to Heracles (which has a spatial distribution that is largely contained within ∼4 kpc from the Galactic Centre).

ii) Before performing any chemical composition comparisons, I correct the abundances for systematic trends with surface gravity. Systematic abundance variations trends with $\log g$ can be caused, one one hand, by real physical chemical composition variations as a function of evolutionary stage and/or, on the other, by systematic errors in elemental abundances as a function of stellar parameters. The former chiefly impact elements such as C, N, and O, whose atmospheric abundances are altered by mixing during evolution along the giant branch. The latter impact various elements in distinct, though more subtle, ways (see discussion in Weinberg et al., 2021). Surface gravity distributions of various substructures differ in important ways (Figure 3.1), so that such systematic abundance trends with $\log g$ can induce spurious artificial chemical composition differences between substructures. I thus follow a procedure similar to that outlined by Weinberg et al. (2021) to correct each elemental abundance using the full parent sample. As systematic trends with $\log g$ are more important towards the low and high ends of the $\log g$ distribution, I restrict the sample to stars within the $1 < \log g < 2$ range. I then fit a second order polynomial to the [X/H]-$\log g$ relation, and calculate the difference between that fit and the overall [X/H] median. The difference between these two quantities for any given $\log g$ is then added to the original [X/H] values so as to produce a flat relation between $[X/H]_{corrected}$ and $\log g$. I then use these values to determine corrected [X/Fe] abundances. In a recent study, Eilers et al. (2021) pointed out that simple corrections for abundance trends as a function of $\log g$ could erase real differences associated with abundance gradients within the Galaxy. That is because a magnitude limited survey may cause an artificial dependence of $\log g$ on distance. the study aims at contrasting the chemical compositions of substructures that are in principle associated with spatially self-contained progenitors. Thus, systematic differences linked to spatial

abundance variations within each structure are irrelevant for the purposes, so a straightforward correction for abundance variations with $\log g$ are perfectly acceptable for the goals.

iii) Upon obtaining corrected abundances for every halo substructure, I determined the uncertainties in the abundances using a bootstrapping resampling with replacement method (utilising the `astropy.stats.bootstrap` routine by Price-Whelan et al., 2018). I generated 1,000 realisations of the [X/Fe]-[Fe/H] chemical composition planes for every element and every halo substructure sample in order to assess the scatter in the abundance distribution. For example, I generated 1,000 realisations of the [C/Fe]-[Fe/H] distribution for GES by drawing 2,353 values from the observed distribution, with replacement (where 2,353 is the size of the GES sample).

iv) For each one of the 1,000 bootstrapped realisations of a chemical composition plane of a halo substructure, I determine the [X/Fe] value at a given metallicity ($[\mathrm{Fe/H}]_{\mathrm{comp}}$) that is covered by both halo substructures being compared by taking a 0.05 dex slice in [Fe/H] around $[\mathrm{Fe/H}]_{\mathrm{comp}}$ and determining the median value for stars in that [Fe/H] interval. This yields 1,000 [X/Fe] median values for each of the thirteen elements studied for every halo substructure (and disc sample) compared.

v) I take the mean and standard deviation of the medians distribution for every [X/Fe] as the representative [X/Fe] and uncertainty value, respectively, and use these to quantitatively compare the chemical abundances between two populations. This sample median from the mean of the bootstrap medians is always close to the full sample median itself.

vi) Upon obtaining the mean and uncertainty chemical abundance values for every halo substructure at $[\mathrm{Fe/H}]_{\mathrm{comp}}$ (for a range of thirteen reliable elemental abundances in APOGEE), I quantitatively compare the chemical compositions across halo substructures adopting a χ^2 statistic to assess the chemical similarities between different substructures. This quantity was computed by using the following relation:

$$\chi^2 = \sum_i \frac{\left([\mathrm{X/Fe}]_{i,\mathrm{sub}} - [\mathrm{X/Fe}]_{i,\mathrm{ref}}\right)^2}{\left(\sigma^2_{[\mathrm{X/Fe}]_{i,\mathrm{sub}}} + \sigma^2_{[\mathrm{X/Fe}]_{i,\mathrm{ref}}}\right)}, \tag{3.1}$$

where $[\mathrm{X/Fe}]_{\mathrm{sub}}$ and $[\mathrm{X/Fe}]_{\mathrm{ref}}$ are the abundances of the halo substructure and the compared reference stellar population, respectively, and $\sigma_{[\mathrm{X/Fe}],\mathrm{sub}}$ and $\sigma_{[\mathrm{X/Fe}],\mathrm{ref}}$ are the corresponding uncertainties to those abundance values. Since GES is the halo substructure for which the sample is the largest, I use this substructure as the main reference against which all other substructures, as well as *in situ* disc populations are contrasted.

vii) Lastly, in order to infer if two stellar populations present consistent chemical abundances in a statistical manner, I determine the probability value of the χ^2 result for twelve degrees of freedom using the `scipy` (Virtanen et al., 2020) `stats.chi2.cdf` routine. In addition to the χ^2 value, I also compute a metric of separation (defined as $\Sigma_{[X/Fe]}$), that is calculated by setting the denominator of Eq 3.1 equal to 1. This separation metric provides an additional way to quantify how similar the chemical compositions of two halo substructures are that is unaffected by the sample size (as smaller halo substructure samples will have larger uncertainties on their mean abundance values).

viii) For the case of Heracles and Aleph, as the selection of these substructures relies heavily on the use of [Al/Fe] and [Mg/Fe], respectively, I remove these elements when comparing these substructures, and reduce the numbers of degrees of freedom to eleven when calculating the χ^2 probability value.

In order to develop a more clear notion of the meaning of the resulting χ^2 values resulting from the above comparisons I perform an additional exercise aimed at gauging the expected χ^2 values for the cases where two samples are identical to each other, or very different. To accomplish this, I draw, for each substructure, three $N_{\rm sub}$-sized random samples, two from the high-α and one from the low-α disc samples, where $N_{\rm sub}$ is the size of the sample of that substructure. I then calculate, for each substructure, two χ^2 values, one resulting from the comparison of the high-α disc against itself, and the other from the comparison of the high-α disc against the low-α disc samples. As the high- and low-α disc both cover a similar range in [Fe/H], and their abundances vary with [Fe/H], I select a narrow bin in [Fe/H] from which to draw the high- and low-α disc samples (namely, between $-0.45 <$ [Fe/H] < -0.35). This enables us to obtain random samples of high- and low-α disc populations at the same [Fe/H], and allows us to directly compare the mean and scatter values of the chemical abundances using the χ^2 method.

The reader may inspect the resulting χ^2 and probability (p_{χ^2}) values obtained in Table 3.2. Here, a $p_{\chi^2} \sim 1$ signifies that two populations are statistically equal, and $p_{\chi^2} \sim 0$ means that they are statistically different. For the quantitative comparisons, I employ a threshold of $p_{\chi^2} = 0.1$ as the benchmark, where I will deem two substructures to be statistically similar if their associated probability value is higher than $p_{\chi^2} > 0.1$, and different if below $p_{\chi^2} < 0.1$.

The resulting quantitative comparison between the halo substructures indicates that approximately half of the halo substructures are statistically equal with regards to their chemical abundances, whilst the other half are statistically different. For example, the χ^2 comparison between the GES and the three Sequoia samples imply that these four substructures are statistically the same, as I find that the *GC*, *field*, and *H3* Sequoia

samples all have a high probability of being statistically similar to the GES substructure ($0.26 < p_{\chi^2} < 0.85$). I find this also to be the case for the LMS-1 substructure, for which I obtain a probability value of 0.5. Similarly, an ever closer match is found for the GES-Arjuna comparison, yielding a probability value of 0.91. Along similar lines, I find that when comparing the Nyx to the high-α disc, I obtain a probability value of 0.79, reinforcing the initial hypothesis that the Nyx is not an accreted substructure, but instead is a stellar population constituted of high-α disc stars. Moreover, I find that when comparing Heracles, Sgr dSph, and Thamnos with the GES that the probability of these substructures being statistically equal is $\sim$0. This result is not entirely surprising, as all these substructures are postulated to be debris from separate accretion events, and thus should present differences in their chemical abundances. Interestingly, I find two surprising results: i) despite the Aleph substructure presenting qualitatively the same chemistry as the low-α disc, its χ^2 value yields a probability of 0.07, suggesting that these are not as similar as initially hypothesised; ii) although Heracles occupies a position in several chemical composition planes that appears to follow a single sequence with the high-α disc, the χ^2 yielded when comparing this substructure to the high-α disc indicate that these are statistically different (with a probability value of p_{χ^2}=0).

For the complete resulting probability values obtained when comparing the chemistry between every halo substructure, as well as the high- and low-α disc, I refer the reader to Fig 3.18.

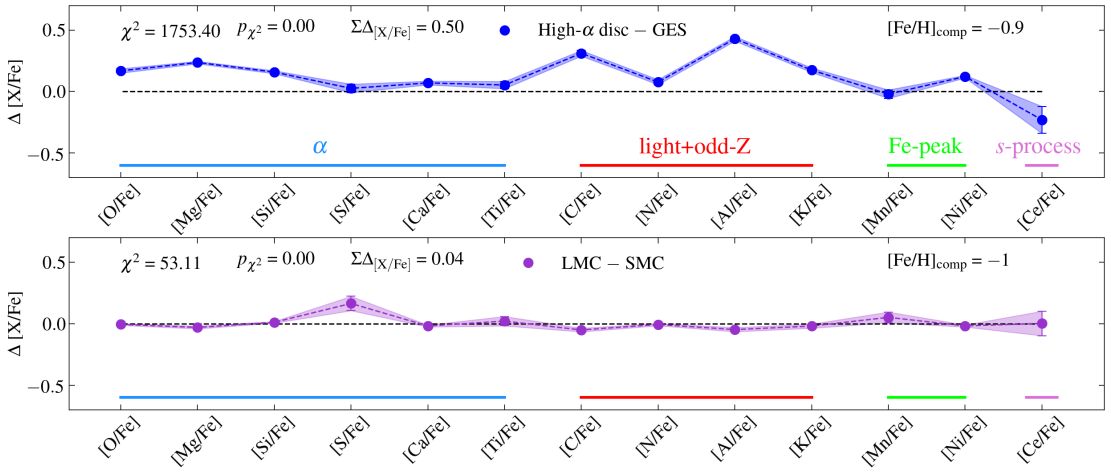

FIGURE 3.14: Δ[X/Fe] differences between the resulting mean values obtained using the procedure outlined in Section 3.5 (at $[\mathrm{Fe/H}]_{\mathrm{comp}}$) for the *Gaia*-Enceladus/Sausage substructure and the high-α disc stars (top) and for the Large and Small Magellanic Cloud (LMC/SMC) samples from Hasselquist et al. (2021) (bottom) in thirteen different chemical abundance planes, grouped by their nucleosynthetic source channel. The shaded regions illustrate the uncertainty on this Δ[X/Fe] value. Also illustrated in the top right/left are the $\chi^2/p_{\chi^2}/[\mathrm{Fe/H}]_{\mathrm{comp}}$ values for the comparison between these two populations. As can be seen from the abundance values, the χ^2 value, and the p_{χ^2} value, it is evident that the GES/high-α disc and the LMC/SMC are quantitatively different given their chemical compositions.

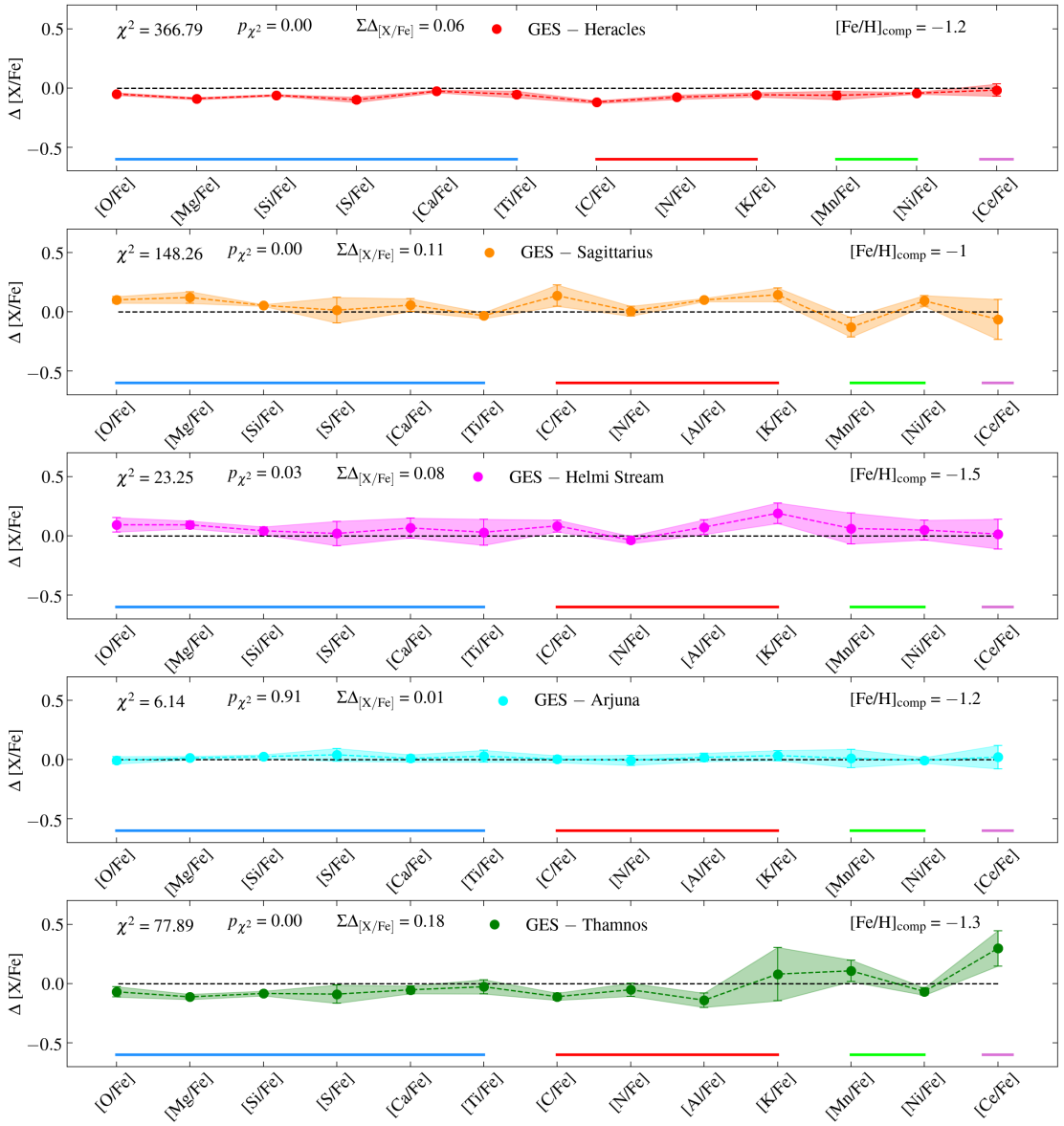

FIGURE 3.15: The same mean and mean error abundance values as shown in Fig 3.14 but comparing the Heracles, Sagittarius dSph, Helmi stream, Arjuna, and Thamnos substructures with the *Gaia*-Enceladus/Sausage substructure. I note that those substructures with fewer stars present larger uncertainties in their Δ[X/Fe] value

.

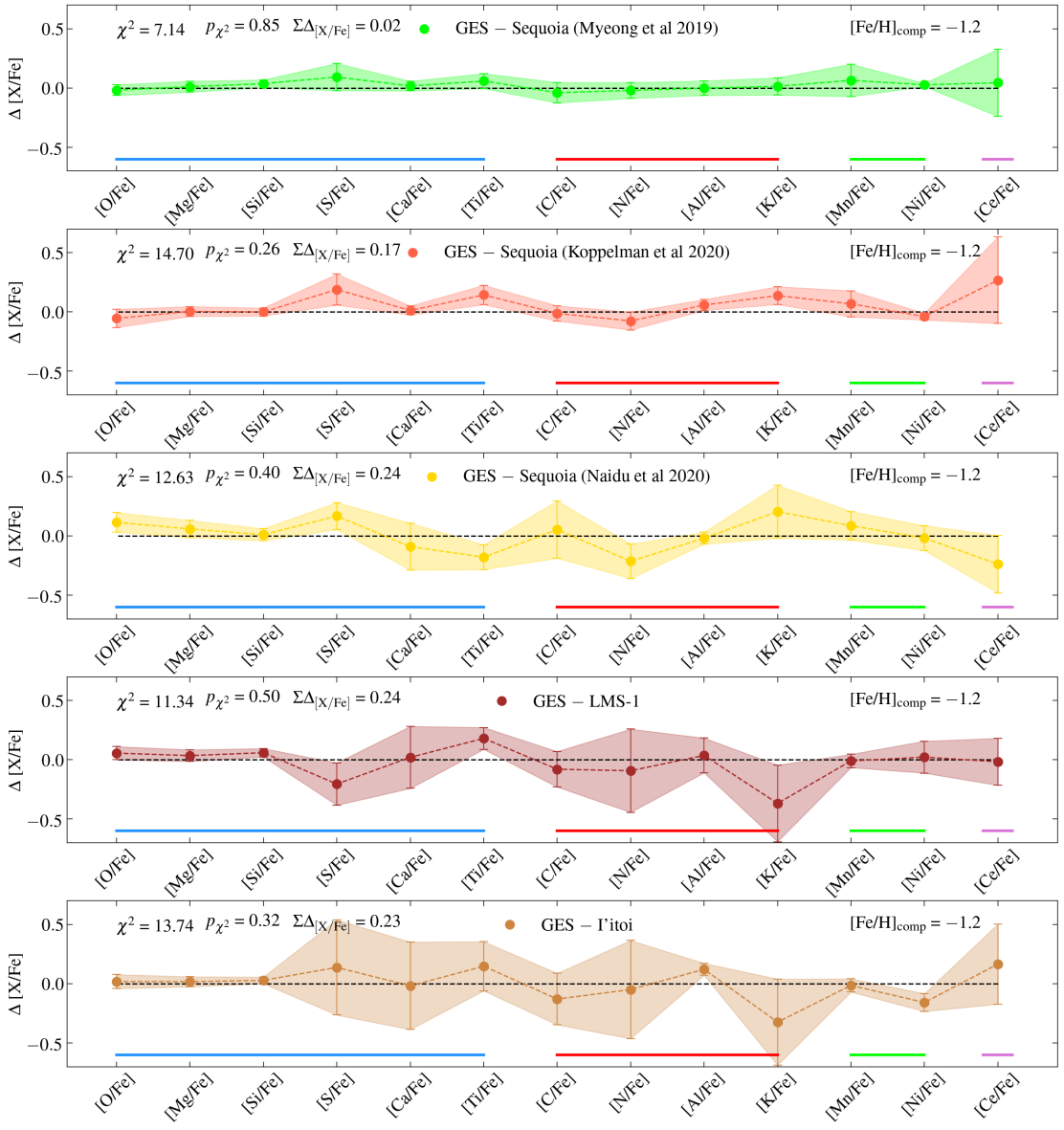

FIGURE 3.16: The same as Fig 3.15 but comparing the three Sequoia samples, LMS-1, and I'itoi substructures with the *Gaia*-Enceladus/Sausage substructure.

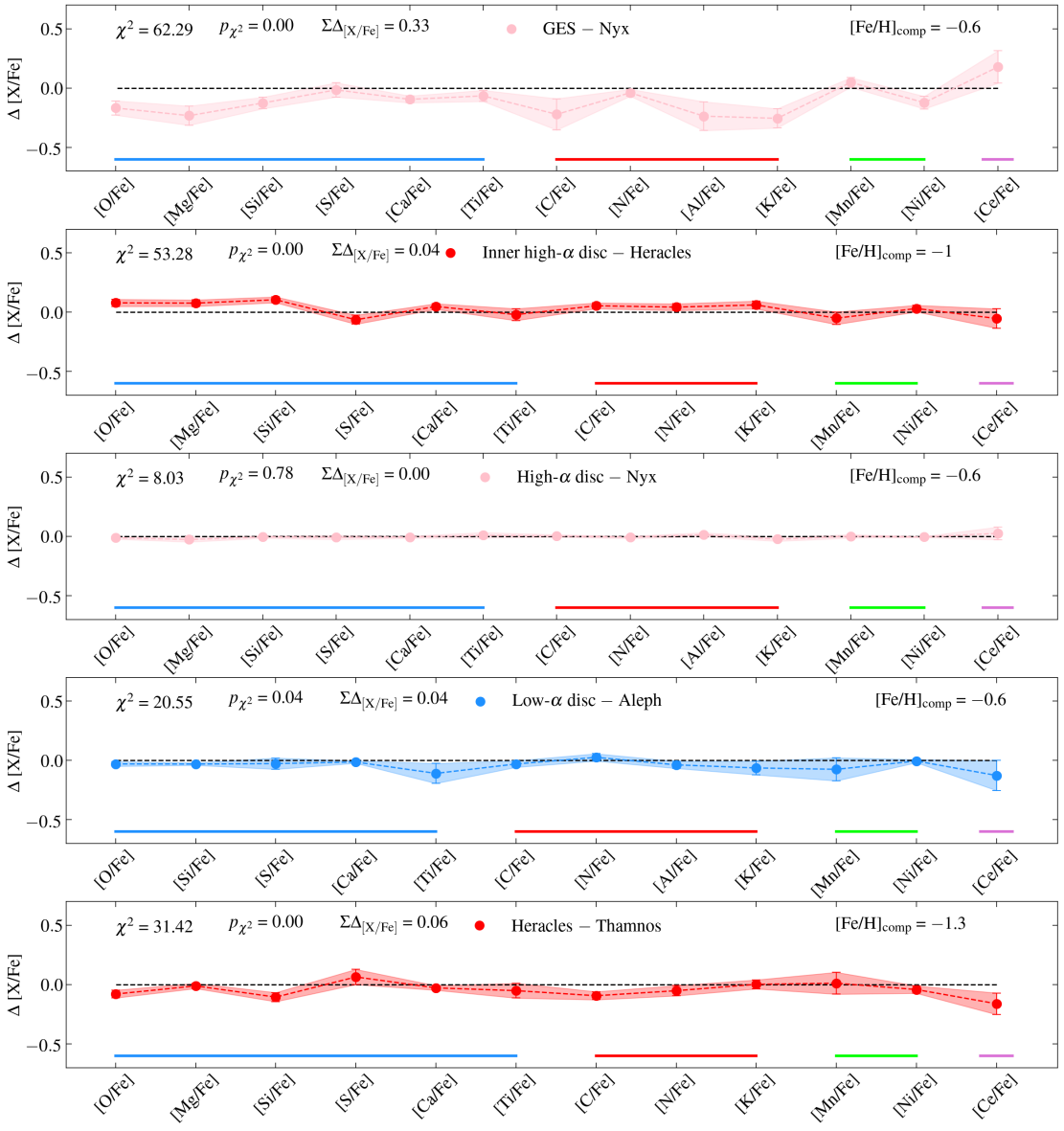

FIGURE 3.17: The same as Fig 3.14 but comparing the Nyx substructures with the *Gaia*-Enceladus/Sausage substructure and the high-α discs, as well as a comparison between the Heracles and inner high-α disc, Heracles and Thamnos, and Aleph and the low-α disc.

Compared samples	$[Fe/H]_{comp}$	χ^2	p_{χ^2}	$\Sigma\Delta_{[X/Fe]}$	highα-highα χ^2	highα-lowα χ^2
Highα disc-GES	–0.9	1753.4	0.00	0.50	9.78	4622.96
LMC-SMC	–1.1	53.9	0.00	0.04	10.05	1517.67
GES-Heracles	–1.3	366.8	0.00	0.06	10.74	507.43
GES-Sgr dSph	–1.0	148.3	0.00	0.11	8.55	542.27
GES-Helmi stream	–1.2	23.2	0.03	0.08	6.61	153.93
GES-Sequoia (*GC*)	–1.2	7.1	0.85	0.02	3.40	207.94
GES-Sequoia (*field*)	–1.3	14.7	0.26	0.16	4.04	210.68
GES-Sequoia (*H3*)	–1.9	12.6	0.4	0.24	3.42	229.83
GES-Thamnos	–1.4	77.9	0.00	0.18	8.82	162.81
GES-LMS-1	–2.1	11.3	0.5	0.23	6.27	371.65
GES-Arjuna	–1.3	6.1	0.91	<0.01	5.48	230.82
GES-I'itoi	–2.1	13.7	0.32	0.23	6.75	123.99
GES-Nyx	–0.6	62.3	0.00	0.33	6.45	1246.71
highα disc-Nyx	–0.6	8.0	0.78	<0.01	6.45	1246.71
lowα disc-Aleph	–0.6	20.5	0.04	0.04	8.82	195.69
Inner high-α disc-Heracles	–1	53.3	0.00	0.04	10.74	507.43
Heracles-Thamnos	–1.3	31.4	0.0	0.06	8.82	162.81

TABLE 3.2: From left to right: compared halo substructures, [Fe/H] value used to compare the two compared substructures, resulting χ^2 value from the comparison between the listed halo substructures, the probability value the χ^2 result falls upon for a χ^2 test with twelve (or eleven for the case of Heracles and Aleph) degrees of freedom, the metric separation $\Sigma\Delta_{[X/Fe]}$, χ^2 value between two randomly chosen high-α disc samples of the same size as the smallest substructure compared, χ^2 value between a randomly chosen high-α and low-α disc sample of the same size as the smallest substructure compared. The LMC/SMC samples were taken from Hasselquist et al. (2021).

3.6 Discussion

3.6.1 Summary of substructure in the stellar halo

Having qualitatively and quantitatively compared the chemical abundances of all the halo substructures under study, in this Section I discuss the results obtained for each identified substructure in the context of previous work.

3.6.1.1 Heracles

Stars from this substructure follow low energy, often eccentric orbits with low L_z, being largely phase-mixed in velocity and action space. All these features are to be expected in the scenario where Heracles was a massive system that merged early in the history of the Milky Way. Under this hypothesis, dynamical friction would have driven the system quickly into low energy orbits, sinking it into the heart of the Galaxy (Horta et al., 2021a; Pfeffer et al., 2021)

The chemical compositions of the stars associated with Heracles are in broad agreement with this scenario. The distribution of Heracles in the α-Fe plane does not display the α-Fe knee or shin components of chemically evolved systems (McWilliam, 1997), which suggests that its star formation ceased before the contribution of supernovae type Ia became substantial (Horta et al., 2021a). In Horta et al. (2021a) I checked that this result was not an effect of the chemical composition criteria adopted in the selection of Heracles stars by comparing them with a similarly selected GES sample, which did display a clear α-Fe knee signature. Furthermore, Heracles occupies a locus in different chemical planes that resembles that of low mass galaxies of the Milky Way and/or accreted populations. In particular Horta et al. (2021a) show that the stars associated with Heracles make up a clump in the [Mg/Mn]-[Al/Fe] plane in the region occupied by accreted and/or chemically unevolved populations, characterised by low [Al/Fe] and high [Mg/Mn].

Recent work by Lane et al. (2021) suggests that the concentration associated with Heracles in E-L_z space could be an artifact of the APOGEE selection function, so the authors caution that the reality of this halo substructure should be further tested. As discussed extensively in Horta et al. (2021a), phase mixing makes it especially hard to discriminate accreted systems from their *in situ* counterparts co-located in the inner few kpc of Milky Way on the sole basis of kinematics. Nonetheless, theoretical predictions predict their existence (e.g. Fragkoudi et al., 2020; Kruijssen et al., 2020; Pfeffer et al., 2021, Horta et al., 2022, in prep.). Detailed chemistry is thus crucial to tease out the remnants of

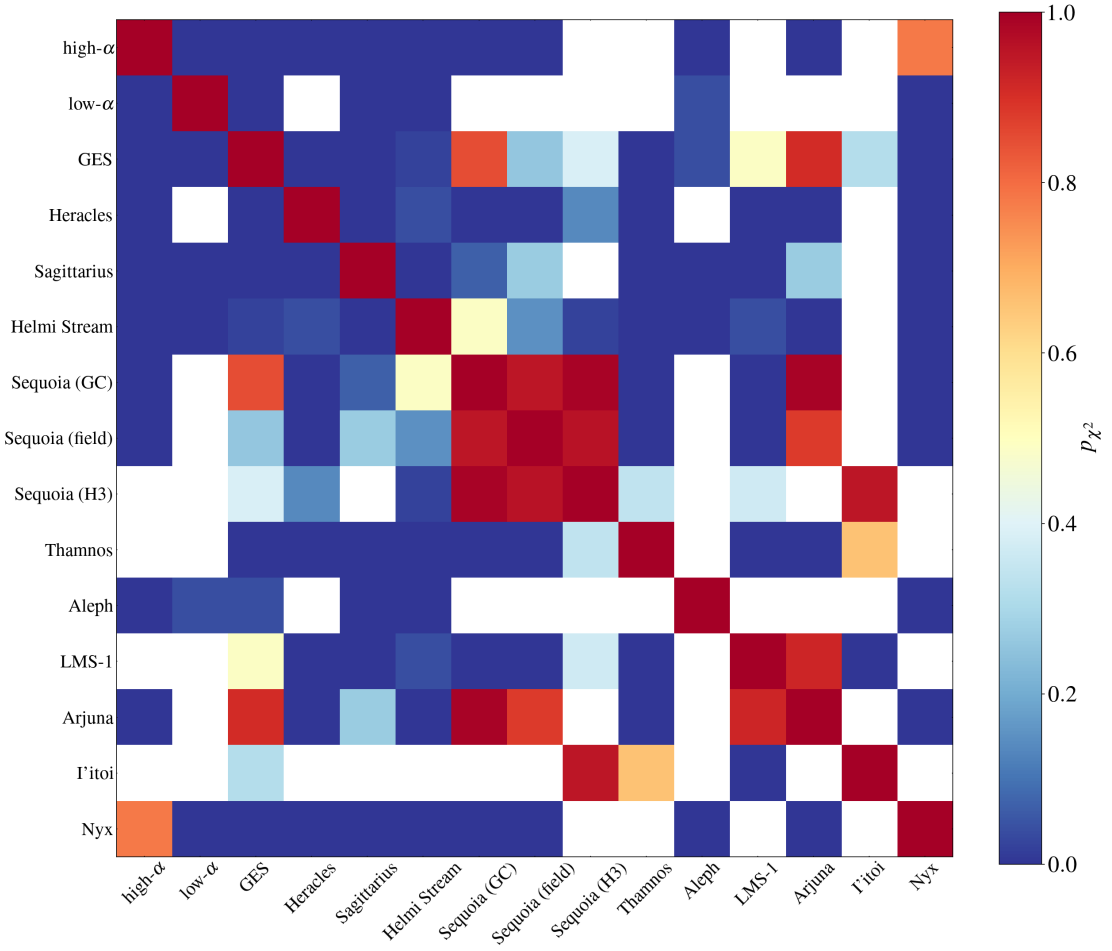

FIGURE 3.18: Confusion matrix of the probability values (estimated using the χ^2 calculated using Eq 3.1) obtained when comparing the chemical compositions of all the halo substructures with each other and with a high-/low-α discs. Here, each substructure is compared with its counterpart using a [Fe/H] value that is well covered by the data (see Fig B.15 in Appendix B.8 for further details), where red(blue) signifies a high(low) probability of two systems being statistically equal given their chemical compositions. Comparisons with blank values are due to the two substructures being compared not having any overlap in [Fe/H].

accreted systems from the maze of *in situ* populations overlapping in the inner few kpc of the Galaxy.

For that reason, I examine closely the comparison between the abundance patterns of Heracles data and the inner high-α disc at the same [Fe/H] (Fig. 3.17). the χ^2 analysis shows that the two populations differ chemically with high statistical significance ($\chi^2 = 53.3$, p_{χ^2}=0, similar to the value obtained when comparing the LMC to the SMC, see Table 3.2). To check whether this result is sensitive to the choice of $[Fe/H]_{comp}$, I reran the analysis adopting $[Fe/H]_{comp}$=–0.9 and $[Fe/H]_{comp}$=–0.95 obtaining χ^2 value of 36.45 and 44.82, respectively, which corresponds to a probability value of p_{χ^2}=0 in both cases.

Examining more closely the contrast between the abundance patterns of Heracles and the inner high-α disc I find that they differ in interesting ways. By far the elements displaying the largest differences are oxygen, magnesium, and silicon, whose abundances are lower in Heracles than in the inner high-α disc. At face value, this difference implies less SNII enrichment in Heracles than in the inner high-α disc, possibly reflecting a lower star formation rate. A similar, but smaller, difference is seen in carbon, nitrogen, and potassium. Interestingly (as in the case of GES, see Section 3.6.1.2), I find [Ce/Fe]$\sim$0, suggesting a small contribution to chemical enrichment from the *s*-process nucleosynthesis channel.

I point out that it is possible that the chemical properties ascribed to Heracles may be to some extent influenced by the selection method, which is partly based on chemistry. That selection, however, is far from arbitrary. It is rather informed by the fact that the distribution of inner Galaxy stellar populations form a clear clump in the accreted/-chemically unevolved region of the [Mg/Mn]-[Al/Fe] plane (see Figure 1 of Horta et al., 2021a). Our χ^2 analysis shows that Heracles presents an almost unique abundance pattern, differing in a (sometimes small, yet) statistically significant way from most stellar populations under study. For instance, I find that the abundance patterns of Heracles and GES are different (i.e., $p_{\chi^2} = 0$). This is also the case when comparing Heracles to the Sequoia (all three samples), Arjuna, Thamnos, and Nyx. This result reinforces the hypothesis from Horta et al. (2021a) that Heracles is likely the remnant of a separate early/massive accretion event.

I conclude by stating that the data are consistent with Heracles being the remnant of a satellite that merged with the Milky Way in its early history. Further studies based on an expanded set of elemental abundances for a larger sample, as well as detailed modelling, based both on cosmological numerical simulations and standard chemical evolution prescriptions, are required to definitively establish the origin of Heracles.

3.6.1.2 *Gaia*-Enceladus/Sausage

Since its discovery (Belokurov et al., 2018; Helmi et al., 2018), the *Gaia*-Enceladus/Sausage (GES) substructure has been extensively studied, both from an orbital and chemical compositions perspective (e.g., Hayes et al., 2018; Mackereth et al., 2019b; Koppelman et al., 2019a; Vincenzo et al., 2019; Aguado et al., 2020; Feuillet et al., 2020; Simpson et al., 2020; An & Beers, 2021; Horta et al., 2021a; Hasselquist et al., 2021; Buder et al., 2022; Carrillo et al., 2022). In this work, I have identified a large sample of GES stars, and have shown that stars belonging to this population are characterized

by intermediate-to-high orbital energies and high eccentricity, displaying no significant systemic disc-like rotation.

The chemical compositions of the GES substructure are characterised by lower [α/Fe] at [Fe/H] -1.6, than high-α disc for most α elements (namely Mg, O, Si, Ca, S), in agreement with previous work (e.g., Hayes et al., 2018; Haywood et al., 2018; Helmi et al., 2018; Mackereth et al., 2019b; Horta et al., 2021a; Buder et al., 2022), and displays an α-knee at [Fe/H]~-1.1 (see Fig 3.19). The stellar populations of GES are also characterised by lower Al, C, and Ni than *in situ* populations, resembling the abundance patterns of stars from satellites of the Milky Way (Horta et al., 2021a; Hasselquist et al., 2021). They also occupy the accreted/unevolved region of the [Mg/Mn]-[Al/Fe] plane. In summary, the chemical compositions of GES confirm the results from previous studies, and reinforce the idea that this halo substructure is the remnant of an accreted satellite whose debris dominate the local/inner regions of the stellar halo.

3.6.1.3 Sequoia

The Sequoia substructure was initially discovered due to the highly unbound and retrograde orbits of its constituent stars and associated globular clusters (e.g., Barbá et al., 2019; Matsuno et al., 2019; Myeong et al., 2019), which made it easily distinguishable from *in situ* populations. Since its discovery, several groups have sought to identify it using different surveys. It has also been examined by Koppelman et al. (2020) on the basis of N-body simulations by Villalobos & Helmi (2008), suggesting that, rather than a separate system, Sequoia may constitute a fringe population of stars in low eccentricity retrograde orbits left over after the GES merger. In this work, I have selected the Sequoia substructure by employing three independent definitions, derived from the Myeong et al. (2019), Koppelman et al. (2019c), and Naidu et al. (2020) works, respectively.

When inspecting the chemical distribution of these three independent Sequoia samples in multiple chemical composition planes, I have found that the Sequoia samples defined by Myeong et al. (2019), Koppelman et al. (2019c), and Naidu et al. (2020) occupy a similar locus in all chemical composition planes, that resembles that of low mass satelite galaxies of the MW and/or accreted populations, displaying low Mg, Al, C, and Ni, that overlap with the GES substructure. Furthermore, when running a quantitative χ^2 comparison between the three Sequoia samples, I find that their chemical compositions are indistinguishable from each other, yielding a high probability value of p_{χ^2}=0.94 for the comparison between the Koppelman et al. (2020) samples and Naidu et al. (2020) samples, p_{χ^2}=0.95 between the Koppelman et al. (2020) and Myeong et al. (2019) samples, and p_{χ^2}=0.99 for that between the Myeong et al. (2019) and Naidu et al. (2020)

samples. Therefore I conclude, reassuringly, that the chemical composition I obtain for the Sequoia system does not depend on the selection criterion adopted.

As in the case of the systems discussed above, Sequoia occupies the accreted/unevolved region of the [Mg/Mn]-[Al/Fe] plane, which is encouraging given that two of those samples were selected purely on the basis of orbital parameters. Interestingly, I note that the Naidu et al. (2020) sample appears to be simply the metal-poor tail of the Myeong et al. (2019) and Koppelman et al. (2019c) samples.

A quantitative comparison of these Sequoia samples with GES shows that all four populations have consistent and similar chemistry. More specifically, I find that the Myeong et al. (2019), Koppelman et al. (2019c), and Naidu et al. (2020) Sequoia samples yield a probability value of p_{χ^2}=0.85, p_{χ^2}=0.26, and p_{χ^2}=0.4, respectively. At face value, this chemical similarity corroborates the hypothesis raised by Koppelman et al. (2020), that stars with low eccentricity and retrograde orbits with relatively high energies could have resulted from the GES merger.

The hypothesis advanced by Koppelman et al. (2020) embodies a falsifiable prediction of a metallicity difference between the two systems. Such a difference would be expected had Sequoia been originally associated with the stellar populations located in the outskirts of GES. They argue that, for a GES system of $M_\star \sim 10^{9.6}$M$_\odot$, the metallicity gradient expected between the outer regions stripped first (i.e., Sequoia) and the main body (i.e., GES) would be of the order of ∼0.3 dex. I exclude from that test the sample selected by Naidu et al. (2020), since it adopts a metallicity cut which would bias the results. The mean metallicities inferred when adopting either the Myeong et al. (2019) or the Koppelman et al. (2019c) Sequoia samples are $\langle$[Fe/H]$\rangle = -1.41$ and –1.31, respectively. In contrast, I obtain $\langle$[Fe/H]$\rangle = -1.19$ for the GES sample, suggesting a difference of ∼0.1-0.2 dex, which is roughly consistent with the prediction by Koppelman et al. (2020). It is interesting, however, that no difference in abundance pattern exists between Sequoia and GES at fixed [Fe/H], which under Koppelman et al. (2020)'s hypothesis would suggest the absence of abundance ratio gradients in the GES progenitor. At face value, this result is at odds with the observations of existing satellites of the Milky Way. For instance, an [α/Fe] gradient is known to be present in the Sgr dSph (e.g., Hayes et al., 2020; Hasselquist et al., 2021). The latter difference may however be explained away as resulting from the occurrence of recent episodes of star formation in the Sgr dSph, which would have a strong impact on [α/Fe] of the younger populations (e.g., Hasselquist et al., 2021). It is thus conceivable that the absence of a detectable [α/Fe] difference between Sequoia and GES results from an early quenching of star formation.

the samples for GES and Sequoia cover in a statistically meaningful way a wide range of metallicities, so that they lend themselves nicely to a more detailed comparison of

the distributions of those two systems in the α-Fe plane. A crucial diagnostic is the metallicity of the "α-knee", $[Fe/H]_{knee}$ (Section 3.4.1), which is strongly sensitive to the details of the star formation history of the system. In recent studies, Matsuno et al. (2019), Monty et al. (2020), and Aguado et al. (2020) suggest that Sequoia is characterised by a substantially lower $[Fe/H]_{knee}$ than GES. To test that hypothesis, I perform a piece-wise linear fit to the GES and Sequoia samples in order to accurately determine the position of the $[Fe/H]_{knee}$ in those two systems, in a manner similar to the approach followed by Mackereth et al. (2019b).

The resulting fits (solid lines) and 1-σ dispersions (shaded regions) are displayed along with respective samples for GES (blue), Sequoia (green and red for the Myeong et al., 2019; Koppelman et al., 2019c, samples, respectively) in Figure 3.19. The piece-wise function was determined using the `PiecewiseLinFit` function included as part of the `pwlf` package (Jekel & Venter, 2019). Due to its low metallicity upper limit, the Sequoia sample from Naidu et al. (2020) is excluded from the comparison. The $[Fe/H]_{knee}$ values for GES and the two Sequoia samples are within $\sim$0.1 dex from each other. The largest difference in fact is that between the Myeong et al. (2019) and Koppelman et al. (2019c), with the latter resulting in a larger $[Fe/H]_{knee}$. This result suggests the absence of significant differences in the star formation histories of the two systems, despite the slightly different mean metallicities discussed above. Since the $[Fe/H]_{knee}$ parameter is considerably less sensitive to uncertainties due to selection effects, I conclude that the precursors of GES and Sequoia underwent similar star formation histories, which supports the hypothesis that they were once different components of the same system.

In a recent paper, Naidu et al. (2021) propose that Sequoia, rather than constituting the outskirts of GES, was instead one of its satellites. That notion is predicated on their estimated ratio between the masses of the two systems (roughly 1/10) and their chemical composition differences. Naidu et al. (2021) call particular attention to the large metallicity gradient implied by an association between Sequoia and GES, referring as well to the difference in $[Fe/H]_{knee}$ from the literature. the results call into question the existence of an important difference in $[Fe/H]_{knee}$ and mean metallicity, thus possibly accommodating comfortably the possibility of an association between the two systems.

Along those lines, in a recent work Matsuno et al. (2021) determined the abundances of 12 Sequoia stars on the basis of high-resolution spectra obtained with the Subaru High Dispersion Spectrograph. Their Sequoia sample was selected following the criteria by Koppelman et al. (2019c). Matsuno et al. (2021) compared their chemical compositions to those of GES members selected from Nissen & Schuster (2010) and Reggiani et al. (2017). The authors found that the abundances of Na, Mg, and Ca differed from GES for 8 out of the 10 stars in the cleaned Sequoia sample, at the 2σ level, which is at odds

with the findings presented in this work. Thus, I decided to double-check the results by running Matsuno et al. (2021)'s methodology on the data. I fit a quadratic polynomial to the GES data and estimated the residuals of the Sequoia sample stars relative to the polynomial value at their measured [Fe/H]. Because APOGEE does not yield reliable sodium abundances at low metallicities, I replaced that element by aluminium to run this test, as it is the APOGEE element sharing a nucleosynthetic source that is closest to that of Na. Out of the 45 Sequoia stars (selected as in Myeong et al. (2019)) that fall within the $-1.8 <$ [Fe/H] < -1.4 metallicity range adopted by Matsuno et al. (2021), I find that 42/40/43 stars fall *within* 2σ of the quadratic polynomial fit to the GES sample when examining the Mg/Al/Ca abundance planes. When the Koppelman et al. (2019c) Sequoia sample is considered, I find that 22/22/23 out of the total 26 stars match the abundances of Mg/Al/Ca. In conclusion, when replicating the procedure performed by Matsuno et al. (2021) on the basis of APOGEE data, I find that the majority of the sample (>90%) falls within 2σ of the [X/Fe]-[Fe/H] quadratic polynomial fit to the GES sample. This test confirms the finding that Sequoia and GES are very similar in the chemical space sampled by APOGEE. The reason for the discrepancy between the results and those by Matsuno et al. (2021) is unclear.

In summary, the chemical composition data are possibly consistent with a common origin between Sequoia and GES, although further data and modeling are required to fully clarify the matter.

3.6.1.4 Helmi stream

The Helmi stream is a halo substructure that appears to jut out of the Galactic disc. It is characterised by stars on highly perpendicular (i.e., high $L_\perp$ and v_z) and prograde orbits (Helmi et al., 1999; Koppelman et al., 2019b), which appear to form a pillar at high orbital energies in the prograde wing of the E-L_z plane (see Fig 3.4). Despite this substructure being discovered decades ago, its chemical compositions have not been studied in great detail, largely due to the difficulty of obtaining a high confidence sample with reliable chemical composition information.

Our results on the chemical compositions of the Helmi stream imply that, unsurprisingly, this substructure presents chemistry that is typical of accreted populations and/or dwarf satellites (i.e., low Mg, Al, C, and Ni). I also find that, despite it being selected purely on a kinematic and position basis, it occupies the accreted/unevolved region of the [Mg/Mn]-[Al/Fe] which, combined with its orbital properties, confirms its accreted nature. Furthermore, I find that, when comparing this halo substructure with the others studied in this work, the Helmi stream differs statistically from all other halo

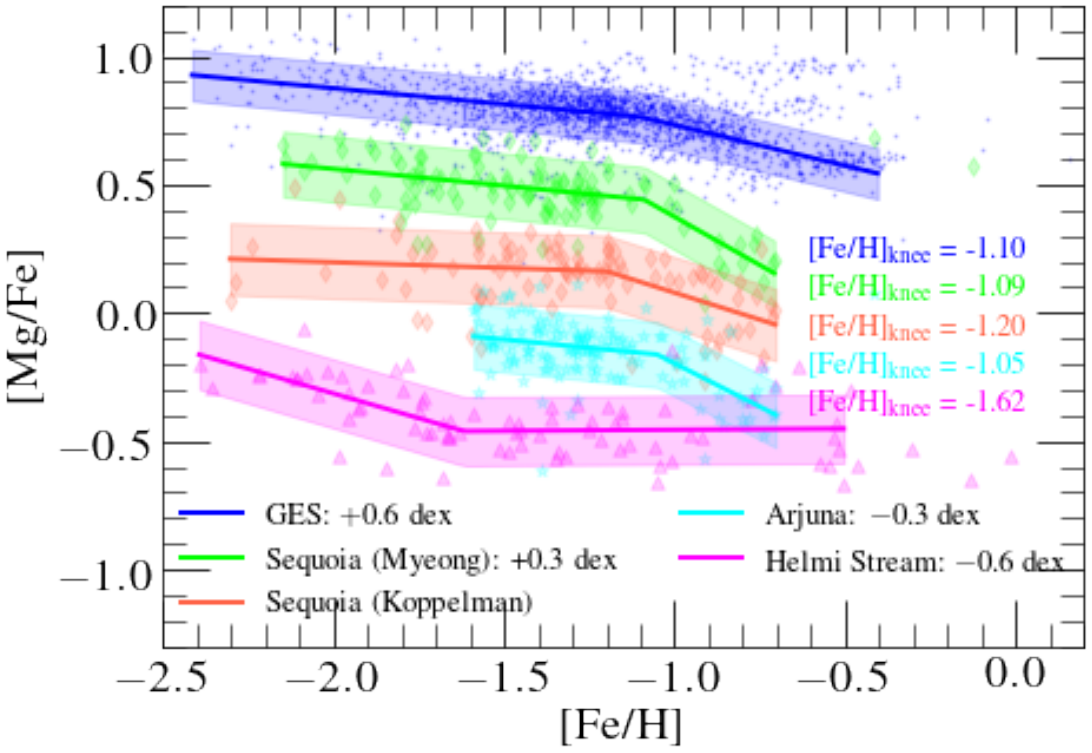

FIGURE 3.19: Piece-wise polynomial fit (solid line) and 1-σ dispersion (shaded region) for GES, Sequoia, Arjuna, and Helmi stream samples. Data and fits are displaced vertically for clarity. The resulting $[Fe/H]_{knee}$ values are shown. The [Mg/Fe]-[Fe/H] knee of GES and Sequoia are within 0.1 dex from each other, with the largest difference being found between the two Sequoia samples. By the same token, $[Fe/H]_{knee}$ for Arjuna differs from that GES by only 0.05 dex. The star formation efficiencies of these systems, as indicated by $[Fe/H]_{knee}$, seem not to have been substantially different. Conversely, for the Helmi stream I find an "inverted" knee, that occurs at $[Fe/H]_{knee}\sim$–1.7, suggestive of a very different star formation history when compared to GES, Sequoia, and Arjuna.

substructures. In Figure 3.19 I display the data for the Helmi stream alongside a piece-wise polynomial fit performed in the same way as described for GES and the Sequoia samples. Interestingly, the best fit for the Helmi stream indicate the occurrence of an "inverted knee", whereby the slope of the relation between [Mg/Fe]-[Fe/H] becomes less negative. As discussed above for the case of the Sgr dSph, this is the signature of a burst of star formation. This is a very interesting result, which merits further investigation on the basis of a larger sample.

3.6.1.5 Arjuna

The existence of this substructure was proposed by Naidu et al. (2020) as part of the H3 survey (Conroy et al., 2019). Naidu et al. (2020) show that the MDF of the retrograde component of the halo displays three peaks, which they ascribe to Arjuna (the most metal-rich), Sequoia, and I'itoi (the most metal-poor, see Fig 3.3). Naidu et al. (2021)

argue that Arjuna corresponds to the outer parts of the GES progenitor, which, according to their fiducial numerical simulation was stripped early in the accretion process, thus preserving the highly retrograde nature of the GES approaching orbit. In additional support to that proposition, Naidu et al. (2021) point out that the peak [Fe/H] and mean [α/Fe] of Arjuna are in excellent agreement with those of GES, which in turn should be consistent with a much lower metallicity gradient in the GES progenitor than suggested by Koppelman et al. (2020).

The detailed quantitative comparison of the chemical compositions of Arjuna and GES (Figure 3.15) shows that the similarity of these two systems indeed encompasses a broader range of elemental abundances, leading to a $p_{\chi^2} = 0.91$. In addition, the distributions of Arjuna and GES stars in the α-Fe plane are also very similar, with the two values for $[\mathrm{Fe/H}]_{\mathrm{knee}}$ agreeing within 0.05 dex (see Fig 3.19).

Therefore, the results are at face value in agreement with the suggestion by Naidu et al. (2021) that the stars associated with the Arjuna substructure were originally part of GES. That association predicts a very low metallicity gradient for GES at the time of the merger with the Milky Way. Further theoretical and observational work is required to ascertain the reality of that prediction (see discussion in, e.g., Horta et al., 2021a; Naidu et al., 2021).

3.6.1.6 I'itoi

Similarly to Arjuna, the I'itoi substructure is a high-energy retrograde substructure identified by Naidu et al. (2020). However, it is comprised by more metal-poor stars (see Fig 3.3) than its high-energy retrograde counterparts, Arjuna and Sequoia. Naidu et al. (2021) propose that I'itoi was in fact a satellite of GES, based on its low metallicity and high energy retrograde orbit. the detailed comparison of the chemistry of GES and I'itoi suggests that their abundance patterns are consistent with a $p_{\chi^2} = 0.32$ (Figure 3.16),. I point out, however, that this result is highly uncertain, given the relatively small size of the I'itoi sample and its low metallicity ($[\mathrm{Fe/H}]_{\mathrm{comp}} = -2.1$), which places its stars in a regime where ASPCAP abundances are relatively uncertain. The matter needs revisiting on the basis of more detailed chemical composition studies applied to a larger sample.

3.6.1.7 Thamnos

Initially conjectured by its discoverers to be the amalgamation of two smaller systems (Koppelman et al., 2019c), Thamnos is a substructure that occupies a locus in the

retrograde wing of the velocity and IoM planes. It is comprised of stars with intermediate orbital energy (i.e., E$\sim$–1.8$\times10^5$ km^2 s^{-2}) and fairly eccentric orbits ($e\sim$0.5), that occupies a position at the foot of GES in the Toomre diagram.

As in the case of most orbital substructures in this study, I find that the locus occupied by Thamnos in the Ni-Fe, C-Fe, and [Mg/Mn]-[Al/Fe] chemical planes resembles that of low-mass satellite galaxies and accreted populations of the Milky Way. However, Thamnos distinguishes itself from other substructures by showing a relatively high [α/Fe] ratio, although not as high as Heracles. In fact, Thamnos does not match the abundance pattern of any other substructure in this study.

3.6.1.8 Aleph

Aleph was identified in a study of the stellar halo based on the H3 survey (Naidu et al., 2020). In this work I identify Aleph members by selecting from the parent sample stars that satisfy the selection criteria outlined in Naidu et al. (2020). I have also searched for stars that are included in both the sample by Naidu et al. (2020) and in APOGEE DR17 (highlighted in the chemical abundance figures with purple edges). As described in their work, this substructure is comprised of stars on very strongly prograde orbits with low eccentricity, which appear to follow the same distribution as the Galactic disc component, although at higher J$_z$ values.

I find that the locus occupied by Aleph in various chemical planes is placed somewhere in between low- and high-α disc stars, while sitting squarely within the *in situ* region of the [Mg/Mn]-[Al/Fe] plane. This is also the case for the two stars contained in both the sample by Naidu et al. (2020) and in the APOGEE DR17 data. the quantitative comparison of the Aleph chemistry with that of the low-α disc suggests a statistically different, albeit on the borderline ($\chi^2 = 20.55$ and $p_{\chi^2} = 0.04$). This is in fact not surprising, seeing as the distribution of Aleph stars on the Mg-Fe plane straddles both the high and low-α discs (Figure 3.6). These results suggest that Aleph may be a stellar population comprised of a mix of warped/flared low-α disc, and high-α disc stars, which also explains its location within the locus of *in situ* stellar populations in the [Mg/Mn]-[Al/Fe] plane.

3.6.1.9 LMS-1

LMS-1 is a metal-poor substructure comprised of stars on mildly prograde orbits at intermediate/high orbital energies. Yuan et al. (2020) identified this substructure by applying a clustering algorithm to SDSS and LAMOST data in the E-L$_z$ plane. Although

it presents great overlap with the GES in IoM space, it is suggested to be an independent substructure based on the detection of a metallicity peak in the MDF of the stars included within the E-L_z box defining this system (Naidu et al., 2020). Yuan et al. (2020) also note that there are potentially several globular clusters with similar metallicity and orbital properties. In this work, I identified LMS-1 candidates adopting the same selection criteria as Naidu et al. (2020)'s, obtaining a relatively small sample of only 31 stars.

I examine the distribution of LMS-1 stars in various chemical planes, concluding that its chemistry is consistent with those of other accreted systems, with all its stars falling in the "accreted/unevolved" region of the [Mg/Mn]-[Al/Fe] plane. Furthermore, the ∼0.5 probability value obtained when comparing this halo substructure with GES suggests that *at face value* LMS-1 could be part of either of the omnipresent GES substructure. However, these comparisons are made at $[Fe/H]_{comp} = -2.1$, where the samples are small and ASPCAP abundances are relatively more uncertain and *in situ* and accreted structures tend to converge towards the same locus in the regions of chemical space sampled by APOGEE (e.g., Horta et al., 2021a). Moreover, given its location in IoM space, it is possible that the LMS-1 sample is importantly contaminated by GES stars.

As mentioned in Section 3.6.1.4, Jean-Baptiste et al. (2017a) show that a single accretion event can lead to multiple overdensities in orbital space (see also Koppelman et al., 2020). Due to the chemical similarity between LMS-1 and GES, and the close proximity between these two halo substructures in orbital planes (see Fig 3.4), an association between these two systems seems tempting. However, I defer a firmer conclusion to a future when more elemental abundances are obtained for a larger sample of both LMS-1 and GES candidates.

3.6.1.10 Nyx

The Nyx substructure is conjectured to be a stellar stream in the solar vicinity of the Milky Way (Necib et al., 2020). Given the chemical compositions obtained for this substructure in this work and its strong overlap with the high-α disc in all the chemical planes studied, I suggest that the Nyx is likely comprised by *in situ* high-α disc populations. the quantitative estimate of the similarity between Nyx and the stars from the high-α disc yields a very low χ^2 with associated likelihood probability of 0.78. I note that the stars in common between the sample and that of Necib et al. (2020) seem to boldly confirm this result. Along these lines, I note that the result is in agreement with a recent study focused on studying the chemical compositions of the Nyx substructure

(Zucker et al., 2021), who also conjecture Nyx to be comprised of Galactic (high-α) disc populations.

3.7 Conclusions

The unequivocal association with accretion events of halo substructures identified on the basis of orbital information alone is extremely difficult, as demonstrated by recent numerical simulations (e.g., Jean-Baptiste et al., 2017a; Koppelman et al., 2020; Naidu et al., 2021). Substructure in integrals of motion space can also be influenced or even artificially created by survey selection effects (Lane et al., 2021). Because the chemical compositions of halo substructures contain a fossilised record of the evolutionary histories of their parent galaxies, abundance pattern information can help linking substructure in orbital space to their progenitor systems.

In this work I have utilised a cross-matched catalogue of the latest APOGEE (DR17) and *Gaia* (EDR3) data releases in order to study the chemo-dynamic properties of substructures previously identified in the stellar halo of the Milky Way. I have successfully distinguished stars in the APOGEE DR17 catalogue that are likely associated with the following substructures: *Gaia*-Enceladus/Sausage, Sagittarius dSph, Heracles, Helmi stream, Sequoia, Thamnos, Aleph, LMS-1, Arjuna, I'itoi, Nyx, Icarus, and Pontus. Using the wealth of chemical composition information provided by APOGEE, I have examined the distributions of the stellar populations associated with these substructures in a range of abundance planes, probing different nucleosynthetic channels. I performed a quantitative comparison of the abundance patterns of all the substructures studied in order to evaluate their mutual associations, or lack thereof. Below I summarise the main conclusions:

- I show that the chemical compositions of the majority of the halo substructures so far identified in the Galactic stellar halo (namely, *Gaia*-Enceladus/Sausage, Heracles, Sagittarius dSph, Helmi stream, Sequoia, Thamnos, LMS-1, Arjuna, I'itoi) present chemical compositions which resemble those of low-mass satellites of the MW and/or accreted populations. There are however a couple of exceptions, namely Nyx and Aleph, that do not follow this pattern and instead present chemical properties similar to those of populations formed *in situ*. Furthermore, in Appendix B.1 I discuss the nature of Icarus, concluding that this substructure is likely comprised of stars formed *in situ*, for which the ASPCAP abundances are unreliable.

- The chemical properties of the inner-Galaxy Heracles substructure differ from those of its co-located low-metallicity high-α disc counterparts in a statistically significant way. Abundances of α elements oxygen, magnesium, and silicon are lower in Heracles than in its co-spatial high-α disc counterparts, suggesting that the ratio of SNII/SNIa enrichment in Heracles has been lower in that system than in the early disc. By the same token, Heracles is found to have higher [α/Fe] ratios than GES which, as suggested by Horta et al. (2021a), is an indication of an early truncation of star formation and the resulting absence of an α-knee in the former system. The abundance pattern of Heracles is indeed found to differ from all of the other substructures studied in this work. Further studies based on additional elemental abundances for larger samples, as well as detailed numerical modelling, are required to definitively ascertain the existence of this system and more thoroughly characterise its properties.

- I show that a large fraction of the substructures studied (namely, Sequoia, Arjuna, LMS-1, I'itoi) present chemistry indistinguishable from that of the omnipresent *Gaia*-Enceladus/Sausage. These findings bring into question the independence of these substructures, which are at least partially overlapping with GES in kinematic planes (see Fig 3.4). In view of these similarities, claims in the literature about the nature of Sequoia as being originally a higher angular momentum component located in the outskirts of GES (Koppelman et al., 2020), a satellite of GES (Naidu et al., 2021), or an altogether unrelated system (Myeong et al., 2019) may need to be reexamined. The possibility that Sequoia was a detached, but much less massive galaxy than GES is likely challenged by their chemical similarity. On the other hand, confirmation that it, or Arjuna, might be the remains of populations originally located in the outskirts of GES depends crucially on the magnitude of chemical composition gradients one should expect for dwarf galaxies at $z \approx 2$, and on whether that is a sufficiently discriminating criterion.

- I found that the halo hosts substructures which differ from GES in a statistically significant way. Three among those susbstructures display chemistry that is genuinely suggestive of an accreted nature, namely Heracles, Thamnos, and the Helmi stream (although for the latter this conclusion is not firm due to uncertainties in the chemistry and small sample size).

- Conversely, the chemistry of the two remaining substructures, Nyx and Aleph, is indistinguishable from that of *in situ* populations. I conjecture that Nyx forms part of the high-α disc. For the case of Aleph, I suggest that it is likely comprised of stars both from the low-α (flared/warped) disc as well as stars from the high-α disc.

- the results suggest that the local/inner ($R_{GC} \lesssim 20$kpc) halo is comprised of the debris from at least three massive accretion events (Heracles, GES, and Sagittarius) and two lower mass debris (Thamnos and Helmi stream). Upcoming large spectroscopic surveys probing deeper into the outer regions of the stellar halo (beyond $R_{GC} \sim 20$kpc) will likely uncover the debris from predicted lower-mass/more recent accretions (e.g., van den Bosch et al., 2016, Horta et al. 2022, in prep), and will enable the full characterisation of those already known. Conversely the precise contribution of massive accretion to the stellar populations content of the inner few kpc of the halo is still to be fully gauged. Heracles is likely the result of a real accretion event, likely the most massive to have ever happened in the history of the Milky Way, but we are still scratching its surface.

This chapter presents a chemical composition study of substructures identified (primarily) on the basis of phase-space and orbital information in the stellar halo of the Milky Way. Current and upcoming surveys will continue to map the stellar halo and will provide further clues to the nature and reality of phase-space substructures discovered in recent years. For the inner regions of the Galaxy and the local halo, the Milky Way Mapper (Kollmeier et al., 2017) and the Galactic component of the MOONS GTO survey (Gonzalez et al., 2020) will provide revolutionising chemo-dynamical information for massive samples. For the outer regions of the stellar halo, the WEAVE (Dalton et al., 2014), 4MOST (de Jong et al., 2019), and DESI (DESI Collaboration et al., 2016) surveys will provide spectroscopic data for millions of stars in both high and low resolution. In addition, in this work I have only studied the chemistry of phase-mixed accretion events. However, there is a plethora of halo substructures in the form of stellar streams that has not been studied in this work and also require to be fully examined (see Li et al. 2021 for a recent example). The advent of surveys like S^5 (Li & Gnedin, 2019) will aid in such endeavours. All this information, when coupled with the exquisite astrometry and upcoming spectroscopic information from the *Gaia* satellite, will provide the necessary information for further discoveries and examinations of substructure in the stellar halo of the Milky Way.

Chapter 4

On the mass contribution from globular clusters to the Galaxy

4.1 Introduction

As mentioned in Chapter 1, globular clusters (GC) play a pivotal role in the mass assembly history of galaxies. For the case of the Milky Way, GCs encode information about how the Galaxy has assembled its mass over time. The pioneering work by Searle & Zinn (1978), who used the Galactic GC population to infer that GCs found in the outer Galactic halo region formed over a longer period than those found in the inner-halo region, were the first to utilise GC stellar populations to place constraints on the mass assembly history of the Galaxy. In their work, the authors showed that GCs found in the outer Galactic halo region formed over a longer period than those found in the inner-halo region, leading to the conclusion that the former population originated from accreted satellite systems. This concept has since been refined with improved measurements of ages and chemical abundances, leading to the discovery of a bifurcation in the age-metallicity distribution of Galactic GCs (Marín-Franch et al., 2009), where the young and metal-poor branch traces the population of GCs that are thought to result from satellite galaxy accretion (e.g., Forbes & Bridges, 2010; Leaman et al., 2013). Similarly, this division is also reflected in the α and Fe compositions of GCs with metallicities between $-1.5 < \mathrm{[Fe/H]} < -1$, whereby accreted GCs typically present lower $[\alpha/\mathrm{Fe}]$ for a given [Fe/H] in comparison to their *in situ* counterparts (e.g., Horta et al., 2020). The results obtained from these observational studies fit well in the present cosmological framework, the Λ-CDM model (e.g., Schaeffer & Silk, 1985; Frenk & White, 2012). In this cosmological paradigm, larger galaxies engulf smaller satellite galaxies and grow through a process of hierarchical mass assembly. As a result, a substantial fraction of

the GCs from those accreted galaxies may survive the merger, depending on the details of the accretion, as suggested by various observational results (e.g., Brodie & Strader, 2006; Myeong et al., 2019; Massari et al., 2019; Koppelman et al., 2019b; Kruijssen et al., 2019b; Forbes, 2020).

To elucidate the role GCs play in the formation and mass assembly of their host galaxies, it is vital to first understand how GCs form and evolve in a cosmological context. The leading GC formation scenarios propose a framework in which GCs formed in the turbulent discs of their host galaxies at z ∼2-3, where, due to tidal shocks (Gnedin, 2001) and the so called "cruel cradle effect" (Kruijssen et al., 2012a), GCs formed *in situ* were largely destroyed (Elmegreen, 2010; Kruijssen et al., 2011; Kruijssen, 2014, 2015). As galaxies evolved, mergers redistributed GC systems of accreted satellites onto the host galaxies, typically depositing them in the outer regions of the stellar halo component, where mass loss via evaporation takes place in a longer timescale.

The question of how much stellar mass in the halo arises from GC dissolution and/or evaporation emerges as a natural implication from the above theoretical framework. In an attempt to answer such a question, over the last decade there has been substantial work focusing on the identification of GC stars that have been stripped from their parent GC, and now reside in the halo field of the Galaxy (e.g., Martell & Grebel, 2010; Martell et al., 2016; Schiavon et al., 2017b; Koch et al., 2019; Hanke et al., 2020, Kisku et al., in prep). In these studies, stars arising from GC dissolution and/or evaporation were identified either by selecting field stars that present high nitrogen and low carbon abundances, or by identifying stars with strong CN bands, a feature that implies a higher N content and one that is typically found in the so called "second population" (SP) GC stars (for a full review, see Bastian & Lardo, 2018). Such studies have focused on both the outer regions of the stellar halo (Martell & Grebel, 2010; Martell et al., 2016; Koch et al., 2019), and within the inner few kiloparsecs from the Galactic Centre (Schiavon et al., 2017b). Specifically, Martell et al. (2016) focused on metal poor ([Fe/H] ≤ –1.3) sample from the twelfth APOGEE data release and identified halo field stars that present high [N/Fe] and [Al/Fe] values, thus selecting former SP GC escapee candidates. Using the number ratio of N-rich stars to halo field stars, Martell et al. (2016) obtained an estimate for the contribution from dissolved SP GC stars to the outer regions of the stellar halo to be on the order of 2-3%. A similar estimate was also obtained in a more recent study using the SEGUE data (Yanny et al., 2009b) by Koch et al. (2019), which found a value of∼2.6%. Separately, Schiavon et al. (2017b) analysed APOGEE data for stellar populations within ∼3 kpc of the Galactic Centre and found a much larger fraction of N-rich stars than their outer halo counterpart. In their study, Schiavon et al. (2017b) identified field stars that presented high [N/Fe] and low [C/Fe] compared to the main population at a given metallicity, and determined a minimum contribution to the

stellar halo from dissolved and/or evaporated SP GC stars of approximately∼13-17%. This results in a much higher contribution rate than in the outer halo, by a factor of∼4-5.

Furthermore, recent theoretical studies making use of the suite of E-MOSAICS hydrodynamical cosmological simulations (Pfeffer et al., 2018; Kruijssen et al., 2019a) have assessed the contribution of stars dissolved from GCs to the stellar halo field for ∼25 Milky Way analogues. The results from these works predict a smaller contribution from SP GC stars than observational estimates, predicting a total contribution of the order of ∼1% (Reina-Campos et al., 2019) for the outer halo region and ∼0.2-9% for the inner Galaxy (Hughes et al., 2020). Although the predicted fractions at face value do not match that of the observed fractions, an inner-to-outer halo ratio discrepancy is still predicted.

In connection with the mass contribution of dissolved GC stars to the Galactic stellar halo, the question of the spatial distribution of GC escapees is also an important one, and similarly, its stellar density as a function of Galactocentric distance. Answering these questions is non-trivial due to the difficulty in correcting the observed number of a tracer population to the total underlying sample. Along the same lines, estimates of the stellar mass are rigidly connected to the derived mass normalisation per tracer star, which generally relies on intricate calibration and stellar models. Moreover, GCs are typically associated to the stellar halo component of the Galaxy, and with no previous knowledge of the density profile of GC escapees, it is important to first understand how the stellar halo is spatially distributed. This information can be used as a guide to understand the density profile of GC-escapee stars, and will serve later for assessing the contribution of N-rich stars to the stellar halo field.

Recently, Iorio et al. (2018) modelled the density of the stellar halo using a cross-matched sample of *Gaia*-2MASS RR Lyrae stars. In that work, several density profiles ranging in parameter complexity were tested, and it was found that the stellar halo was best fit by a triaxial ellipsoid, rotated with respect to the Galactic reference frame (in which the X axis connects the Sun to the Galactic Centre) by $\sim 70°$; such rotation was thought to be introduced by a single massive merger event. Using Red Giant Branch (RGB) stars from the APOGEE fourteenth data release Mackereth et al. (2019b) also found this to be the case. The same study estimated a total halo stellar mass on the order of $\sim 1.3 \times 10^9$ M$\odot$ when considering the halo as an assembly of many individual components in the [Mg/Fe]-[Fe/H] plane. This result is in agreement with the recent work of Deason et al. (2019), based on RGB number counts and extrapolation of the Einasto (1965) profile, which also suggests a higher mass for the stellar halo of $\sim 1.4 \times 10^9$ M $\odot$. These works utilised existing density models to understand the shape and density profile of the stellar halo component of the Galaxy. Using such density modelling procedures, they were able

to estimate the total mass of the stellar halo within a given Galactocentric radius. Such methods can be applied in theory to any tracer stellar population, enabling the estimation of mass as a function of Galactocentric radius while accounting for selection effects induced by observational data.

In this Chapter, I build on the previous work by Mackereth et al. (2019b), and present a density profile, mass estimate, and a percentage contribution to the stellar halo from likely SP GC (i.e. N-rich) stars arising from GC dissolution and/or evaporation as a function of Galactocentric distance. This is accomplished via density modelling of APOGEE red giant stars, selected on the basis of their chemical compositions. the methodology allows for the assessment of the stellar mass contained in the complete halo and the N-rich samples, as well as their corresponding mass as a function of Galactocentric distance. As explained in Mackereth et al. (2019b), the APOGEE red giant star counts are corrected for their respective normalisation, via the reconstruction of the APOGEE DR16 selection function and using stellar evolution models, which enables the estimation of the stellar density profiles to good accuracy.

This Chapter is organised as follows: Section 5.2 presents the selection of likely halo APOGEE red giant stars, and the criteria to determine N-rich stars residing in the stellar halo field. In Section 5.3, I briefly describe the density modelling procedure, based on the work by Bovy et al. (2016) and Mackereth et al. (2017), including allowances for the APOGEE-2 selection function. In Section 5.4, I present the main results of the paper. Section 4.5 includes the discussion of the results in the context of previous studies, for which I then summarize the results in Section 4.6, and provide the conclusions.

4.2 Data and Sample

In this chapter, I use data from the sixteenth data release of SDSS-IV (Ahumada et al., 2019a), which contains refined elemental abundances (Jönsson et al., 2020) for stars observed both by the Apache Point Observatory Galactic Evolution Environment (APOGEE: Majewski et al., 2017) and its successor, APOGEE-2, one of four Sloan Digital Sky Survey–IV (SDSS–IV, Blanton et al., 2017) experiments. With twin spectrographs (Wilson et al., 2019) mounted to the 2.5-m Sloan Telescope (Gunn et al., 2006) at Apache Point Observatory in New Mexico and the 2.5-m du Pont Telescope at Las Campanas Observatory, APOGEE-2, includes high resolution (R$\sim$22,500), high signal-to-noise ratio (SNR>100 pixel^{-1}), near-infrared (1.5–1.7μm) spectra of over 450,000 stars sampling all parts of the Milky Way. These spectra are used to derive accurate stellar atmospheric parameters, radial velocities and the abundances for up to 25 atomic elements. Targets were selected from the 2MASS point–source catalogue with a

dereddened $(J - Ks) \geq 0.3$ colour cut in up to three apparent H-band magnitude bins. Reddening corrections were determined using the Rayleigh–Jeans Colour Excess method (RJCE; Majewski et al., 2011). Corrections are obtained by applying the method to the combined 2MASS (Skrutskie et al., 2006) and Spitzer– IRAC surveys GLIMPSE–I,–II (Churchwell et al., 2009), and –3D when available, or 2MASS combined with WISE photometry (Wright et al., 2010). A more in–depth description on the APOGEE survey, data reduction pipeline, and the target selection can be found in Majewski et al. (2017), Holtzman et al. (2015), Nidever et al. (2015), Jönsson et al. (2020), Zasowski et al. (2013), and Zasowski et al. (2017). All the APOGEE data products used in this Chapter are those output by the standard data reduction and analysis pipeline. The data are first reduced with a custom pipeline (Nidever et al., 2015; Jönsson et al., 2020). The data are then thoroughly checked, before being fed into the APOGEE Stellar Parameters and Chemical Abundances Pipeline (ASPCAP; García Pérez et al., 2016; Jönsson et al., 2020). ASPCAP makes use of a specifically computed spectral library (Zamora et al., 2015; Holtzman et al., 2018; Jönsson et al., 2020), calculated using a customised H-band line list (Shetrone et al., 2015, Smith et el, in prep), from which then the outputs are then analysed, calibrated, and tabulated (Holtzman et al., 2018).

I make use of the distances for the APOGEE DR16 catalogue generated by Leung & Bovy (2019a), using the `astroNN` python package (for a full description, see Leung & Bovy, 2019b). These distances are determined using a previously trained astroNN neural-network, which predicts stellar luminosity from spectra using a training set comprised of stars with both APOGEE spectra and *Gaia* DR2 parallax measurements (Gaia Collaboration, 2018). The model is able to predict simultaneously distances and account for the parallax offset present in *Gaia*-DR2, producing high precision, accurate distance estimates for APOGEE stars, which match well with external catalogues and standard candles.

The sample adopted in this study is restricted to stars contained in the statistical sample[1] of APOGEE DR16 located within fields with extinction information and that satisfy the following criteria: $0.5 < \log g < 3.5$, $3500 < T_{\rm eff} < 4750$ K, $-2.5 <$ [Fe/H] < -1, $d_{\rm err}/d < 0.2$ (where d and $d_{\rm err}$ are the distance and distance error, respectively). Here the $T_{\rm eff}$ and $\log g$ cuts were made in order to target RGB stars whose C,N and Al abundances are unaffected by dredge up processes. I note here that I use the calibrated ASPCAP abundances, rather than those from other abundance pipelines (e.g., BACCHUS, astroNN).

[1]Stars belonging to the statistical sample are those which were selected at random from 2MASS and are included in fields with completed cohorts.

I also remove stars that are in fields in close proximity to the Galactic Centre by excluding fields within 10° in l from the Galactic Centre and $|b| < 10°$ for which dust extinction is most difficult to correct, as well as those which contained globular clusters (GCs) used for APOGEE calibration. Furthermore, since the aim is to study the Galaxy's stellar halo field population, I remove 1,781 stars in the APOGEE DR16 statistical sample that are known to reside in GCs, adopting the GC memberships established by Horta et al. (2020). Lastly, since I am focused on selecting dissolved and/or evaporated SP GC stars in [N/Fe] space, I applied further cuts to ensure I were only considering stars where [N/Fe] is robustly determined, and removed any stars that had a `N_FE_FLAG` warning set by ASPCAP. I also ensured stars in the sample had reliable Fe, C and Al abundances by checking the `C_FE_FLAG` and `AL_FE_FLAG` warnings were set to zero, and by removing any stars with [Fe/H], [C/Fe], and/or [Al/Fe] set to –9999. the final working halo sample is comprised of 1455 stars.

Next, I define SP GC stars by identifying nitrogen rich (N-rich) stars present in the stellar halo field population of the Milky Way. To identify N-rich stars, I make use of the publicly available code `XDGMM`[2] (Holoien et al., 2017), and fit a two component Gaussian mixture model (GMM) to the halo sample [N/Fe]–[Fe/H] distribution, with the expectation that N-rich stars will stand out in this plane. This software uses the extreme deconvolution (XD) algorithms (Bovy et al., 2011) to identify components in an n dimensional space, and allows us to determine the N-rich star field sample statistically by accounting for the uncertainties and correlations in the measurement errors. I then refine the N-rich star selection by only considering stars with carbon abundances below [C/Fe] $< +0.15$, to ensure that these stars present the low [C/Fe] abundances typical of SP GC stars, and remove four stars from the sample. the final sample of N-rich stars is comprised of 46 stars. Fig. 4.1 shows the distribution of the selected N-rich stars and the halo field population in the [N/Fe] - [Fe/H] plane, where the lowest N-rich star nitrogen abundance is [N/Fe]$\sim$+0.5, in agreement with values from other samples (e.g., Martell et al., 2016; Schiavon et al., 2017b; Nataf et al., 2019). To check whether the metallicity distribution function (MDF; shown in the top panel of Fig. 4.1) of the likely halo and N-rich star samples are statistically equal, I perform a two-sided Kolmogorov-Smirnov (KS) test, for which I obtain a resulting *p-value* of approximately$\sim$0.75. Therefore, I can reject the null hypothesis that these two samples originate from different parent distributions and trust that they are statistically the same with a high degree of confidence; this indicates that the N-rich stars display a similar MDF as the halo field population. However, the N-rich star sample is clearly separated from the halo field sample in their nitrogen distribution function (right panel of Fig. 4.1).

[2]https://github.com/tholoien/XDGMM

I plot the nitrogen abundances of the normal and N-rich halo field stars as a function of their respective carbon and aluminium abundances in Fig. 4.3 and Fig. 4.2, respectively. Those abundances are overlaid on data for stars residing in three GCs (NGC 6205, NGC 6904, NGC 7078) whose metallicities span the same range as the N-rich star sample (i.e. $-2.5 < \mathrm{[Fe/H]} < -1$), and for which I have substantial GC members, using the APOGEE GC sample from Horta et al. (2020). By comparing the N-rich star sample to GC stars, I aim to discern if the N-rich stars present the typical light element variations of SP GC stars (Bastian & Lardo, 2018). The data for the GC members display two clear sequences in Figure 4.3, corresponding to the loci of the FP and SP stars, with the latter typically showing $\mathrm{[N/Fe]} > +0.5$. Stellar evolution along the giant branch runs in parallel along each sequence, where more evolved, more luminous, lower $\log g$ stars have higher [N/Fe] and lower [C/Fe]. The well known N-C anti-correlation in GCs connects stars of same evolutionary stage in each sequence, so that FP stars have higher [C/Fe] and lower [N/Fe] than their SP counterparts. With that in mind, the bottom panel suggests that the stars at the bottom of the SP sequence, with $\mathrm{[N/Fe]}\sim+0.5$ and $\mathrm{[C/Fe]}\sim+0.2$ have no counterparts in the FP sequence. Those would be stars with lower [N/Fe] and higher [C/Fe] than the bottom of the FP sequence, which itself is located at $\mathrm{[C/Fe]}\sim+0.1$ and $\mathrm{[N/Fe]}\sim-0.1$. I hypothesise that such stars are lacking in the sample due to a combination of effects. Firstly, these stars relatively high T_{eff} and $\log g$, which makes CN lines, upon which nitrogen abundances rely, too weak for reliable N abundances. Secondly, the ASPCAP grid has a [N/Fe] floor at –0.25.

Figure 4.2 shows a correlation between [N/Fe] and [Al/Fe] for the N-rich star sample, with the majority of these presenting $\mathrm{[Al/Fe]} > 0$, again occupying the same locus as the SP GC stars. I also report that N-rich stars display a much greater mean [Al/Fe] ($\simeq 0.3$) than the normal halo field population ($\mathrm{[Al/Fe]} \simeq -0.2$). I also checked whether the N-rich population differed from its normal halo counterpart in terms of its neutron-capture element abundances, since those were found to be enhanced in SG GC stars by Cunha et al. (2017). The only neutron-capture element for which APOGEE DR16 provides abundances for the sample is Ce. I found no statistically significant difference in [Ce/Fe] between the two samples.

In a recent paper, Fernández-Trincado et al. (2019) suggest that SP GC stars must have $\mathrm{[Al/Fe]}>+0.5$ in order to be considered true SP GC star candidates. In fact, adoption of such a restrictive criterion would lead to a severe underestimate of the N-rich population in both the field and GC sample. Stars belonging to NGC 6205, NGC 5904, and NGC 7078 from the Horta et al. (2020) GC sample display a clear bimodality in the carbon-nitrogen plane, where the SP GC stars occupy a locus positioned at higher [N/Fe], congregating above their FP counterparts. This bimodality is also observed in the aluminium-nitrogen plane. In the bottom panel of Fig. 4.2, the SP GC stars (i.e.

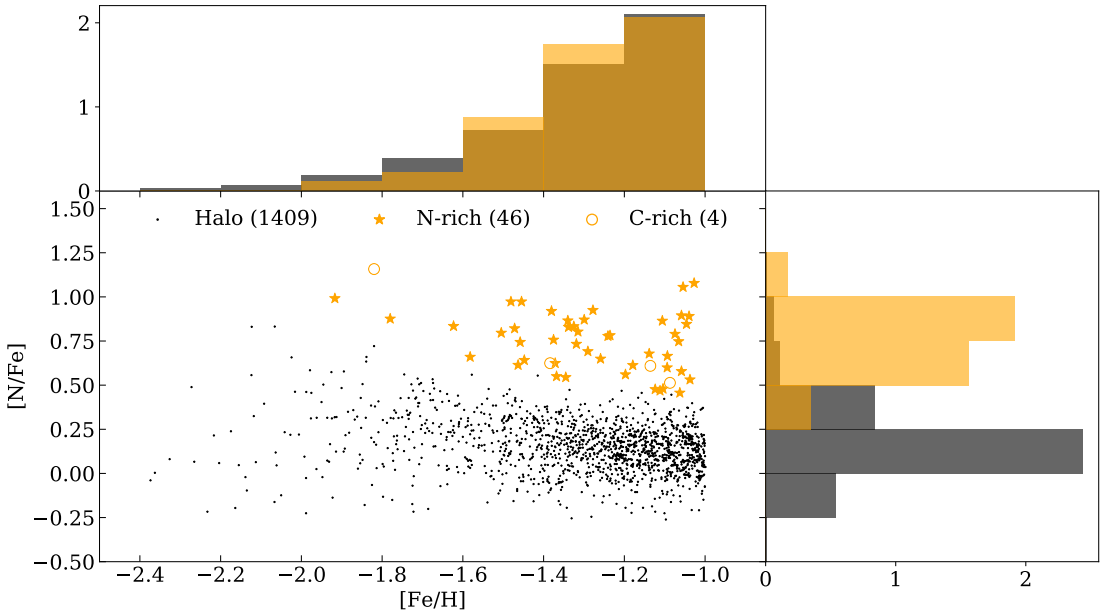

FIGURE 4.1: [N/Fe] vs [Fe/H] distribution of the halo field star sample (black dots) and the selected N-rich stars (orange stars) used in this work. Histograms highlight the MDF (top) and nitrogen distribution function (right) of both samples, normalised by the total star number of stars in each sample. Both samples share the same MDF, however can be clearly distinguished in the [N/Fe] distribution, with the mean N-rich star [N/Fe] value sitting approximately$\sim$0.7 dex higher than the mean halo field [N/Fe] abundance. Open circles at high [N/Fe] values are the N-rich stars that did not satisfy the [C/Fe] < 0.15 criterion. The numbers stated in brackets quantify the number of stars in each sample.

the filled triangles not overlapping with the halo population) clearly present [Al/Fe] abundances that fall below [Al/Fe]=+0.5. Thus, since the N-rich star sample occupies the same locus as the SP GC stars in both the carbon-nitrogen and aluminium-nitrogen planes, applying an [Al/Fe] $> +0.5$ cut to the sample would lead to a similarly severe underestimate in the number of N-rich stars in the field. In addition, it has been shown by several authors (e.g., Carretta et al., 2009; Nataf et al., 2019; Mészáros et al., 2020) that the extent of the Mg-Al anti-correlation varies from GC to GC, making a strict cutoff in Al difficult to implement.

Finally, I show the spatial distribution of the halo field population and the N-rich star sample in Fig. 4.4, represented with the same symbols as in Fig. 4.1. Before correcting for the APOGEE selection function or modelling the stellar density, it is immediately clear that the halo field population (black) occupies a vast range of heights above the Galactic midplane, reaching values of $Z\sim$20 kpc. The same applies to the N-rich stars, however these do not display as large a Galactocentric distance range. Interestingly, I find that a significant fraction of the N-rich stars occupy a position close to the Galactic Centre, within an approximate radius of $R_{\rm GC}\sim$3 kpc. The remaining N-rich stars are scattered at higher Z and Y values. It has already been shown that N-rich stars make

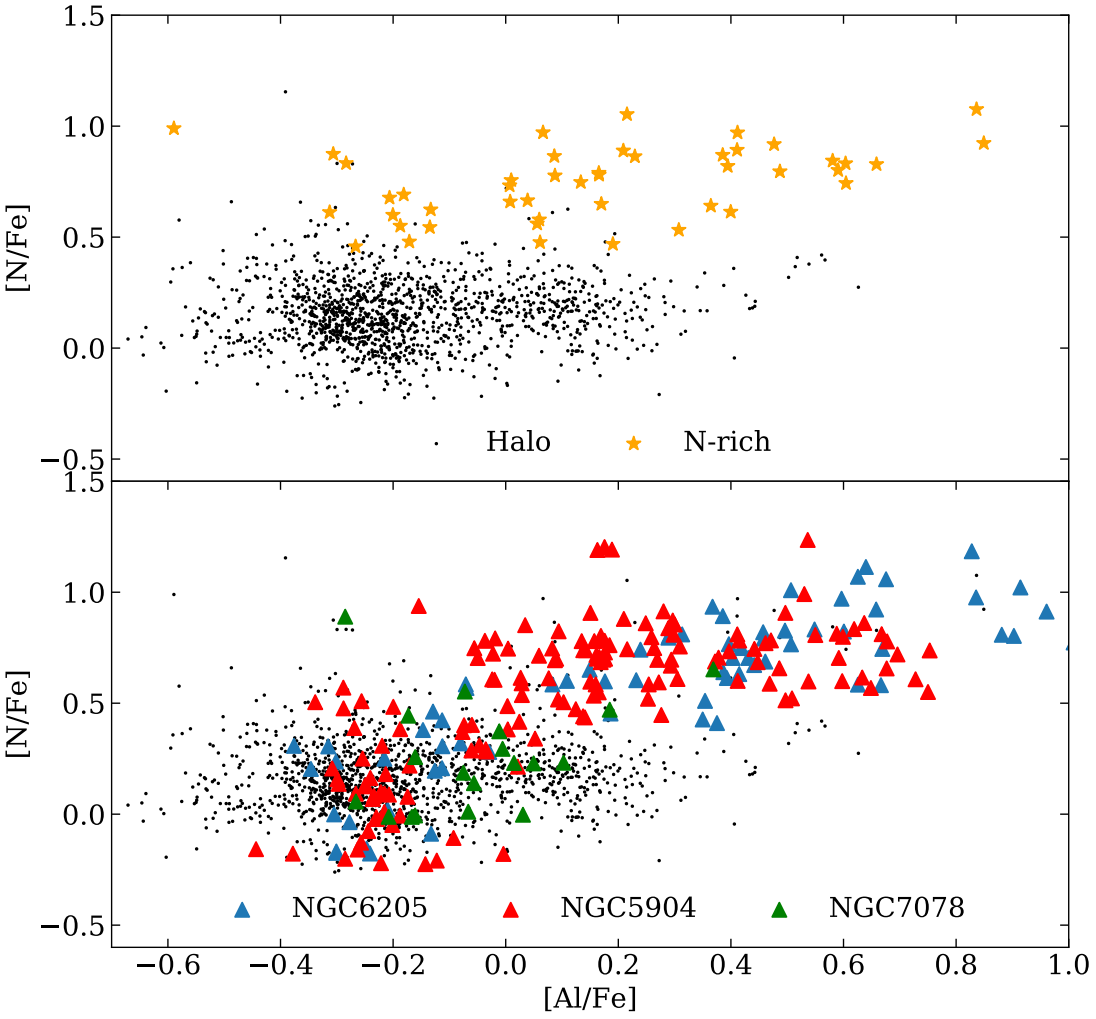

FIGURE 4.2: The same stars plotted from Fig. 4.3 in the [N/Fe] vs. [Al/Fe] plane. Despite a small fraction of N-rich stars displaying [Al/Fe] < 0 dex, the majority occupy the same locus as the SP GC stars that display high [Al/Fe] abundances.

up a significant fraction of the inner Galaxy (Schiavon et al., 2017b) and to a lesser extent of the outer halo (Martell et al., 2016; Koch et al., 2019), therefore the initial findings are in agreement with results from previous studies.

4.3 Density Modelling

In this section, I briefly describe the method employed for fitting the underlying number density of stars in the Milky Way's halo from APOGEE observations, which I represent here as $\nu_*(X,Y,Z—\tau)$, in units of stars kpc^{-3}. The computation of this quantity requires allowances to be made for the survey selection function, which is non-trivial due to the pencil beam nature of APOGEE, the presence of inhomogeneous dust extinction along the lines of sight, the target selection criteria imposing different H magnitude limits,

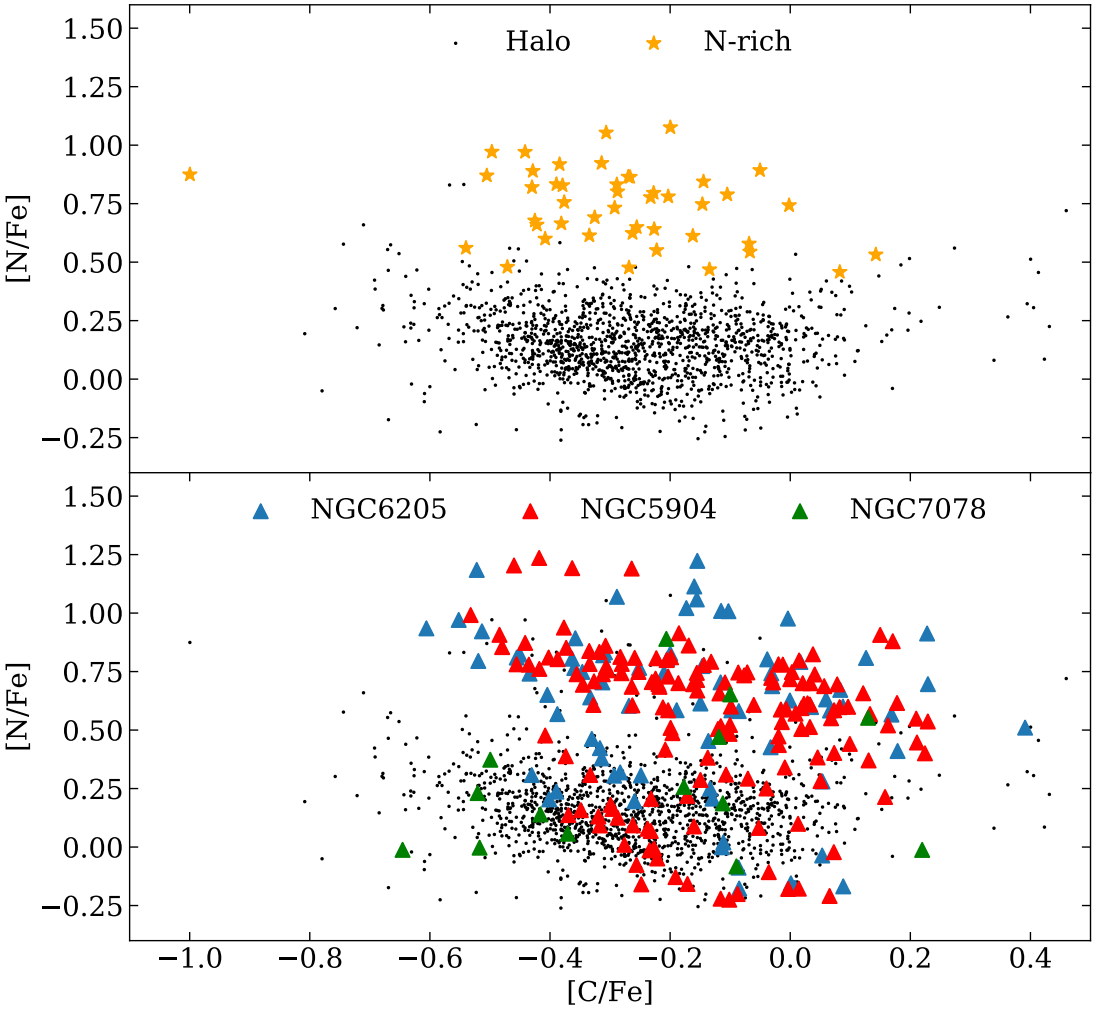

FIGURE 4.3: [N/Fe] vs. [C/Fe] distribution for the N-rich stars (top) and for stars from the APOGEE GC sample for three representative clusters (bottom) derived using the same procedure as in Horta et al. (2020). The black points are the same in both panels, and represent the halo field population. The N-rich star sample mimics the behaviour of SP GC stars of similar metallicity, occupying the same locus on this plane. Note that the N-rich stars with the highest [C/Fe] have no counterparts in the FP sequence. This is due to a combination of factors. Stars within that high [C/Fe] regime have higher T_{eff} and log$g$ and low [N/Fe], which makes CN lines weaker. Moreover, there is a [N/Fe] floor in ASPCAP at –0.25.

and the use of tracers, RGB stars, that are not standard candles. the main goal is to determine density laws that describe the spatial distributions of the stellar halo and the N-rich samples separately. In this way, the number of observed normal field and N-rich stars can be converted into actual densities, in units of stars pc^{-3} at the solar radius (N_{R_0}). This density law can then be used to estimate the number of halo or N-rich stars APOGEE would have observed if it covered the full sky. Moreover, using stellar evolution models I can estimate the mass density. This value can then be estimated within a chosen volume by integrating an accurate density law for the halo and N-rich star samples, respectively. It is also straightforward to use the separate density laws to

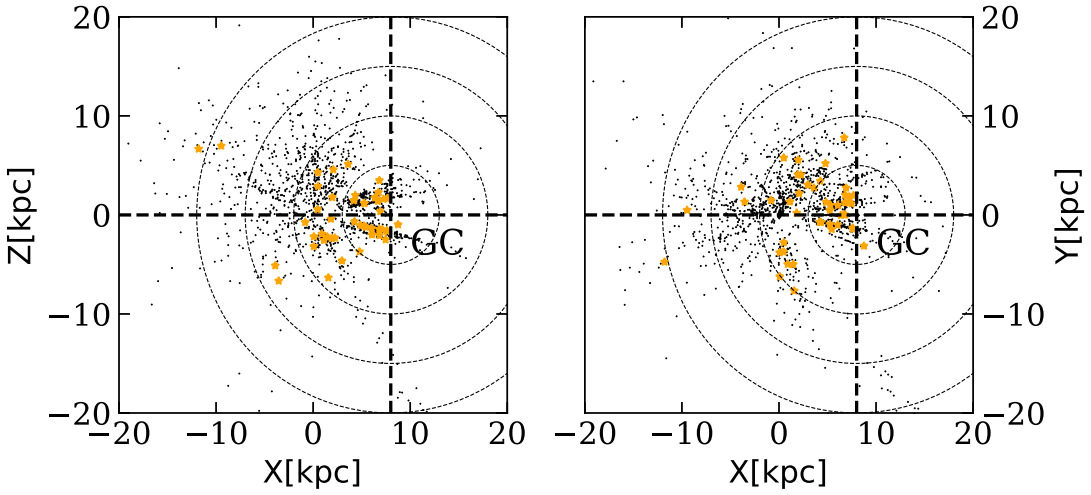

FIGURE 4.4: Spatial distribution in heliocentric X - Z and X - Y of the APOGEE DR16 field (black dots) and N-rich star (orange stars) samples between –2.5 < [Fe/H] < –1. The crosshair signifies the position of the Galactic Centre. The dashed circled lines denote spherical radius bins of 5 kpc in size, signifying a 5, 10, 15, and 20 kpc distance from the Galactic Centre.

determine the ratio of mass density between N-rich stars and halo field stars, resulting in the fractional number of N-rich to total halo field stars, given as a percentage, as a function of position in the Galaxy. By following this procedure, I aim to determine if the ratio of N-rich stars is constant throughout the Milky Way, and if N-rich stars follow a similar density profile to that of the stellar halo field population.

Our methodology is an adaptation of that used by Mackereth et al. (2017) and Bovy et al. (2012); Bovy (2014); Bovy et al. (2016). I employ a modified version of their publicly available code[3]. Despite the method following that of these previous studies, I summarize the key steps here for clarity and completeness. For a full description of the fitting method, I refer the interested reader to Section 3.1 from Mackereth et al. (2019b). The main steps are summarised as follows:

(1) I fit different density functional forms for the density profile to the APOGEE N-rich star sample using a maximum likelihood fitting procedure, based on the assumption that star counts are well modelled by an inhomogeneous Poisson point process[4], which takes into account the APOGEE selection function. For the halo sample, I adopt the functional form from Mackereth et al. (2019b) (see Eq. 4.1 in Section 4.3.1) for two reasons: Firstly, the sample employed in their study is extremely similar to that used here; and secondly, their model describes the data well (see Section 5.4).

[3]Available at https://github.com/jmackereth/halo-mass and https://github.com/jobovy/apogee-maps, respectively.

[4]See Daley & Vere-Jones (2003) for a more detailed definition of an inhomogeneous Poisson point process.

(2) I determine the best-fitting density model for the N-rich star sample by calculating the Bayesian Information Criterion (BIC Schwarz, 1978) and the logarithmic maximum likelihood value, $\ln(\mathcal{L}_{\max})$, for each model, and choosing that with the lowest BIC value (see Section 4.3.2 and Section 4.3.3 for a description of the models tested and the selection of the best fitting model, respectively). the selected halo density profile includes a single exponential disc profile to account for the contribution of the (thick) disc component to the sample. I find that by including this disc fraction parameter to the model, I am able to quantify the fraction of the sample that belongs to the (thick) disc and that would affect the fitting procedure. Moreover, given the metallicity cut, the contribution by the thin disk to the sample is negligible, so I do not include that component in the model. Using this density law for the halo, and the resulting best fitting model for the N-rich stars, I initiate a Markov-Chain Monte-Carlo (MCMC) sampling of the posterior probability distribution function (PDF) of the parameters fitted in each density law. I adopt the median and standard deviation of one-dimensional projections of the MCMC chain as the best-fit parameter values and uncertainties.

(3) As the fitting procedure does not fit for the normalisation of the density N_{R_0} (the number surface density of halo or N-rich stars at the solar neighbourhood in stars pc^{-3}), I compute this quantity by comparing the observed number of halo or N-rich stars in the metallicity bin adopted to that which would be observed in APOGEE for the fitted density model if $N_{\mathrm{R}_0} = 1$ star pc^{-3}. I then employ this number-density quantity (N_{R_0}) to obtain the true number of stars given by the best-fitting halo or N-rich density model within a given volume. This number density can then be converted into a mass density using stellar evolution models. Since the aim is to determine the contribution of N-rich stars as a function of Galactocentric distance, I take the ratio of the mass densities yielded for the N-rich star sample and the halo sample. This allows us to compare the ratio of GC dissolution in different spatial regions of the Galaxy, and potentially place constraints on the origin of the contribution of dissolved GC stars to the Galaxy's stellar halo mass budget, and the mass assembly history of the Milky Way.

Our method corrects for the effects induced by interstellar extinction using combined 3D maps of the Milky Way derived by Marshall et al. (2006) for the inner disc plane and those derived for the majority of the APOGEE footprint by Green et al. (2019), adopting conversions $A_{\mathrm{H}}/A_{\mathrm{K_s}} = 1.48$ and $A_{\mathrm{H}}/E(B - V) = 0.46$ (Schlafly & Finkbeiner, 2011; Yuan et al., 2013). Any fields with no dust data (10 fields) were removed from the analysis. I adopt the combination of Marshall et al. (2006) and Green et al. (2019) dust maps because Bovy et al. (2016), who assessed the relative merits and limitations of a number of available maps in the literature, determined that this combination of dust maps provides the best fits when performing density modelling on APOGEE data for a trace population.

4.3.1 Halo Density Model

I aim to discern the profile that best describes the halo field sample. Recent work modelling the Galactic stellar halo using RR Lyrae stars found that the stellar halo is well modelled by a triaxial density ellipsoid, angled at roughly 70° with respect to the axis connecting the Sun and the Galactic Centre (Iorio et al., 2018; Iorio & Belokurov, 2019), but can also be well modelled by a single power law (SPL). Along the same lines, Mackereth et al. (2019b) used the APOGEE DR14 data and the corresponding APOGEE selection function, and found that the mono-abundance populations in the [Fe/H] range selected in that work are well modelled by a triaxial SPL density ellipsoid with a "cut-off" term. The cut-off term accounts for the ignorance regarding the extent of the sample outside of the observed range, and includes a scale parameter β corresponding to the scale length (such that $h_{r_e} = 1/\beta$). This density profile also includes a disc term, modelled by an exponential disc profile with scale height $h_z = 0.8$ kpc and scale length $h_R = 2.3$ kpc (Mackereth et al., 2017), to account for any contamination from the thicker components of the high [α/Fe] disc, parameterised by the factor $f_{\rm disc}$. Hereafter, I refer to this model as TRI-CUT-DISC.

Since I am modelling a similar metal-poor halo sample as that one modelled in Mackereth et al. (2019b), with a very similar MDF, I adopt the functional form from their best-fitting profile to model the stellar halo field population. That density profile is given by:

$$\upsilon_*(r_e) \propto (1 - f_{\rm disc}) r_e^{-\alpha} \exp(-\beta r_e) + f_{\rm disc} \upsilon_{*,\rm disc}. \tag{4.1}$$

The density is normalised such that the density at the Sun (i.e., $\upsilon_*(r_{e,0})$) is equal to unity, and r_e defines the ellipsoidal surfaces on which the density is constant, given by:

$$r_e^2 = X_g^2 - \frac{Y_g^2}{p^2} - \frac{Z_g^2}{q^2}, \tag{4.2}$$

where p and q describe the Y_g-to-X_g and Z_g-to-X_g axis ratios, respectively, and (X_g, Y_g, Z_g) are the Cartesian coordinates relative to the Galactic Centre. The best-fitting model found in Iorio et al. (2018) included an allowance for the variation in q with r_e, with a scale length of$\sim$13 kpc. In this work I assume q does not vary with elliptical radius, and constrain both shape parameters q and p to be < 1, forcing the longest axis to be that in the X_g direction. As in Mackereth et al. (2019b), I allow the orientation of the density ellipsoid to vary, applying a transformation defined by the unit vector $\hat{z}$ along the transformed Z axis, and the angle of rotation (from the original X axis) of the ellipsoid about this transformed axis, ϕ. In practice, $\hat{z}$ is sampled uniformly (with the MCMC algorithm) by de-projecting samples from an equal-area rectangular projection of the unit sphere. Employing this method, $\hat{z}$ is represented by two parameters, η and

θ, such that $\hat{z} = (\sqrt{1-\eta^2}\cos\theta,\ \sqrt{1-\eta^2}\sin\theta,\ \eta)$. Here η is sampled uniformly between –1 and 1, and θ between 0 and 2π. Such a transformation generally has little impact on the measurement of the total mass, as the parameters tend to define an ellipsoid which is roughly aligned with the Sun's position. For all parameters I adopt uninformative priors, and set the allowed exponent α and parameter β range to be positive. For the remaining parameters, only a range of [0,1] is permitted.

4.3.2 N-rich star density models

With no pre-conception of the density distribution of N-rich stars in the Galaxy, it is important to test several different density models for the N-rich sample, and statistically evaluate which model best fits the data. In this subsection, I describe the range of density models fitted to the N-rich star data, and provide the analytical function for clarity and completeness.

I begin by fitting the simplest model to the N-rich star sample, a spherical power law (SPL). This model is described analytically as:

$$\nu_*(r_\mathrm{e}) \propto r^{-\alpha}, \tag{4.3}$$

where r is given by Eq. 4.2 when equating p and q to unity. This profile assumes the density is prescribed by spherical shells, with no flattening along any axis. A flattening parameter along the Z axis (q) can be introduced to obtain an axisymmetric profile (AXI), which is described by Eq. 4.3, assuming r is given by Eq. 4.2, and equating p to one. Similarly, a separate flattening parameter along the Y axis (p) can be introduced to obtain a triaxial profile (TRI), governed by the shape of a triaxial ellipsoid. Alongside these three single power law density models, I choose also to fit the model described in Section 4.3.1 (TRI-CUT-DISC), employed to fit the stellar halo field data.

In addition to the profiles mentioned above, I fit two further profiles that are not part of the single power law family. The first is an exponential disc profile from Mackereth et al. (2017) (DISC), given by:

$$\nu_*(r_\mathrm{e}) \propto \exp(-h_\mathrm{R}(R-R_0) - h_\mathrm{z}|z|), \tag{4.4}$$

where R and z are the radial and vertical axes in a cylindrical coordinate system, respectively, h_R and h_z are the radial and vertical scale lengths, and R_0 is the Galactocentric radius of the Sun. I believe that by testing a disc profile, I will be able to discern if the N-rich star sample is better described by a disc density model, and thus if it has a high contribution to the Galactic disc component. The second additional profile fitted is a

broken power law (BPL). This density model resembles that of a single power law (see Eq 4.3), however has a break radius denoting a change in the slope of the model, given by a change in the value of α. The broken power law is given by:

$$\nu_*(r_e) \propto \begin{cases} r^{-\alpha_{\rm in}} & \text{if} \quad R < R_{\rm break} \\ r^{-\alpha_{\rm out}} & \text{if} \quad R > R_{\rm break}, \end{cases} \tag{4.5}$$

where $\alpha_{\rm in}$ is the power law exponent inside the break radius (i.e. $R_{\rm break}$), and $\alpha_{\rm out}$ is the exponent outside the break radius. By fitting a broken profile, I will be able to test the hypothesis in which the N-rich star sample is governed by a break between an inner and outer component, potentially linked to the different N-rich star ratios found in previous studies for different spatial regions.

For all the models presented I adopted uninformative priors, as performed in Section 4.3.1. For the parameters of the exponential disc profile, I set a permitted scale length range of [0,10] (kpc). For the permitted range of the break radius of the broken power law, I permit values between [0,20] (kpc), a range of Galactocentric distances that is relatively well covered by the data.

4.3.3 Identification of best-fitting density model

In this subsection, I describe the methodology employed to select the best fitting N-rich star profile from the density models described in Section 4.3.2. I choose the Bayesian Evidence ratio as the figure of merit to identify the best-fitting model. I assume that the posterior distributions are nearly Gaussian, and that therefore the Bayesian Evidence ratio can be approximated by the Bayesian Information Criterion (BIC; Schwarz, 1978), defined as:

$$BIC = d(\tau) ln(N_*) - 2ln(\mathcal{L}_{\rm max}), \tag{4.6}$$

where $d(\tau)$ is the number of free parameters in the density model, N_* is the number of stars in the sample, and $\ln(\mathcal{L}_{\rm max})$ is the logarithm of the maximum value of the likelihood.

The best fitting model is that for which the BIC value is the lowest. The BIC statistic penalises models with a large number of free parameters, such that for two models with the same $\ln(\mathcal{L}_{\rm max})$ value, the one fewer free parameters is preferred. The results from this comparison are listed in Section 4.4.2, displayed in Table 5.1. For the fit of each profile to the N-rich star data, I refer the reader to Appendix C.1.

4.3.4 Mass estimation

I follow the work by Bovy et al. (2012) and Mackereth et al. (2019b), and estimate the mass for the halo and N-rich samples. Although the methodology is fully described in Mackereth et al. (2019b), I briefly explain the procedure for estimating the mass within an APOGEE star sample for clarity. Upon finding a best-fitting model and its associated uncertainty for a distribution of stars, the measurement of the mass can be computed by employing the normalisation of the rate function:

$$\lambda(O|\tau) = \nu_*(X,Y,Z|\tau) \times |J(X,Y,Z;l,b,D)| \times \rho(H,[J-K_s]_0,[\mathrm{Fe/H}]|X,Y,Z) \times S(l,b,H), \quad (4.7)$$

where $\nu_*(X,Y,Z|\tau)$ is the stellar number density in rectangular coordinates, in units of stars kpc^{-3}. $—J(X,Y,Z;l,b,D)—$ is the Jacobian of the transformation from rectangular (X,Y,Z) to Galactic (l,b,D) coordinates, and $\rho(H,[J-K_s]_0,[\mathrm{Fe/H}]|X,Y,Z)$ represents the density of stars in magnitude, colour, and metallicity space given a spatial position (X,Y,Z), in units of stars per arbitrary volume in magnitude, colour, and metallicity space. $S(l,b,H)$ is the survey selection function (see Bovy et al., 2016; Mackereth et al., 2017, for details), which denotes the fraction of stars successfully observed in the survey's colour and magnitude range, and includes dust extinction effects.

I perform this mass-estimation procedure on both the total halo and N-rich star samples by calculating the number of stars seen by APOGEE for a given density model normalised to unity at the Solar position, $N(\nu_{*,0} = 1)$. That number is obtained by integrating the rate function over the observable volume of the survey. This integral is given by:

$$N(\nu_{*,0}=1) = \int_{\mathrm{fields}} d\mathrm{field}\, dD\, \lambda(\mathrm{field},D) = \int d\mathrm{field}\, d\mu\, \frac{D^3(\mu)\log(10)}{5} \nu_*([R,\phi,z](\mathrm{field},\mu|\tau)) \times \mathfrak{S}(\mathrm{field},\mu), \quad (4.8)$$

where the density and effective selection function (namely, $\mathfrak{S}(\mathrm{field},\mu)$) are calculated along APOGEE sightlines on a grid linearly spaced in distance modulus μ. Since the true number of observed stars is given by:

$$\mathrm{N_{obs}} = \mathrm{A\,N}(\mu_{*,0}=1), \quad (4.9)$$

comparison of the expected number count for a normalised density model with the true observed number of stars in the sample provides the proper amplitude, A, which is then

equivalent to the true number density of RGB stars at the Sun, $\mu_{*,0}$, when considering either the halo or N-rich star sample.

The number density in concentric triaxial ellipsoids can also be calculated as a function of Galactocentric distance. Once a best-fitting model for a specific sample of APOGEE stars is estimated, the number density can be computed on a grid of $\nu_*([\mathrm{R},\phi,\theta])$ over a chosen volume. I can then compute this value as a function of Galactocentric radius by integrating along the ϕ and θ axis, which can later be converted into stellar-mass density using stellar evolution models. In either case, the number counts in RGB stars can be converted into the mass of the entire underlying population. To do so, I use the PARSEC isochrones (Bressan et al., 2012; Marigo et al., 2017), weighted with a Kroupa (2001) IMF. The average mass of RGB stars $\langle M_{\mathrm{RGB}} \rangle$ observed in APOGEE is then calculated by applying the same cuts in $(J - K_s)_0$ and $\log g$ to the isochrones. The fraction of the stellar mass in giants, ω, is given by the ratio between the IMF weighted sum of isochrone points within the RGB cuts and those of the remaining population. The conversion factor between RGB number counts and total stellar mass can then simply be calculated using:

$$\chi([\mathrm{Fe/H}]) = \frac{\langle M_{\mathrm{RGB}} \rangle([\mathrm{Fe/H}])}{\omega([\mathrm{Fe/H}])}. \tag{4.10}$$

As explained in Mackereth et al. (2019b), the factor for each field and each selection in [Fe/H] is computed by adjusting the limit in $(J - K_s)_0$ to reflect the minimum $(J - K_s)_0$ of the bluest bin adopted in that field, and only considering isochrones that fall within $-2.5 < [\mathrm{Fe/H}] < -1$. The edges in colour binning for each field are accounted for by the integration over $\rho[(J - K_s)_0, H]$ for the effective selection function. Mackereth et al. (2019b) used Hubble Space Telescope photometry to show that the factors determined using their method are reliable against systematic uncertainty arising from the choice of stellar evolution models.

Once the normalisation for the sample is obtained, I integrate the normalised density models described by 400 samples from the posterior distributions of their parameters to attain the total mass within a population, and the total mass as a function of Galactocentric radius for that same population. To avoid over-extrapolation from the fits to the halo density, I only integrate for the mass within a $1.5 < r < 15$ kpc range, for which the data are well contained.

4.4 Results

4.4.1 Fit to the halo sample

I perform the fitting procedure described in Section 5.3 to the APOGEE halo sample, to ensure that the prescribed density provides a good fit to the data. Since it has recently been shown that the APOGEE DR14 star sample between –2.5 < [Fe/H] < –1 is well defined by a triaxial SPL density ellipsoid, which included a cut-off term and freedom to rotate around its axis (Mackereth et al., 2019b), I choose to fit this profile to the sample. This profile also included a parameter to account for the fraction of the disc in the sample, described by an exponential disc profile. The resulting best-fitting profile, obtained running 10,000 realisations of the model, follows a moderately steep power law, yielding a value of $\alpha \simeq 3.48\ ^{+0.05}_{-0.07}$, with a slight flattening along the Y axis ($p = 0.76\ ^{+0.03}_{-0.04}$), and slightly more flattened along the Z axis, with $q = 0.46 \pm 0.01$, which is in good agreement with previous results (e.g., Deason et al., 2011; Xue et al., 2015; Iorio et al., 2018; Mackereth et al., 2019b). I find the β cut-off parameter to be$\sim$0.01, indicating a scale length which is well outside the range of the data, of the order of $h_{\mathrm{r_e}} \sim 100$ kpc, and that the triaxial ellipsoid is consistent with a minor rotation around the Z axis, $\theta = 3.6 \pm 0.5$ degrees, and a slighly larger rotation along the X axis, $\phi = 14\ ^{+11}_{-9}$ degrees. the results also show that the halo sample has low contamination from the disc, given by the low $f_{\mathrm{disc}} = 0.08\ ^{+0.16}_{-0.06}$ value. The samples from the posterior distribution of parameters given by the data are illustrated in a corner plot in Fig. 4.5, which shows that the posterior distributions are well behaved and converge towards a single value. Alongside the samples, I show in the top right panel the observed distance modulus μ distribution as predicted by a triaxial disc cut-off profile (black) and a spherical power law (blue) with an exponent that best fits the data ($\alpha \simeq 3.2$), compared to the real APOGEE data. Given that the triaxial disc cut-off power law fits the data well, and yields parameter estimates within agreement with values from previous studies, I choose to use this model as the best fit density profile.

It is interesting to compare the best estimate of the halo enclosed mass and normalisation with those by Mackereth et al. (2019b). Using the triaxial disc cut-off power law profile and the APOGEE star counts, I obtain a halo normalisation $\rho_{*,0} = 1.3\ ^{+0.1}_{-0.2} \times 10^{-4}$ M$_\odot$ pc^{-3}, and a total stellar halo mass $\mathrm{M}_{*,\mathrm{halo}} = 8.3\ ^{+1.5}_{-1.3} \times 10^8$ M$_\odot$, by using Eq 4.8 and integrating over the full observable volume (i.e. r$\sim$1.5-15 kpc). I find the total stellar halo mass estimate to be larger by a factor of 1.5 than that obtained by Mackereth et al. (2019b) for the same density profile using APOGEE DR14 data, and suggest it is likely due to the different volumes employed to integrate the density (Mackereth et al. (2019b) integrated the halo volume within a Galactocentric distance ranging from 2 < r < 70

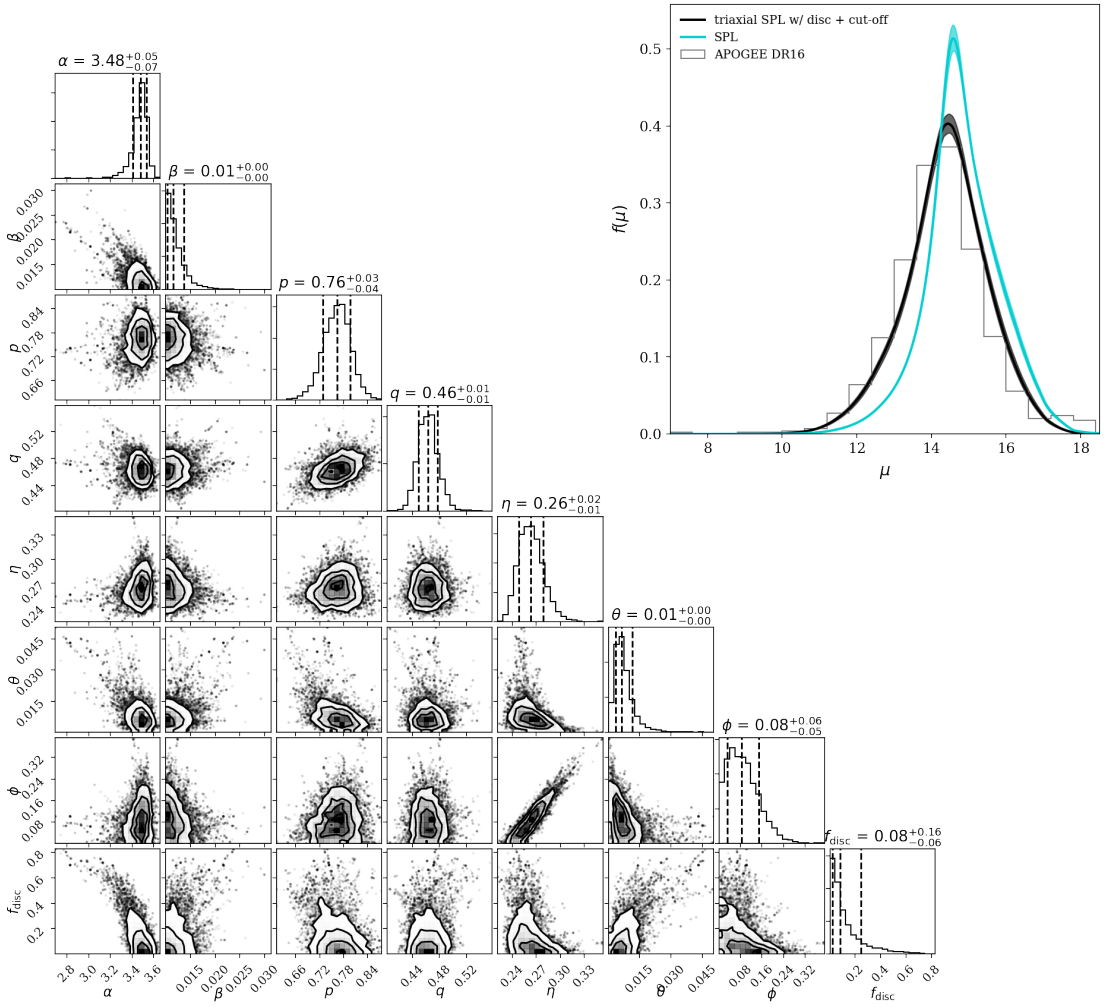

FIGURE 4.5: Corner plot showing the posterior 10,000 samples of the parameters for the adopted triaxial disc cut-off single power law (TRI-CUT-DISC) model when fit to the full statistical likely halo sample (1409 stars) between –2.5 < [Fe/H] < –1. The posterior distributions are well behaved, and converge to a median value. The best fit profile has a mildly steep power law of $\alpha \simeq 3.5$, and is slightly flattened along its Y and Z axes. The inset panel (top right) shows the distance modulus μ distribution predicted by the best fit model (black), and the best fit SPL (blue) of similar $\alpha \simeq 3.2$, where the thickness of each line signifies the 1-σ spread. The grey histogram represents the real APOGEE data, and shows that the TRI-CUT-DISC profile provides a better quality fit.

kpc). Furthermore, within the uncertainties, I find the total halo mass estimate to be in borderline agreement with the estimated 4-7 $\times$ 10^8 M$\odot$ from the review by Bland-Hawthorn & Gerhard (2016), and to be smaller than the$\sim$$10^9$ M$\odot$ estimate presented in the work of Deason et al. (2019), or the sum of individual MAPS in Mackereth et al. (2019b).

Density profile	Δ BIC	$\Delta \ln(\mathcal{L}_{\max})$
SPL	34.3	19.3
AXI	**0.0**	**0.0**
TRI	2.2	0.5
TRI-CUT-DISC	10.0	2.6
BPL	60.9	17.6
DISC	9.1	12.0

TABLE 4.1: Summary of the results for a sample of density profiles used to fit the N-rich star sample. The models tested are: a single power law (SPL), an axisymmetric power law (AXI), a triaxial power law (TRI), a triaxial power law with a disc and cut-off term (TRI-CUT-DISC), a broken power law (BPL), and an exponential disc (DISC). For each model, I report the Bayesian Information Criterion (BIC) and maximum logarithmic likelihood differences between the best fit model (bold) and the remaining models, calculated by taking 10,000 MCMC samples and using the median posterior parameter values.

4.4.2 Fitting the N-rich star sample

In this subsection, I describe the density modelling of the chemically defined N-rich stars. I test six different density profiles ranging in the number of free parameters, and calculate the $\ln(\mathcal{L}_{\max})$ and BIC values in order to estimate the best fit density profile. The models of choice are described in detail in Section 4.3.2, and are summarised as follows: a single power law (SPL), an axisymmetric power law (AXI), a triaxial power law (TRI), the triaxial disc cut-off profile used to fit the halo sample (TRI-CUT-DISC), a broken power law (BPL), and an exponential disc profile (DISC). Employing the method described in Section 4.3.3, I have obtained the BIC and $\ln(\mathcal{L}_{\max})$ for the six models tested, which are listed in Table 5.1. The fit of each profile to the N-rich star data is shown in Fig. C.1 in Appendix C.1. I draw 10,000 samples from the posterior of each model, for which I take the median value as the best fit parameters for each profile. I then compute the BIC and $\ln(\mathcal{L}_{\max})$. As is evident from the resulting BIC values from Table 5.1 (and from Fig. C.1), the AXI profile is the best fitting profile. However, I find the N-rich star sample can also be well fitted by the TRI-CUT-DISC and TRI profiles.

Once I obtain the best fitting profile, I perform the density fitting procedure described in Section 5.3 on the N-rich star sample, and obtain a density profile that provides an exquisite fit to the data. After running 10,000 MCMC iterations, I obtain a density profile with a slope of $\alpha = 4.47^{+0.23}_{-0.22}$, which is much steeper than that of the halo profile. Furthermore, I find the N-rich profile to have roughly the same flattening along the Z axis as the halo profile (namely, $q = 0.47^{+0.05}_{-0.04}$).

The resulting samples from the posterior distribution of parameters given by the data are shown in the corner plot illustrated in Fig. 4.6, which shows that the posterior distributions are well behaved and converge to a median value. In addition to the

resulting MCMC samples, I show the distance modulus μ distribution predicted by the best fit model (orange) and a spherical power law (blue) with an exponent that best fits the data ($\alpha \simeq 3.9$), compared to the real N-rich star APOGEE data. Using the best profile and APOGEE N-rich star counts, I obtain an N-rich normalisation $\rho_{0,\mathrm{N-rich}} = 3.1\ ^{+0.6}_{-0.5} \times 10^{-6}$ M$\odot$ pc^{-3}. Given the reasonable fit to the N-rich star data by the axisymmetric power law, I choose to use this profile as the best fitting N-rich density profile. However, I point out that the TRI and TRI-CUT-DISC profiles also provide a good quality fit to the N-rich star data, and yield a normalisation value that is consistent, within the uncertainties, with the value obtained for the AXI profile. Moreover, I find that when assessing the contribution of N-rich stars to the stellar halo field using either the TRI or TRI-CUT-DISC profiles as the best fitting N-rich star model, I obtain the same results as for the AXI profile, within the uncertainties.

The resulting density profiles for the halo (black) and N-rich star (orange) samples are displayed as a function of spherical radius in Fig. 4.7. It is clear that, while the halo density appears to decrease at a slower rate with increasing radius, the N-rich star sample exhibits a much greater decrease at high radii, and a much higher density within r $\lesssim$ 3 kpc, in comparison to the halo field population.

4.4.3 Contribution of dissolved/evaporated Globular Clusters to the stellar halo of the Milky Way

Under the assumption that N-rich stars result from GC dissolution, it is interesting to estimate the total stellar mass contained in dissolved GC stars, in order to assess their total contribution to the total stellar-halo mass budget. Besides an estimate of the contribution to the stellar-halo budget by stars that once belonged to GCs, another output from the method is the spatial distribution of those stars. In this section, I estimate the mass density contributed from the halo and N-rich samples respectively as given by the best fitting density models as a function of distance from the Galactic Centre. Then I estimate the ratio between the mass in N-rich stars and the total stellar-halo mass. To determine the total mass contributed by field stars from GC origin to the stellar halo, I assume the ratio of "first population" (FP) to "second population" (SP) stars in GC to be 2 SP stars for every 1 FP star, adopting the minimal scenario proposed by Schiavon et al. (2017b). Although other FP-to-SP GC star ratios have been proposed (e.g. Bastian & Lardo, 2015; Cabrera-Ziri et al., 2015), I chose to focus solely on the "minimal scenario" as it has been shown by Schiavon et al. (2017b) that other scenarios can be excluded due to the predicted total GC star number counts exceeding the expected number of total halo stars. I then take the ratio of the disrupted GC mass with halo mass, to assess the mass contribution of the former to the halo field as

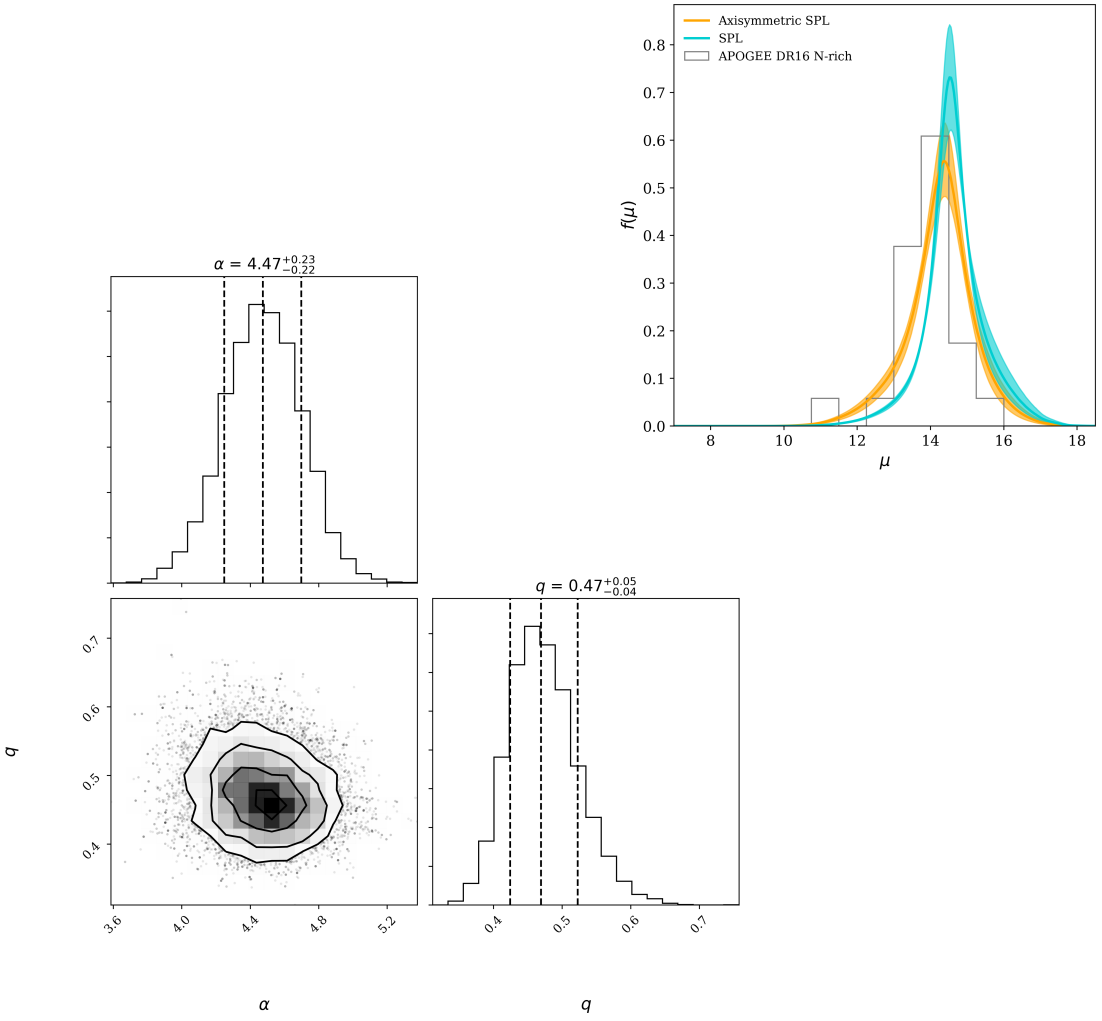

FIGURE 4.6: The same as in Fig. 4.5, however for the 46 N-rich stars displayed in Fig. 4.1 fitted by an axisymmetric single power law (AXI). As in Fig. 4.5, the posterior distributions are well behaved. The best fit model displays a steeper exponent $\alpha \simeq 4.5$ in comparison to the halo sample, but shows that it is similarly flattened along the Z axis. As in Fig. 4.5, the inset panel displays the predicted distance modulus μ distribution predicted by the best fit profile (orange) and a best fit SPL with $\alpha \simeq 3.9$ (blue), compared to the N-rich star data.

a function of Galactocentric distance. Performing this exercise will not only lead to a deeper understanding of the origin of disrupted GC stars (and in consequence N-rich stars), but it will also provide a more clear understanding of the mass contribution from GC destruction to the total stellar halo mass budget.

I determine the mass in spherical annuli for both N-rich and halo stars, which in turn enables us to determine the mass from each sample as a function of spherical radius, as well as the ratio between the samples. As mentioned above, to estimate the mass contribution by stars that once belonged to GCs, I need to account for the contribution by former GC stars whose abundance patterns do not differ from that of the field population at same metallicity, which can be accounted for by assuming the FP-SP GC star

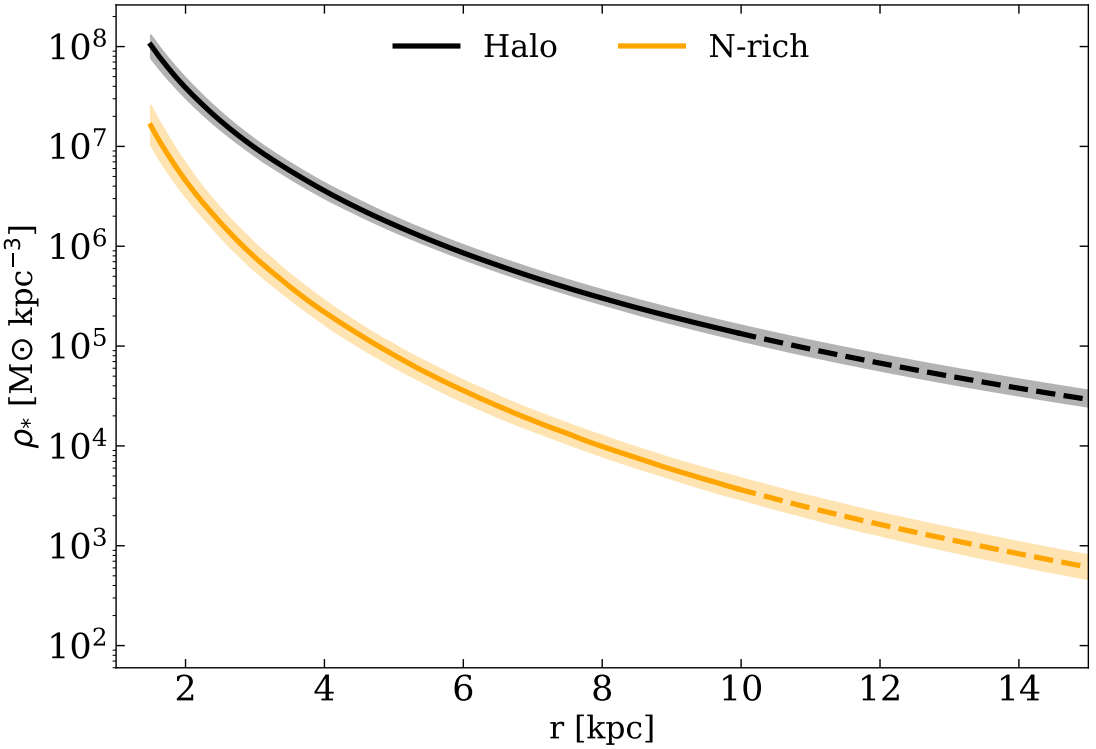

FIGURE 4.7: Integrated density as a function of spherical radius for the best fitting density profiles of the halo (black) and the N-rich (orange) star samples. The shaded regions mark the 16^{th} and 84^{th} percentile uncertainties. The dashed line indicates the region where, due to low sample numbers, the density is not strongly constrained. Both the halo and N-rich density profile follow a similar pattern within the outer r $\gtrsim$ 3 kpc region, however the N-rich density decreases more steeply.

ratio predicted from the minimal scenario.

Upon determining the density of both N-rich and halo stars as a function of Galactocentric distance, I focus the attention on estimating the ratio between N-rich stars and the total stellar halo. The results from this ratio estimation are shown as the black solid line in Fig. 4.8, where the N-rich to halo ratio, hereafter denoted as ζ, is given as a percentage. The shaded grey regions signify the 16^{th} and 84^{th} percentiles. In a similar fashion to Fig. 4.7, I choose to compute ζ between a $1.5 < r < 15$ kpc range, for which is covered relatively well by the data. the results show that ζ increases rapidly with decreasing radius, growing from a value of $\zeta = 2.7^{+1.0}_{-0.8}\%$ at r = 10 kpc to a value of $\zeta = 16.8^{+10.0}_{-7.0}\%$ at r = 1.5 kpc. Moreover, around the solar neighbourhood (i.e., r = 8 kpc), I find the ratio to be $\zeta = 3.3^{+1.1}_{-1.0}\%$. Therefore, the estimates reveal approximately an eight-fold increase of the N-rich star to halo contribution in the inner Galactocentric regions, in agreement with previous findings (Schiavon et al., 2017b).

Under the assumption of the minimal scenario presented in Schiavon et al. (2017b), whereby the ratio of FP to SP is 1-to-2, I estimate the ratio of dissolved GC stars to halo field stars to be $\zeta_{\rm tot} = 27.5^{+15.4}_{-11.5}\%$ at r = 1.5 kpc. Along the same lines, I

obtain an estimate of $\zeta_{\rm tot} = 4.2^{+1.5}_{-1.3}\%$ at r = 10 kpc. the results show that when accounting for selection effects in the observational data, the contribution of stars arising from GC dissolution and/or evaporation to the total stellar halo field is greater by a factor of$\sim$7-9 in the inner few kiloparsecs when compared to the outer regions of the Galaxy. Furthermore, I report that when repeating the methodology employing another well fitting density profile for the N-rich stars (in this case the TRI and TRI-CUT-DISC models), I find that, within the uncertainties, the results remain unchanged, thus validating both the estimates and procedure.

Now that I have shown the mass fraction contribution of stars arising from GC disruption to the halo field of the Galaxy as a function Galactocentric distance, I can compute an estimation of the mass contributed from GC escapees to any given volume or spherical shell. I chose to estimate the mass contributed by stars arising from GC destruction, under the minimal scenario assumption, within a volume spanning a radius between 1.5 and 3 kpc from the Galacic centre. For this shell volume, I obtain a total mass from stars arising from GC dissolution of $\rm M_{GC,inner} = 5.6^{+2.8}_{-1.8} \times 10^7$ M$\odot$. Similarly, I compute the total mass of stars arising from GC disruption within a shell of$\sim$13.5 kpc in radius (from 1.5 kpc to 15 kpc), and find a mass estimate of $\rm M_{GC,total} = 9.6^{+4.0}_{-2.6} \times 10^7$ M$\odot$. Thus, the results show that disrupted GC stars contribute a significant amount of mass to the stellar halo of the Galaxy. This notable mass contribution is observed at all Galactocentric scales, however is more dominant at smaller radii, as shown in Fig. 4.8.

4.5 Discussion

The results obtained in Fig. 4.8 suggest that the fraction of N-rich star mass as a function of halo field mass is much greater in the inner regions of the Galaxy when compared to the outer regions. In agreement with observational estimates (Martell & Grebel, 2010; Carollo et al., 2013; Martell et al., 2016; Schiavon et al., 2017b; Fernández-Trincado et al., 2019; Koch et al., 2019; Lee et al., 2019), and theoretical predictions (Tremaine et al., 1975; Gnedin et al., 2014; Reina-Campos et al., 2019; Hughes et al., 2020), I hypothesise that N-rich stars result from the destruction of pre-existing GCs. Assuming this hypothesis is correct, the findings may have important repercussions for the current understanding of the formation and evolution of the Galactic GC system, the presence of multiple stellar populations in GCs, possibly the formation and evolution of the Milky Way bulge, and even the mass assembly history of the Galaxy. In the following subsections, I discuss and compare the results from the stellar halo density modelling and mass estimation to previous work.

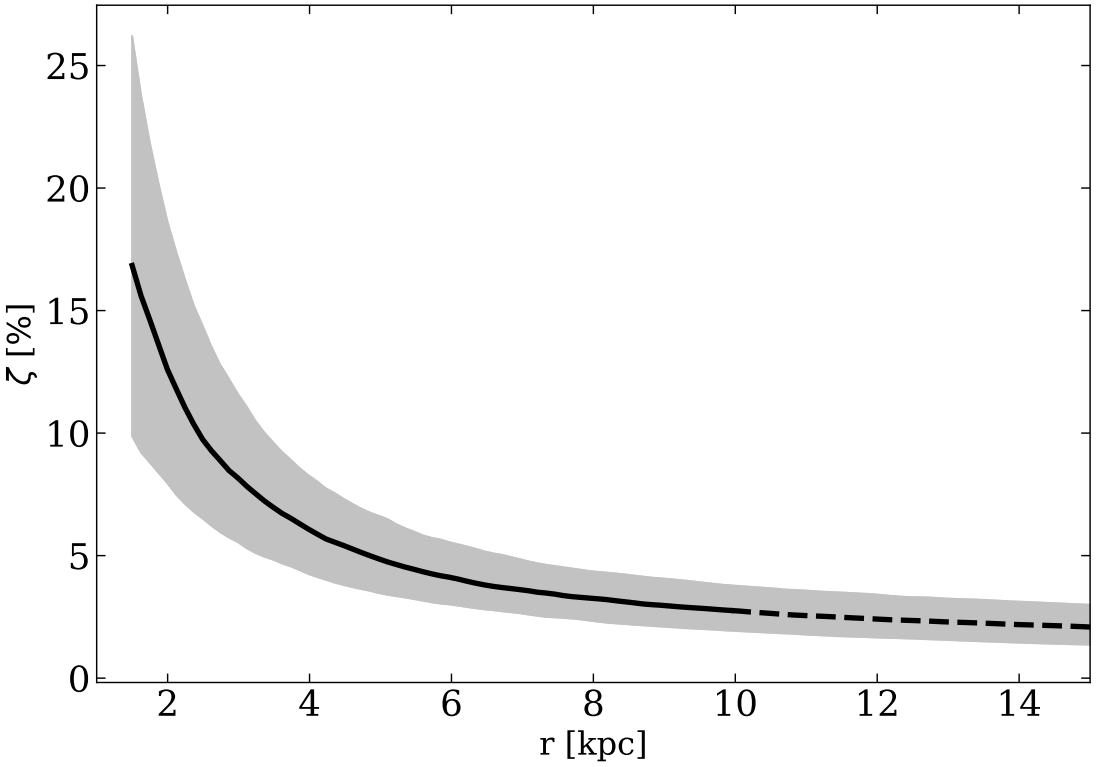

FIGURE 4.8: Mass density percentage ratio of N-rich stars and halo field stars as a function of spherical radius. The black solid line signifies the median value, while the shaded regions show the 16^{th} and 84^{th} percentile uncertainties. The dashed line indicates the Galactocentric distance range where the density is not well constrained due to low numbers of N-rich stars. The mass density percentage ratio drops from $\zeta = 16.8^{+10.0}_{-7.0}\%$ at r = 1.5 kpc to a value of $\zeta = 2.7^{+1.0}_{-0.8}\%$ at r = 10 kpc. Under the minimal scenario assumption, one can multiply ζ by 1.5, and subtract the FP stars from the halo field, to obtain the total contribution from disrupted GC stars to the stellar halo.

4.5.1 Comparison with previous halo density work

In this section, I perform a detailed comparison of the findings with those from previous works. The contrasting method employed in this work allows for an interesting comparison, one that will help shed light into the nature of the density of the stellar halo of the Galaxy.

The majority of early work focused on modelling the density of the Galactic stellar halo employed different stellar types as tracers of the halo population, including either Main Sequence Turn Off (MSTO) stars (Morrison et al., 2000; Jurić et al., 2008) or Blue Horizontal branch (BHB) stars (Yanny et al., 2000), for which the photometry is relatively easily calibrated to provide accurate distances [5]. By fitting single power-law

[5]Listed in this subsection are only a few of the more recent examples of an extensive list of studies focused on estimating the density of the stellar halo. For a more comprehensive account of previous work see Helmi (2008).

models of the form:

$$\rho(r_{\rm e}) = r_{\rm e}^{-\alpha}, \tag{4.11}$$

these groups found an exponent of $\alpha\sim3$ and find a flattening requirement (given by Eq 4.2 when equating $p = 1$) to fit star counts well. A pivotal work by Deason et al. (2011) showed that BHB stars in SDSS could be best fit by introducing a break radius at $r_{\rm b}\sim27$ kpc in their exponential profile, thus fitting a broken exponential, for which the inner slope is shallow $\alpha_{\rm in}\sim2.3$, and the outer slope is steep, $\alpha_{\rm out}\sim4.6$. Along those lines, Whitten et al. (2019) used a BHB sample from a cross-match of Pan-STARRS and GALEX data, and studied their relative age-distribution across the Galactic halo. The results from this work showed that the BHB relative age-distribution of the Milky Way is also best modelled by a broken profile, finding an older population within the ($R_{\rm GC}\sim14$ kpc) break radius. Another crucial study by Xue et al. (2015) used SDSS-SEGUE giants to show that such a profile can be accommodated with a single power law of steep exponent $\alpha\sim4.2$, with flattening parameter q varying as a function of Galactocentric distance between $q\sim0.5$ and 0.8. Later, Iorio et al. (2018) found that a similar profile provided a good fit to a sample of RR Lyrae stars within a Galactocentric distance of$\sim$30 kpc, such that $\alpha\sim2.96$ with $0.57 < q < 0.75$. A recent study found that the APOGEE DR14 giant data were best fit by a similar single power-law profile, however with the inclusion of a disc and cut-off term (Mackereth et al., 2019b), such as the model employed to fit the halo sample in this study. The power law slope obtained for this model was found to be steep $\alpha\sim3.5$, presenting a flattened triaxial ellipsoid, $p\sim0.73$ and $q\sim0.56$, slightly rotated in the Z and Y axes.

The behaviour resulting from the fit to the APOGEE data is similar to work from the literature. Fitting a likely halo sample of stars with metallicities between –2.5 < [Fe/H] < –1, I find the data are well matched by a triaxial profile with a moderately steep exponent $\alpha\sim3.5$, flattened with $p\sim0.8$ and $q\sim0.5$. I also find the triaxial ellipsoid to be minorly rotated to the Z and Y axes, by $\theta\sim3$-4 degrees and $\phi\sim14$ degrees, respectively. Finally, since the data is all contained within a $\sim$20 kpc radius, the issue of flattening beyond the break radius found in other studies is irrelevant to this work. Thus, I can conclude that the resulting profile and its associated parameters values are consistent with the results found in previous studies.

4.5.2 The contribution of GCs to the stellar halo of the Galaxy

4.5.2.1 Mass ratio of stars arising from GC dissolution and/or evaporation

Employing the method described in Section 5.3, I have assessed the fraction of the halo stellar mass contributed by N-rich stars as a function of Galactocentric distance between

$1.5 < r < 15$ kpc. I have shown that N-rich stars contribute a $\zeta = 16.8^{+10.0}_{-7.0}\%$ to the halo field at$\sim$1.5 kpc from the Galactic Centre (see Fig. 4.8), resulting in a much larger contribution when compared to the outer regions of the Galaxy (i.e. r$\sim$10 kpc) for which I find a ratio of $\zeta = 2.7^{+1.0}_{-0.8}\%$. Under the assumption of the minimal scenario proposed by Schiavon et al. (2017b), whereby the ratio of FP-to-SP GC star is assumed to be 2 SP stars for every 1 FP star, I estimate the total contribution from disrupted star clusters$\sim$1.5 kpc from the Galactic Centre to be $\zeta_{\rm tot} = 27.5^{+15.4}_{-11.5}\%$. Along those lines, I estimate the contribution from GC dissolved stars to the stellar halo at r = 10 kpc to be $\zeta_{\rm tot} = 4.2^{+1.5}_{-1.3}\%$. Within the uncertainties, the estimate for the contribution by stars that once belonged to GCs to the stellar halo mass budget at Galactocentric distances of r = 10 kpc is in agreement with the low bound of the 2-5% estimate from the literature for the halo of the Galaxy (Martell et al., 2016; Koch et al., 2019; Reina-Campos et al., 2019). Similarly, the estimate for the contribution at r = 1.5 kpc from the Galactic Centre is in agreement with the 19-24% estimate from Schiavon et al. (2017b), but is only partly in agreement with the theoretical predictions from Hughes et al. (2020). Specifically, within the uncertainties, the estimate falls in the upper range of the predictions provided by the E-MOSAICS suite of simulations, which predict a contribution ranging between 0.3 and 14% for Milky Way analogs, depending on a galaxy's accretion history.

Interestingly, the largest fractional contribution to the stellar mass budget by disrupted globular clusters is attained in the simulations by Hughes et al. (2020) by galaxies that underwent a phase of intense accretion in their early lives. Mackereth et al. (2018), analysing EAGLE simulations (Schaye et al., 2015; Crain et al., 2015) established a link between those types of accretion histories with the (rare) presence of an α bimodality in the simulated galaxies' disk populations. According to Hughes et al. (2020), the physical basis for this connection is the high gas pressure brought about by intense accretion which, on one hand lowers the gas consumption timescale leading up to formation of an α-enhanced population, and on the other hand creates an environment that is hostile to globular cluster survival.

In this context, it is important to notice that (Kisku et al., 2021) studied the abundance patterns of N-rich stars in the inner Galaxy, suggesting that roughly 1/2 of the N-rich stars with [Fe/H] < -1 were actually accreted, and were likely associated with Heracles identified by Horta et al. (2021a).

4.5.2.2 Mass in dissolved GCs

As mentioned in Section 4.4.3, the methodology enables us to determine the mass for both the stellar halo and for N-rich stars within a sphere of any given radius. Under

the minimal scenario assumption (see Section 4.4.3), I estimate a total stellar mass arising from GC remnants, within a shell ranging from 1.5 – 15 kpc in radius around the Galactic Centre, to be $M_{GC,total} = 9.6^{+4.0}_{-2.6} \times 10^7$ M$\odot$. the estimates confirm theoretical predictions by different groups ($\sim 10^7$ - 10^8 M$\odot$, Tremaine et al., 1975; Gnedin et al., 2014). Furthermore, I find that the estimated mass from stars arising from GC disruption and/or evaporation to be approximately$\sim$3-4 times greater than the total mass in all existing Galactic GCs ($\sim 2.8 \times 10^7$ M$\odot$, Kruijssen & Portegies Zwart, 2009). This result would imply that the Galactic GC system was initially four to five times larger, where approximately only one fourth/fifth survived, resulting in the$\sim$150 GCs observed today. However, due to the metallicity cuts employed in this study, the estimated mass is biased low, since it does not include the mass from stars arising from disruption and/or evaporation of GCs with [Fe/H] > -1. Moreover, the estimate only accounts for GCs that were massive enough to develop multiple populations (MP). It is likely that GCs were formed with masses below that threshold that nevertheless were destroyed, contributing only FP stars to the field population. Those of course are not accounted for by the chemical tagging, so that the estimated contribution of GCs to the stellar mass budget of halo field populations should be taken as a lower limit.

By the same token, since the results show that there is a much higher contribution of dissolved GC stars in the inner galaxy, I estimated the total stellar mass arising from GC disruption, within a hollow sphere of 1.5 - 3 kpc in radius around the Galactic Centre, to be $M_{GC,inner} = 5.6^{+2.8}_{-1.8} \times 10^7$ M$\odot$. I find the estimate to be greater than the predicted$\sim 10^7$ M$\odot$ from Gnedin et al. (2014). Similarly, within the uncertainties, I find the result to be slightly smaller than the estimate given in Schiavon et al. (2017b), who found that the mass in destroyed GCs within 2 kpc to be a factor of 6-8 higher than the mass of existing GCs. The difference is due to three factors: (1) the different volumes included in the calculation; (2) the different models for the inner halo adopted, and (3) the different metallicity ranges considered.

4.5.3 Supporting evidence for the GC origin of N-rich stars

Despite the growing evidence for the GC origin of N-rich stars, there have been many alternate scenarios proposed for the formation of such population. Such alternative formation channels range from the notion that N-rich stars are the oldest stellar population in the Galaxy which formed in high density environments (Bekki, 2019), to the idea that N-rich stars were formed in the same molecular clouds that GCs were formed in, however were never gravitationally bound to them. In this subsection, I discuss the results from

previous studies which have shown, using measurements other than chemical compositions, that N-rich stars are likely formed from the dissolution and/or evaporation of GCs.

The availability of the 6D phase space information provided by the *Gaia* survey has made possible the estimation of the integrals of motion (hereafter IoM) of stars in the Milky Way. Such properties are adiabatic invariants, and thus retain some information about the origin of their parent population. A recent study by Savino & Posti (2019) determined the IoM for a sample of 65 CN-strong stars, from the work by Martell & Grebel (2010), as well as for the Galactic GC system. In their study, a direct comparison of the IoM values, as well as the metallicity values, was performed for every N-rich-GC pair, associating a likelihood of these being from the same distribution. The results from that study showed that a considerable fraction of CN-strong stars display the same IoM values as existing GCs, thus supporting the notion that N-rich stars arise from GC dissolution and/or evaporation.

A similar chemo-dynamical analysis of halo stars and Galactic GCs was performed by Hanke et al. (2020). In that study, three separate methodologies were employed to attempt to link halo stars to existing GCs. These ranged from statistically linking halo stars positioned nearby existing Galactic GCs, to linking CN-strong stars (i.e. N-rich stars) kinematically to existing GCs, to attempting to find halo stars which displayed similar kinematics to those CN-strong stars. The authors showed that over 60% of their N-rich star population presented IoM which could be statistically linked to known GCs, and that around$\sim$150 halo stars could be associated with a GC origin. Separately, a study by Tang et al. (2020) performed a comparison between the IoM of$\sim$100 CN-strong (metal poor) stars from the LAMOST DR5 data set with metal poor halo stars. The authors from this study concluded that the CN-strong stars do not present similar kinematics to the halo field population, but resembled that of the inner halo where there is a high density of GCs with similar chemical compositions. Based on their kinematic results, the authors supported a GC origin for the CN-strong stars. In a final remark, I find the findings of Tang et al. (2020) to be in agreement with the results from Carollo et al. (2013). Using an independent sample CN-strong stars, these authors found that these follow the velocity distribution of the "inner halo population" (IHP, as defined in their work).

The kinematic results from the aforementioned work, when coupled with the results from chemical composition studies (e.g., Martell & Grebel, 2010; Martell et al., 2016; Schiavon et al., 2017b; Koch et al., 2019; Lee et al., 2019), support the hypothesis that N-rich stars arise from the disruption and/or evaporation of GCs.

4.6 Summary and Conclusions

In this Chapter, I report a study of the spatial variation of the density of N-rich and normal halo field stars. In this way I assessed the contribution of N-rich stars, and by inference that of dissolved GCs, to the stellar mass budget of the Galactic halo, as well as its variation as a function of Galactocentric distance. A summary of the results is listed as follows:

- I identified in a parent sample of 1455 halo stars with –2.5 < [Fe/H] < –1, using a Gaussian Mixture Model, 46 N-rich stars that are distributed throughout the Galaxy (see Fig. 4.1 and Fig. 4.4), and are not bound to existing GCs. The N-rich stars present a N-C abundance anti-correlation and an N-Al abundance correlation (see Fig. 4.3 and Fig. 4.2, respectively), and are likely second population stars that once were bound to a GC (which may or may not still exist) and now reside in the halo field of the Galaxy.

- I show that once the survey selection effects are accounted for (see Appendix A in Mackereth et al., 2019a for details), the halo APOGEE data between –2.5 < [Fe/H] < –1 are well fit by a triaxial single power law with exponent $\alpha\sim3.5$, and flattening parameters $p\sim0.8$, $q\sim0.5$, with major axis only slightly misaligned with the axis connecting the Sun and the Galactic centre.

- Similarly, I show that the APOGEE N-rich star data between –2.5 < [Fe/H] < –1 are well fit by an axisymmetric profile, defined by a single power law of slope $\alpha\sim4.5$. The best fitting model is flattened along the Z axis, with a flattening value similar to that of the halo sample $q\sim0.5$ (see Fig. 4.6).

- I find a contribution of N-rich stars to the stellar halo of $\zeta = 16.8^{+10.0}_{-7.0}\%$ at r = 1.5 kpc. However, this ratio drops by a factor of ∼6 at large Galactocentric distances (r = 10 kpc), where I estimate a contribution of $\zeta = 2.7^{+1.0}_{-0.8}\%$.

- Assuming that the ratio of first population-to-second population stars in GCs is 1-to-2, I find that stars arising from GC disruption contribute $\zeta_{\rm tot} = 27.5^{+15.4}_{-11.5}\%$ to the mass of the stellar halo at∼1.5 kpc from the Galactic Centre. Conversely, the contribution of GC escapees at larger Galactocentric distances (i.e. r = 10 kpc) is lower, namely $\zeta_{\rm tot} = 4.2^{+1.5}_{-1.3}\%$. Such estimates are in agreement (within the uncertainties) with previous estimates from the literature for the inner Galaxy (e.g., Schiavon et al., 2017b) and the outer Galactic halo (e.g., Martell et al., 2016; Koch et al., 2019).

- I integrate the total stellar mass between –2.5 < [Fe/H] < –1 and 1.5 < r < 15 kpc using Eq 4.8 and the best-fitting halo profile, and estimate the mass of the stellar halo to be $M_{*,halo} = 8.3\ ^{+1.5}_{-1.3} \times 10^{8}$ M$\odot$.

- I integrate the total stellar mass between –2.5 < [Fe/H] < –1 and 1.5 < r < 15 kpc using Eq 4.8 and the best-fitting N-rich model, and estimate the mass from N-rich stars to be $M_{*,N-rich} = 6.4\ ^{+2.6}_{-1.7} \times 10^{7}$ M$\odot$.

- Using the same technique, and under the assumption of a 1:2 first:second population GC ratio, I estimate the total stellar mass between –2.5 < [Fe/H] < –1 and 1.5 < r < 15 kpc arising from GC dissolution and/or evaporation to be $M_{GC,total} = 9.6\ ^{+4.0}_{-2.6} \times 10^{7}$ M$\odot$. For a spherical volume ranging from 1.5-3 kpc, I obtain an estimated mass of $M_{GC,inner} = 5.6^{+2.8}_{-1.8} \times 10^{7}$ M$\odot$. This total dissolved/evaporated GC mass is approximately 3-4 times greater than the total mass in all existing Galactic GCs (namely, $\sim$2.8$\times10^{7}$ M$\odot$ Kruijssen & Portegies Zwart, 2009).

- I speculate that the increased contribution of GC dissolution towards the inner regions of the Galaxy may be associated with enhanced merger activity in the early life of the Milky Way. Some of these merging systems (e.g., Heracles Horta et al., 2021a) may have brought with them a population of extragalactic N-rich stars (Kisku et al., 2021). In addition, the enhanced merging activity in the early life of the Milky Way may also have given rise to conditions that led to efficient *in situ* formation and destruction of GCs, leaving behind a large population of N-rich stars in the inner Galaxy field.

In this Chapter, I have mapped the spatial distribution of N-rich stars in the Galactic halo, determining their contribution to the stellar mass budget as a function of Galactocentric distance.

The results presented in this chapter constrain the mass contribution from GC disruption and/or evaporation to the total mass of the stellar halo, but also provide insights into the mass assembly history of the Milky Way. In the future, the order of magnitude increase in halo samples afforded by upcoming surveys such as WEAVE (Dalton et al., 2014) and 4MOST (de Jong et al., 2019) will place key constraints on the understanding of the mass assembly of the Milky Way halo, and the role played by GCs in this process.

Chapter 5

On the chemical properties of globular clusters in the Milky Way

5.1 Introduction

Globular clusters (GC) retain pivotal clues that help reconstruct the mass assembly history of galaxies like the Milky Way (see Chapter 1 and Chapter 4 for further details). However, the nature and origin of GCs in the Galaxy is another important and interesting astrophysical question that still remains unanswered. For decades, this has been the focus of various studies (e.g., Searle & Zinn, 1978; Fall & Rees, 1985; Ashman & Zepf, 1992; Brodie & Strader, 2006), aiming at using age, chemical composition, and phase-space information in order to, on one hand, understand the origin of the Galactic GC system, and on the other constrain the early history of mass assembly of the Milky Way. Key to that enterprise is to discern which of the Galactic GCs were formed *in situ* and which were accreted. In the last decade, the availability of precise ages (Marín-Franch et al., 2009; VandenBerg et al., 2013) has led to the discovery of the bifurcation in the age-metallicity relation of Galactic GCs (Marín-Franch et al., 2009; Forbes & Bridges, 2010; Leaman et al., 2013), which, combined with results from high-resolution hydrodynamical cosmological simulations of Milky Way analogues, has further constrained the origin the Galactic GC system (Kruijssen et al., 2019b; Myeong et al., 2019). Furthermore, the advent of the Gaia survey (Gaia Collaboration, 2018), and the resulting precise 6D phase-space information have made possible a much better characterization of the properties of the Galactic GC system.

Along those lines, a recent study by Massari et al. (2019) presented a new classification of the Galactic GC system in terms of the kinematic properties of its members. By studying their distribution in integral of motions (hereafter, IOM) space, Massari et al. (2019) established an association of each GC to one of the following main groups: Main Disk (MD), Main Bulge (MB), Gaia Enceladus (GE), Sagittarius (Sag), Helmi Streams (H99), Sequoia (Seq), Low Energy (LE) and High Energy (HE).

The 16th data release of the Sloan Digital Sky Survey (DR16: Ahumada et al., 2019a) includes data for over 450k stars from the APOGEE survey (Majewski et al., 2017), placing us in an advantageous position to obtain detailed chemical-abundance information for stars that are members of a significant fraction of the total Galactic GC population (Mészáros et al., 2015; Schiavon et al., 2017b; Mészáros et al., 2018; Masseron et al., 2019; Nataf et al., 2019). Such data will substantially further the understanding of the origin of the Galactic GC system, and in the process will help constrain the assembly history of the Milky Way. In this paper, I present an examination of the chemical properties of the GC groups identified by Massari et al. (2019). the goal is to check whether subgroups that are defined purely on the basis of orbital properties can also be distinguished in terms of their chemical properties. In the process it is also possible to verify whether the chemical compositions are consistent with the star formation and chemical enrichment histories expected from the systems they are associated with. In this chapter, I present results aimed at disentangling the origin of the Galactic GC system via a careful examination of their chemical abundance compositions, using a GC catalogue determined using the sixteenth data release of the APOGEE survey (Section 5.2). In detail, in Section 5.3 I describe the sample used and the criteria adopted to define GC membership; in Section 5.4 I present the results obtained from the examination of the chemical properties of the kinematically defined GC groups; and in Section 5.5 I summarise the findings of this chapter and present the main results and conclusions.

5.2 Data

I use data from the sixteenth data release of SDSS-IV (Ahumada et al., 2019a), which contains refined elemental abundances (Jönsson et al., 2020) from the APOGEE-2 survey (Majewski et al., 2017), which is one of four SDSS-IV (Blanton et al., 2017) experiments. APOGEE-2 is a near-infrared high-signal-to-noise ratio (S/N $>$ 100 pixel^{-1}), high-resolution (R $\sim$22,500) spectroscopic survey of over 450,000 Milky Way stars in the near-infrared H Band (1.5–1.7 μm). Observations were based on two twin NIR spectrographs (Wilson et al., 2019) attached to the 2.5 m telescopes at Apache Point (Gunn et al., 2006), and Las Campanas Observatories. Targets were selected in general from

the 2MASS point-source catalogue, employing a dereddened $(J-Ks) \geq 0.3$ colour cut in up to three apparent H magnitude bins. Reddening corrections were determined using the Rayleigh-Jeans Colour Excess method (RJCE; Majewski et al., 2011), based on NIR photometry from the 2MASS point source catalogue (Skrutskie et al., 2006), and mid-IR data from the Spitzer-IRAC GLIMPSE-I,-II, and -3D (Churchwell et al., 2009) when available from WISE (Wright et al., 2010). A more in-depth description of the APOGEE survey, target selection, raw data, data reduction and spectral analysis pipelines can be found in Majewski et al. (2017), Holtzman et al. (2015), Nidever et al. (2015),García Pérez et al. (2016), Jönsson et al. (2018), Zasowski et al. (2017), respectively. All the APOGEE data products used in this paper are those output by the standard data reduction and analysis pipeline. The data are first processed (Nidever et al. (2015) & Jönsson et al, in prep.) before being fed into the APOGEE Stellar Parameters and chemical-abundances Pipeline (ASPCAP; García Pérez et al., 2016, Jönsson et al in prep). ASPCAP makes use of a specifically computed spectral library (Zamora et al., 2015; Holtzman et al., 2018, and Jönsson et al, in prep), calculated using a customised H-band line-list (Shetrone et al., 2015, Cunha et al., in prep.), from which the outputs are analysed, calibrated, and tabulated (Holtzman et al., 2018).

5.3 Globular cluster sample and membership

5.3.1 Main sample

In this subsection, I describe the method employed for determining the GC sample in APOGEE DR16. I build on previous work that has derived a GC sample in earlier data releases of APOGEE (Mészáros et al., 2015; Schiavon et al., 2017b; Nataf et al., 2019) and use the GC catalogues from Harris (1996), Baumgardt & Hilker (2018) and Baumgardt et al. (2019) in order to establish GC membership of stars in the DR16 sample. The methodology employed for identifying GC members is two-fold: the first step comprises the determination of an initial sample based on the values from the aforementioned catalogues. For this, I make use of data on GC positions (Galactic latitude and longitude), radial velocities, the radial velocity dispersions, tidal radii and mean metallicity values.

I use these values, and the values provided by APOGEE DR16 catalogue, to associate any star to be a member of a GC if:

$i) \mid [\mathrm{Fe/H}]_{\star} - \langle [\mathrm{Fe/H}]_{GC} \rangle \mid \leq 0.5$

ii) $\mid rv_{\star} - \langle rv_{GC} \rangle \mid \leq 2\,\sigma_{GC}$

iii) $d_{proj} \leq 2\,r_{vir}$

where [Fe/H] is the iron abundance, $rv_{\star}$ is the stellar heliocentric radial velocity, σ_{GC} is the cluster's radial velocity dispersion, d_{proj} is the projected distance between the star and the GC centre, and r_{vir} is the cluster's tidal radius. For GCs which are known to present a spead in metallicity (namely, NGC 6715, Terzan 5 and ω Cen), criterion *i*) was ommitted. The GC iron abundances and centre coordinates were extracted from the 2010 edition of the Harris catalogue (Harris, 1996), whereas the GC radial velocities, velocity dispersions, and tidal radii were obtained from the latest versions of the Baumgardt & Hilker catalogue[1],[2] (Baumgardt & Hilker 2018; Baumgardt et al. 2019). The stellar data come from APOGEE.

The first step of the procedure consisted of the application of criteria *(i)* to *(iii)* above, which yielded a preliminary sample of ∼3,650 stars. Having obtained this preliminary sample, the second step involved examining the metallicity distribution functions (MDFs) of the candidates selected in the first pass, which adopted a very broad [Fe/H] search interval. If the MDF peaked at a value within 0.3 dex from the Harris catalogue value, and the distribution did not present tails of more than 0.3 dex away from the mean [Fe/H] value, all candidates were deemed GC members. For those cases in which the MDF peaked within 0.3 dex of the Harris catalogue value, but presented a broader, less peaked, distribution, the sample was further cleaned through σ-clipping, as follows. I computed the mean and standard deviation of the [Fe/H] values, and then conducted the σ-clipping procedure by removing any member candidates that presented [Fe/H] abundances 1 σ away from the mean. However, for most GCs the resulting clipped MDF still presented tails in the distribution, so I had to perform a second σ clipping, removing stars that deviated from the mean [Fe/H] value by more than 2 times the newly computed σ value. Figure 5.1 illustrates the σ-clipping method employed and how successfully it works in defining GC candidate members from our initial sample, removing any false positives. For a full visualization of all the MDF cuts performed on the 43 GCs in the final main GC sample and the resulting radial velocity distribution, see Appendix D.1. I found that, by conducting this methodology, I was able to minimise false positives and obtain a reliable sample of GC members in APOGEE DR16. For 11 GCs from the original sample, fewer than 3 star members could be identified, so these GCs were removed from consideration.

[1] `http://physwww.mcmaster.ca/~harris/mwgc.dat`
[2] `https://people.smp.uq.edu.au/HolgerBaumgardt/globular/`

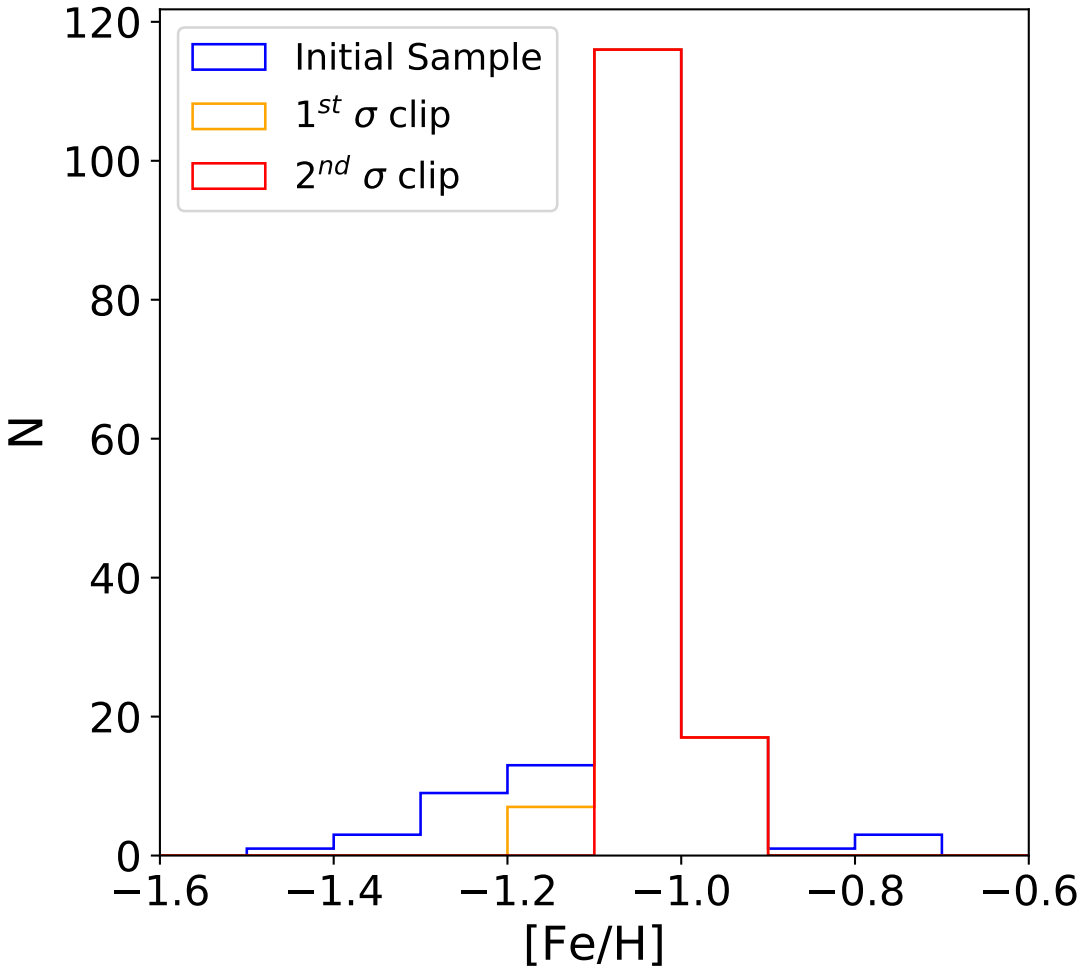

FIGURE 5.1: Example of the σ-clipping method employed to determine GC candidate members from the initial sample. The mean metallicity value from the Harris catalogue for NGC 6121 is [Fe/H] = –1.16, which lies very close to the peak of the distribution of our sample.

The final sample contained 3,090 stars, associated with 46 GCs. Our selection procedure is quite conservative and likely excludes GC members. However, sample purity is more important for the goals than completeness. The mean elemental abundances, *rv* values, and associated standard deviations for the member stars for each GC are listed in Table 5.1. For GCs with large [Fe/H] spreads (namely, ω Cen, NGC 6715 and Terzan 5), mean abundances are not entirely meaningful. Moreover, in such cases the mean abundance ratios do not necessarily reflect those of the environments the GCs were born. Therefore, I removed these clusters from consideration. With this additional cut, the final working sample contains 1728 stars associated with 43 GCs.

Recently, Mészáros et al. (2020) performed a careful GC membership analysis, obtaining a sample that is very similar to ours. They proceeded to study star-to-star internal abundance variations in GCs, with data based on the BACCHUS (Masseron et al.,

2016) abundance pipeline. I have repeated our entire analysis adopting both (Mészáros et al., 2020) member sample and abundances and obtained the same results as presented in this paper.

5.3.2 Globular cluster groups

In this subsection I briefly discuss how the GCs in the sample are distributed across the kinematic groups defined by Massari et al. (2019) (see Fig 5.2). From the main sample of 43 GCs, I find that 9 can be associated to the MD group, 10 to the MB, 9 to the GE dwarf spheroidal, 5 to the H99, 6 to the LE group and 1 to the Seq dwarf spheroidal. An additional 5 GCs from the sample could not be unambigously associated to a single group by Massari et al. (2019). The GC NGC 3201 could be associated to either of the GE or Seq group, NGC 5904 could belong to either GE or H99, and Liller 1 is listed as unclassified. Similarly, NGC 6388 is originally classified as a MB GC by (Massari et al., 2019). However, recent work has shown that NGC 6388 can be associated to the Sequoia accretion event based on its eccentric-retrograde orbit (Myeong et al., 2019). For this work, I initially follow the Massari et al. (2019) classification and include NGC 6388 in the MB subgroup, and study its chemical-abundances in order to discern if this GC is from *in situ* or accreted origin. Along the same lines, since it has recently been shown that NGC 3201 could be associated kinematically to the Sequoia dwarf remnant (Myeong et al., 2019), I choose to include these GCs in the Seq group. The remaining two GCs for which Massari et al. (2019) do not find a clear subgroup association (namely, NGC 5904 and Liller 1) are initially marked as unclassified and are discussed in Section 5.4.3. For the final list of the GCs obtained in the main sample and the kinematic group association see Table 5.3.

5.3.3 Elemental abundances and orbital parameters

In this paper, I report an examination of the APOGEE DR16 chemical-compositions for GCs from various subgroups. Specifically, I focus on studying trends in α-element abundances as a function of [Fe/H] to gain insights into the nature of the subgroups. Our goal is to examine how the kinematic classification by Massari et al. (2019) maps into chemical composition space. In so doing I expect to constrain the nature of the progenitors of the various sub-systems making up the Galactic halo, given the relation between chemical compositions stellar populations and their histories of star formation and chemical enrichment. This also makes possible a more clear distinction between GCs formed *in situ* from those belonging to accreted systems

Name	<[Fe/H]>	<[Si/Fe]>	<V_{los}> (km/s)	Name	<[Fe/H]>	<[Si/Fe]>	<V_{los}> (km/s)
NGC 104	–0.72±0.04	0.23±0.04	–18.8±7.3	NGC 6397	–2.02±0.04	0.3±0.06	19.5±2.8
NGC 288	–1.26±0.04	0.29±0.03	–44.5±2.2	NGC 6441	–0.39±0.12	0.13±0.13	10.8±15.3
NGC 362	–1.09±0.04	0.13±0.04	223.6±5.3	NGC 6522	–1.04±0.06	0.22±0.10	–12.8±7.6
NGC 1851	–1.07±0.04	0.14±0.05	320.7±5.9	NGC 6539	–0.39±0.09	0.2±0.07	33.8±4.4
NGC 1904	–1.5±0.07	0.15±0.04	207.4±2.6	NGC 6540	–1.01±0.03	0.21±0.04	–14.4±1.1
NGC 2808	–1.04±0.06	0.15±0.06	103.4±8.4	NGC 6544	–1.44±0.05	0.22±0.04	–38.6±4.6
NGC 3201	–1.35±0.05	0.16±0.04	495.4±3.3	NGC 6553	–0.16±0.1	0.09±0.07	0.2±9.5
NGC 4590	–2.24±0.07	0.33±0.05	–94.0±3.2	NGC 6656	–1.69±0.05	0.29±0.11	–146.6±5.6
NGC 5024	–1.92±0.04	0.25±0.08	–60.8±3.4	NGC 6715	—	—	—
NGC 5053	–2.15±0.15	0.38±0.09	42.9±1.3	NGC 6723	–1.0±0.06	0.25±0.03	–93.5±3.4
ω Cen	—	—	—	NGC 6752	–1.47±0.03	0.25±0.05	–26.3±4.7
NGC 5272	–1.4±0.06	0.17±0.07	–146.2±4.1	NGC 6760	–0.71±0.1	0.19±0.05	–1.5±5.8
NGC 5466	–1.78±0.06	0.19±0.12	108.1±1.0	NGC 6809	–1.75±0.04	0.23±0.05	176.1±3.6
NGC 5904	–1.19±0.05	0.18±0.05	53.8±4.9	NGC 6838	–0.73±0.04	0.22±0.03	–22.7±2.1
NGC 6121	–1.04±0.03	0.34±0.04	70.9±3.4	NGC 7078	–2.28±0.05	0.31±0.07	–104.3±5.2
NGC 6171	–0.97±0.06	0.32±0.08	–33.8±3.1	NGC 7089	–1.46±0.06	0.19±0.07	–3.6±5.5
NGC 6205	–1.46±0.04	0.21±0.07	–246.3±5.2	Terzan 2	–0.82±0.05	0.26±0.02	133.2±1.4
NGC 6218	–1.26±0.03	0.26±0.05	–40.7±3.1	Terzan 5	—	—	—
NGC 6229	–1.25±0.05	0.19±0.06	–137.8±2.7	Pal 5	–1.24±0.02	0.11±0.04	–58.9±0.5
NGC 6254	–1.49±0.04	0.27±0.05	75.8±3.9	Pal 6	–0.81±0.09	0.28±0.07	172.9±2.3
NGC 6341	–2.22±0.03	0.31±0.07	–118.2±6.7	Pal 10	0.09±0.06	0.0±0.01	–32.7±4.9
NGC 6380	–0.72±0.05	0.21±0.02	–1.8±7.8	Liller 1	–0.03±0.05	0.01±0.05	61.8±3.5
NGC 6388	–0.54±0.06	–0.03±0.1	80.1±10.5	HP 1	–1.14±0.07	0.22±0.06	40.9±4.8

TABLE 5.1: From left to right, GC name, mean [Fe/H], mean [Si/Fe], and mean radial velocity obtained for the final list of GCs in the main GC sample from APOGEE DR16.

Name	E [km^2/s^2]	L$_Z$ [10^3 kpc * km/s]	Name	E [km^2/s^2]	L$_Z$ [10^3 kpc * km/s]
NGC 104	-50892^{+74}_{-94}	$0.62^{+0.01}_{-0.01}$	NGC 6397	-66705^{+193}_{-190}	$0.33^{+0.01}_{-0.01}$
NGC 288	-41116^{+1125}_{-947}	$-0.34^{+0.03}_{-0.03}$	NGC 6441	-93869^{+2812}_{-3479}	$0.21^{+0.03}_{-0.03}$
NGC 362	-41406^{+1436}_{-1391}	$-0.07^{+0.01}_{-0.01}$	NGC 6522	-129873^{+1043}_{-737}	$0.01^{+0.01}_{-0.01}$
NGC 1851	-21934^{+537}_{-521}	$-0.22^{+0.02}_{-0.04}$	NGC 6539	-88145^{+1367}_{-1378}	$-0.18^{+0.00}_{-0.00}$
NGC 1904	-26641^{+655}_{-650}	$-0.17^{+0.05}_{-0.04}$	NGC 6540	-108006^{+1814}_{-2001}	$0.18^{+0.01}_{-0.01}$
NGC 2808	-39859^{+541}_{-690}	$0.13^{+0.01}_{-0.01}$	NGC 6544	-85401^{+474}_{-386}	$-0.07^{+0.02}_{-0.02}$
NGC 3201	6964^{+1307}_{-1402}	$-1.65^{+0.02}_{-0.02}$	NGC 6553	-101735^{+2577}_{-1883}	$0.25^{+0.02}_{-0.02}$
NGC 4590	-1010^{+1311}_{-801}	$1.27^{+0.02}_{-0.01}$	NGC 6656	-49027^{+204}_{-294}	$0.47^{+0.01}_{-0.01}$
NGC 5024	-14407^{+851}_{-861}	$0.33^{+0.01}_{-0.02}$	NGC 6715	22391^{+3784}_{-3525}	$0.79^{+0.01}_{-0.01}$
NGC 5053	-18934^{+925}_{-645}	$0.29^{+0.02}_{-0.02}$	NGC 6723	-85738^{+958}_{-1010}	$-0.02^{+0.01}_{-0.01}$
ω Cen	-66584^{+413}_{-271}	$-0.35^{+0.01}_{-0.01}$	NGC 6752	-69155^{+484}_{-522}	$0.41^{+0.01}_{-0.01}$
NGC 5272	-26985^{+454}_{-549}	$0.42^{+0.01}_{-0.01}$	NGC 6760	-78723^{+322}_{-265}	$0.34^{+0.01}_{-0.01}$
NGC 5466	18295^{+2946}_{-3170}	$-0.54^{+0.04}_{-0.04}$	NGC 6809	-69856^{+220}_{-212}	$0.09^{+0.01}_{-0.01}$
NGC 5904	-4945^{+2821}_{-2685}	$0.16^{+0.01}_{-0.01}$	NGC 6838	-56897^{+99}_{-92}	$0.67^{+0.00}_{-0.00}$
NGC 6121	-78561^{+289}_{-377}	$-0.07^{+0.02}_{-0.02}$	NGC 7078	-44942^{+811}_{-912}	$0.55^{+0.02}_{-0.02}$
NGC 6171	-93415^{+343}_{-259}	$0.06^{+0.01}_{-0.01}$	NGC 7089	-24793^{+1316}_{-1645}	$-0.15^{+0.04}_{-0.03}$
NGC 6205	-55754^{+314}_{-363}	$-0.2^{+0.01}_{-0.01}$	Terzan 2	-142240^{+1564}_{-1992}	$-0.04^{+0.00}_{-0.00}$
NGC 6218	-9536^{+878}_{-819}	$0.06^{+0.11}_{-0.13}$	Terzan 5	-139676^{+2229}_{-2447}	$-0.02^{+0.01}_{-0.01}$
NGC 6229	-77618^{+518}_{-442}	$0.24^{+0.01}_{-0.01}$	Pal 5	-9666^{+3131}_{-2722}	$0.88^{+0.08}_{-0.08}$
NGC 6254	-76969^{+692}_{-537}	$0.25^{+0.01}_{-0.01}$	Pal 6	-96285^{+1413}_{-1744}	$-0.01^{+0.00}_{-0.01}$
NGC 6341	-49372^{+809}_{-728}	$-0.05^{+0.01}_{-0.01}$	Pal 10	-59725^{+733}_{-648}	$0.6^{0.01}_{-0.01}$
NGC 6380	-105529^{+3090}_{-2754}	$-0.02^{+0.01}_{-0.01}$	Liller 1	–	–
NGC 6388	-101561^{+1853}_{-1486}	$-0.13^{+0.01}_{-0.01}$	HP 1	-114308^{+5219}_{-3012}	$-0.01^{+0.01}_{-0.01}$

TABLE 5.2: From left to right, GC name, mean orbital energy, and mean angular momentum obtained for the final list of GCs in the main GC sample from APOGEE DR16 using the `MWPotential2014` (Bovy, 2015). There is no 6D phase-space information for Liller 1 provided in Vasiliev, 2019, thus I am unable to obtain IOM for this GC.

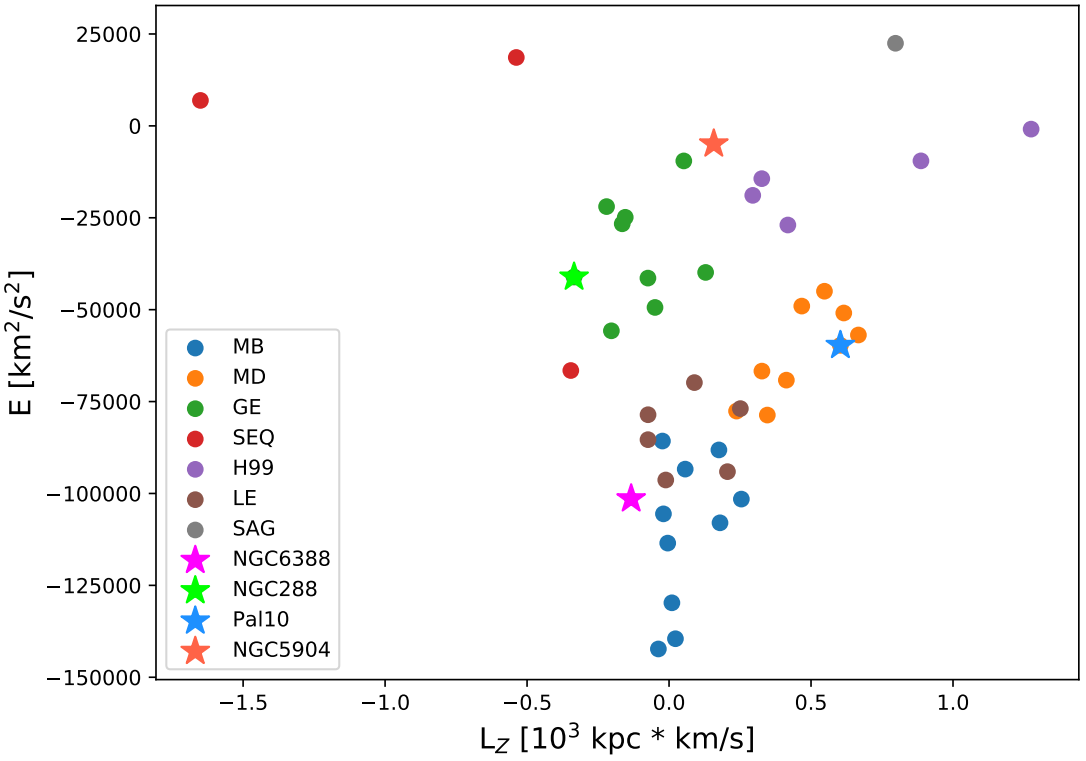

FIGURE 5.2: Orbital energy and vertical action as a function of orbital azimuthal action for the 46 GCs obtained in the initial main sample, divided into the kinematic associations identified by Massari et al. (2019).

I focus on calibrated abundances (Jönsson et al., 2018), which have been compared in detail with independent determinations by other groups. Of relevance to this work, Jönsson et al. (2018) show that Si abundances, although differing from those of some of the other groups by statistically significant zero-point shifts, show no trends with stellar parameters. Since the results depend fundamentally on relative differences between abundances from a homogeneous set, such small zero-point effects are not important. The α-element of choice for this study is silicon. I use the [Si/Fe] abundances, as silicon has been shown in previous data releases to be one of the most reliable α-abundance measurements in APOGEE (Jönsson et al., 2018). Magnesium is another α-element for which APOGEE provides exquisite abundances, however it is affected by internal GC evolution (e.g., Bastian & Lardo, 2018), so I remove it from consideration when using the main sample. In order to verify that the choice of α-element does not affect the conclusions, I performed the analysis adopting [Mg/Fe] from first population stars and found that the results are unchanged. In addition, I compared the mean [Si/Fe] with those from the compilation by Pritzl et al. (2005), finding our values to be slightly lower, of the order of $\sim$ 0.1 dex. Again, such a small zero-point difference has no impact on the results.

Orbital parameters were estimated for the sample of GCs as follows. I calculated the

Kinematic Group	Associated GCs
Main-Disc	NGC 7078(30), NGC 6760(11), NGC 6838(37), NGC 6218(62), NGC 6397(46), NGC 6752(97), NGC 104(176), NGC 6656(35), Pal 10(3)
Main-Bulge	NGC 6539(6), NGC 6171(51), Terzan 2(4), NGC 6553(23), NGC 6380(15), NGC 6522(6), **NGC 6388(24)**, NGC 6540(4), NGC 6723(7), HP 1(12)
Gaia-Enceladus	NGC 1904(17), NGC 2808(66), NGC 6205(80), NGC 6229(6), NGC 6341(10), NGC 362(49), NGC 7089(26), NGC 1851(30), NGC 288(35), **NGC 5904(167)**
Sequoia	NGC 5466(7), NGC 3201(114), **NGC 6388(24)**
Sagittarius	—
Helmi streams	NGC 5024(18), NGC 5053(11), NGC 4590(13), NGC 5272(110), Pal 5(3), **NGC 5904(167)**
Low-Energy	NGC 6809(60), Pal 6(5), NGC 6441(28), NGC 6121(140), NGC 6254(59), NGC 6544(21)
High-Energy	–
XXX	**Liller 1(4)**

TABLE 5.3: GCs obtained in APOGEE DR16 associated to the kinematic subgroups as defined in Massari et al. (2019), after removing GCs with less than 3 star members. The GCs highlighted in bold are associations that are uncertain. The number of APOGEE member stars associated to each GC are given in parentheses.

action integrals for each of the 46 GCs using the potential defined by Bovy (2015, `MWPotential2014`), using the publicly available code `galpy` [3] (Bovy, 2015; Mackereth & Bovy, 2018). In order to obtain reliable kinematic measurements, I draw 100 samples for each of the 6-D phase-space parameters given by the GC table in Vasiliev (2019), and obtain 100 estimates of the orbital parameters for each cluster, for which I then take the median and standard deviation as the value and associated uncertainty. Fig. 5.2 displays the energy (E) values obtained using this method as a function of the azimuthal action (L_Z) for all the GCs in the main sample, colour-coded by subgroup association. Highlighted as star symbols are GCs which display peculiar [Si/Fe] when compared to the remaining GCs in the same subgroup. I find that the orbital energy values differ

[3] `http://github.com/jobovy/galpy`

from those of Massari et al. (2019). Such differences can be traced back to the adoption of different Galactic potentials with different total masses—while Massari et al. (2019) adopted a McMillan potential (McMillan, 2017), the one adopted in this work was `MWPotential2014` (Bovy, 2015). I assessed the impact of Galactic potential choice on the results by re-running the calculations using the McMillan potential, and found that the GC associations to the various subgroups were unchanged, and are consistent with those found in Massari et al. (2019).

5.4 Results

5.4.1 Disc, Bulge and Low Energy GCs

In Fig. 5.3 I show the mean [Si/Fe] chemical-abundance measurements as a function of [Fe/H] for the MD (blue symbols), MB (orange symbols) and LE (red symbols) kinematically identified subgroups. Also plotted are the data for the GC Liller 1 (yellow dot), which is discussed in Section 5.4.3. At first glance the three subgroups occupy roughly the same locus in [Si/Fe] space, resembling the region of abundance space occupied by field stars from the disc and bulge components of the Milky Way (e.g., Hayden et al., 2015). Within the errors, the MD population displays a low-metallicity [Si/Fe] plateau until reaching [Fe/H] abundance values of approximately [Fe/H] $\simeq -0.6$, for which according to the Milky Way's Disc field population, I would expect a knee towards lower [Si/Fe] values (Alves-Brito et al., 2010). When considered in aggregate, the three subgroups display a clear knee at about [Fe/H]$\sim$–0.8, with a plateau at [Si/Fe]$\sim$+0.25 at lower metallicities and a trend of decreasing [Si/Fe] for increasing [Fe/H] at [Fe/H]–0.8, which mimics the behaviour of field stars. One GC deviates clearly from this trend, namely NGC 6388, with very low [Si/Fe]$\sim$0.0 at [Fe/H]$\sim$– 0.5. I discuss this interesting GC separately in Section 5.4.4.

When the three subgroups are considered separately, however, the relatively small number of GCs in the sample prevents the unequivocal identification of a "knee" in the Si-Fe plane for any of the subgroups in Figure 5.3. In the case of the MB subgroup, the sample does not contain enough GCs at [Fe/H] – 0.8 to firmly establish the existence of a low metallicity [Si/Fe] plateau. The LE subgroup straddles properly both [Fe/H] sides of the "knee" and the GCs seem to follow the same trend as the field population, but the sample is too small for a solid conclusion. The sample for the MD subgroup covers a wide range in [Fe/H] towards the metal-poor side of the knee, but contains only one GC on the metal-rich end, whose position on the Si-Fe is consistent with the existence of a knee in that subgroup. Again, the sample is not large enough at [Fe/H]– 0.8 for a robust

conclusion. The GC on the metal-rich end of the MD subgroup is Pal 10. I checked to see whether the orbital properties of this cluster match those of the MD GC population. In Fig 5.2 I show that Pal 10 does follow a disc-like orbit, displaying energy values of E∼–6000 km^2/s^2 and following a prograde orbit (i.e. L_Z ∼0.7 10^3 kpc km/s), therefore it is likely to belong to the MD subgroup. All in all, the MB and MD subgroups follow the trend defined by the field population, thus I conclude that these subgroups share an *in situ* origin. Since the origin of the LE subgroup is contentious, the locus of GCs from that subgroup merits some attention. the results show that the GCs from this subgroup occupy the same locus in [Si/Fe] vs [Fe/H] space as the MD/MB GCs. This result is in line with the similarity of these subgroups in E-L_Z space, (see Fig. 5.2 of this paper and Fig. 3 of Massari et al., 2019) I note, however, that at [Fe/H] −1.5 it is almost impossible to distinguish between accreted and *in situ* GCs in the Si-Fe plane, so that an accreted origin for the three most metal-poor GCs in the LE group (namely, NGC 6254, NGC 6544 and NGC 6809) cannot be ruled out.

In summary, from the point of view of kinematics, the low energy defining this subgroup makes it hard to distinguish it from the MD/MB subgroups (Fig. 5.2). On the basis of the chemistry, while the metal-rich GCs NGC 6441, Pal 6 and NGC 6121 are clearly associated with the the MD/MB subgroups, the association of the more metal-poor GCs NGC 6254, NGC 6544 and NGC 6809 is more uncertain, given that accreted and *in situ* GCs occupy the same locus in the Si-Fe plane for those metallicities. I conclude that, while the overal trend on the Si-Fe plane of the LE GCs in the sample suggests an *in situ* origin, the position of that subgroup in IOM space does not preclude some of the members of that category having an accreted origin.

Finally, I highlight the case of NGC 6388. Although that GC is classified by Massari et al. (2019) as belonging to the MB subgroup, it is characterized by very low [Si/Fe] (∼–0.03), departing by $\sim 2\sigma$ from the mean [Si/Fe] of that subgroup at [Fe/H] ∼ –0.5. I discuss this GC in more detail in Section 5.4.4.

5.4.2 Accreted subgroups

In this subsection, I examine the distribution of GCs of accreted origin in the Si-Fe plane. Our analysis focuses on the following subgroups: H99, GE, and Seq. The data for these GCs are displayed in Fig 5.4. We first focus on a comparison between the positions occupied by the accreted and *in situ* clusters. Our results show that the GCs associated with the three putative accreted systems all fall on the same locus in the [Si/Fe] plane, positioned on average at lower [Si/Fe] values than the MD and MB population (illustrated in Fig 5.4 as grey points). This is commonly interpreted as

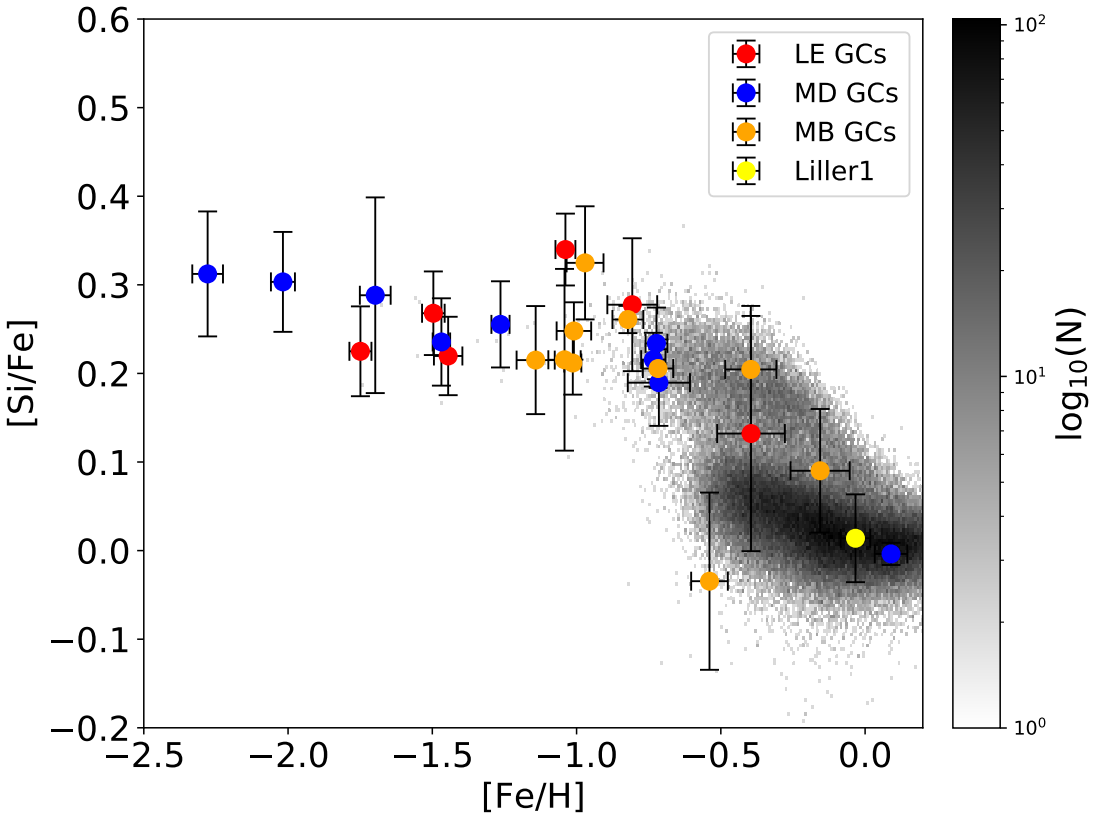

FIGURE 5.3: Mean [Si/Fe] vs [Fe/H] chemical-abundances for the Low Energy (red), Main Bulge (orange) and Main Disc (blue) GC subgroups, illustrated alongside Liller 1 (yellow), with the 1 σ spread represented in black error bars. In grey I show the Galactic disc and bulge field populations defined kinematically according to Massari et al. (2019). From these abundance plots, by accounting for the 1 σ spread uncertainties, I find that the more [Fe/H] rich LE GCs, namely NGC 6121, NGC 6441 and Pal 6 can be categorized to be from *in situ* origin. The other three LE GCs still occupy the same locus as the MD/MB subgroups, however due to their low [Fe/H] abundances and position in the IOM space (Fig 5.2), it is possible that these more metal-poor GCs could be from an accreted origin. Furthermore, I find that Liller 1 occupies the same locus as the *in situ* GCs, which coupled with its high [Fe/H] value can be classified as a MB GC.

the result of a history of star formation and chemical enrichment typical of low-mass galaxies, which differs from that of the Milky Way (e.g., Tolstoy et al., 2009). The accreted origin of the GCs that are kinematically associated with GE, H99 and Seq is further confirmed by the fact that their position in the [Si/Fe] plane mimics that of field populations linked with past accretion events (Hayes et al., 2018; Mackereth et al., 2018). I calculate the mean [Si/Fe] abundace given by GCs in the –1.5 < [Fe/H] < –1 regime for both the accreted and *in situ* populations, and find that the accreted groups display on average [Si/Fe] = +0.17± 0.05, whereas the *in situ* subgroups display a higher average abundance [Si/Fe] = +0.25± 0.03. This means that the two distributions differ at the $\sim$ 91.5% level.

Having established that the accreted subgroups occupy a locus of lower [Si/Fe] than that

of *in situ* populations, I now turn to a discussion of the relative positions of the GCs from the three accreted subgroups in the Si-Fe space. As pointed out above, the GCs associated with the GE, H99, and Seq subgroups occupy the same locus on the abundance plane, within the errors. Such similarity in chemical space can be understood in two possible ways. On one hand, the different accreted subgroups may be associated to three separate similar-mass satellites. Alternatively, some, or perhaps all of them, could be part of the same accreted satellite. Consideration of the kinematic properties of the three systems may help distinguish between these scenarios. The GE system is strongly bound and mildly retrograde, whereas the other two groups are slightly less bound, with Seq being strongly retrograde and H99 strongly prograde. Massari et al. (2019) argue that two of the GCs associated with the Sequoia system (namely, NGC 3201 and ω Cen) have a relatively high probability of belonging to GE. Moreover, they point out that the Sequoia system's position in IOM space coincides with that of debris that Helmi et al. (2018) ascribe to Gaia-Enceladus.

Along the same lines, Massari et al. (2019) analysed the Helmi stream GCs employing the methodology described in Koppelman et al. (2019b), and found that, when accounting for the age uncertainties, H99 occupies a locus in age-metallicity space that is consistent with the *Gaia*-Enceladus and Sequoia GC subgroups. Moreover, it has been shown that the field populations of the *Gaia*-Enceladus, Sequoia, and Helmi Stream occupy the same locus in [Mg/Fe] vs [Fe/H] and [Al/Fe] vs [Fe/H] planes (Koppelman et al., 2019a), and that the Helmi Stream displays an MDF which peaks at a value of [Fe/H] $\sim$ –1.5 (Koppelman et al., 2019b), similar to value at which the Gaia-Enceladus MDF peaks (Helmi et al., 2018; Mackereth et al., 2018).

We conclude that the combined evidence from GC subgroup chemistry and kinematics is suggestive of either a common origin for the Sequoia, Helmi Stream and Gaia-Enceladus stellar systems, or that these subgroups are associated with satellites which underwent similar chemical enrichment histories.

In closing this subsection I comment on the interesting case of NGC 288. On the basis of kinematics, Massari et al. (2019) assign it unambiguously to the GE subgroup, with a retrograde orbit and high orbital energy (see Fig 5.2). However, its elemental abundances place it squarely on the *in situ* branch, $\sim 2\sigma$ off the mean of the GE subgroup at the same [Fe/H]. I checked to see if this result survives when other α-elements are considered, and find that NGC 288 also displays [Mg/Fe] and [Ca/Fe] values $\sim 2\ \sigma$ away from the mean of the GE subgroup, with the GE subgroup presenting mean values of $\langle[\mathrm{Mg/Fe}]\rangle_{GE} = +0.17 \pm 0.07$ and $\langle[\mathrm{Ca/Fe}]\rangle_{GE} = +0.19 \pm 0.04$, respectively, and NGC 288 displaying $[\mathrm{Mg/Fe}]_{NGC\,288} = +0.31 \pm 0.04$ and $[\mathrm{Ca/Fe}]_{NGC\,288} = +0.26 \pm 0.09$, for the same [Fe/H].

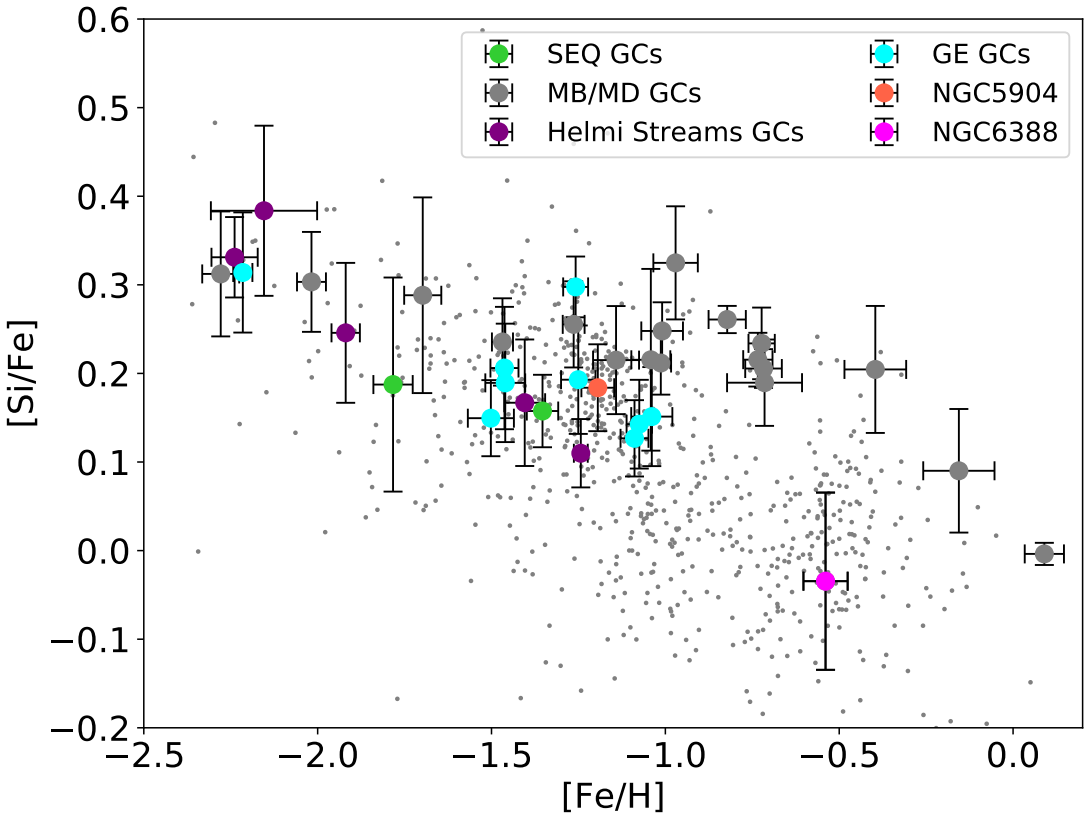

FIGURE 5.4: Mean [Si/Fe] vs [Fe/H] for the GE (cyan), Seq (green), H99 (purple) and MD/MB (grey) GC subgroups, illustrated alongside NGC 5904 (red) and NGC 6388 (magenta), with the 1 σ spread represented in black error bars. In grey I show the halo field population defined as in Massari et al. (2019). The GE, Seq and H99 accreted dwarf spheroidal subgroups occupy the same locus, displaying lower mean [Si/Fe] values to the GCs from the MD and MB populations at the same metallicity range –1.5 < [Fe/H] < –1. According to galaxy chemical-evolution models, this suggests that either: both accreted dwarf spheroidals must have had a similar chemical-evolution history and therefore have been of similar mass, or that some, possibly all, originate from the same accretion event. Below [Fe/H] < –1.5, the *in situ* and accreted groups are indistinguishable in the Si-Fe plane. NGC 288 displays higher [Si/Fe] values than the rest of the GE subgroup GCs ($\sim$ 0.15 dex greater) of similar metallicity, however displays a clear accreted-like orbit (see Fig 5.2). NGC 5904 clearly occupies the same locus as the accreted population of GCs. However, due to the uncertainties in the measurements, it is impossible to suggest to which accreted subgroup NGC 5904 belongs to. Along the same lines, NGC 6388 occupies the same locus as the [Fe/H]-rich halo field population, which coupled with its retrograde orbit hints that this GC belongs to an accreted subgroup.

It is difficult to reconcile the orbital and chemical properties of NGC 288, so I suggest that NGC 288 is likely an accreted GC with a peculiar chemical composition.

5.4.3 NGC 5904 and Liller 1

The study by Massari et al. (2019) did not assign Liller 1 to any particular kinematic subgroup, and concluded that NGC 5904 could be associated with either the GE or

H99 subgroup. In this subsection I examine these GCs' positions in chemical space to see whether that information can help clarify whether they have an accreted or *in situ* origin.

I first compare the [Si/Fe] vs [Fe/H] abundance measurements obtained for Liller 1 with the other identified subgroups (see Fig. 5.3). The results show that within the uncertainties, Liller 1 occupies the same locus in the [Si/Fe] vs [Fe/H] abundance plane as the *in situ* population, and therefore belongs to either the MD or MB subgroup. Unfortunately, there is no 6D phase-space information for Liller 1 (see Vasiliev, 2019, for details), and therefore I am unable to place kinematic constraints on the origin of this GC. Furthermore, Liller 1 is quite metal rich, with a mean value of $<[Fe/H]>_{Liller\,1} \simeq$ –0.03± –0.05, which is much higher than the metallicities of the accreted GCs. Thus, the results suggest that Liller 1 has an *in situ* origin, agreeing with previous studies (e.g. Bica et al., 2016).

In the case of NGC 5904, the results show that the mean abundances place it on the same locus as the GCs associated to the accreted subgroups. Therefore, within the uncertainties the results suggest that NGC 5904 has an accreted origin (agreeing with the suggestion by Massari et al., 2019). However, since it is impossible to distinguish the accreted groups in Si-Fe space, I cannot establish an association of NGC 5904 to any particular accreted subgroup.

5.4.4 NGC 6388

As pointed out in Section 5.4.1, NGC 6388 displays a very low [Si/Fe] abundance ratio, departing significantly from the locus of the MB subgroup, to which it was associated by Massari et al. (2019). Its position on the Si-Fe plane is consistent with an extrapolation towards high metallicity of the trend established by the accreted subgroups at [Fe/H] –1. It also falls on top of the accreted field population in Fig. 5.4. The mean abundances for NGC 6388 are based on values for 24 members, which I consider to be statistically robust. Specifically, the mean silicon abundance of NGC 6388 members ($<[Si/Fe]>$ = –0.03±0.1) deviates from that of the high α sequence at same [Fe/H] ($<[Si/Fe]>_{high\alpha}$ = +0.17±0.05) by $\sim 2\ \sigma$. It is also lower than that of the low α sequence ($<[Si/Fe]>_{low\alpha}$ = +0.02±0.04) by $\sim 1\ \sigma$. I note, however, that Carretta & Bragaglia (2018) obtained abundances for a comparable sample of NGC 6388 members, obtaining ∼0.4 dex higher mean [Si/Fe]. Wallerstein et al. (2007) also obtained a ∼0.3 dex higher mean [Si/Fe], although their mean abundances of Ti and Ca were around solar or lower (∼+0.06 and –0.05, respectively), depending on the $\log g$ adopted. On the other hand, Mészáros et al.

(2020) analysed the APOGEE spectra using a different pipeline, obtaining similar results to those presented in this paper.

In order to check whether the result is due to systematics in the [Si/Fe] abundance ratios of NGC 6388 stars, I examined the abundances of other α-elements, such as Mg and Ca. For the latter element I found $\langle$[Ca/Fe]$\rangle$ = +0.09 ± 0.11, which is lower than the values for the MB population at the same [Fe/H] ([Ca/Fe] = +0.19 ± 0.02), deviating at the $\sim$ 1 σ level. Before estimating mean [Mg/Fe], one needs to select GC members that are not affected by the multiple population phenomenon. In order to isolate NGC 6388 stars belonging to the so-called "first population", I proceeded as follows. I use [N/Fe] in order to identify first population stars, since this abundance ratio is strongly enhanced in their second population counterparts (see, e.g. Renzini et al., 2015; Schiavon et al., 2017a; Bastian & Lardo, 2018). I define as first population stars those located within the bottom quartile of the [N/Fe] distribution of NGC 6388 members. By proceeding in this way, I am confident that I managed to isolate a subsample of first population GC stars, whose Mg abundances are not affected by the multiple populations phenomenon. For this subsample, I obtained $\langle$[Mg/Fe]$\rangle$ = +0.07 ± 0.11, which again is lower than the mean value for the MB population ($\langle$[Mg/Fe]$\rangle$ = +0.27 ± 0.06) by $\sim$ 2 σ.

It is worth noticing that the relative position of NGC 6388 in α-Fe space is not the same according to different α-elements. When Si is considered, NGC 6388 falls below the low-α sequence at the 1 σ level. On the other hand, the cluster falls on top of the low-α sequence when Mg or Ca are considered.

Due to NGC 6388 being a bulge GC, positioned in a crowded and dense field, it is likely that the sample is contaminated by field stars, mainly in the GC foreground. To ensure the previous findings are robust, I minimise field contamination by considering only N-rich stars, which belong to the "second-population" GC population stars. To obtain a clean sample of "second population" stars, I select only stars located at the top quartile of the [N/Fe] distribution. For second-population NGC 6388 stars defined in that manner, I find an average of $\langle$ [Si/Fe] $\rangle$ = –0.07 ± 0.08, which places NGC 6388 even further away from the *in situ* population. This solidifies the initial findings, and confirms that NGC 6388 displays lower [Si/Fe] abundances than those of other MB GCs of similar metallicity.

Myeong et al. (2019) studied the properties of NGC 6388 in detail, showing that, on one hand, it is consistent with an accreted origin on account of its kinematic properties, but on the other its combination of age and metallicity places it on top of the relation defined by the *in situ* GC population for those two parameters (see also Kruijssen et al., 2019b). I determined the orbital energy and azimuthal action of NGC 6388 (see Fig 5.2), finding its orbit to be retrograde, in agreement with Myeong et al. (2019), but

cannot distinguish between a possible association to the MB, LE, or the Seq subgroups. Furthermore, Milone et al. (2019) classified NGC 6388 as a Type II GC, based on the ratio of first-population to second-population stars. They also obtain the IOM of this GC, and conclude that NGC 6388 is likely from an accreted origin.

I summarise the results for NGC 6388 as follows: 1) the [Si/Fe] abundance for this GC differs from that of the MB/MD population at the 2 σ level; 2) it differs from that of the low-α at the 1 σ level; 3) Figure 5.4 shows that NGC 6388 falls on top of the accreted *field* halo populations in the Si-Fe plane; 4) its position in the IOM does not provide a unique distinction between an accreted or *in situ* origin. In view of these results, it is fair to conclude that the data suggest a possible accreted origin for NGC 6388.

5.5 Conclusions

In this work, I have employed the sixteenth data release from the SDSS/APOGEE survey in order to map the kinematic properties of Galactic GCs into their positions in the chemical compositions space. I contrast positions, and APOGEE abundances and radial velocities with information gathered from the 2010 edition of the Harris GC catalogue (Harris, 1996) and the Baumgardt & Hilker GC catalogue (Baumgardt & Hilker, 2018; Baumgardt et al., 2019) to obtain a primary GC sample in APOGEE, which I refine to obtain an accurate GC membership list. I obtain a final main GC sample of 3090 stars, associated with 46 GCs, from which then ω Cen, Terzan 5 and NGC 6715 are removed for reasons detailed in Section 5.3.1, leaving us with a sample of 1,728 stars associated with 43 GCs. I assign membership to various kinematic subgroups according to the classification by Massari et al. (2019). I then examine the distributions of the various GC subgroups in chemical space, more specifically the plane defined by α and Fe abundances. After excluding GCs with fewer than three member stars, I identify in the sample 9 GCs associated to the MD group, 10 to the MB, 9 to the GE dwarf spheroidal, 5 to the H99, 6 to the LE group, 2 to the Seq dwarf spheroidal and 0 to the Sag dwarf spheroidal. Furthermore, I find 2 GCs (namely, Liller 1 and NGC 5904) for which there remains an uncertain association.

I make use of Si abundance measurements in APOGEE as the tracer of α-elements abundance, and plot them as a function of [Fe/H] with the goal of gaining insight into the nature of the different kinematic subgroups. In this comparison, I search for any possible plateau or knees that may present themselves in an [α/Fe] vs [Fe/H] plane. the results and conclusions are unchanged by adoption of the sample and abundances presented by Mészáros et al. (2020). Our conclusions can be summarised as follows:

1. When considered together the *in situ* GC subgroups (Main Disk and Main Bulge, MD and MB) and the low-energy group (LE) follow the overall trend of the *in situ* populations (MB and MD) in chemical space, with a [Si/Fe]∼+0.25 plateau at low metallicity and a change of slope (so-called "knee") at [Fe/H]∼–0.8.

2. GCs from accreted subgroups, namely Gaia-Enceladus (GE), Helmi streams (H99), and Sequoia (Seq) fall on the same area of chemical space as accreted field populations. This locus is characterized by [Si/Fe] + 0.2 at –1.5 [Fe/H] –1.0, going down to solar or near sub-solar [Si/Fe] for [Fe/H]∼ –0.5. At [Fe/H] –1.5, GCs from the accreted and *in situ* subgroups are indistinguishable in the Si-Fe plane.

3. When examined separately, the MD, MB, and LE subgroups track the field population, however due to the relatively small sample size these subgroups do not sample the metallicity space densely enough to define the trend separately from the other subgroups. Three out of six of the LE GCs (namely, NGC 6121, NGC 6441 and Pal 6) fall on the high-metallicity side of the knee and follow the trend of the field populations, leading to the conclusion that they have an *in situ* origin. The three metal-poor GCs from the LE subgroup (namely, NGC 6254, NGC 6544 and NGC 6809) fall in the region of Si-Fe where accreted and *in situ* GCs are indistinguishable, so their origin is less certain. I conclude that the chemical properties of the LE subgroup as a whole are consistent with an *in situ* origin, but given its borderline position in IOM space, individual clusters belonging to this subgroup could have an accreted origin.

4. GCs from the accreted H99 and GE subgroups occupy the same position in chemical space. That is also the case for the GCs in the Seq group, but since the sample contains only two Seq GCs, the result for that subgroup is not as firm. This result suggests that GCs from these subgroups are associated to accreted satellites of similar masses, or possibly originating from one common progenitor. Based on its position on the IOM space, it is possible that the GCs from the Seq and GE subgroups actually once belonged to the same system, as suggested by other groups (e.g., Massari et al., 2019).

5. NGC 6388 is found to present Si, Mg, and Ca abundances that are considerably lower than those of other GCs in the main bulge subgroup and similar [Fe/H]. The evidence from other studies in the literature is not conclusive, so more studies exploring other spectral regions and different α-elements are required to ascertain the low-α nature of this GC. Considering the orbital characteristics, a confirmation of this result will lend strong support to the notion that NGC 6388 was in fact accreted to the Milky Way, as also suggested by other groups (e.g. Milone et al., 2019; Myeong et al., 2019).

6. NGC 288 is found to present Si, Ca and Mg abundances that are considerably higher than those of other accreted GCs of similar [Fe/H]. It is characterized by a highly unbound retrograde orbit. I conclude that NGC 288 is an unusual GC where the kinematic properties suggest an accreted origin which is not fully compatible with the its chemistry. More work is needed to clarify the origin of this object.

7. Comparison of the mean [Si/Fe] vs [Fe/H] chemical compositions of Liller 1 and NGC 5904 with those of the different kinematic subgroups suggests that Liller 1 possibly associated with the *in situ* subgroups and that NGC 5904 was likely accreted. I cannot, on the basis of the extant data, establish to which accreted subgroup this GC is associated.

In summary, the information provided by the sixteenth APOGEE data release has enabled a study of the chemical-abundances of the Galactic GC system, shedding light on the origin of a reasonably representative sample of the Milky Way GC system. The combination of the chemical-abundance information delivered by APOGEE and the kinematic 6D phase-space information provided by Gaia provides interesting insights into the origin of the Milky Way GCs. Expansion of such data bases to a larger sample of Galactic GCs will shed new light on the Galaxy's early mass assembly history.

Chapter 6

Conclusions

This thesis presents novel results obtained via an analysis of the stellar halo and globular cluster components of the Milky Way (MW), that shed light into the mass assembly history and formation of the MW. In this chapter, I attempt to bind these findings together into a coherent new picture of the formation of the Milky Way, framing them within the context of the body of literature discussed in the introduction chapter. In addition, I discuss possible future avenues of exploration that derive naturally from the body of work presented in this thesis.

A key result of this thesis has been the discovery of Heracles, a stellar population located within the innermost regions of the stellar halo, which given its chemo-dynamic characteristics, is postulated to be the debris from an ancient and massive disrupted satellite galaxy accreted by the Milky Way (see Chapter 2). In detail, I showed that this halo substructure presents chemical abundance distributions which are typical of low-mass satellite galaxies of the MW and/or accreted populations, and that it displays low orbital energies, thus sitting deep in the potential of the MW (at small Galactocentric radii). I also compared its chemical properties to that of expectations from the EAGLE cosmological simulations, and showed that halo substructures like Heracles do occur in Milky Way-mass galaxies.

Following the discovery of Heracles, in Chapter 3 I examine the nature and reality of all the halo substructures identified so far in the Galactic stellar halo by analysing their chemical compositions using the APOGEE survey. In detail, I use the latest *Gaia* and APOGEE data to identify stars that are likely to belong to the following substructures in the stellar halo: Heracles, *Gaia*-Enceladus/Sausage (GES), Sagittarius dSph, the Helmi stream, Sequoia, Thamnos, Aleph, LMS-1, Arjuna, I'itoi, Nyx, Icarus, and Pontus. I examine the distributions of all substructures in chemical space, considering the abundances of elements sampling various nucleosynthetic pathways. In doing so, I found that

the chemical properties of all halo substructures –minus Aleph and Nyx– resemble those of dwarf satellites of the Milky Way, such as the Sagittarius dSph. An important result was the finding that abundance pattern of Heracles differs from those populations formed *in situ* and from all other substructures in a statistically significant manner. In addition, I also showed that the abundance patterns of Sequoia (selected in various ways), Arjuna, LMS-1, and I'itoi are indistinguishable from that of the omnipresent GES, indicating a possible common origin, whereas the abundance patterns of the Helmi stream and Thamnos substructures are different from all other halo substructures, indicating that they may be debris from separate accreted satellites. Lastly, I found that the chemical properties of Nyx and Aleph are very similar to those of disc stars, implying that these substructures likely have an *in situ* origin. In summary, the results presented on the chemical compositions of halo substructure in the Milky Way have helped establish the reality and nature of stellar halo populations, all of which place vital constraints on the mass assembly history of the Galaxy.

In addition to halo substructures and the role of accreted satellites in the build up of mass of the Galactic stellar halo, the origin of the Galactic globular clusters (GC) system and its mass contribution to the total stellar halo mass budget are pivotal questions related to the mass assembly history of the MW. To this end, in Chapter 4, I presented a density profile that describes the density distribution of both the stellar halo and N-rich stars. The latter are deemed to be second population GC stars currently inhabiting the halo field. I then used these stellar density profiles to show that, when accounting for the APOGEE selection function, the innermost regions of the stellar halo (at $R_{GC} \lesssim 3$ kpc) there is a much higher incidence of GC escapee stars ($\sim$27%) than in more distant regions ($R_{GC} \sim 10$ kpc) of the stellar halo ($\sim$4%). These results corroborate previous estimates based on observed number counts. I also showed that within a spherical shell from 1.5 to 15 kpc in radius, the total stellar mass arising from dissolved and/or evaporated GCs is on the order of $M_{GC,total} = 9.6^{+4.0}_{-2.6} \times 10^7$ $M_\odot$.

In a similar vein, in Chapter 5 I presented novel results on the chemical compositions of Galactic GCs that help shed light on their nature and origin. In detail, I determined a homogeneous GC sample comprising 49 GCs in the APOGEE DR16 catalogue, and compared their [Si/Fe] and [Fe/H] abundances with those from accreted and *in situ* field stars to associate GCs to previously postulated accreted debris, building on previous work that attempted to associate GCs to accretion events based purely on kinematic information.

All together, the results presented in this thesis highlight the importance of disentangling Galactic stellar halo populations to unveil the past and mass assembly history of the Galaxy. While in this thesis I have reported results that help further unveil the

assembly history of the Milky Way, there remain key questions that still need to be solved. One vital open question is "*How many major*[1] accretion events has the Milky Way undergone?" In the last decade, many studies have reported the discovery of halo substructures postulated to be the debris from individual disrupted satellite galaxies (e.g., Belokurov et al., 2018; Helmi et al., 2018; Myeong et al., 2019; Koppelman et al., 2019c; Naidu et al., 2020; Yuan et al., 2020; Horta et al., 2021a; Re Fiorentin et al., 2021; Malhan et al., 2022). However, many of these findings are based solely on results using orbital information from *Gaia*, which can lead to misidentifications of new halo substructures that in fact belong to other (possibly already known) progenitors (e.g., Jean-Baptiste et al., 2017a; Koppelman et al., 2020). In Chapter 3 I showed the importance of using chemical abundance information to ascertain the reality of halo substructures, and via a chemical abundance study showed that many halo substructures resemble the omnipresent *Gaia*-Enceladus/Sausage accretion and/or populations formed *in situ*. My findings have helped elucidate the reality of these halo populations, and in summary suggest that the Milky Way likely has undergone three major accretions (namely, Heracles, *Gaia*-Enceladus/Sausage, Sagittarius dSph) and a number of lower-mass ones (Thamnos, Helmi Stream, Cetus, Pontus). However, there are still many steps that need to be taken before establishing a full picture of the accretion history of the Galaxy.

More specifically concerning the nature of Heracles, another important question that needs answering is "*Is Heracles fully contained within the inner ∼4 kpc from the Galactic Centre as reported, or do the debris span wider spatial regimes?*" Theoretical expectations suggest that whilst the bulk of the debris from an early and massive cannibalised satellite galaxy (as believed Heracles to be) may be predominantly contained within small Galactocentric radii (Pfeffer et al., 2020; Dillamore et al., 2022, Horta et al in prep), there should be some fraction of stars that occupy larger distances. Assessing to what spatial extent the incidence of Heracles stars inhabit will be a key question that shall hopefully be answered with the advent of SDSS-V, (see Fig 6.1 for details). Along those lines, other obvious questions that still remain unsolved are "*How many accreted debris reside in these innermost ∼4 kpc of the Galactic stellar halo?* and "*Is Heracles (and other early accreted satellites) indistinguishable in chemo-dynamical space from the oldest in situ halo populations in the Milky Way's stellar halo?*" The answer to these two questions will shed light on the earliest stages of formation of the Galaxy. So far, the latest observational data support the notion that an accreted population inhabits these innermost regions (i.e., Heracles). However, the oldest in situ halo must also reside in this region. Dissentangling the differences between these two populations seems, at

[1]Here major refers to satellite galaxies with a stellar mass of $M_\star \times 10^8 M_\odot$ or so.

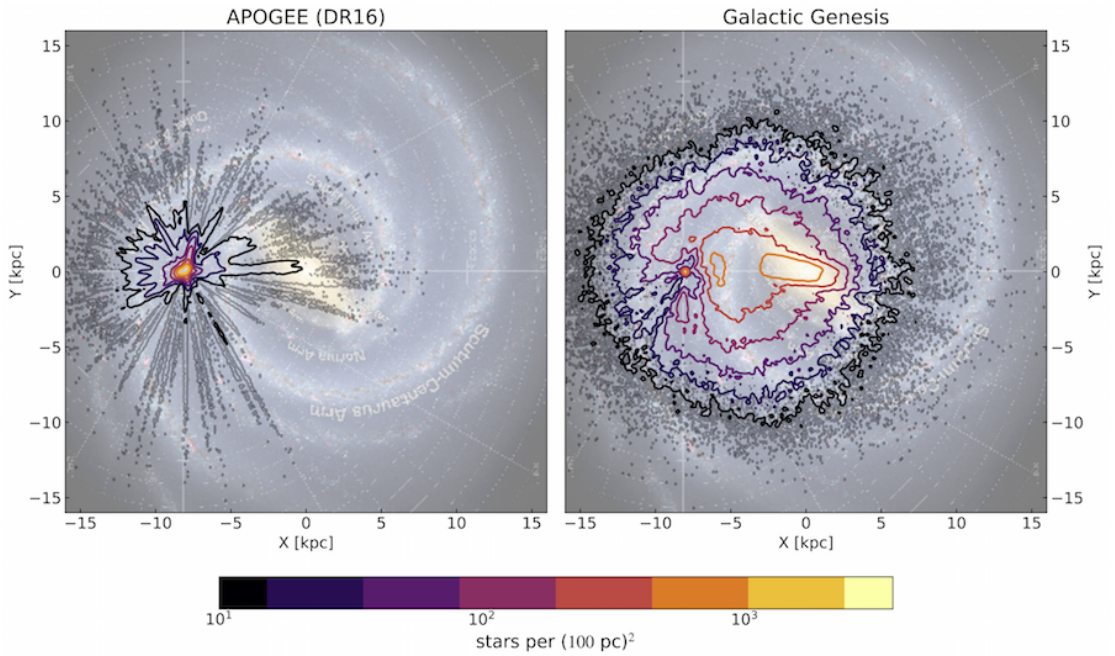

FIGURE 6.1: Midplane target surface density of the APOGEE DR16 catalog (left) and the Milky Way Mapper's (MWM) Galactic Genesis Survey (right). The maps show an artist rendition of the face-on Milky Way beneath the target density contours. MWM's Galactic Genesis' survey will be able to observe ∼70,000 stars within ∼ 4 kpc from the Galactic Centre below [Fe/H] < –1, delivering exquisite chemical compositions (for up to ∼20 different elemental species) and radial velocities, that when combined with the astrometry from *Gaia*, would yield the largest chemo-dynamical data set of metal-poor stars in the innermost regions of the Galaxy. This unprecendented amount of information, would allow me to fully unmask the stellar content and history of the little studied innermost halo. Along those lines, the sheer number of high-resolution chemo-dynamical measurements for metal-poor stars throughout the Galaxy will hopefully allow one to assess the spatial extent of the Heracles substructure. *Image credit: NASA/JPL-Caltech/R. Hurt (background), J. Bird*

present time, non-trivial. In a similar vein, studies on the properties of Galactic globular clusters predict that an accretion event like Heracles should have occured in the Milky Way (i.e., "Kraken"/"Koala" Kruijssen et al., 2020; Forbes, 2020). Whilst Heracles overlaps in the Lindblad diagram with this predicted accretion event, a definitive connection between them is yet to be established.

Interestingly, there may be a connection between the fact that there is evidence for an accreted debris in the innermost Milky Way halo, and that the incidence of disrupted/evaporated globular cluster stars (i.e., N-rich stars) increases by a factor of ∼5 in this region when compared to the outer halo. In Kisku et al. (2021), we showed that many of these N-rich stars present chemo-dynamical features that are consistent with Heracles. Thus, it is possible that Heracles either brought in GCs which were destroyed during the merger, or that the Heracles-Milky Way interaction caused in situ GCs in this region to be destroyed at a higher rate than in the outer halo. Moreover, theoretical expectations suggest that Milky Way-mass haloes that resemble the Galaxy chemically (i.e., present

an α-bimodality) assemble their mass early (Mackereth et al., 2018) and typically have a higher number of disrupted/evaporated globular cluster stars in their inner "bulge" region Hughes et al. (2020), in line with the results presented in this thesis. All in all, it seems that these two findings may be related. In addition, these results will have ramifications for our understanding of the origin of the Galactic globular cluster system. Thus, chemo-chrono-dynamically characterising Galactic globular clusters, as done in this thesis and in previous works (e.g., Forbes, 2020; Kruijssen et al., 2020; Callingham et al., 2022), should also help elucidate the assembly history of the Galaxy.

The findings presented in this work were only possible thanks to the extensive work performed by the APOGEE and *Gaia* survey teams. The efforts of these large collaborations (amongst many others) supply the necessary observational data that enable studies like the ones contained in this thesis. Moreover, the efforts of collaborations developing and updating state-of-the-art cosmological simulations (such as the EAGLE simulations used in Chapter 2) provide the necessary theoretical perspective to ground these observational results. In combination, these large-scale stellar surveys and cosmological simulations provide the necessary tools to fully characterise the Galactic stellar halo, and in turn unveil the Milky Way's mass assembly history and formation.

6.1 Future work

Prospects for deeper insights on the mass assembly history and formation of the Galaxy are strong in the near future. The oncoming splurge of spectroscopic/astrometric/photometric data from future *Gaia* missions and upcoming large-scale stellar surveys (SDSS-V Kollmeier et al., 2017; WEAVE Dalton et al., 2014; 4MOST de Jong et al., 2019; DESI DESI Collaboration et al., 2016; MOONS Gonzalez et al., 2020), that will allow to mine the data for detailed kinematics, chemical abundances, and ages, will provide the full chemo-chrono-kinematic picture to fully disentangle the properties of different Galactic components.

The shear increased number and improved quality of observations delivered in the next few years will compaginate nicely the state-of-the-art data supplied by improved simulations of galaxy formation. As an example, the advent of the FIRE-3 cosmological simulations, which will enable the input of different sub-grid models for the treatment of chemical enrichment in post-processing, will be revolutionary for understanding the chemical abundance distribution of different stellar populations in MW-like galaxies, and for the genesis of different chemical elements. Another exciting suite of high-resolution zoom-in simulations that will be available will be ARTEMIS. These simulations will deliver a suite of forty-five Milky Way-like galaxies, providing the largest suite of Milky

Way-like haloes at a similar resolution to FIRE. These zoom-in simulations (including the existing Auriga, NIHAO, Vintergartan, and Hestia simulations), alongside larger cosmological simulations like EAGLE, Illustris, CoCo, amongst others, will provide the necessary theoretical tools to ground the Milky Way in a cosmological setting. Relating to this thesis, comparing these predictions to high-quality observations will be pivotal for studies focused on disentangling the origin of substructures in the stellar halo. In turn, contrasting observational data with predictions from cosmological simulations will help place the Galaxy in a cosmological setting.

In summary, the future is very bright for the field of Galactic archaeology.

Appendix A

A.1 High- and Low-α disks in action space

In this appendix I briefly present the distribution of disk stars in action space, to inform the discussion of accreted and *in situ* populations in Section 2.4. I start by distinguishing high- and low-α disk stars. For that purpose I display the parent sample on the Mg-Fe plane in Figure A.1, where the lines defining each sub-sample are drawn on top of the data. Metal-poor stars are removed in order to minimize contamination by halo stars.

High- and low-α disk stars are displayed in action and energy space in Figure A.2. The arrows indicate the approximate loci of stars belonging to the each sub-sample. The orange arrow points to the location of low-α disk stars (e.g., Bovy et al., 2012; Bensby et al., 2014; Nidever et al., 2014; Hayden et al., 2015; Mackereth et al., 2017; Queiroz et al., 2020b), which are characterised by high angular momentum, small energy scatter, and low radial (J_r) and vertical (J_z) actions. There are, however, outliers towards higher E, J_r, and Jz, which are due to contaminants from the GE/S system and possibly other accreted systems.

The high-α disk is dominated by two major structures. For constant L_z, these two high-α subgroups occupy significantly different and well separated values of J_r and energy. The most important for the purposes of this paper is strongly rotational, overlapping substantially with the low-α disk at high L_z, but also extending towards $L_\mathrm{z} \sim 0$ and presenting larger scatter towards higher E, J_r, and J_z (magenta arrow). The other component presents higher energy at $L_\mathrm{z}/10^3$1 kpc kms^{-1} and merges with the other components at higher L_z, being associated with the *Splash* population (see Belokurov et al., 2019) (green arrow).

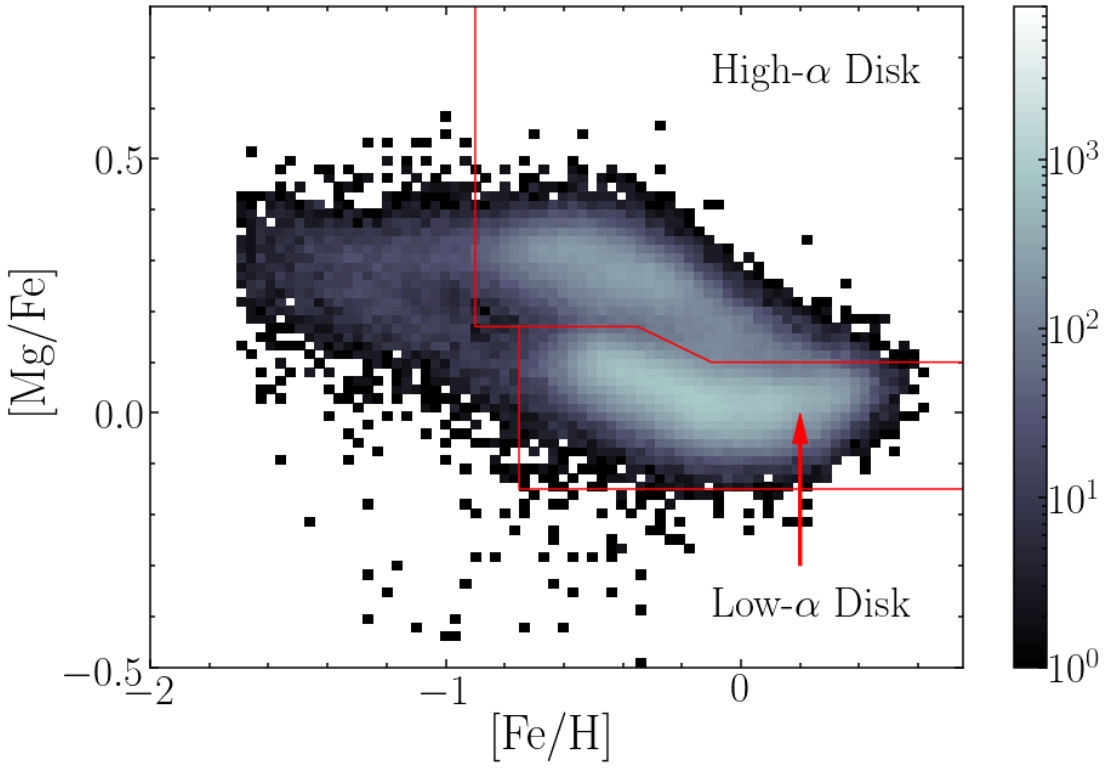

FIGURE A.1: Definition of high- and low-α disks on the Mg-Fe plane. We added a ± 0.04 dex "cushion" in [Mg/Fe] around the dividing line in order to minimize inter-contamination between the two samples.

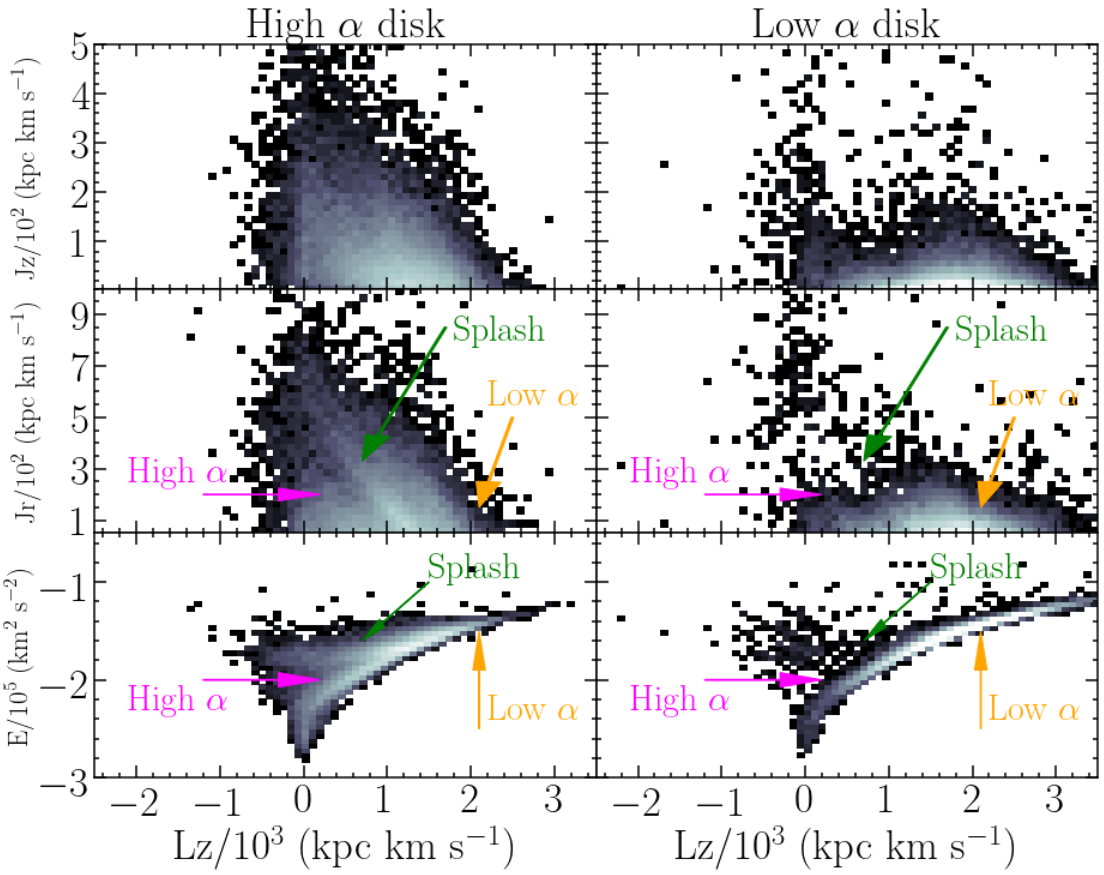

FIGURE A.2: Distribution of high- and low-α disk populations in action space. The orange arrow indicates the rough position of the low-α/thin disk populations, the magenta arrow that of the standard high-α/thick disk populations, and the green arrow that of stars associated with the *Splash*.

Appendix B

B.1 The reality of Icarus

The Icarus substructure is a metal-poor, [Mg/Fe]-poor structure that was identified by Re Fiorentin et al. (2021) using the APOGEE DR16 and GALAH DR3 data. I have attempted to identify Icarus star members by employing the criteria listed by Re Fiorentin et al. (2021), and identified only one potential member within the parent sample described in Section 3.2.1.9. I thus decided to retrieve the DR17 properties of the 41 Icarus stars presented by Re Fiorentin et al. (2021) on the basis of APOGEE DR16 data.

I found that only 3 out of the 41 Icarus candidates have $T_{\rm eff}$ and $\log g$ characteristic of red giant stars. The remaining 38 stars have stellar parameters consistent with a main sequence or subgiant nature (Figure B.1), which is the reason why the selection criteria described in Section 5.2 excluded them from the parent sample. This finding is confirmed by the positions of the Icarus member sample in the *Gaia* colthe-magnitude diagram shown in Figure B.2. Icarus was conjectured to be an accreted substructure in the Galactic disc based largely on chemical abundance information. However elemental abundances for sub-giant and main-sequence, and particularly for M dwarfs, were not very reliable in APOGEE DR16 (although see Birky et al., 2020; Souto et al., 2020). Therefore, I decided to perform some checks to see if the resulting abundances for these (primarily) M dwarf stars are reliable in APOGEE DR17.

I checked the `STAR_FLAG` and `ASPCAP_FLAG` flags of the 41 Icarus stars determined by Re Fiorentin et al. (2021). The results from this examination showed that: *i)* 25/41 stars had a "`BRIGHT_NEIGHBthe`", "`PERSIST_HIGH`", "`PERSIST_LOW`", "`LOW_SNR`", `SUSPECT_BROAD_LINES`, `SUSPECT_ROTATION`", `MULTIPLE_SUSPECT`", flag set in their `STAR_FLAG`, suggesting the occurrence of various issues with the observed spectra of these stars, which can lead up to uncertainties in stellar parameters and elemental abundances; *ii)* 40/41 stars had one or more of the following ASPCAP_FLAGs raised: "`STAR_WARN`",

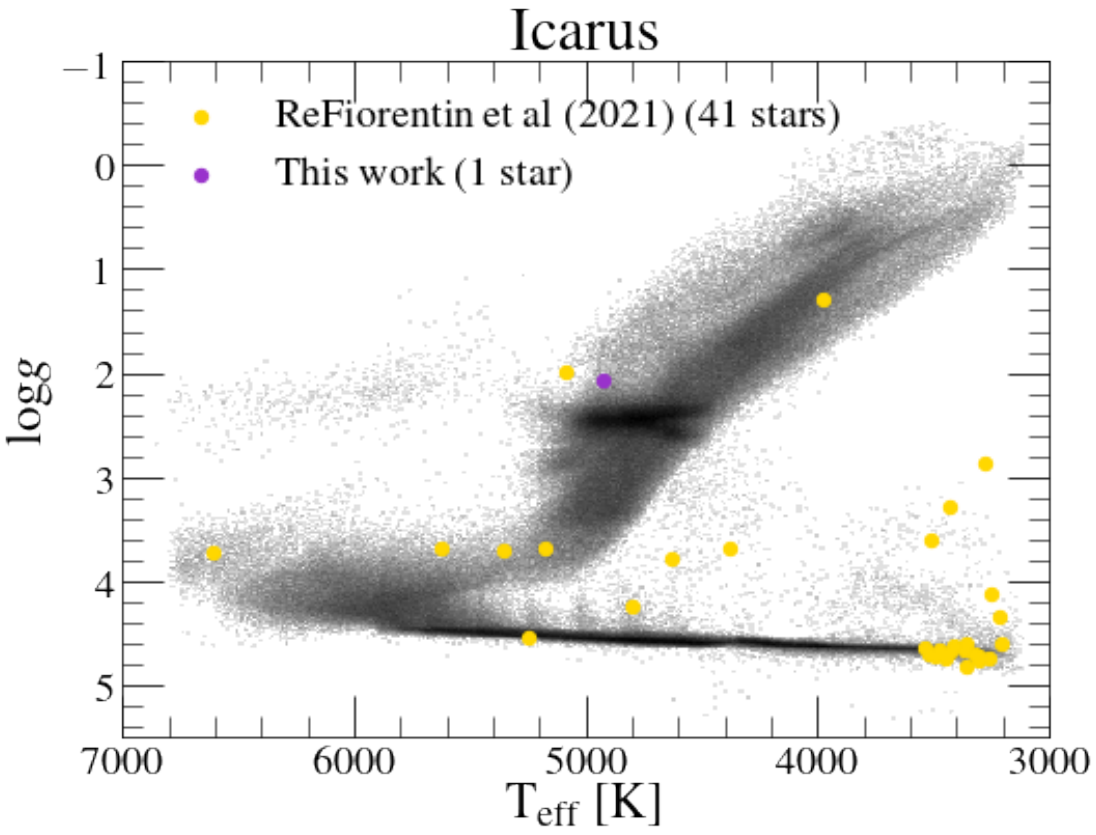

FIGURE B.1: Kiel diagram of the parent sample used in this work, the Icarus star identified in this paper (purple), and the Icarus stars identified by Re Fiorentin et al. (2021) (yellow), using APOGEE DR17 data.

"COLthe_TEMPERATURE_WARN", "SN_WARN", "VSINI_WARN", "VMICRO_WARN", "N_M_WARN", "TEFF_WARN", "LOGG_WARN", suggesting that the results from the ASPCAP analysis for these stars are likely uncertain.

In light of these results, I chose to exclude Icarus from this study, and suggest that this substructure is not the debris from a cannibalised dwarf galaxy, but is rather likely comprised of (primarily) M-dwarf stars with unreliable APOGEE abundances in the disc of the Milky Way.

B.2 The chemical compositions of Pontus according to APOGEE

As I have only been able to identify two star members belonging to the Pontus halo substructure, I will refrain from making any strong statement about its chemistry. However, based solely on the chemical compositions of the two member stars I have identified in this work, I find that the Pontus substructure presents elevated abundances in α-elements (namely, in O, Mg, Si), low C, Al, Ti, and Ce, and approximately solar Mn and Ni. The

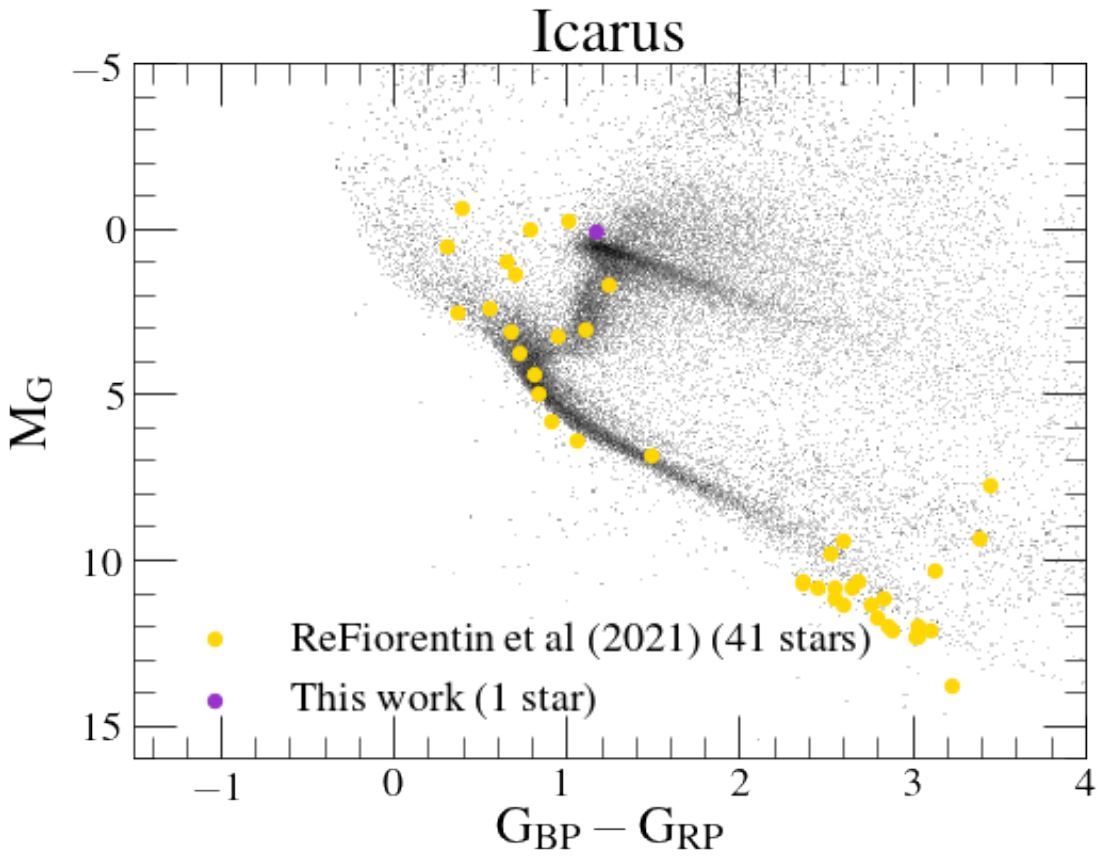

FIGURE B.2: The same samples as in Fig B.1, now in the *Gaia* colthe magnitude diagram using *Gaia* EDR3 data.

two stars I find associated with the Pontus substructure display similar chemical compositions to that of other halo substructures and/or satellite galaxies of the Milky Way. Although it is impossible to attribute any similarities or differences on the basis of two stars alone, given the close proximity between these two Pontus stars and Thamnos in the E-L_z plane, it is tempting to associate the former to the later. However, a larger sample of Pontus stars with reliable chemistry is required to ascertain this speculation.

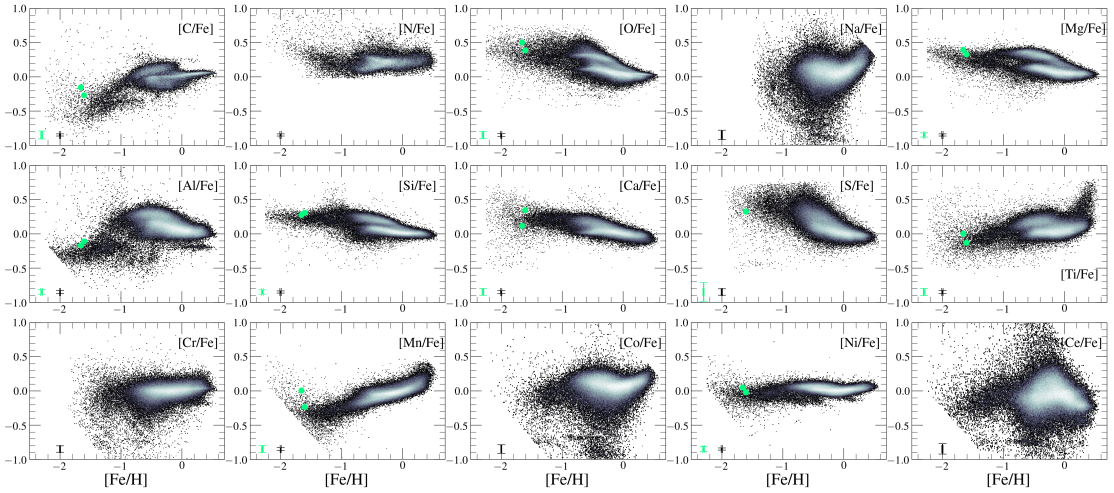

FIGURE B.3: Pontus stars (light green points) in every chemical composition plane studied in this work, from carbon to cerium. I note that for the C and N plots, I restrict the sample to stars with $1 < \log g < 2$, to account for dredge-up effects in the red giant branch, and for all abundances, I also make the following cuts: `X_FE_FLAG` $= 0$ and `X_FE_ERR` < 0.15. For the case of N, Na, Cr, Co, and Ce, the `X_FE_ERR` < 0.15 restriction removes the two Pontus stars, and for S it removes one.

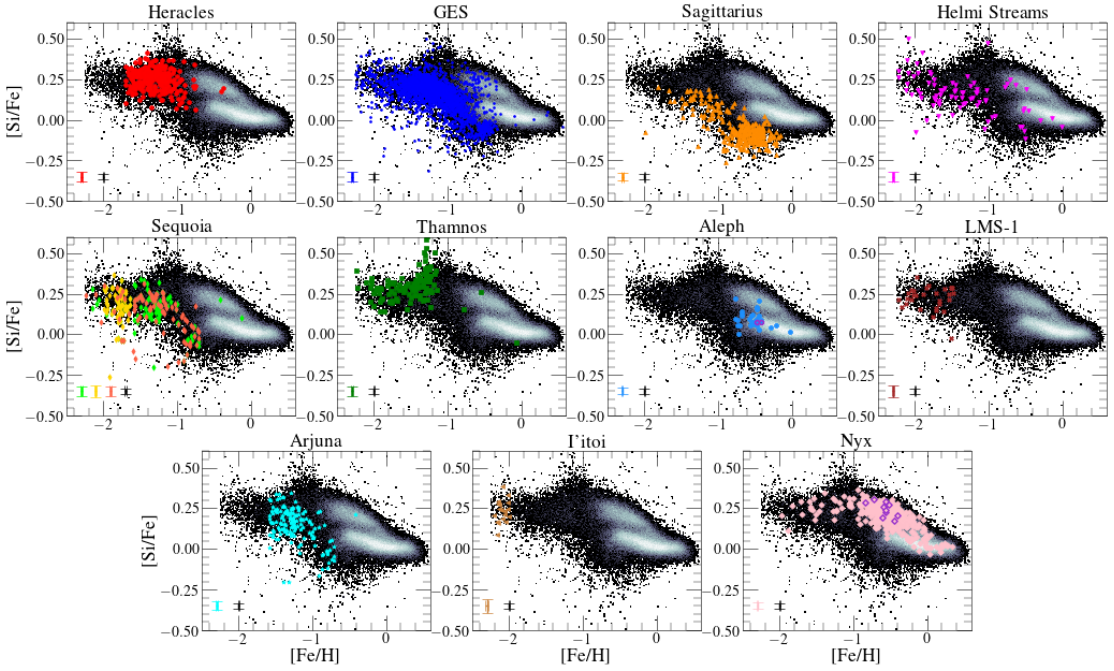

FIGURE B.4: The same illustration as Fig. 3.6 in the Si-Fe plane.

TABLE B.1: Mean orbital parameter values for each substructure studied in this work. I note that the the angular momentum, actions, orbital energy, eccentricity, maximum height above the plane, perigalacticon, and apogalacticon are computed using the McMillan (2017) potential.

Name	(v_R,v_ϕ,v_z) (kms^{-1})	(L_x,L_y,L_z) (kpc kms^{-1})	(J_r,J_ϕ,J_z) (kpc kms^{-1})
Heracles	(1.98±106.31, 11.66 ± 68.19, 2.35 ± 90.40)	(–1.63±148.57, − −3.76± 190.74, 26.47 ± 117.23)	(104.85±77.97, 29.42 ± 116.92, 160.81 ± 115.25)
Gaia-Enceladus/ Sausage	(–3.02±179.09, 6.87 ± 46.65, 5.69 ± 123.71)	(16.37±469.05, 69.90 ± 866.59, 15.38 ± 260.42)	(1043.02±449.16, 29.81 ± 260.10, 735.78 ± 650.55)
Sagittarius	(184.78±66.70, 105.56 ± 124.02, 124.94 ± 65.12)	(460.23±345.39, 3982.96± 1388.07, 735.78 ± 860.83)	(1164.12±575.14, 713.83± 871.68, 3030.59 ± 1236.89)
Helmi stream	(– 34.50±131.06, 150.67 ± 60.45, – – 63.37 ± 164.74)	(– 449.24±1210.39, 106.21 ± 1666.54, 1165.73 ± 274.68)	(793.40±1352.24, 1177.70± 280.38, 1353.60 ± 569.47)
Sequoia (*GC*)	(33.02±165.33, – – 172.78 ± 103.35, 17.01 ± 106.54)	(546.64±855.13, 124.07 ± 889.85, – – 1483.30 ± 778.86)	(1140.20±682.65, – – 1460.83 ± 774.12, 518.01 ± 406.26)
Sequoia (*field*)	(17.82±180.71, – – 89.64 ± 63.59, 26.30 ± 152.67)	(240.73±708.25, 104.55 ± 992.64, – – 707.92 ± 328.93)	(1116.81±493.20, – – 692.00 ± 323.36, 1000.38 ± 794.71)
Sequoia (*H3*)	(29.49±139.60, – – 171.34 ± 89.95, 9.26 ± 133.64)	(694.57±805.68, 220.29 ± 1025.37, – – 1439.97 ± 778.89)	(838.67±932.26, – – 1417.29 ± 775.90, 709.11 ± 609.28)
Thamnos	(13.05±87.02, – – 118.38 ± 40.33, – – 12.71 ± 71.43)	(92.86±294.91, 133.09 ± 461.47, – – 849.80 ± 192.88)	(266.58±91.32, – – 829.93 ± 189.28, 187.87 ± 148.79)
Aleph	(–4.04±38.55, 212.50 ± 23.29, − −14.04 ± 33.63)	(–345.82±656.52, – – 124.49±369.04, 2040.06± 422.91)	(44.06±35.72, 2055.17 ± 427.09, 188.46 ± 10.46)
LMS-1	(5.61±93.13, 125.65 ± 34.12, 16.73 ± 94.98)	(–201.77±698.43, 68.87 ± 901.47, 824.52 ± 131.36)	(254.87±110.66, 836.90 ± 132.36, 660.16 ± 470.59)
Arjuna	(20.83±175.58, – – 153.31 ± 86.74, 33.47 ± 133.44)	(613.03±1025.87, – – 4.17 ± 1043.82, – – 1283.14 ± 632.18)	(1479.70±2099.64, – – 1263.86 ± 625.65, 775.53 ± 663.40)
I'itoi	(19.61±99.41, – – 156.35 ± 63.47, 59.13 ± 133.86)	(562.58±1064.28, – – 375.26 ± 1092.75, – – 1360.07 ± 422.32)	(455.74±548.87, – – 1338.53 ± 419.21, 897.37 ± 615.83)
Nyx	(133.85±21.27, 158.01 ± 26.21, 5.73 ± 48.88)	(–57.72±164.31, 17.24 ± 365.47, 1242.37 ± 276.75)	(291.19±104.29, 1258.34± 278.25, 55.49 ± 54.31)

TABLE B.2: Table B.1 continued.

Name	E (km^2s^{-2})	(ecc,z_{max},R_{peri},R_{apo}) (–,kpc,kpc,kpc)
Heracles	–224860.22±15322.44	(0.81±0.12, 1.67 ± 0.85, 0.33 ± 0.24, 3.01 ± 1.02)
Gaia-Enceladus/ Sausage	–142394.72±12519.88	(0.93±0.06, 9.84 ± 6.14, 0.61 ± 1.03, 17.15 ± 5.22)
Sagittarius	–107654.44±17153.96	(0.69±0.20, 35.74 ± 17.68, 8.81 ± 7.34, 38.12 ± 17.86)
Helmi stream	–127688.22±18244.58	(0.65±0.15, 16.37 ± 9.37, 3.97 ± 1.36, 24.05 ± 20.67)
Sequoia (*GC*)	–126706.32±17892.71	(0.73±0.10, 11.11 ± 9.01, 4.13 ± 2.49, 26.55 ± 14.52)
Sequoia (*field*)	–126553.68±7592.99	(0.85±0.05, 13.82 ± 6.05, 1.84 ± 0.78, 22.62 ± 5.72)
Sequoia (*H3*)	–132658.56±20758.16	(0.65±0.13, 10.70 ± 10.07, 4.22 ± 2.31, 22.88 ± 16.63)
Thamnos	–169972.44±5539.53	(0.57±0.10, 3.10 ± 1.60, 2.47 ± 0.70, 9.05 ± 1.08)
Aleph	–146048.56±9553.77	(0.18±0.07, 4.06 ± 0.56, 8.46 ± 2.00, 12.06 ± 2.73)
LMS-1	–156766.37±10493.48	(0.61±0.06, 7.04 ± 2.75, 2.59 ± 0.54, 10.89 ± 1.95)
Arjuna	–125020.44±22921.19	(0.74±0.12, 17.13 ± 23.15, 3.70 ± 2.27, 31.73 ± 34.98)
I'itoi	–136512.56±18198.76	(0.55±0.16, 10.87 ± 6.53, 4.84 ± 1.98, 18.09 ± 10.51)
Nyx	–161398.10±8604.29	(0.50±0.08, 1.58 ± 0.85, 3.78 ± 0.95, 11.20 ± 1.98)

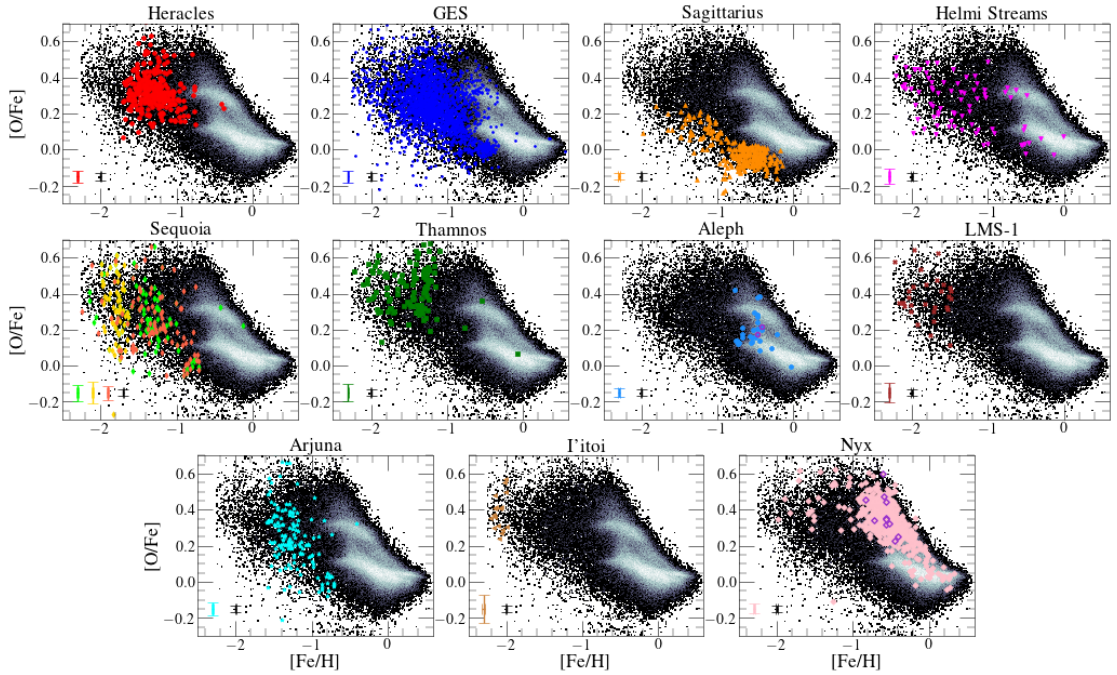

FIGURE B.5: The same illustration as Fig. 3.6 in the O-Fe plane.

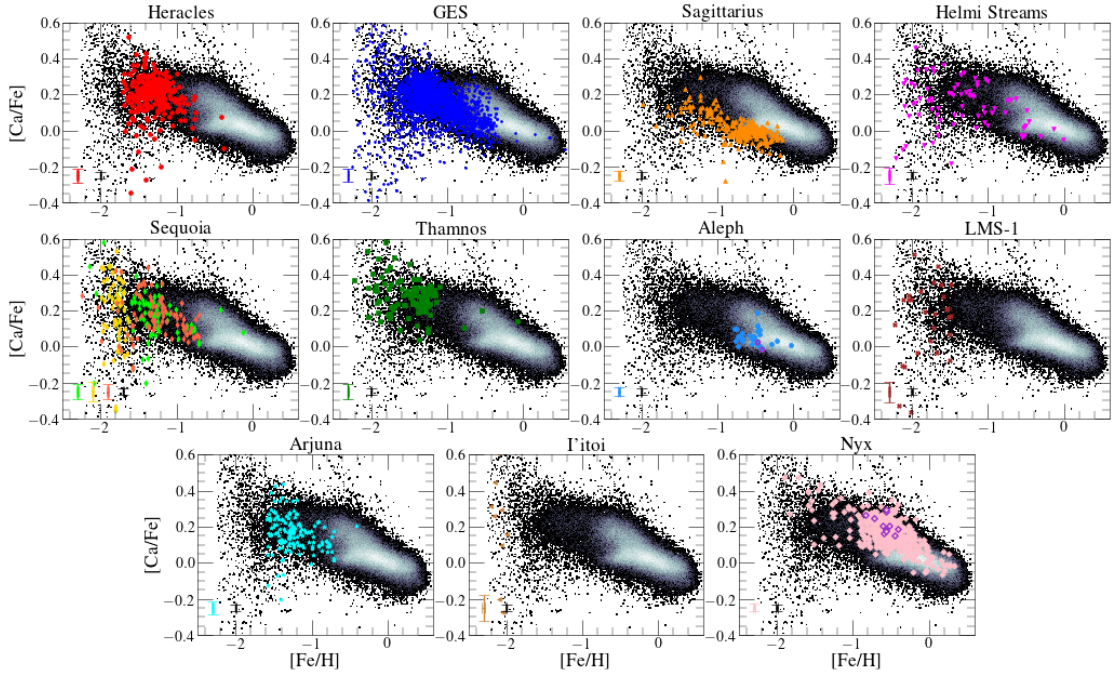

FIGURE B.6: The same illustration as Fig. 3.6 in the Ca-Fe plane.

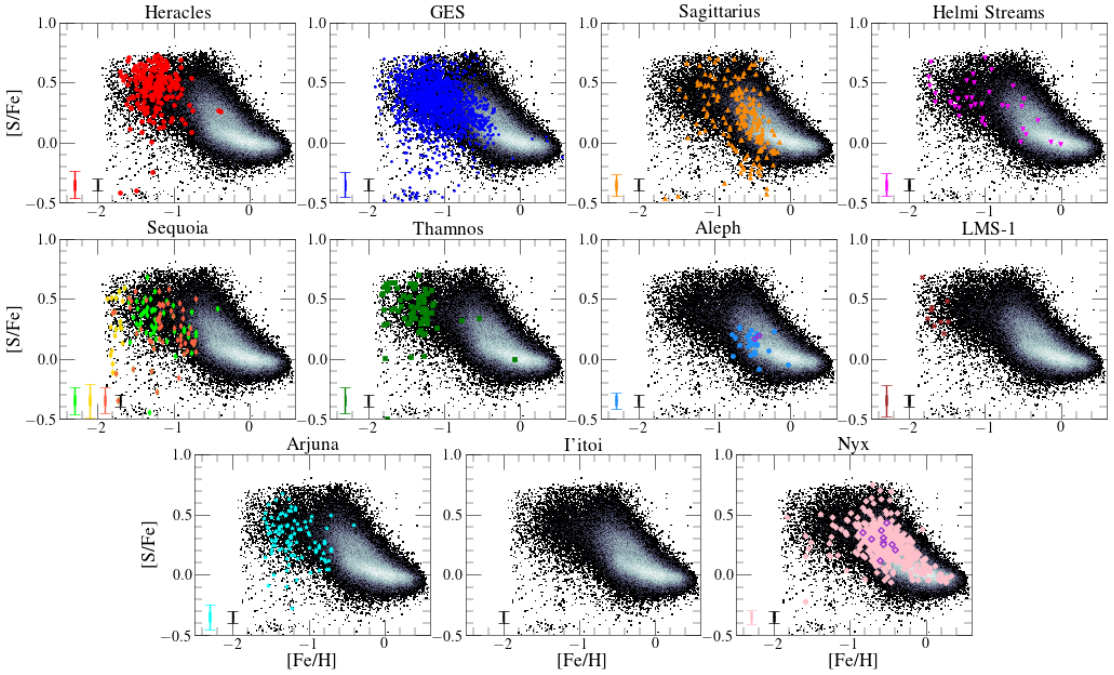

FIGURE B.7: The same illustration as Fig. 3.6 in the S-Fe plane. I note that the grid limit appears clearly in this plane at the lowest [Fe/H] and highest [S/Fe] values.

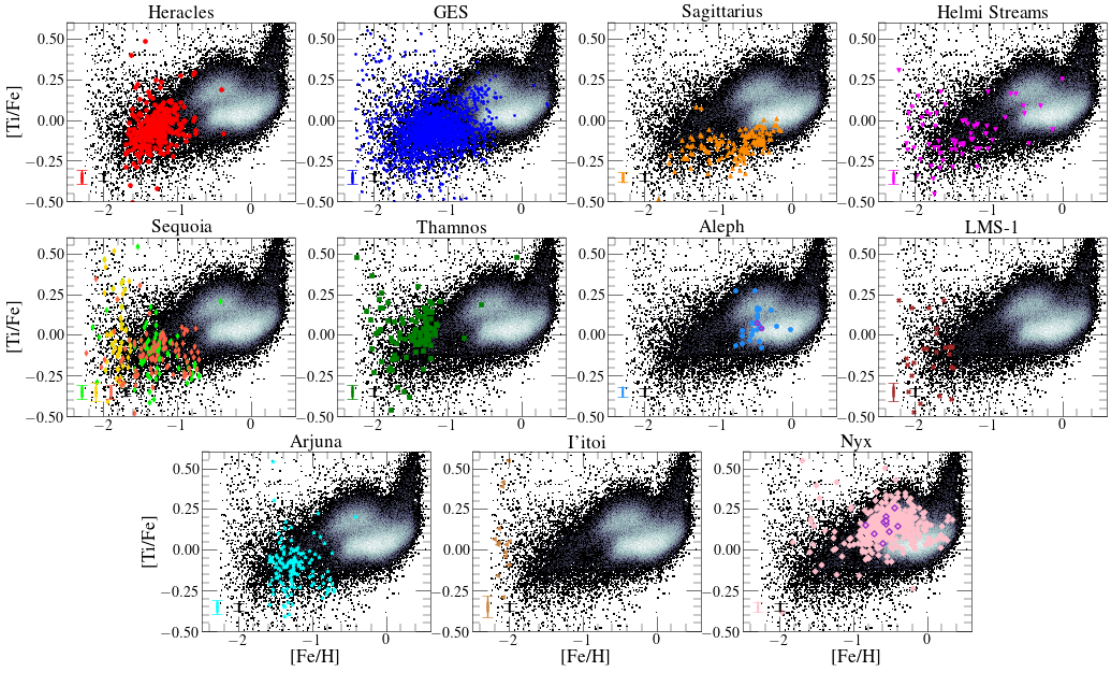

FIGURE B.8: The same illustration as Fig. 3.6 in the Ti-Fe plane.

TABLE B.3: Mean ⟨[X/Fe]⟩ abundance values for every halo substructure identified in this study. As I only identified 2(1) stars belonging to Pontus(Icarus), I exclude these halo substructures from this table.

⟨[X/Fe]⟩	Heracles	*Gaia*-Enceladus/ Sausage	Sagittarius	Helmi stream	Sequoia (*GC*)	Sequoia (*field*)
⟨[C/Fe]⟩	–	–	–	–	–	–
	0.30±0.18	0.30±0.29	0.38±0.14	0.35±0.36	0.31±0.32	0.37±0.23
⟨[N/Fe]⟩	0.26±0.18	0.19±0.37	0.04±0.14	0.22±0.33	0.13±0.34	0.15±0.35
⟨[O/Fe]⟩	0.32±0.09	0.24±0.19	–	0.27±0.16	0.26±0.17	0.24±0.18
			0.01±0.08			
⟨[Na/Fe]⟩	–	0.02±0.51	–	0.21±0.48	0.14±0.50	0.05±0.51
	0.01±0.42		0.34±0.27			
⟨[Mg/Fe]⟩	0.28±0.06	0.16±0.14	–	0.19±0.14	0.17±0.13	0.14±0.16
			0.03±0.08			
⟨[Al/Fe]⟩	–	–	–	–	–	–
	0.13±0.09	0.21±0.23	0.44±0.08	0.25±0.21	0.29±0.17	0.28±0.20
⟨[Si/Fe]⟩	0.25±0.06	0.14±0.13	–	0.16±0.12	0.15±0.10	0.13±0.16
			0.05±0.10			
⟨[Ca/Fe]⟩	0.19±0.12	0.15±0.18	0.01±0.07	0.14±0.16	0.16±0.17	0.15±0.19
⟨[Ti/Fe]⟩	–	–	–	–	–	–
	0.04±0.13	0.04±0.20	0.15±0.09	0.11±0.20	0.07±0.21	0.09±0.17
⟨[Cr/Fe]⟩	–	–	–	–	–	–
	0.13±0.33	0.10±0.40	0.07±0.19	0.04±0.36	0.04±0.41	0.18±0.40
⟨[Mn/Fe]⟩	–	–	–	–	–	–
	0.32±0.14	0.28±0.22	0.20±0.10	0.23±0.20	0.33±0.18	0.28±0.17
⟨[Co/Fe]⟩	–	–	–	–	–	–
	0.19±0.36	0.09±0.44	0.16±0.15	0.06±0.37	0.08±0.44	0.08±0.42
⟨[Ni/Fe]⟩	–	–	–	–	–	–
	0.03±0.08	0.07±0.15	0.14±0.06	0.06±0.10	0.11±0.10	0.09±0.11
⟨[Ce/Fe]⟩	–	–	–	–	–	–
	0.15±0.24	0.11±0.36	0.00±0.26	0.12±0.34	0.12±0.42	0.17±0.39
⟨[Fe/H]⟩	–	–	–	–	–	–
	1.30±0.21	1.18±0.42	0.72±0.34	1.39±0.55	1.41±0.36	1.31±0.37

TABLE B.4: Table B.3 continued.

⟨[X/Fe]⟩	Sequoia ($H3$)	Thamnos	Aleph	LMS-1	Arjuna	I'itoi	Nyx
⟨[C/Fe]⟩	–	–	0.01±0.07	–	–	–	0.07±0.09
	0.25±0.43	0.17±0.28		0.46±0.23	0.33±0.22	0.40±0.59	
⟨[N/Fe]⟩	0.23±0.39	0.12±0.36	0.17±0.08	0.29±0.39	0.11±0.29	0.23±0.53	0.08±0.16
⟨[O/Fe]⟩	0.31±0.17	0.43±0.13	0.19±0.09	0.38±0.11	0.23±0.17	0.41±0.12	0.33±0.11
⟨[Na/Fe]⟩	0.44±0.55	0.24±0.57	0.02±0.26	0.38±0.49	–	0.71±0.56	0.04±0.32
					0.01±0.46		
⟨[Mg/Fe]⟩	0.22±0.13	0.33±0.08	0.17±0.06	0.28±0.09	0.14±0.13	0.34±0.05	0.32±0.08
⟨[Al/Fe]⟩	–	–	0.12±0.07	–	–	–	0.24±0.12
	0.33±0.19	0.06±0.23		0.30±0.10	0.26±0.20	0.33±0.07	
⟨[Si/Fe]⟩	0.17±0.10	0.30±0.10	0.10±0.05	0.22±0.07	0.14±0.11	0.23±0.07	0.21±0.06
⟨[Ca/Fe]⟩	0.17±0.22	0.26±0.18	0.06±0.04	0.10±0.27	0.17±0.10	0.19±0.48	0.17±0.08
⟨[Ti/Fe]⟩	–	0.01±0.17	0.07±0.10	–	–	0.04±0.27	0.15±0.09
	0.06±0.29			0.11±0.20	0.10±0.16		
⟨[Cr/Fe]⟩	0.09±0.45	–	–	–	–	0.23±0.41	–
		0.05±0.40	0.04±0.11	0.12±0.40	0.16±0.37		0.05±0.16
⟨[Mn/Fe]⟩	–	–	–	–	–	0.01±0.13	–
	0.32±0.22	0.37±0.18	0.08±0.05	0.30±0.22	0.32±0.17		0.15±0.09
⟨[Co/Fe]⟩	0.07±0.46	0.02±0.41	0.02±0.22	–	–	0.19±0.46	0.06±0.26
				0.02±0.52	0.13±0.40		
⟨[Ni/Fe]⟩	–	–	0.03±0.02	–	–	–	0.06±0.04
	0.09±0.14	0.04±0.12		0.05±0.12	0.09±0.09	0.01±0.13	
⟨[Ce/Fe]⟩	–	–	–	–	–	0.02±0.35	–
	0.13±0.42	0.13±0.31	0.12±0.29	0.17±0.25	0.13±0.39		0.16±0.29
⟨[Fe/H]⟩	–	–	–	–	–	–	–
	1.80±0.09	1.53±0.36	0.53±0.17	1.83±0.25	1.24±0.24	2.14±0.10	0.55±0.29

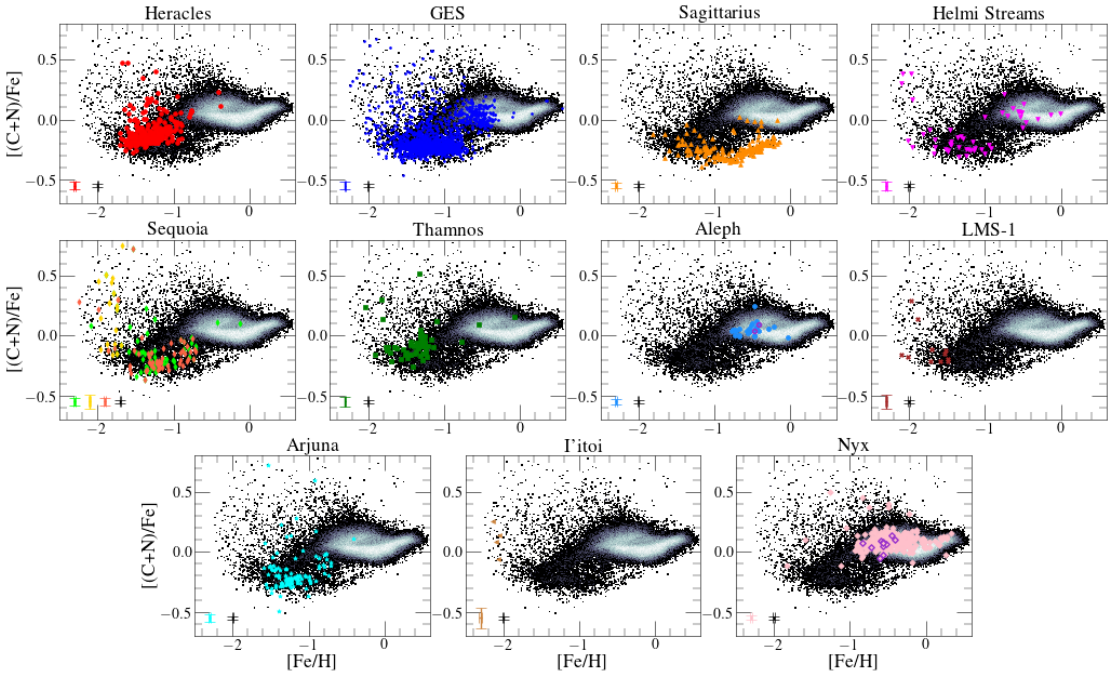

FIGURE B.9: The same illustration as Fig. 3.6 in the (C+N)-Fe plane.

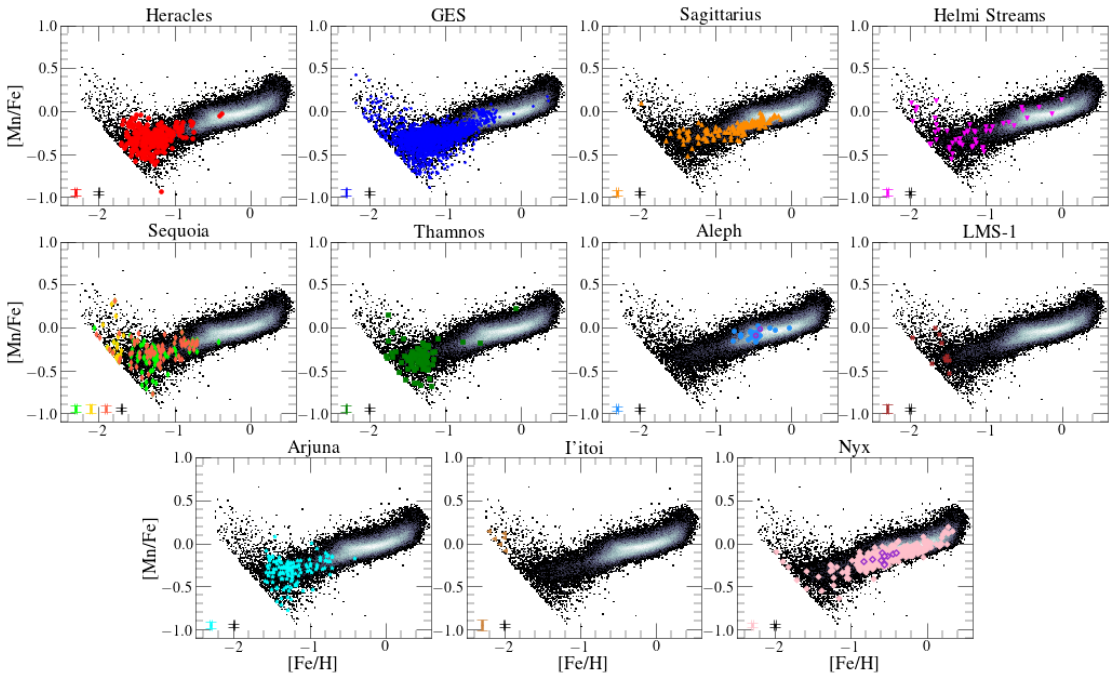

FIGURE B.10: The same illustration as Fig. 3.6 in the Mn-Fe plane. I note that the grid limit appears clearly in this plane at the lowest [Fe/H] values.

B.3 Chemical and kinematic properties of halo substructures

B.4 α-elements

B.5 (C+N)/Fe

B.6 Iron-peak elements

B.7 Odd-Z elements

B.8 [Fe/H] used to compare substructures

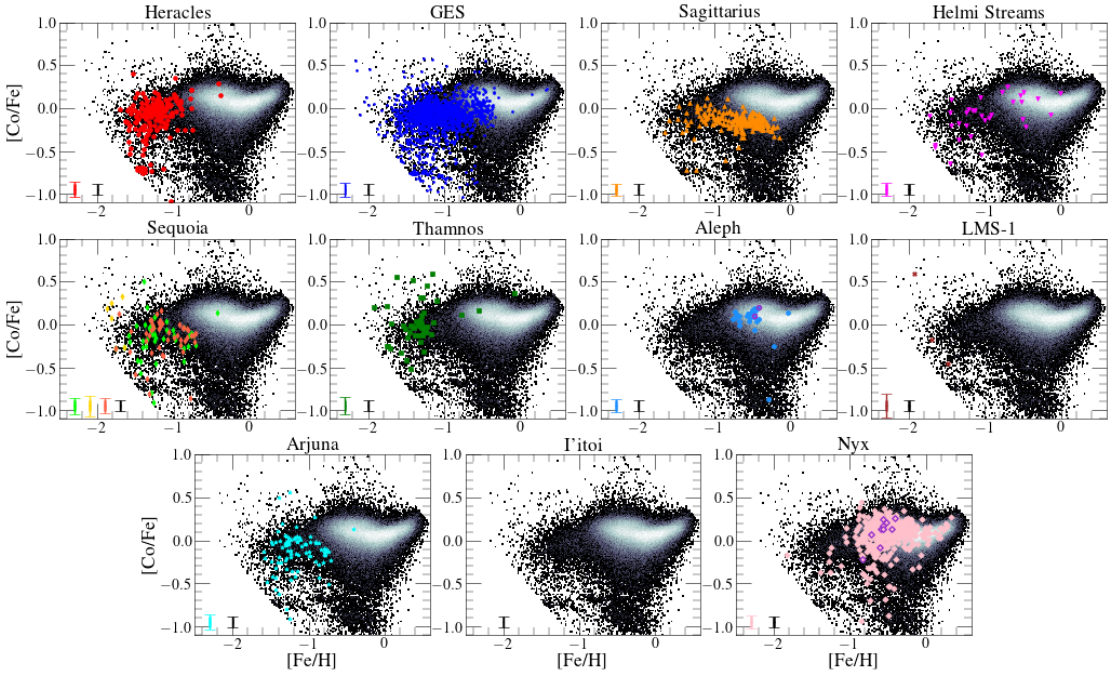

FIGURE B.11: The same illustration as Fig. 3.6 in the Co-Fe plane. I note that the grid limit appears clearly in this plane at the lowest [Fe/H] values.

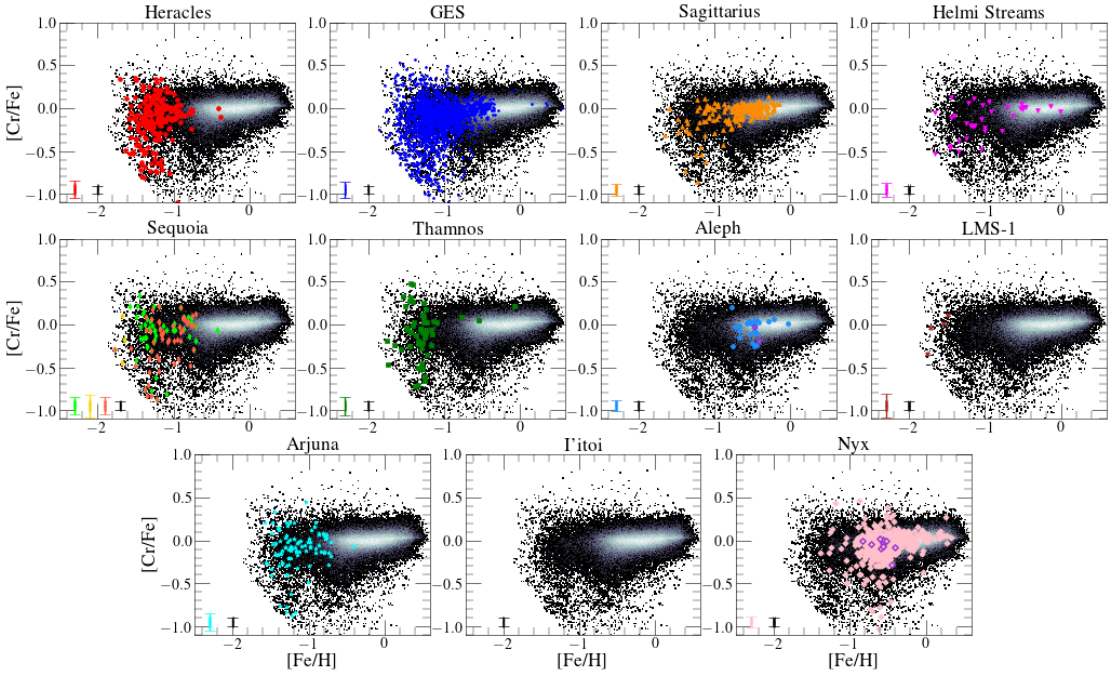

FIGURE B.12: The same illustration as Fig. 3.6 in the Cr-Fe plane. I note that the grid limit appears clearly in this plane at the lowest [Fe/H] values.

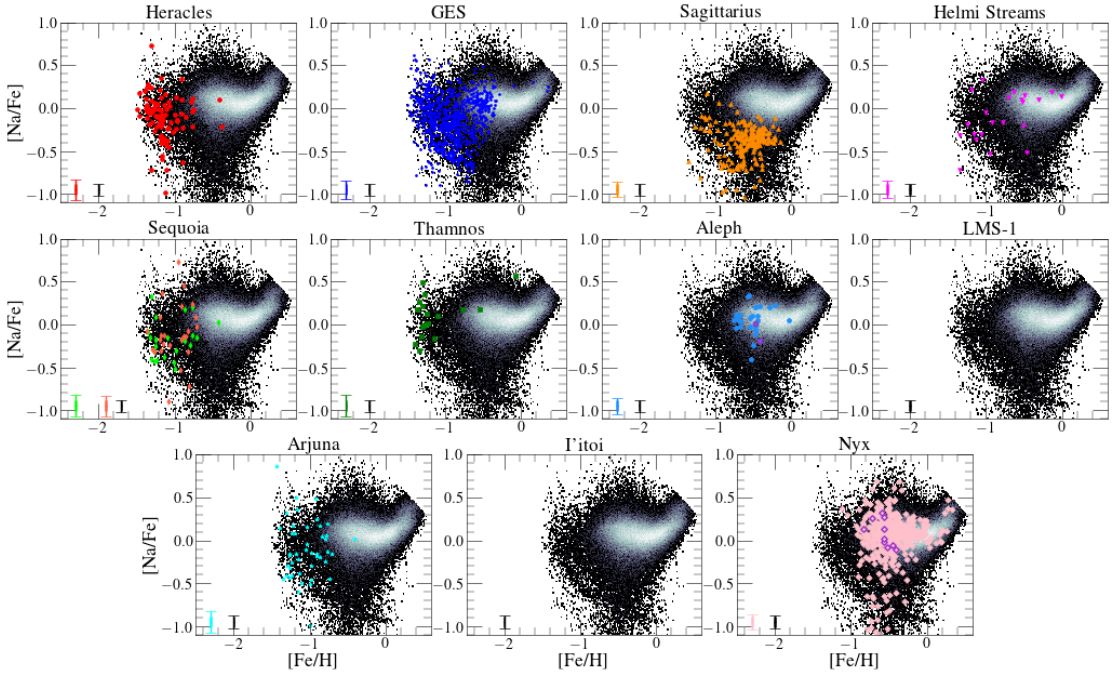

FIGURE B.13: The same illustration as Fig. 3.6 in the Na-Fe plane. I note that the grid limit appears clearly in this plane at the lowest [Fe/H] values.

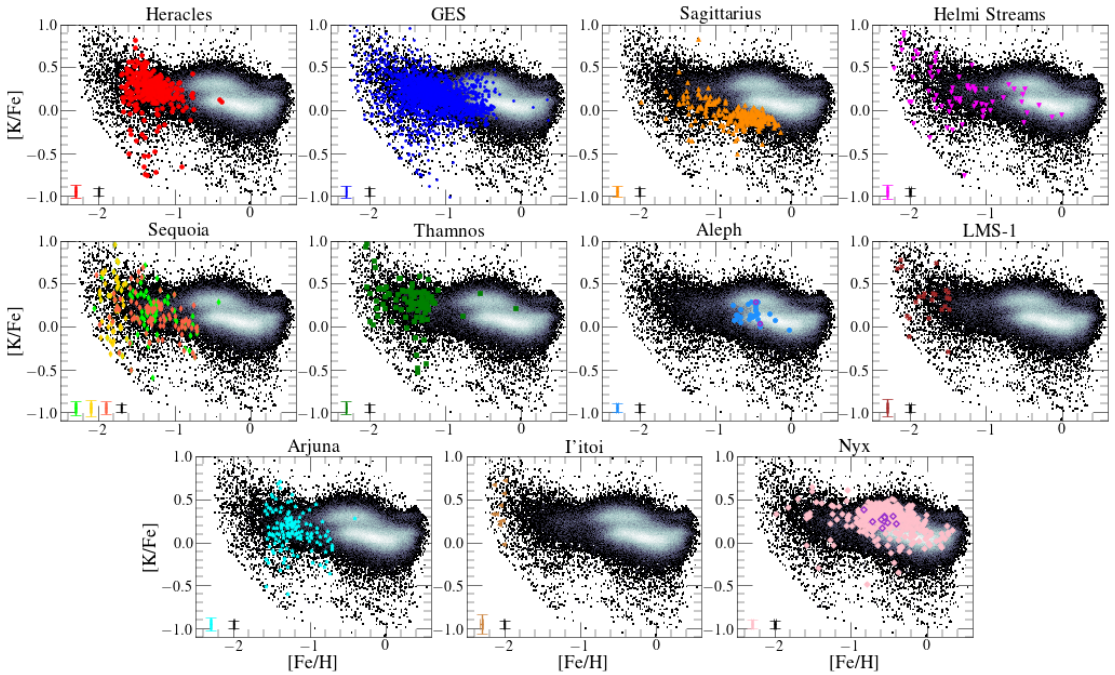

FIGURE B.14: The same illustration as Fig. 3.6 in the K-Fe plane. I note that the grid limit appears clearly in this plane at the lowest [Fe/H] values.

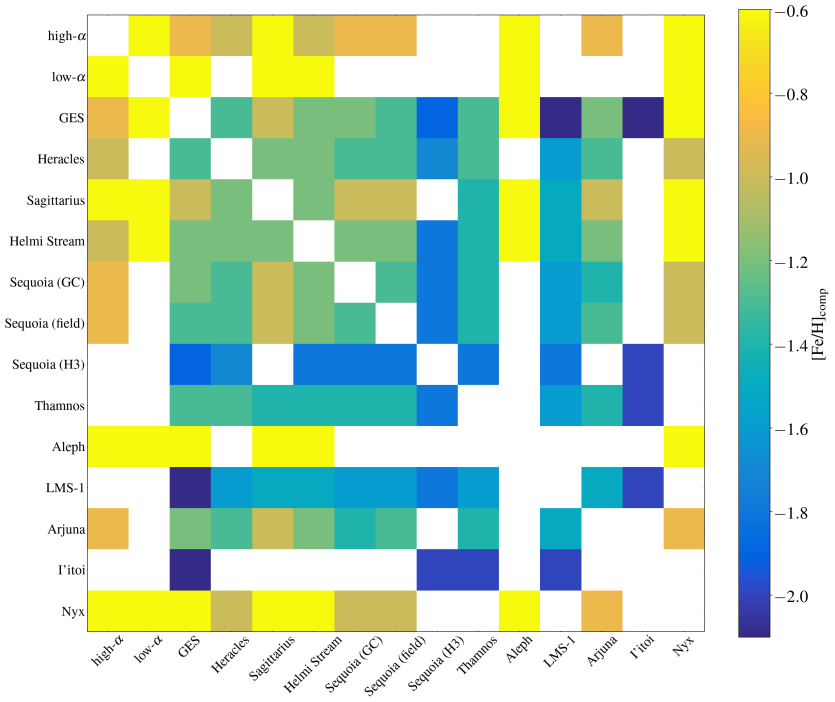

FIGURE B.15: $[Fe/H]_{comp}$ used to obtain the results from Fig 3.18 when comparing every halo substructure with all the other substructures and with a high-/low-α disc sample.

Appendix C

C.1 Fitting the N-rich star sample

I set out to determine the best fit model to the sample of N-rich stars. Our methodology consists on fitting several different stellar halo density models and determining their logarithmic maximum likelihood ($\ln(\mathcal{L}_{\rm max})$) and Bayesian Information Criterion (BIC, Schwarz, 1978) values (see Section 4.3.3). I then compare the values obtained for each density model, and take the profile with the lowest BIC value to be our best fit model. If two models obtain the same $\ln(\mathcal{L}_{\rm max})$ value, the BIC value gives preference to the model with the lowest number of free ranging parameters, therefore choosing the simplest model.

As described in Section 4.3.2, our N-rich sample is fit by a spherical single power law (SPL), an axisymmetric single power law (AXI), a triaxial power law (TRI), a rotated triaxial power law with the inclusion of a cut-off term and a disc contamination parameter (TRI-CUT-DISC), a broken power law (BPL), and an exponential disc profile (DISC). The resulting BIC and $\ln(\mathcal{L}_{\rm max})$ values obtained using the median posterior parameter of the 10,000 MCMC realisations for each model are listed in Table 5.1. From our results, I find that the best fit model to our N-rich sample is the AXI model, and therefore choose to use this model for the remainder of the analysis. However, as is apparent from Fig. C.1, the TRI and TRI-CUT-DISC density profiles also provide good fits to the N-rich star data. Moreover, I repeat the methodology for determining the percentage ratio contribution of N-rich stars to the halo field employed in the main body of the paper using the TRI and TRI-CUT-DISC profile as the best-fitting N-rich models, in order to check if our results vary when adopting a different model for the N-rich star sample. The results from this comparison show that our initial findings remain unchanged, and suggest that the N-rich star sample can either be well modelled by the AXI, TRI, and TRI-CUT-DISC profiles.

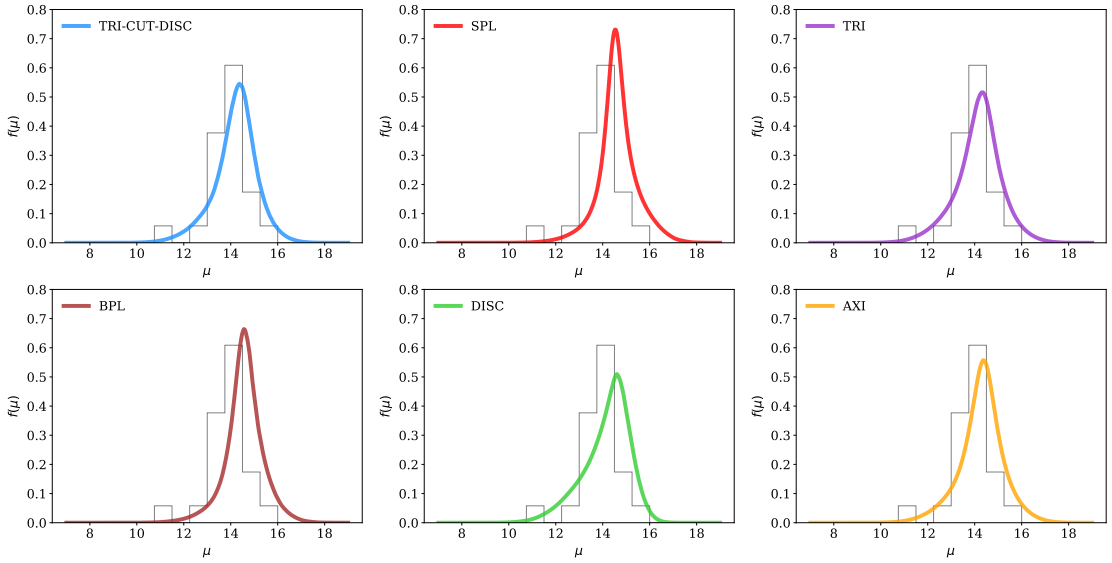

FIGURE C.1: Density profile fits to the N-rich star data from Section 5.2. Each profile is obtained by taking the median posterior parameter value obtained from the 10,000 MCMC samples. The AXI profile is the best-fitting profile, closely followed by the TRI and TRI-CUT-DISC profile.

Density profile	Best-fit parameters
SPL	α=$3.86^{+0.21}_{-0.18}$
AXI	α=$\mathbf{4.47^{+0.23}_{-0.22}}$, q=$\mathbf{0.47^{+0.05}_{-0.04}}$
TRI	α=$4.54^{+0.26}_{-0.24}$, p=$0.85^{+0.09}_{-0.10}$, q=$0.44^{+0.05}_{-0.05}$
TRI-CUT-DISC	α=$4.30^{+0.12}_{-0.31}$, β=$0.03^{+0.03}_{-0.02}$, p=$0.60^{+0.21}_{-0.09}$, q=$0.41^{+0.11}_{-0.07}$, η=$0.20^{+0.03}_{-0.04}$, θ=$0.06^{+0.2}_{-0.06}$ [°], ϕ=$0.25^{+0.07}_{-2.38}$ [°], $f_{\rm disc}$=$0.04^{+0.11}_{-0.03}$
BPL	$\alpha_{\rm in}$=$3.19^{+0.52}_{-0.46}$, $\alpha_{\rm out}$=$6.05^{+1.25}_{-1.37}$, $R_{\rm break}$=$8.13^{+2.03}_{-1.82}$[kpc]
DISC	$1/h_{\rm R}$=$0.41^{+0.04}_{-0.04}$[kpc^{-1}],$1/h_{\rm Z}$=$0.64^{+0.09}_{-0.08}$[kpc^{-1}]

TABLE C.1: Resulting best-fit parameters for the different functional density forms fitted to the N-rich star sample. The best-fitting model (AXI) is highlighted in bold.

Appendix D

D.1 GC metallicity and radial velocity distribution functions

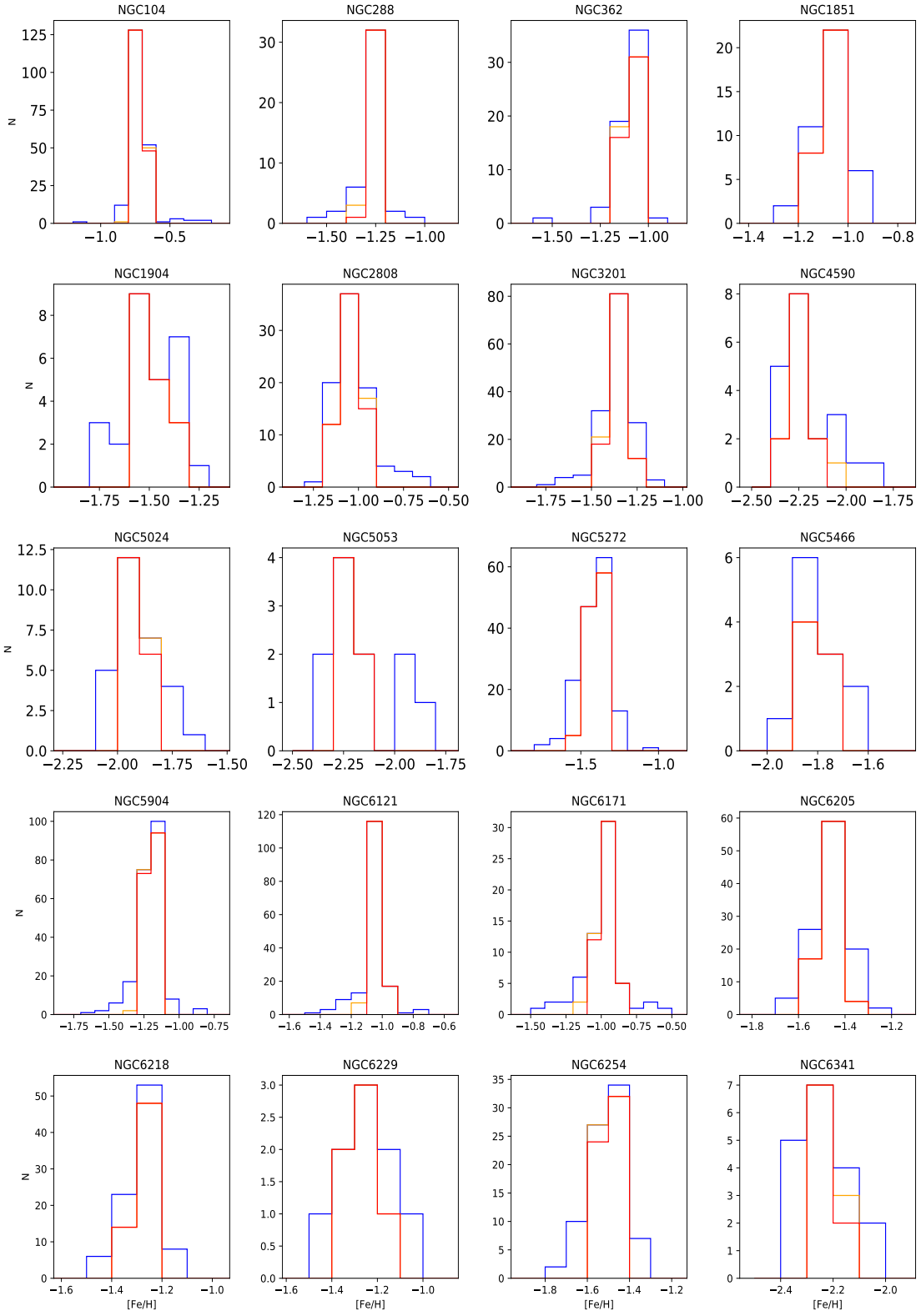

FIGURE D.1: Metallicity distribution functions for the GCs in the main sample. The blue histogram represents the GC members obtained before employing the MDF sigma clip cut, for which the resulting members are highlighted as the yellow histogram. The red histogram are the resulting members after performing a second MDF sigma clip. Recall that for each GC a different clip was applied, depending on the cluster and the MDF distribution.

.

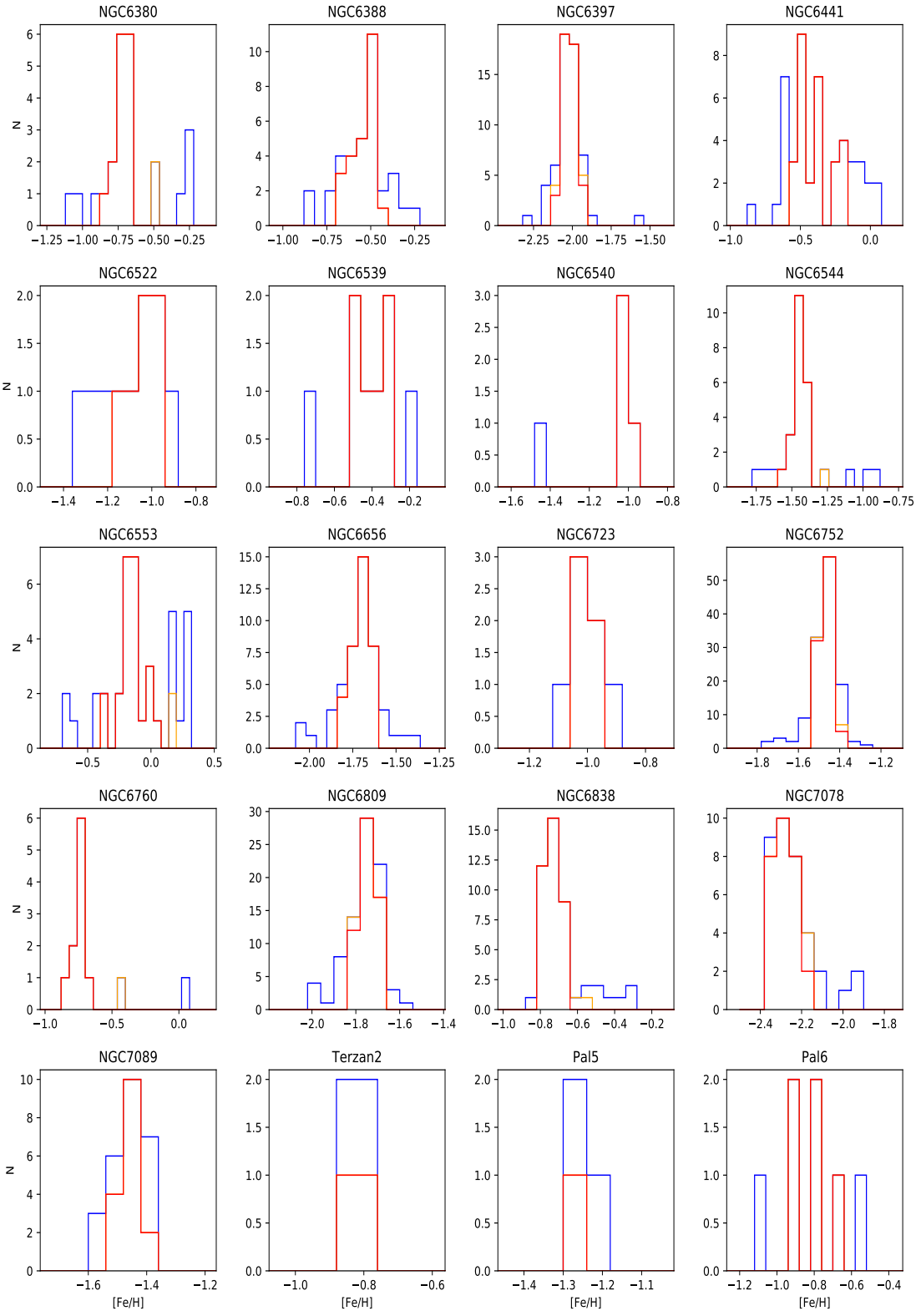

FIGURE D.2: Fig D.1 continued.

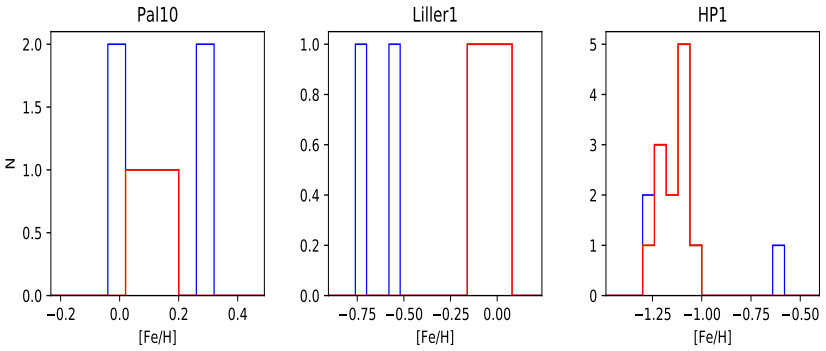

FIGURE D.3: Fig D.1 continued.

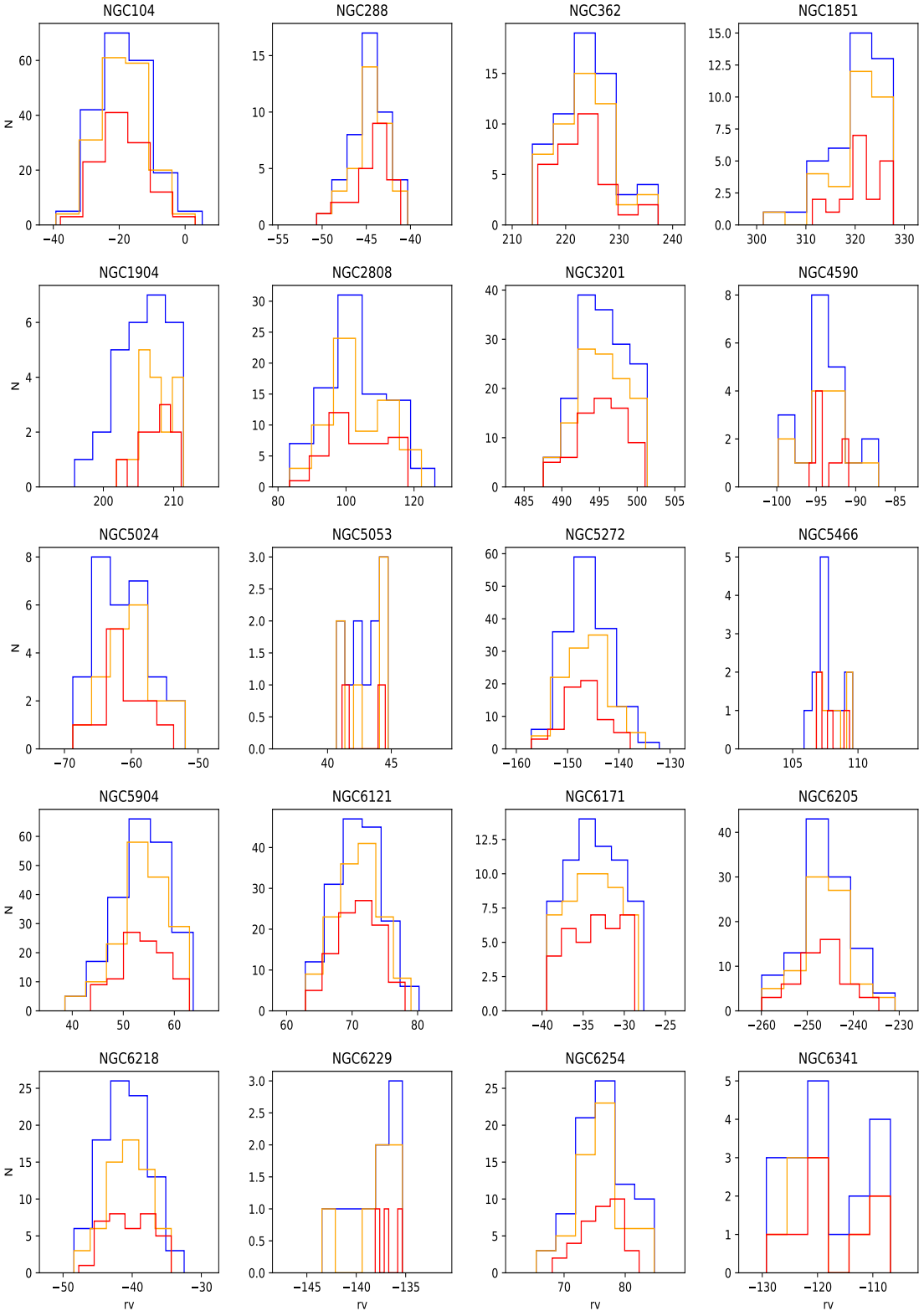

FIGURE D.4: Radial velocities (in units of km/s) for the GCs in the main sample. The blue histogram represents the GC members obtained before employing the MDF sigma clip cut, for which the resulting members are highlighted as the yellow histogram. The red histogram are the resulting members after performing a second MDF sigma clip.

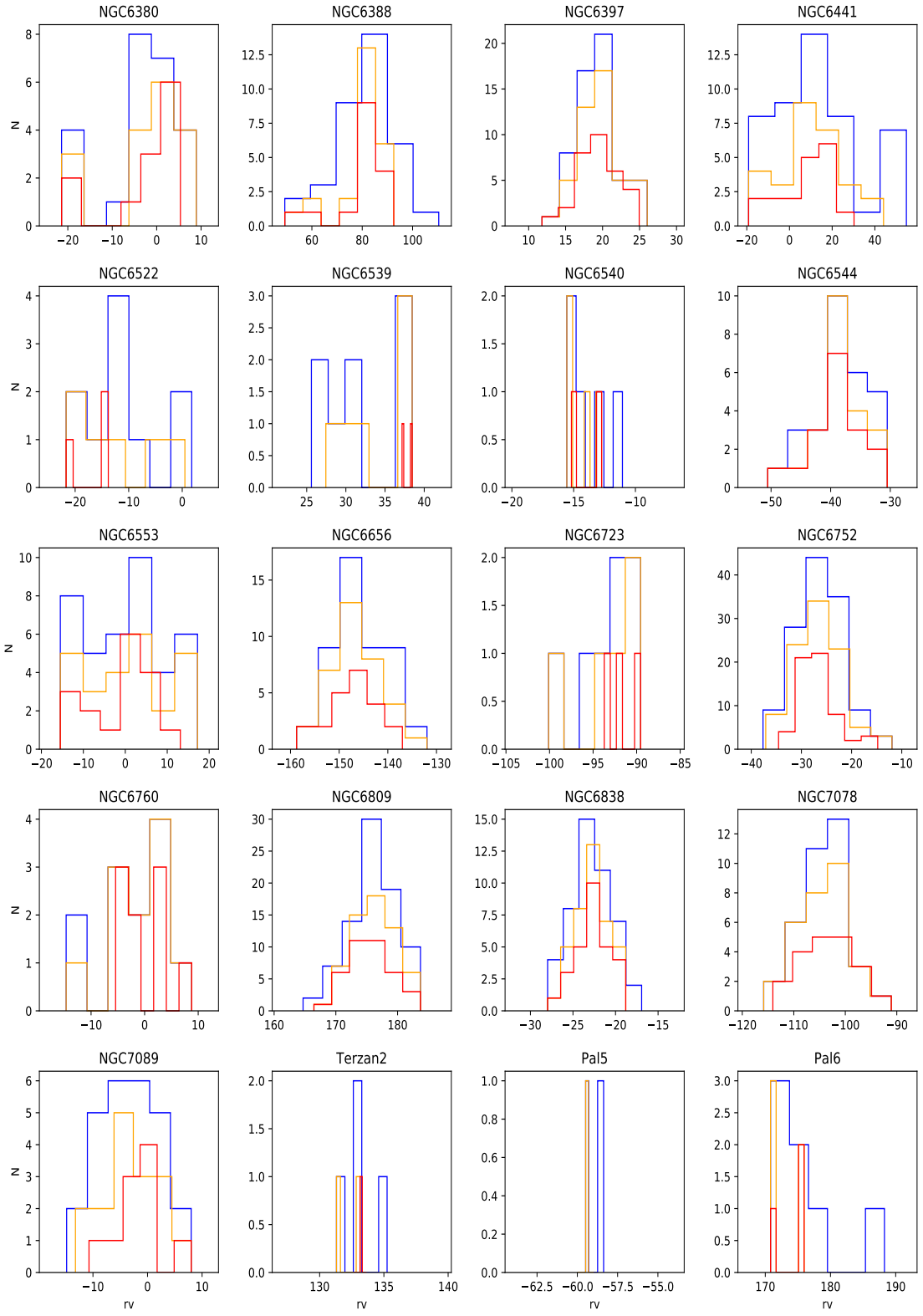

FIGURE D.5: Fig D.4 continued.

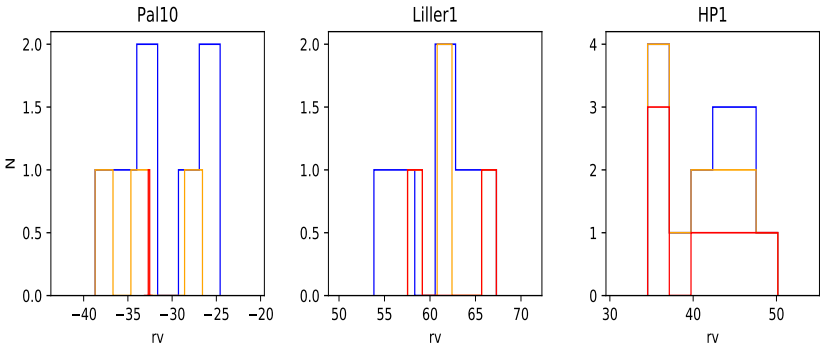

FIGURE D.6: Fig D.4 continued.

Bibliography

Abadi M. G., Navarro J. F., Steinmetz M., Eke V. R., 2003, ApJ, 597, 21

Abadi M. G., Navarro J. F., Steinmetz M., 2006, MNRAS, 365, 747

Abdurro'uf Accetta K., Aerts C., Silva Aguirre V., Ahumada R., Ajgaonkar N., Filiz Ak N., Alam S., 2021, arXiv e-prints, p. arXiv:2112.02026

Adibekyan V. Z., Sousa S. G., Santos N. C., Delgado Mena E., González Hernández J. I., Israelian G., Mayor M., Khachatryan G., 2012, A&A, 545, A32

Agertz O., et al., 2020, VINTERGATAN I: The origins of chemically, kinematically and structurally distinct discs in a simulated Milky Way-mass galaxy (`arXiv:2006.06008`)

Aguado D. S., et al., 2020, arXiv e-prints, p. arXiv:2012.01430

Ahumada R., Prieto C. A., Almeida A., Anders F., Anderson S. F., Andrews B. H., Anguiano B., Arcodia R., 2019a, The Sixteenth Data Release of the Sloan Digital Sky Surveys: First Release from the APOGEE-2 Southern Survey and Full Release of eBOSS Spectra (`arXiv:1912.02905`)

Ahumada R., Allende Prieto C., Almeida A., Anders F., 2019b, arXiv e-prints, p. arXiv:1912.02905

Allende Prieto C., Beers T. C., Wilhelm R., Newberg H. J., Rockosi C. M., Yanny B., Lee Y. S., 2006, ApJ, 636, 804

Alves-Brito A., Meléndez J., Asplund M., Ramírez I., Yong D., 2010, A&A, 513, A35

An D., Beers T. C., 2021, arXiv e-prints, p. arXiv:2104.09737

Anders F., Chiappini C., Santiago B. X., Rocha-Pinto H. J., Girardi L., 2014, A&A, 564, A115

Andrews B. H., Weinberg D. H., Schönrich R., Johnson J. A., 2017, ApJ, 835, 224

Arentsen A., et al., 2020a, arXiv e-prints, p. arXiv:2006.08641

Arentsen A., et al., 2020b, MNRAS, 491, L11

Arentsen A., et al., 2020c, MNRAS, 496, 4964

Ashman K. M., Zepf S. E., 1992, ApJ, 384, 50

Baade W., 1946, PASA, 58, 249

Bahcall J. N., Tremaine S., 1981, ApJ, 244, 805

Barbá R. H., Minniti D., Geisler D., Alonso-García J., Hempel M., Monachesi A., Arias J. I., Gómez F. A., 2019, ApJ Letters, 870, L24

Barbuy B., Chiappini C., Gerhard O., 2018, Annual Review of Astronomy and Astrophysics, 56, 223

Bastian N., Lardo C., 2015, MNRAS, 453, 357

Bastian N., Lardo C., 2018, Annual Review of Astronomy and Astrophysics, 56, 83

Baumgardt H., Hilker M., 2018, MNRAS, 478, 1520

Baumgardt H., Hilker M., Sollima A., Bellini A., 2019, MNRAS, 482, 5138

Beaton R. L., Oelkers R. J., Hayes C. R., Covey 2021, arXiv e-prints, p. arXiv:2108.11907

Beers T. C., Christlieb N., 2005, Annual Review of Astronomy and Astrophysics, 43, 531

Beers T. C., Drilling J. S., Rossi S., Chiba M., Rhee J., Führmeister B., Norris J. E., von Hippel T., 2002, ApJ, 124, 931

Bekki K., 2019, MNRAS, p. 2345

Bell E. F., et al., 2008, ApJ, 680, 295

Belokurov V., 2013, Nature, 57, 100

Belokurov V., et al., 2006, The Astrophysical Journal, 642, L137

Belokurov V., Erkal D., Evans N. W., Koposov S. E., Deason A. J., 2018, MNRAS, 478, 611

Belokurov V., Sanders J. L., Fattahi A., Smith M. C., Deason A. J., Evans N. W., Grand R. J. J., 2019, arXiv e-prints, p. arXiv:1909.04679

Belokurov V., Sanders J. L., Fattahi A., Smith M. C., Deason A. J., Evans N. W., Grand R. J. J., 2020, MNRAS, 494, 3880

Bennett M., Bovy J., 2019, MNRAS, 482, 1417

Bensby T., Feltzing S., Lundström I., Ilyin I., 2005, A&A, 433, 185

Bensby T., Feltzing S., Oey M. S., 2014, A&A, 562, A71

Bica E., Ortolani S., Barbuy B., 2016, PASA, 33, e028

Binney J., 2012, MNRAS, 426, 1324

Binney J., Wong L. K., 2017, MNRAS, 467, 2446

Binney J., Gerhard O., Spergel D., 1997, MNRAS, 288, 365

Birky J., Hogg D. W., Mann A. W., Burgasser A., 2020, ApJ, 892, 31

Bland-Hawthorn J., Gerhard O., 2016, Annual Review of Astronomy and Astrophysics, 54, 529

Blanton M. R., Bershady M. A., Abolfathi B., Albareti F. D., 2017, ApJ, 154, 28

Blitz L., Spergel D. N., 1991, ApJ, 379, 631

Bonaca A., Conroy C., Wetzel A., Hopkins P. F., Kereš D., 2017, ApJ, 845, 101

Bovy J., 2014, galpy: Galactic dynamics package (ascl:1411.008)

Bovy J., 2015, ApJ, 216, 29

Bovy J., Hogg D. W., Roweis S. T., 2011, Annals of Applied Statistics, 5, 1657

Bovy J., Rix H.-W., Liu C., Hogg D. W., Beers T. C., Lee Y. S., 2012, ApJ, 753, 148

Bovy J., Nidever D. L., Rix H.-W., Girardi L., Zasowski G., Chojnowski S. D., 2014, ApJ, 790, 127

Bovy J., Rix H.-W., Schlafly E. F., Nidever D. L., Holtzman J. A., Shetrone M., Beers T. C., 2016, ApJ, 823, 30

Bovy J., Leung H. W., Hunt J. A. S., Mackereth J. T., García-Hernández D. A., Roman-Lopes A., 2019, MNRAS, 490, 4740

Bowen I. S., Vaughan A. H. J., 1973, , 12, 1430

Bressan A., Marigo P., Girardi L., Salasnich B., Dal Cero C., Rubele S., Nanni A., 2012, MNRAS, 427, 127

Brodie J. P., Strader J., 2006, Annual Review of Astronomy and Astrophysics, 44, 193

Buck T., 2019, Monthly Notices of the Royal Astronomical Society, 491, 5435–5446

Buder S., Lind K., Ness M. K., Feuillet D. K., Horta D., Galah Collaboration 2022, MNRAS, 510, 2407

Bullock J. S., Boylan-Kolchin M., 2017, Annual Review of Astronomy and Astrophysics, 55, 343

Bullock J. S., Johnston K. V., 2005, ApJ, 635, 931

Burbidge E. M., Burbidge G. R., Fowler W. A., Hoyle F., 1957, Reviews of Modern Physics, 29, 547

Bureau M., Aronica G., Athanassoula E., Dettmar R. J., Bosma A., Freeman K. C., 2006, MNRAS, 370, 753

Burstein D., 1979, ApJ, 234, 829

Cabrera-Ziri I., et al., 2015, MNRAS, 448, 2224

Callingham T. M., Cautun M., Deason A. J., Frenk C. S., Grand R. J. J., Marinacci F., 2022, arXiv e-prints, p. arXiv:2202.00591

Campello R. J. G. B., Moulavi D., Sander J., 2013, in Pei J., Tseng V. S., Cao L., Motoda H., Xu G., eds, Advances in Knowledge Discovery and Data Mining. Springer Berlin Heidelberg, Berlin, Heidelberg, pp 160–172

Cao L., Mao S., Nataf D., Rattenbury N. J., Gould A., 2013, MNRAS, 434, 595

Carlin J. L., Sheffield A. A., Cunha K., Smith V. V., 2018, ApJ Letters, 859, L10

Carollo D., et al., 2007, Nature, 450, 1020

Carollo D., et al., 2010, ApJ, 712, 692

Carollo D., Martell S. L., Beers T. C., Freeman K. C., 2013, ApJ, 769, 87

Carretta E., Bragaglia A., 2018, Astronomy and Astrophysics, 614, A109

Carretta E., et al., 2009, A&A, 505, 117

Carrillo A., Hawkins K., Jofré P., de Brito Silva D., Das P., Lucey M., 2022, arXiv e-prints, p. arXiv:2202.10416

Chiappini C., Romano D., Matteucci F., 2003, MNRAS, 339, 63

Chiba M., Beers T. C., 2000, ApJ, 119, 2843

Churchwell E., et al., 2009, PASA, 121, 213

Cioni M. R. L., 2009, A&A, 506, 1137

Cirasuolo M., MOONS Consortium 2016, in Skillen I., Balcells M., Trager S., eds, Astronomical Society of the Pacific Conference Series Vol. 507, Multi-Object Spectroscopy in the Next Decade: Big Questions, Large Surveys, and Wide Fields. p. 109

Clarkson W., et al., 2008, ApJ, 684, 1110

Conroy C., et al., 2019, ApJ, 883, 107

Cooper A. P., et al., 2010, MNRAS, 406, 744

Cooper A. P., Parry O. H., Lowing B., Cole S., Frenk C., 2015, MNRAS, 454, 3185

Crain R. A., et al., 2015, MNRAS, 450, 1937

Cunha K., et al., 2017, ApJ, 844, 145

DESI Collaboration Aghamousa A., Aguilar J., Ahlen S., Alam S., Allen L. E., 2016, arXiv e-prints, p. arXiv:1611.00036

Daley D., Vere-Jones D., 2003, doi:10.1007/b97277,

Dalton G., et al., 2014, in Ramsay S. K., McLean I. S., Takami H., eds, Society of Photo-Optical Instrumentation Engineers (SPIE) Conference Series Vol. 9147, Ground-based and Airborne Instrumentation for Astronomy V. p. 91470L (`arXiv:1412.0843`), doi:10.1117/12.2055132

Das P., Hawkins K., Jofré P., 2020, MNRAS, 493, 5195

De Lucia G., Helmi A., 2008, MNRAS, 391, 14

De Silva G. M., Freeman K. C., Bland-Hawthorn J., Martell S., de Boer E. W., Asplund M., 2015, MNRAS, 449, 2604

Deason A. J., Belokurov V., Evans N. W., 2011, MNRAS, 416, 2903

Deason A. J., et al., 2012, MNRAS, 425, 2840

Deason A. J., Belokurov V., Evans N. W., Johnston K. V., 2013, ApJ, 763, 113

Deason A. J., Belokurov V., Sanders J. L., 2019, MNRAS, 490, 3426

Deason A. J., Fattahi A., Frenk C. S., Grand R. J. J., Oman K. A., Garrison-Kimmel S., Simpson C. M., Navarro J. F., 2020, MNRAS, 496, 3929

Deason A. J., et al., 2021, MNRAS, 501, 5964

Debattista V. P., Ness M., Gonzalez O. A., Freeman K., Zoccali M., Minniti D., 2017, MNRAS, 469, 1587

Di Matteo P., 2016, PASA, 33, e027

Di Matteo P., Haywood M., Lehnert M. D., Katz D., Khoperskov S., Snaith O. N., Gómez A., Robichon N., 2019, A&A, 632, A4

Diemand J., Madau P., Moore B., 2005, MNRAS, 364, 367

Dillamore A. M., Belokurov V., Font A. S., McCarthy I. G., 2022, MNRAS, 513, 1867

Dwek E., et al., 1995, ApJ, 445, 716

Eggen O. J., Lynden-Bell D., Sandage A. R., 1962, ApJ, 136, 748

Eilers A.-C., Hogg D. W., Rix H.-W., Ness M. K., Price-Whelan A. M., Meszaros S., Nitschelm C., 2021, arXiv e-prints, p. arXiv:2112.03295

Einasto J., 1965, Trudy Astrofizicheskogo Instituta Alma-Ata, 5, 87

Eisenstein D. J., Weinberg D. H., Agol E., Aihara H., Allende Prieto C., 2011, ApJ, 142, 72

El-Badry K., et al., 2018, MNRAS, 480, 652

Elmegreen B. G., 2010, ApJ Letters, 712, L184

Fall S. M., Rees M. J., 1985, ApJ, 298, 18

Fattahi A., et al., 2020, MNRAS, 497, 4459

Fernández-Alvar E., et al., 2021, MNRAS, 508, 1509

Fernández-Trincado J. G., Beers T. C., Tang B., Moreno E., Pérez-Villegas A., Ortigoza-Urdaneta M., 2019, MNRAS, 488, 2864

Fernández-Trincado J. G., Chaves-Velasquez L., Pérez-Villegas A., Vieira K., Moreno E., Ortigoza-Urdaneta M., Vega-Neme L., 2020, MNRAS, 495, 4113

Feuillet D. K., Feltzing S., Sahlholdt C. L., Casagrande L., 2020, MNRAS, 497, 109

Feuillet D. K., Sahlholdt C. L., Feltzing S., Casagrande L., 2021, MNRAS, 508, 1489

Font A. S., Johnston K. V., Bullock J. S., Robertson B. E., 2006, ApJ, 638, 585

Font A. S., McCarthy I. G., Crain R. A., Theuns T., Schaye J., Wiersma R. P. C., Dalla Vecchia C., 2011, MNRAS, 416, 2802

Font A. S., et al., 2020, MNRAS, 498, 1765

Forbes D. A., 2020, MNRAS,

Forbes D. A., Bridges T., 2010, MNRAS, 404, 1203

Fowler W. A., Burbidge G. R., Burbidge E. M., 1955, ApJ, 122, 271

Fragione G., Loeb A., 2017, Nature, 55, 32

Fragkoudi F., Di Matteo P., Haywood M., Schultheis M., Khoperskov S., Gómez A., Combes F., 2018, A&A, 616, A180

Fragkoudi F., et al., 2020, MNRAS, 494, 5936

Freeman K., Bland-Hawthorn J., 2002, Annual Review of Astronomy and Astrophysics, 40, 487

Frenk C. S., White S. D. M., 2012, Annalen der Physik, 524, 507

Fuhrmann K., 1998, A&A, 338, 161

Fulbright J. P., McWilliam A., Rich R. M., 2007, ApJ, 661, 1152

Gaia Collaboration 2018, A&A, 616, A1

Gaia Collaboration Brown A. G. A., Vallenari A., Prusti T., de Bruijne J. H. J., Babusiaux C., Biermann M., 2020, arXiv e-prints, p. arXiv:2012.01533

Gallino R., Arlandini C., Busso M., Lugaro M., Travaglio C., Straniero O., Chieffi A., Limongi M., 1998, ApJ, 497, 388

García Pérez A. E., et al., 2013, ApJ Letters, 767, L9

García Pérez A. E., et al., 2016, ApJ, 151, 144

García Pérez A. E., et al., 2018, ApJ, 852, 91

Gerhard O., 2002, Social Science Research, 100, 129

Gilmore G., Reid N., 1983, MNRAS, 202, 1025

Gilmore G., Randich S., Asplund M., Binney J., Bonifacio P., Gaia-ESO Survey Team 2012, The Messenger, 147, 25

Gnedin O. Y., 2001, Astronomical and Astrophysical Transactions, 20, 39

Gnedin O. Y., Ostriker J. P., Tremaine S., 2014, ApJ, 785, 71

Goddard D., et al., 2017, MNRAS, 465, 688

Gómez F. A., Minchev I., O'Shea B. W., Beers T. C., Bullock J. S., Purcell C. W., 2013, MNRAS, 429, 159

Gonzalez O. A., Gadotti D., 2016, in Laurikainen E., Peletier R., Gadotti D., eds, Astrophysics and Space Science Library Vol. 418, Galactic Bulges. p. 199 (arXiv:1503.07252), doi:10.1007/978-3-319-19378-6_9

Gonzalez O. A., et al., 2011, A&A, 530, A54

Gonzalez O. A., Mucciarelli A., Origlia L., Schultheis M., 2020, arXiv e-prints, p. arXiv:2009.00635

Grand R. J. J., et al., 2018, MNRAS, 474, 3629

Grand R. J. J., et al., 2020, MNRAS, 497, 1603

Gravity Collaboration 2019, A&A, 625, L10

Green G. M., Schlafly E. F., Zucker C., Speagle J. S., Finkbeiner D. P., 2019, arXiv e-prints, p. arXiv:1905.02734

Gunn J. E., Siegmund W. A., Mannery E. J., Owen R. E., 2006, ApJ, 131, 2332

Hanke M., Koch A., Prudil Z., Grebel E. K., Bastian U., 2020, arXiv e-prints, p. arXiv:2004.00018

Harris W. E., 1996, VizieR Online Data Catalog, p. VII/195

Hasselquist S., et al., 2017, ApJ, 845, 162

Hasselquist S., et al., 2019, ApJ, 871, 181

Hasselquist S., et al., 2020, arXiv e-prints, p. arXiv:2008.03603

Hasselquist S., Hayes C. R., Lian J., Weinberg D. H., Zasowski G., Horta D., 2021, arXiv e-prints, p. arXiv:2109.05130

Hawkins K., Jofré P., Masseron T., Gilmore G., 2015, MNRAS, 453, 758

Hayden M. R., et al., 2015, The Astrophysical Journal, 808, 132

Hayes C. R., et al., 2018, ApJ, 852, 49

Hayes C. R., et al., 2020, ApJ, 889, 63

Haywood M., Di Matteo P., Lehnert M. D., Katz D., Gómez A., 2013, A&A, 560, A109

Haywood M., Di Matteo P., Lehnert M. D., Snaith O., Khoperskov S., Gómez A., 2018, ApJ, 863, 113

Helmi A., 2008, Annual Review of Astronomy and Astrophysics, 15, 145

Helmi A., 2020, arXiv e-prints, p. arXiv:2002.04340

Helmi A., de Zeeuw P. T., 2000, MNRAS, 319, 657

Helmi A., White S. D. M., de Zeeuw P. T., Zhao H., 1999, , 402, 53

Helmi A., Babusiaux C., Koppelman H. H., Massari D., Veljanoski J., Brown A. G. A., 2018, , 563, 85

Hogg D. W., Eilers A.-C., Rix H.-W., 2019, The Astronomical Journal, 158, 147

Holoien T. W. S., Marshall P. J., Wechsler R. H., 2017, ApJ, 153, 249

Holtzman J. A., Shetrone M., Johnson J. A., Allende Prieto C., 2015, ApJ, 150, 148

Holtzman J. A., et al., 2018, ApJ, 156, 125

Horta D., et al., 2020, MNRAS, 493, 3363

Horta D., et al., 2021a, MNRAS, 500, 1385

Horta D., Hughes M. E., Pfeffer J. L., Bastian N., Kruijssen J. M. D., Reina-Campos M., Crain R. A., 2021b, MNRAS, 500, 4768

Horta D., et al., 2021c, MNRAS, 500, 5462

Horta D., Ness M. K., Rybizki J., Schiavon R. P., Buder S., 2022, MNRAS, 513, 5477

Howard C. D., Rich R. M., Reitzel D. B., Koch A., De Propris R., Zhao H., 2008, ApJ, 688, 1060

Hubble E. P., 1926, ApJ, 64, 321

Hughes M. E., Pfeffer J. L., Martig M., Reina-Campos M., Bastian N., Crain R. A., Kruijssen J. M. D., 2020, MNRAS, 491, 4012

Ibata R. A., Gilmore G., Irwin M. J., 1994, , 370, 194

Ibata R. A., Wyse R. F. G., Gilmore G., Irwin M. J., Suntzeff N. B., 1997, ApJ, 113, 634

Ibata R., Irwin M., Lewis G. F., Stolte A., 2001, ApJ Letters, 547, L133

Iorio G., Belokurov V., 2019, MNRAS, 482, 3868

Iorio G., Belokurov V., Erkal D., Koposov S. E., Nipoti C., Fraternali F., 2018, MNRAS, 474, 2142

Jean-Baptiste I., Di Matteo P., Haywood M., Gómez A., Montuori M., Combes F., Semelin B., 2017a, A&A, 604, A106

Jean-Baptiste I., Di Matteo P., Haywood M., Gómez A., Montuori M., Combes F., Semelin B., 2017b, A&A, 604, A106

Jekel C. F., Venter G., 2019, pwlf: A Python Library for Fitting 1D Continuous Piecewise Linear Functions. `https://github.com/cjekel/piecewise_linear_fit_py`

Jofré E., Petrucci R., Saffe C., Saker L., Artur de la Villarmois E., Chavero C., Gómez M., Mauas P. J. D., 2015, A&A, 574, A50

Johnson J. A., 2019, Science, 363, 474

Johnston K. V., Spergel D. N., Hernquist L., 1995, ApJ, 451, 598

Johnston K. V., Law D. R., Majewski S. R., 2005, ApJ, 619, 800

Johnston K. V., Bullock J. S., Sharma S., Font A., Robertson B. E., Leitner S. N., 2008, ApJ, 689, 936

Jönsson H., et al., 2018, ApJ, 156, 126

Jönsson H., et al., 2020, arXiv e-prints, p. arXiv:2007.05537

Jurić M., et al., 2008, ApJ, 673, 864

Kaempf T. A., de Boer K. S., Altmann M., 2005, A&A, 432, 879

Kafle P. R., Sharma S., Lewis G. F., Bland-Hawthorn J., 2012, ApJ, 761, 98

Kafle P. R., Sharma S., Lewis G. F., Bland-Hawthorn J., 2014, ApJ, 794, 59

Khoperskov S., Haywood M., Snaith O., Di Matteo P., Lehnert M., Vasiliev E., Naroenkov S., Berczik P., 2021, MNRAS, 501, 5176

Kisku S., et al., 2021, MNRAS,

Kobayashi C., Nakasato N., 2011, ApJ, 729, 16

Kobayashi C., Karakas A. I., Lugaro M., 2020, ApJ, 900, 179

Koch A., Grebel E. K., Martell S. L., 2019, A&A, 625, A75

Kollmeier J. A., et al., 2017, SDSS-V: Pioneering Panoptic Spectroscopy (`arXiv:1711.03234`)

Koposov S. E., et al., 2012, ApJ, 750, 80

Koppelman H. H., Helmi A., Massari D., Price-Whelan A. M., Starkenburg T. K., 2019a, arXiv e-prints, p. arXiv:1909.08924

Koppelman H. H., Helmi A., Massari D., Roelenga S., Bastian U., 2019b, A&A, 625, A5

Koppelman H. H., Helmi A., Massari D., Price-Whelan A. M., Starkenburg T. K., 2019c, A&A, 631, L9

Koppelman H. H., Bos R. O. Y., Helmi A., 2020, A&A, 642, L18

Kordopatis G., et al., 2013, MNRAS, 436, 3231

Kroupa P., 2001, MNRAS, 322, 231

Kruijssen J. M. D., 2014, Classical and Quantum Gravity, 31, 244006

Kruijssen J. M. D., 2015, MNRAS, 454, 1658

Kruijssen J. M. D., Portegies Zwart S. F., 2009, The Astrophysical Journal, 698, L158–L162

Kruijssen J. M. D., Pelupessy F. I., Lamers H. J. G. L. M., Portegies Zwart S. F., Icke V., 2011, MNRAS, 414, 1339

Kruijssen J. M. D., Maschberger T., Moeckel N., Clarke C. J., Bastian N., Bonnell I. A., 2012a, MNRAS, 419, 841

Kruijssen J. M. D., Pelupessy F. I., Lamers H. J. G. L. M., Portegies Zwart S. F., Bastian N., Icke V., 2012b, MNRAS, 421, 1927

Kruijssen J. M. D., Pfeffer J. L., Crain R. A., Bastian N., 2019a, MNRAS, 486, 3134

Kruijssen J. M. D., Pfeffer J. L., Reina-Campos M., Crain R. A., Bastian N., 2019b, MNRAS, 486, 3180

Kruijssen J. M. D., et al., 2020, arXiv e-prints, p. arXiv:2003.01119

Kunder A., et al., 2012, ApJ, 143, 57

Kunder A., et al., 2020, ApJ, 159, 270

Lane J. M. M., Bovy J., Mackereth J. T., 2021, arXiv e-prints, p. arXiv:2106.09699

Law D. R., Majewski S. R., 2010, ApJ, 714, 229

Law D. R., Johnston K. V., Majewski S. R., 2005, ApJ, 619, 807

Leaman R., VandenBerg D. A., Mendel J. T., 2013, MNRAS, 436, 122

Lee Y.-W., Kim J. J., Johnson C. I., Chung C., Jang S., Lim D., Kang Y., 2019, ApJ Letters, 878, L2

Leung H. W., Bovy J., 2019a, MNRAS, p. 2167

Leung H. W., Bovy J., 2019b, MNRAS, 483, 3255

Li H., Gnedin O., 2019, arXiv e-prints, p. arXiv:1908.00984

Li Y.-S., White S. D. M., 2008, MNRAS, 384, 1459

Li T. S., et al., 2021, arXiv e-prints, p. arXiv:2110.06950

Lind K., et al., 2015, Astronomy &amp$$ Astrophysics, 575, L12

Lindblad B., 1927, MNRAS, 87, 553

Mackereth J. T., Bovy J., 2018, PASA, 130, 114501

Mackereth J. T., Bovy J., 2020, MNRAS, 492, 3631

Mackereth J. T., et al., 2017, MNRAS, 471, 3057

Mackereth J. T., Crain R. A., Schiavon R. P., Schaye J., Theuns T., Schaller M., 2018, MNRAS, 477, 5072

Mackereth J. T., et al., 2019a, MNRAS, 482, 3426

Mackereth J. T., et al., 2019b, MNRAS, 482, 3426

Majewski S. R., Skrutskie M. F., Weinberg M. D., Ostheimer J. C., 2003, ApJ, 599, 1082

Majewski S. R., Zasowski G., Nidever D. L., 2011, ApJ, 739, 25

Majewski S. R., Schiavon R. P., Frinchaboy P. M., Allende Prieto C., Barkhouser R., 2017, ApJ, 154, 94

Malhan K., et al., 2022, ApJ, 926, 107

Maoz D., Mannucci F., Brandt T. D., 2012, MNRAS, 426, 3282

Marigo P., et al., 2017, ApJ, 835, 77

Marín-Franch A., et al., 2009, ApJ, 694, 1498

Marshall D. J., Robin A. C., Reylé C., Schultheis M., Picaud S., 2006, A&A, 453, 635

Martell S. L., Grebel E. K., 2010, A&A, 519, A14

Martell S. L., et al., 2016, ApJ, 825, 146

Martell S. L., et al., 2017, MNRAS, 465, 3203

Massari D., Koppelman H. H., Helmi A., 2019, arXiv e-prints, p. arXiv:1906.08271

Masseron T., Merle T., Hawkins K., 2016, BACCHUS: Brussels Automatic Code for Characterizing High accUracy Spectra (ascl:1605.004)

Masseron T., et al., 2019, A&A, 622, A191

Matsumoto T., Hayakawa S., Koizumi H., Murakami H., Uyama K., Yamagami T., Thomas J. A., 1982, in Riegler G. R., Blandford R. D., eds, American Institute of Physics Conference Series Vol. 83, The Galactic Center. pp 48–52, doi:10.1063/1.33493

Matsuno T., Aoki W., Suda T., 2019, ApJ Letters, 874, L35

Matsuno T., Hirai Y., Tarumi Y., Hotokezaka K., Tanaka M., Helmi A., 2021, arXiv e-prints, p. arXiv:2101.07791

Matteucci F., Greggio L., 1986, A&A, 154, 279

Matteucci F., Grisoni V., Spitoni E., Zulianello A., Rojas-Arriagada A., Schultheis M., Ryde N., 2019, MNRAS, 487, 5363

Matteucci F., Vasini A., Grisoni V., Schultheis M., 2020, MNRAS, 494, 5534

McCarthy I. G., Font A. S., Crain R. A., Deason A. J., Schaye J., Theuns T., 2012, MNRAS, 420, 2245

McMillan P. J., 2011, MNRAS, 414, 2446

McMillan P. J., 2017, MNRAS, 465, 76

McWilliam A., 1997, Annual Review of Astronomy and Astrophysics, 35, 503

McWilliam A., Rich R. M., 1994, ApJ, 91, 749

McWilliam A., Zoccali M., 2010, ApJ, 724, 1491

Mészáros S., et al., 2015, ApJ, 149, 153

Mészáros S., et al., 2018, Monthly Notices of the Royal Astronomical Society, 475, 1633

Mészáros S., Masseron T., García-Hernández D. A., Allende Prieto C., Beers T. C., 2020, MNRAS, 492, 1641

Milone A. P., et al., 2019, arXiv e-prints, p. arXiv:1910.09683

Minniti D., 1996, ApJ, 459, 175

Molloy M., Smith M. C., Evans N. W., Shen J., 2015, ApJ, 812, 146

Monachesi A., et al., 2019, MNRAS, 485, 2589

Montalbán J., et al., 2020, arXiv e-prints, p. arXiv:2006.01783

Monty S., Venn K. A., Lane J. M. M., Lokhorst D., Yong D., 2020, MNRAS, 497, 1236

Morrison H. L., Flynn C., Freeman K. C., 1990, ApJ, 100, 1191

Morrison H. L., Mateo M., Olszewski E. W., Harding P., Dohm-Palmer R. C., Freeman K. C., Norris J. E., Morita M., 2000, ApJ, 119, 2254

Myeong G. C., Evans N. W., Belokurov V., Sanders J. L., Koposov S. E., 2018, ApJ Letters, 863, L28

Myeong G. C., Vasiliev E., Iorio G., Evans N. W., Belokurov V., 2019, MNRAS, 488, 1235

Naab T., Ostriker J. P., 2017, Annual Review of Astronomy and Astrophysics, 55, 59

Naidu R. P., Conroy C., Bonaca A., Johnson B. D., Ting Y.-S., Caldwell N., Zaritsky D., Cargile P. A., 2020, ApJ, 901, 48

Naidu R. P., et al., 2021, arXiv e-prints, p. arXiv:2103.03251

Nassau J. J., Blanco V. M., 1958, ApJ, 128, 46

Nataf D. M., 2017, PASA, 34, e041

Nataf D. M., Udalski A., Gould A., Fouqué P., Stanek K. Z., 2010, ApJ Letters, 721, L28

Nataf D. M., et al., 2019, The Astronomical Journal, 158, 14

Navarro J. F., Steinmetz M., 2000, ApJ, 528, 607

Necib L., et al., 2020, Nature Astronomy,

Nemec J., Nemec A. F. L., 1991, PASA, 103, 95

Ness M., et al., 2013a, MNRAS, 430, 836

Ness M., et al., 2013b, MNRAS, 432, 2092

Ness M., Hogg D. W., Rix H. W., Martig M., Pinsonneault M. H., Ho A. Y. Q., 2016, ApJ, 823, 114

Newberg H. J., Yanny B., Willett B. A., 2009, ApJ Letters, 700, L61

Nidever D. L., Zasowski G., Majewski S. R., Bird J., Robin A. C., 2012, ApJ Letters, 755, L25

Nidever D. L., Bovy J., Bird J. C., Andrews B. H., 2014, ApJ, 796, 38

Nidever D. L., et al., 2015, ApJ, 150, 173

Nidever D. L., et al., 2020, The Astrophysical Journal, 895, 88

Nikakhtar F., et al., 2021, arXiv e-prints, p. arXiv:2104.08394

Nissen P. E., 2004, in McWilliam A., Rauch M., eds, Origin and Evolution of the Elements. p. 154 (`arXiv:astro-ph/0310326`)

Nissen P. E., Schuster W. J., 1997, A&A, 326, 751

Nissen P. E., Schuster W. J., 2010, A&A, 511, L10

Nomoto K., Kobayashi C., Tominaga N., 2013, Annual Review of Astronomy and Astrophysics, 51, 457

Nordlander T., et al., 2019, MNRAS, 488, L109

Norris J., 1987, ApJ Letters, 314, L39

Norris J., Bessell M. S., Pickles A. J., 1985, , 58, 463

Ortolani S., Renzini A., Gilmozzi R., Marconi G., Barbuy B., Bica E., Rich R. M., 1995, , 377, 701

Payne C. H., 1925, PhD thesis, RADCLIFFE COLLEGE.

Peñarrubia J., Walker M. G., Gilmore G., 2009, MNRAS, 399, 1275

Pfeffer J., Kruijssen J. M. D., Crain R. A., Bastian N., 2018, MNRAS, 475, 4309

Pfeffer J. L., Trujillo-Gomez S., Kruijssen J. M. D., Crain R. A., Hughes M. E., Reina-Campos M., Bastian N., 2020, MNRAS, 499, 4863

Pfeffer J., Lardo C., Bastian N., Saracino S., Kamann S., 2021, MNRAS, 500, 2514

Pietrukowicz P., et al., 2015, ApJ, 811, 113

Piffl T., et al., 2014, MNRAS, 445, 3133

Portail M., Wegg C., Gerhard O., Martinez-Valpuesta I., 2015, MNRAS, 448, 713

Portail M., Gerhard O., Wegg C., Ness M., 2017, MNRAS, 465, 1621

Posti L., Helmi A., 2019, A&A, 621, A56

Price-Whelan A., et al., 2018, Astropy/Astropy-V2.0-Paper: Final Draft, Zenodo, doi:10.5281/zenodo.1211397

Pritzl B. J., Venn K. A., Irwin M., 2005, ApJ, 130, 2140

Prochaska J. X., Naumov S. O., Carney B. W., McWilliam A., Wolfe A. M., 2000, ApJ, 120, 2513

Purcell C. W., Bullock J. S., Tollerud E. J., Rocha M., Chakrabarti S., 2011, , 477, 301

Queiroz A. B. A., et al., 2020a, arXiv e-prints, p. arXiv:2007.12915

Queiroz A. B. A., et al., 2020b, A&A, 638, A76

Queiroz A. B. A., et al., 2021, A&A, 656, A156

Rattenbury N. J., Mao S., Sumi T., Smith M. C., 2007, MNRAS, 378, 1064

Re Fiorentin P., Spagna A., Lattanzi M. G., Cignoni M., 2021, ApJ Letters, 907, L16

Reddy B. E., Tomkin J., Lambert D. L., Allende Prieto C., 2003, MNRAS, 340, 304

Reddy B. E., Lambert D. L., Allende Prieto C., 2006, MNRAS, 367, 1329

Reggiani H., Meléndez J., Kobayashi C., Karakas A., Placco V., 2017, A&A, 608, A46

Reid M. J., Brunthaler A., 2020, ApJ, 892, 39

Reina-Campos M., Hughes M. E., Kruijssen J. M. D., Pfeffer J. L., Bastian N., Crain R. A., Koch A., Grebel E. K., 2019, arXiv e-prints, p. arXiv:1910.06973

Renzini A., et al., 2015, MNRAS, 454, 4197

Rich R. M., 1988, ApJ, 95, 828

Rich R. M., 2013, The Galactic Bulge. p. 271, doi:10.1007/978-94-007-5612-0˙6

Rich R. M., Origlia L., Valenti E., 2012, ApJ, 746, 59

Rix H.-W., Bovy J., 2013, , 21, 61

Robertson B., Bullock J. S., Font A. S., Johnston K. V., Hernquist L., 2005, ApJ, 632, 872

Rodriguez-Gomez V., et al., 2016, MNRAS, 458, 2371

Rojas-Arriagada A., et al., 2014, A&A, 569, A103

Rojas-Arriagada A., Recio-Blanco A., de Laverny P., Mikolaitis Š., 2017, A&A, 601, A140

Rojas-Arriagada A., Zoccali M., Schultheis M., 2019, A&A, 626, A16

Rojas-Arriagada A., et al., 2020, MNRAS,

Russell H. N., 1929, ApJ, 70, 11

Ryde N., Schultheis M., Grieco V., Matteucci F., Rich R. M., Uttenthaler S., 2016, ApJ, 151, 1

Sanders J. L., Smith L., Evans N. W., 2019, MNRAS, 488, 4552

Santana F. A., Beaton R. L., Covey K. R., O'Connell J. E., 2021, arXiv e-prints, p. arXiv:2108.11908

Savino A., Posti L., 2019, Astronomy & Astrophysics, 624, L9

Savino A., Koch A., Prudil Z., Kunder A., Smolec R., 2020, arXiv e-prints, p. arXiv:2006.12507

Schaeffer R., Silk J., 1985, ApJ, 292, 319

Schaye J., et al., 2015, MNRAS, 446, 521

Schiavon R. P., Zamora O., Carrera R., Lucatello S., Robin A. C., Ness M., 2017a, MNRAS, 465, 501

Schiavon R. P., Johnson J. A., Frinchaboy P. M., Zasowski G., Mészáros S., 2017b, MNRAS, 466, 1010

Schiavon R. P., Mackereth J. T., Pfeffer J., Crain R. A., Bovy J., 2020, in Bragaglia A., Davies M., Sills A., Vesperini E., eds, IAU Symposium Vol. 351, IAU Symposium. pp 170–173 (arXiv:2002.08380), doi:10.1017/S1743921319007889

Schlafly E. F., Finkbeiner D. P., 2011, ApJ, 737, 103

Schönrich R., Binney J., Dehnen W., 2010, MNRAS, 403, 1829

Schönrich R., Asplund M., Casagrande L., 2011, MNRAS, 415, 3807

Schönrich R., Asplund M., Casagrande L., 2014, ApJ, 786, 7

Schultheis M., et al., 2017, A&A, 600, A14

Schuster W. J., Moreno E., Nissen P. E., Pichardo B., 2012, A&A, 538, A21

Schwarz G., 1978, Annals of Statistics, 6, 461

Scott N., van de Sande J., Sharma S., Bland-Hawthorn J., Freeman K., Gerhard O., Hayden M. R., McDermid R., 2021, ApJ Letters, 913, L11

Searle L., Zinn R., 1978, ApJ, 225, 357

Sesar B., Jurić M., Ivezić Ž., 2011, ApJ, 731, 4

Sestito F., et al., 2019, MNRAS, 484, 2166

Shetrone M. D., Côté P., Sargent W. L. W., 2001, ApJ, 548, 592

Shetrone M., Venn K. A., Tolstoy E., Primas F., Hill V., Kaufer A., 2003, ApJ, 125, 684

Shetrone M., et al., 2015, , 221, 24

Simpson J. D., et al., 2020, arXiv e-prints, p. arXiv:2011.02659

Skrutskie M. F., et al., 2006, ApJ, 131, 1163

Smith R. E., Scoccimarro R., Sheth R. K., 2007, , 75, 063512

Snaith O. N., Haywood M., Di Matteo P., Lehnert M. D., Combes F., Katz D., Gómez A., 2014, ApJ Letters, 781, L31

Sneden C., Cowan J. J., Gallino R., 2008, Annual Review of Astronomy and Astrophysics, 46, 241

Souto D., et al., 2020, ApJ, 890, 133

Spitler L. R., Forbes D. A., 2009, MNRAS, 392, L1

Stanek K. Z., Udalski A., SzymaŃski M., KaŁuŻny J., Kubiak Z. M., Mateo M., KrzemiŃski W., 1997, ApJ, 477, 163

Stebbins J., Whitford A. E., 1947, ApJ, 106, 235

Steinmetz M., Guiglion G., McMillan P. J., Matijevič G. R., 2020, ApJ, 160, 83

Stott J. P., et al., 2014, MNRAS, 443, 2695

Tang B., Fernández-Trincado J. G., Liu C., Yu J., Yan H., Gao Q., Shi J., Geisler D., 2020, ApJ, 891, 28

Timberlake T., 2011, arXiv e-prints, p. arXiv:1112.3635

Tissera P. B., Scannapieco C., Beers T. C., Carollo D., 2013, MNRAS, 432, 3391

Tolstoy E., Hill V., Tosi M., 2009, Annual Review of Astronomy and Astrophysics, 47, 371

Toomre A., 1964, ApJ, 139, 1217

Tremaine S. D., Ostriker J. P., Spitzer L. J., 1975, ApJ, 196, 407

Tsikoudi V., 1979, ApJ, 234, 842

Tully R. B., Fisher J. R., 1977, A&A, 500, 105

Tumlinson J., 2010, ApJ, 708, 1398

VandenBerg D. A., Brogaard K., Leaman R., Casagrand e L., 2013, ApJ, 775, 134

Vasiliev E., 2019, MNRAS, 484, 2832

Vasiliev E., Belokurov V., 2020, MNRAS, 497, 4162

Villalobos Á., Helmi A., 2008, MNRAS, 391, 1806

Vincenzo F., Spitoni E., Calura F., Matteucci F., Silva Aguirre V., Miglio A., Cescutti G., 2019, MNRAS, 487, L47

Virtanen P., et al., 2020, Nature Methods, 17, 261

Vivas A. K., et al., 2001, ApJ Letters, 554, L33

Wallerstein G., et al., 1997, Reviews of Modern Physics, 69, 995

Wallerstein G., Kovtyukh V. V., Andrievsky S. M., 2007, ApJ, 133, 1373

Wang X., et al., 2019, ApJ, 882, 94

Watkins L. L., Evans N. W., An J. H., 2010, MNRAS, 406, 264

Watkins L. L., van der Marel R. P., Sohn S. T., Evans N. W., 2019, ApJ, 873, 118

Wegg C., Gerhard O., 2013, MNRAS, 435, 1874

Weiland J. L., et al., 1994, ApJ Letters, 425, L81

Weinberg D. H., et al., 2019, ApJ, 874, 102

Weinberg D. H., et al., 2021, arXiv e-prints, p. arXiv:2108.08860

Wetzel A. R., 2011, MNRAS, 412, 49

Wheeler J. C., Sneden C., Truran James W. J., 1989, Annual Review of Astronomy and Astrophysics, 27, 279

White S. D. M., Rees M. J., 1978, MNRAS, 183, 341

Whitten D. D., et al., 2019, ApJ, 884, 67

Wilkinson M. I., Evans N. W., 1999, MNRAS, 310, 645

Wilson J. C., Hearty F. R., Skrutskie M. F., Majewski S. R., Holtzman J. A., Eisenstein D., 2019, PASA, 131, 055001

Wright E. L., et al., 2010, ApJ, 140, 1868

Xue X. X., et al., 2008, ApJ, 684, 1143

Xue X.-X., Rix H.-W., Ma Z., Morrison H., Bovy J., Sesar B., Janesh W., 2015, ApJ, 809, 144

Yanny B., et al., 2000, ApJ, 540, 825

Yanny B., Rockosi C., Newberg H. J., Knapp G. R., Adelman-McCarthy 2009a, ApJ, 137, 4377

Yanny B., et al., 2009b, ApJ, 700, 1282

Yong D., et al., 2013, ApJ, 762, 26

Yoshii Y., 1982, , 34, 365

Yuan H. B., Liu X. W., Xiang M. S., 2013, MNRAS, 430, 2188

Yuan Z., Chang J., Beers T. C., Huang Y., 2020, ApJ Letters, 898, L37

Zamora O., et al., 2015, ApJ, 149, 181

Zasowski G., Johnson J. A., Frinchaboy P. M., Majewski S. R., Nidever D. L., 2013, ApJ, 146, 81

Zasowski G., Ness M. K., García Pérez A. E., Martinez-Valpuesta I., Johnson J. A., Majewski S. R., 2016, ApJ, 832, 132

Zasowski G., Cohen R. E., Chojnowski S. D., Santana F., Oelkers R. J., Andrews B., 2017, ApJ, 154, 198

Zasowski G., et al., 2019, ApJ, 870, 138

Zhao G., Zhao Y.-H., Chu Y.-Q., Jing Y.-P., Deng L.-C., 2012, Research in Astronomy and Astrophysics, 12, 723

Zoccali M., et al., 2006, A&A, 457, L1

Zucker D. B., et al., 2021, arXiv e-prints, p. arXiv:2104.08684

de Jong J. T. A., Yanny B., Rix H.-W., Dolphin A. E., Martin N. F., Beers T. C., 2010, ApJ, 714, 663

de Jong R. S., Agertz O., Berbel A. A., Aird J., Alexander D. A., Amarsi A., 2019, The Messenger, 175, 3

van den Bosch F. C., Jiang F., Campbell D., Behroozi P., 2016, MNRAS, 455, 158